Centre Énergie, Matériaux et Télécommunications

THE DEVELOPMENT OF ELECTROCHEMICAL SENSORS FOR BIOMEDICAL APPLICATIONS: IN PARTICULAR, GLUCOSE SENSORS

Par

Khawtar Hasan Ahmed

Thèse présentée pour l'obtention du grade
de Philosophiae Doctor (Ph.D.)
en sciences de l'énergie et des matériaux

Jury d'évaluation

Président du jury et examinateur interne	François Vidal Professeur à l'INRS-ÉMT
Examinateur externe	Ricardo Izquierdo Professeur à l'École de technologie supérieure
Examinateur externe	Sasha Omanovic Professeur à l'Université McGill
Directeur de recherche	Mohamed Mohamedi Professeur à l'INRS-ÉMT

ACKNOWLEDGMENTS

The execution and completion of this thesis were carried out at the Institut National de la Recherche Scientifique (INRS), Quebec, Canada. It has been a long and unforgettable experience that could not have been achieved without the help and guidance of those around me.

First and foremost, I would like to express my deepest gratitude and respect to my supervisor, Prof. Mohamed Mohamedi, for his unwavering support and for welcoming me into his research group. I have learned a great deal from him throughout my doctoral journey. His expertise and guidance were invaluable, whether it was conducting experiments in the lab, preparing for my doctoral exam, or writing articles. He has always been patient, understanding, and supportive during difficult times. He has been an exceptional supervisor, and I feel immensely privileged to have had the opportunity to work under his mentorship. I owe him my sincerest respect and appreciation. Prof. Mohamedi not only shaped my academic growth but also helped me navigate the challenges of research with patience and wisdom.

I am sincerely grateful to the jury members, Prof. François Vidal, Prof. Sasha Omanovic and Prof. Ricardo Izquierdo for reviewing this work. Thank you for your valuable time and precious comments.

I would like to thank my group colleagues: Dr. Alonso, Dr. Naser, Dr. Xiaoying, Dr. Soraya, Dr. Mohamed, Yahia and Ahmad. I am immensely grateful for their constant help and for sharing their knowledge and experience whenever needed, both inside and outside the laboratory. Their guidance truly made this journey memorable and enriched my understanding in new areas.

I would like to thank the technicians and administrative staff in INRS-EMT, especially Christophe Chabanier, Catalin Harnagea, Tatiana Brahmi, Michelle Marcotte, Alex Lacombe, Anouar Amrani for being truly kind and helpful.

I would also like to thank my friends Dr. Sabrin, Abir, Jenan, Samira, Ahmed, Anouar for their unwavering encouragement and emotional support. It truly means a lot.

My deepest gratitude goes to the Libyan Ministry of Education for providing me with a scholarship and funding not only during my master's degree but also throughout my PhD in these past few years. Their generosity and support have contributed significantly to the successful completion of my PhD. I would also like to acknowledge the invaluable support of the following organizations for their support of my work: The Natural Sciences and Engineering Research Council of Canada (NSERC) and the Centre Québécois sur les Matériaux Fonctionnels (CQMF).

Finally, to my family, words cannot fully express how much your love, support, and sacrifices have meant to me throughout this process. To my parents, Atiga Alsalem and Hasan Ahmed, thank you for always believing in me and encouraging me to pursue my dreams. Your love and understanding have been my foundation, and I dedicate this achievement to you.

To my brothers, your support and encouragement has constantly driven me to the best of my capacities and allowed me to push through in difficult times. I am forever grateful for your presence in my life.

To my beloved husband, Hossin Alsharif, thank you for being my rock—your patience, kindness, and understanding have kept me grounded throughout this journey and have pushed me to excel in my work every day.

To my kids, Hebah, Rawan, Mohammed, and Riyad, thank you for your endless love, patience, and joy. Your infectious energy and laughter, along with your constant reminder of what truly matters, have kept me grounded and motivated. I love you all deeply, and just as you have been an inspiration to me, I hope I have become, and continue to be, an inspiration to you.

Khawtar Hasan Ahmad

ABSTRACT

The development of highly efficient, cost-effective, non-enzymatic glucose sensors has become a central focus for researchers and developers aiming to keep pace with the rapidly evolving landscape of fourth-generation, real-time, continuous glucose monitoring technologies. In response to these advancements, we have undertaken a comprehensive study focused on the design and development of advanced electrode materials based on self-supported alpha-manganese dioxide (α-MnO_2) nanostructures. These materials exhibit a synergistic combination of favorable intrinsic characteristics and high catalytic properties, positioning them as highly promising candidates for next-generation non-enzymatic glucose sensing applications.

In this context, the initial approach focused on fabricating carbon-based electrodes, owing to their well-established properties. Specifically, carbon paper (CP) and CP modified with carbon nanotubes (CP/CNTs) were investigated for their electrocatalytic activity toward glucose oxidation. These two electrodes served as effective supports for the direct growth of nanostructured MnO_2-based catalysts, which were successfully synthesized via a hydrothermal method.

The surface morphology, chemical composition, crystalline structure, and vibrational characteristics of the pristine CP, synthesized CP/CNTs composites, and MnO_2 nanostructures were systematically characterized using a suite of analytical techniques. These included scanning electron microscopy (SEM), energy-dispersive X-ray spectroscopy (EDS), X-ray diffraction (XRD), and Raman spectroscopy. To assess their electrochemical performance, the fabricated electrodes were further evaluated through cyclic voltammetry (CV) and chronoamperometry (CA), employing a standard three-electrode electrochemical cell configuration connected to an Autolab potentiostat/galvanostat.

The synthesized MnO_2 nanorod-based electrodes demonstrated superior performance in non-enzymatic glucose sensing. In particular, the free-standing manganese dioxide nanorods on carbon nanotubes (CNTs/MnO_2-NRs) electrode demonstrated significantly enhanced charge transfer kinetics and an increased electroactive surface area, both of which contributed to its superior catalytic efficiency for glucose oxidation. This electrode achieved a high sensitivity of 309.73 $\mu A\ mM^{-1}\ cm^{-2}$ with a low detection limit of 0.19 mM and within a linear detection range spanning 0.5−10 mM, well above the typical physiological glucose levels (3–8 mM). These characteristics underscore its strong potential for accurate and reliable glucose monitoring applications.

The electrode also exhibited excellent durability and outstanding selectivity for glucose, even in the presence of common interfering species such as ascorbic acid and uric acid. Additionally, it exhibited

notable antifouling properties in KCl-containing environments, which are particularly advantageous for maintaining signal stability and sensor longevity in physiologically relevant conditions. These features are critical for achieving reliable and accurate glucose detection within complex biological matrices. The integration of MnO_2 nanorods with CNTs into a freestanding nanostructured architecture not only enhance electron transport and surface reactivity but also offers mechanical stability and design flexibility. Collectively, this innovative configuration holds significant promise for the development of next-generation, high-performance electrochemical sensors with broad applicability across biomedical diagnostics, clinical monitoring, and analytical sensing platforms.

Keywords: Non-enzymatic sensor; glucose oxidation; manganese oxide nanorods; carbon nanotubes; hydrothermal; glucose sensing; interferences selectivity.

RÉSUMÉ

Le développement de capteurs de glucose non enzymatiques hautement efficaces et rentables est devenu une priorité pour les chercheurs et les développeurs qui souhaitent suivre l'évolution rapide du paysage des technologies de surveillance continue du glucose en temps réel de quatrième génération. En réponse à ces avancées, nous avons entrepris étude complète axée sur conception et le développement de matériaux d'électrode avancés basés sur des nanostructures de dioxyde d'alpha-manganèse (α-MnO_2) autoportées. Ces matériaux présentent une combinaison synergique de caractéristiques intrinsèques favorables et de propriétés catalytiques élevées, ce qui en fait des candidats très prometteurs pour les applications de détection non enzymatique du glucose de la prochaine génération.

Dans ce contexte, l'approche initiale s'est concentrée sur la fabrication d'électrodes à base de carbone, en raison de leurs propriétés bien établies. Plus précisément, le papier carbone (PC) et le PC modifié par des nanotubes de carbone (PC/NTC) ont été étudiés pour leur activité électrocatalytique dans l'oxydation du glucose. Ces deux électrodes ont servi de supports efficaces pour la croissance directe de catalyseurs nanostructurés à base de MnO_2, qui ont été synthétisés avec succès par une méthode hydrothermale.

La morphologie de surface, la composition chimique, la structure cristalline et les caractéristiques vibratoires du PC vierge, des composites PC/NTC synthétisés et des nanostructures MnO_2 ont été systématiquement caractérisées à l'aide d'une série de techniques analytiques. Celles-ci comprennent la microscopie électronique à balayage (MEB), la spectroscopie de rayons X à dispersion d'énergie (EDS), la diffraction des rayons X (DRX) et la spectroscopie Raman. Pour évaluer leurs performances électrochimiques, les électrodes fabriquées ont été évaluées par voltampérométrie cyclique (CV) et chronoampérométrie (CA), en utilisant une configuration standard de cellule électrochimique à trois électrodes connectées à un potentiostat/galvanostat Autolab.

Les électrodes synthétisées à base de nanotiges de MnO_2 ont démontré une performance supérieure dans la détection non enzymatique du glucose. En particulier, l'électrode NTC/MnO_2-NRs libre a démontré une cinétique de transfert de charge significativement améliorée et une surface électroactive accrue, qui ont toutes deux contribué à son efficacité catalytique supérieure pour l'oxydation du glucose. Cette électrode a atteint une sensibilité élevée de 309,73 $\mu A\ mM^{-1}\ cm^{-2}$ avec une limite de détection basse de 0,19 mM et dans une plage de détection linéaire couvrant 0,5–10 mM, bien au-dessus des niveaux typiques de glucose physiologique (3–8 mM). Ces caractéristiques soulignent son fort potentiel pour des applications de surveillance du glucose précises et fiables.

L'électrode a également présenté une excellente durabilité et une sélectivité exceptionnelle pour le glucose, même en présence d'espèces interférentes courantes telles que l'acide ascorbique et l'acide urique. En outre, elle présentait des propriétés antisalissures notables dans les environnements contenant du KCl, ce qui est particulièrement avantageux pour maintenir la stabilité du signal et la longévité du capteur dans des conditions physiologiques pertinentes. Ces caractéristiques sont essentielles pour obtenir une détection fiable et précise du glucose dans des matrices biologiques complexes. L'intégration de nanotiges de MnO_2 avec des NTC dans une architecture nanostructurée autoportante améliore non seulement le transport des électrons et la réactivité de la surface, mais offre également une stabilité mécanique et une flexibilité de conception. Collectivement, cette configuration innovante est très prometteuse pour le développement de la prochaine génération de capteurs électrochimiques de haute performance avec une large applicabilité dans les diagnostics biomédicaux, la surveillance clinique et les plates-formes de détection analytique.

Mots-clés: Capteur non enzymatique; oxydation du glucose; nanotiges d'oxyde de manganèse; nanotubes de carbone; hydrothermie; détection du glucose; sélectivité des interférences.

SOMMAIRE RÉCAPITULATIF

Le Développement De Capteurs Électrochimiques Pour Applications Biomédicales: Notamment, Les Capteurs De Glucose

Introduction

Le glucose est une source d'énergie vitale pour le corps humain, produite au cours de la dernière étape de la digestion des glucides. En réponse à l'augmentation du taux de glucose dans le sang, le pancréas sécrète une hormone appelée insuline. L'insuline facilite l'absorption du glucose dans les cellules de l'organisme par le transporteur de glucose de type 4 (GLUT4), ce qui permet aux cellules de le convertir en énergie utilisable. Ce processus permet de réduire l'excès de glucose dans la circulation sanguine et de maintenir une glycémie saine chez les personnes ayant une fonction métabolique normale. La glycémie est un indicateur clé de la santé, en particulier dans la gestion du diabète. Ces taux sont généralement mesurés en millimoles par litre (mmol/L) ou en milligrammes par décilitre (mg/dL). Selon Diabète Québec, la fourchette cible recommandée pour les personnes diabétiques se situe entre 4,0 et 7,0 mmol/L à jeun ou avant un repas, et entre 5,0 et 10,0 mmol/L deux heures après le début d'un repas. Lorsque la glycémie moyenne tombe en dessous de 4,0 mmol/L, elle peut entraîner une hypoglycémie (baisse du taux de sucre dans le sang). À l'inverse, lorsqu'elle dépasse 7,0 mmol/L, on parle d'hyperglycémie (taux de sucre élevé dans le sang). L'hypoglycémie résulte souvent d'un excès d'insuline, ce qui est particulièrement fréquent chez les diabétiques, notamment ceux de type I, qui dépendent essentiellement de l'insulinothérapie pour réguler leur glycémie. Au Canada, la glycémie est généralement évaluée à l'aide d'un test de glycémie à jeun (FPG) ou d'un test d'hémoglobine (A1C). Le test de la glycémie plasmatique à jeun peut être contrôlé par l'utilisateur lui-même à l'aide d'un lecteur de glycémie, tandis que le test de l'hémoglobine A1C est effectué en laboratoire. Le test A1C mesure l'hémoglobine glyquée et détermine la glycémie moyenne sur une période de 2 à 3 mois, la valeur cible étant inférieure à 7,0%. Le diabète est diagnostiqué avec un taux de FPG $\geq$ 7,0 mmol/L ou un taux d'A1C $\geq$ 6,5%. Le prédiabète est défini par un taux de glycémie de $\geq$ 6,1 à $<$ 7,0 mmol/L, ou un taux d'A1C de $\geq$ 6,0% à $<$ 6,5%. En outre, une glycémie $\geq$ 11,1 mmol/L mesurée 2 heures après la consommation d'une solution orale de glucose de 75 g, ou à n'importe quel moment de la journée, indique également un diabète. À titre de référence, des valeurs de glucose de 7,0 mmol/L et 11,1 mmol/L correspondent respectivement à 126 mg/dL et 200 mg/dL, en utilisant le facteur de conversion 1 mmol/L= 18,0182 mg/dL.

Le diabète est un trouble métabolique résultant d'un excès de glucose dans le sang qui ne peut être régulé par l'insuline seule, laquelle joue normalement un rôle central dans le maintien de l'équilibre glycémique. Il existe deux principaux types de diabète: le diabète de type I et le diabète de type II. Le diabète de type I, également appelé insulino-dépendant, est le plus souvent diagnostiqué chez les enfants et les adolescents, représentant environ 10% des personnes touchées par la maladie. Dans cette forme de la maladie, les cellules bêta du pancréas sont détruites par le système auto-immunitaire; il n'y a donc pas de production d'insuline et le glucose ne peut pas pénétrer dans les cellules, ce qui entraîne une accumulation de glucose dans la circulation sanguine. Le diabète de type II, également connu sous le nom de diabète résistant à l'insuline, représente la grande majorité des personnes atteintes de diabète (environ 90%) et touche principalement les adultes. Dans cette forme de diabète, le pancréas produit initialement suffisamment d'insuline, mais les récepteurs cellulaires de l'organisme ne parviennent pas à se lier à l'insuline. En conséquence, la glycémie augmente. Pour compenser cette résistance, le pancréas produit une quantité croissante d'insuline. Avec le temps, cette demande peut épuiser le pancréas, entraînant une diminution de la production d'insuline. Dans les deux types de diabète, le glucose ne peut pas pénétrer dans les cellules de l'organisme, ce qui entraîne son accumulation dans la circulation sanguine et endommage les vaisseaux sanguins. Plusieurs facteurs contribuent au développement du diabète de type II. L'excès de poids et la sédentarité sont les deux facteurs les plus importants. Un mode de vie et une alimentation malsains, le vieillissement, les antécédents familiaux et l'utilisation de certains médicaments sont d'autres facteurs qui contribuent au développement du diabète de type II. La détermination de la glycémie est essentielle pour diagnostiquer et gérer la maladie. Si elle n'est pas contrôlée, elle peut entraîner de graves complications, notamment des maladies cardiovasculaires, des crises cardiaques, de l'arthrite, des accidents vasculaires cérébraux, une perte de vision, une insuffisance rénale, des lésions nerveuses et même l'amputation d'un membre en raison d'une gangrène.

L'acide urique et l'acide ascorbique font partie des molécules électroactives naturellement présentes dans le liquide biologique de l'homme (par exemple, le sérum, le sang ou l'urine) qui peuvent interférer avec la détection du glucose, ce qui peut conduire à des mesures inexactes du glucose. L'acide urique (UA) est le produit final du métabolisme des purines, qui circule dans le sang pour être finalement éliminé par les reins. La concentration normale d'acide urique dans le sang se situe entre 0,18 et 0,42 mmol/L. Cependant, des niveaux élevés peuvent conduire à une condition connue sous le nom d'hyperuricémie et causer la goutte et des troubles liés aux reins. L'acide ascorbique (AA), communément appelé vitamine C, est généralement présent dans le sang à des concentrations plus faibles, comprises entre 0,023 et 0,085 mmol/L. Malgré ces concentrations relativement faibles, l'acide ascorbique joue plusieurs rôles vitaux dans le corps humain, notamment en soutenant le système immunitaire et en protégeant les tissus contre les dommages causés par les radicaux libres. De même, des niveaux élevés de vitamine C peuvent entraîner des problèmes de santé tels que diarrhées, vomissements, maux de tête, calculs rénaux, etc., tandis qu'une carence en vitamine C peut entraîner un risque de scorbut, une affection caractérisée par de la fatigue, des douleurs articulaires et un affaiblissement de l'immunité. Il est donc essentiel de surveiller la concentration de ces molécules pour établir un diagnostic efficace et gérer les soins de santé. Dans la détection électrochimique du glucose, il a été observé que les potentiels d'oxydation des espèces interférentes telles que l'UA et l'AA sont trop proches du potentiel d'oxydation du glucose, ce qui signifie que leurs signaux se chevauchent lors de la détection simultanée de ces molécules électroactives dans un échantillon au niveau d'une électrode nue. Par conséquent, il est essentiel de modifier l'électrode pour détecter les espèces électroactives à différents potentiels d'oxydation, ce qui détermine la sensibilité et la sélectivité du capteur. Les anions chlorure font partie des électrolytes les plus importants du sang (avec le potassium, le sodium et le bicarbonate) qui jouent un rôle vital dans le maintien de l'équilibre physiologique, en particulier dans la régulation de l'équilibre acido-basique (pH) du sang. Alors que la plage de référence typique du potassium dans le sérum sanguin se situe entre 3,5 et 5,0 mmol/L, les niveaux de concentration normaux des ions chlorure se situent entre 96 et 106 mmol/L, bien que cela puisse varier légèrement d'un laboratoire à l'autre. Les écarts par rapport à cette fourchette, souvent dus à des conditions telles que les vomissements, la diarrhée et d'autres maladies, peuvent perturber l'équilibre électrolytique et contribuer à des déséquilibres métaboliques ou à des désordres acido-basiques. Les ions chlorure ont un impact négatif sur la capacité de détection de l'électrode en provoquant un phénomène connu sous le nom d'empoisonnement de la surface ou d'encrassement de l'électrode. Ce phénomène est dû au fait que les ions chlorure sont fortement chimisorbés à la surface des électrodes (par exemple, les électrodes à base de Pt et d'Au). Sur les électrodes en or en particulier, cette interaction peut induire des interférences significatives, ce qui nuit gravement à l'activité électrochimique du capteur et à sa réactivité globale. Ces espèces interférentes ou substances encrassantes peuvent affecter la précision globale. Par conséquent, la sélectivité est un facteur clé pour déterminer la précision du capteur.

La détermination du glucose dans les capteurs électrochimiques implique essentiellement la réaction d'oxydation du glucose, qui entraîne la libération d'électrons sous la forme d'un signal de courant mesurable. La réaction nécessite une enzyme sélective pour catalyser l'oxydation du glucose en D-glucono-δ-lactone, en libérant deux protons et deux électrons de la molécule de glucose. Cette étape est suivie d'une étape d'hydrolyse rapide, au cours de laquelle le D-glucono-δ-lactone s'oxyde en acide gluconique. La réaction d'oxydation du glucose est essentielle dans de nombreux autres domaines tels que l'industrie alimentaire, les piles à combustible, les batteries, etc. Les capteurs électrochimiques sont des dispositifs qui appliquent des principes électrochimiques pour détecter et mesurer l'analyte cible en convertissant un changement physicochimique en un signal électrique quantifiable. Les principaux éléments qui composent les biocapteurs électrochimiques sont: l'élément de reconnaissance biologique, le transducteur électrochimique, le traitement du signal et le système d'affichage. Un élément de reconnaissance biologique (également appelé biorécepteur) est une molécule de reconnaissance biologique (telle qu'une enzyme, un anticorps, un acide nucléique, des microbes) qui interagit spécifiquement avec un analyte cible (tel que des biomolécules, des bactéries, des virus, des métaux lourds). Si l'élément de reconnaissance (élément de détection) est une molécule non biologique (telle qu'une nanomolécule) qui catalyse l'analyte cible d'intérêt, le capteur ne porte pas le terme « bio » et est appelé capteur électrochimique. Pour les capteurs électrochimiques de glucose, dans lesquels les mesures sont basées sur l'oxydation électrochimique du glucose, l'élément de reconnaissance est une enzyme ou un nanocatalyseur qui interagit avec le glucose dans l'échantillon biologique. Le transducteur électrochimique est l'électrode de travail dans les systèmes électrochimiques, qui transforme l'information de reconnaissance (changements biologiques/physiochimiques après l'interaction entre le récepteur et l'analyte) en un signal électrique mesurable qui peut être analysé à l'aide de différentes méthodes (dans ce cas, des techniques électrochimiques). Le signal transformé (signal électrique) est ensuite amplifié, traité dans leurs systèmes respectifs et ensuite affiché sous forme de signal quantifiable (courbes, graphiques, voltammogrammes, nombres). Les capteurs sont classés en différents types en fonction du type de récepteur et du système de transduction du signal/système de détection. En ce qui concerne la détection du glucose et en fonction du récepteur utilisé, il existe deux types de capteurs de glucose: les capteurs de glucose enzymatiques et les capteurs de glucose non enzymatiques. Les capteurs de glucose basés sur le système de transduction du signal sont classés en capteurs électrochimiques et optiques qui s'appuient respectivement sur les technologies électrochimiques et optiques pour détecter les changements de reconnaissance. Les capteurs optiques reposent sur des systèmes de transduction optique, tels que diverses techniques spectroscopiques optiques (par exemple, la fluorescence et la résonance plasmonique de surface (SPR)), pour détecter les concentrations de glucose. Ces systèmes mesurent les changements d'intensité, de longueur d'onde ou de polarisation de la lumière, qui sont directement proportionnels à la concentration de glucose dans l'échantillon. En revanche, les capteurs électrochimiques appliquent des techniques électrochimiques pour détecter les changements électrochimiques, généralement le courant électrique, le potentiel, la conductivité ou l'impédance. En conséquence, les capteurs électrochimiques sont classés en capteurs ampérométriques, voltampérométriques, potentiométriques, conductométriques et impédimétriques. Par exemple, les capteurs ampérométriques mesurent le flux de courant produit par les réactions électrochimiques d'oxydoréduction entre l'analyte cible et l'élément de reconnaissance dans une cellule électrochimique à un potentiel appliqué constant. Les capteurs voltampérométriques, comme les capteurs ampérométriques, reposent sur la mesure du flux de courant dans une cellule électrochimique entre l'électrode de travail (WE) et la contre-électrode (CE). Toutefois, contrairement aux capteurs ampérométriques, le courant de réponse en voltampérométrie est mesuré en fonction d'un potentiel appliqué qui varie au fil du temps. Ce potentiel est généralement balayé linéairement dans une plage prédéterminée, comme on le voit dans des techniques telles que la voltampérométrie cyclique (CV). La courbe courant-potentiel qui en résulte fournit des informations détaillées sur le comportement électrochimique de l'analyte, y compris le glucose. Le signal mesuré obtenu à partir de ces capteurs électrochimiques est directement lié à la concentration de l'analyte cible dans la solution. Les capteurs électrochimiques présentent plusieurs avantages par rapport à d'autres technologies de détection, notamment la simplicité, la stabilité, la rapidité de réponse, le faible coût et la possibilité de miniaturisation. Ils sont également connus pour leur sensibilité et leur sélectivité élevées. En raison de ces avantages, les capteurs électrochimiques sont largement utilisés dans divers domaines, tels que la sécurité alimentaire, les diagnostics médicaux et les soins de santé, les processus industriels, la surveillance de l'environnement, ainsi que dans les applications de biotechnologie et de bio-ingénierie.

Les capteurs électrochimiques de glucose ont joué un rôle essentiel dans la gestion du diabète, en surveillant les niveaux de glucose dans le sang. Au cours des dernières décennies, des progrès significatifs ont été réalisés dans l'amélioration de la conception des capteurs, des matériaux et des technologies afin d'accroître les performances, la facilité d'utilisation et la rentabilité. Les capteurs électrochimiques enzymatiques reposent sur des enzymes telles que la glucose oxydase (GOx) ou la glucose déshydrogénase (GDH) en tant que biocatalyseurs pour l'oxydation du glucose en acide gluconique. L'enzyme glucose oxydase (GOx) a été largement préférée pour ce type de réaction en raison de sa grande spécificité pour le glucose et de sa plus grande stabilité par rapport à d'autres enzymes. La première génération de capteurs de glucose à base de GOx a été introduite par Clark & Lyons en 1962. Cette première conception utilisait une membrane recouverte d'enzyme placée sur une électrode à oxygène pour catalyser l'oxydation du glucose. Dans cette configuration, le GOx catalysait la réaction du glucose avec l'oxygène moléculaire, qui agissait en tant qu'accepteur naturel d'électrons (médiateur) pour produire de l'acide gluconique et du peroxyde d'hydrogène (H_2O_2). Le concept de ces capteurs dépendants de l'oxygène était basé sur la détection du glucose en surveillant la consommation d'oxygène dans la réaction catalysée par GOx. Plus tard, en 1973, Guilbault et Lubrano ont présenté leur premier capteur ampérométrique de glucose, qui déterminait la concentration de glucose en mesurant le H_2O_2 généré dans la réaction enzymatique. Le capteur a détecté le courant libéré par l'oxydation du peroxyde d'hydrogène qui était proportionnel aux concentrations de glucose dans l'échantillon. Cependant, pour que cette réaction se produise à l'électrode de Pt, il fallait des potentiels de fonctionnement relativement élevés, environ +0,6 V par rapport à Ag/AgCl, ce qui présentait un risque d'interférence avec d'autres espèces électroactives présentes dans les fluides biologiques. La réaction d'oxydation du glucose dans ces capteurs de première génération se produit d'abord sur la couche enzymatique, plus précisément au niveau du centre redox actif de l'enzyme glucose oxydase, la flavine adénine dinucléotide (FAD). Au cours de la réaction, le FAD est réduit en $FADH_2$ lorsqu'il accepte les électrons du glucose, ce qui déclenche le cycle catalytique et conduit à la production ultérieure de H_2O_2. Malgré la grande capacité des capteurs basés sur le GOx à réagir spécifiquement au glucose et à fournir des mesures quantitatives du glucose, ils ont été limités par des problèmes d'imprécision dus aux variations et aux limitations de l'oxygène dissous dans les milieux physiologiques, connues sous le nom de « déficit en oxygène », qui affectent directement la réponse du capteur. En outre, les performances de ces capteurs dépendants de l'oxygène étaient également fortement affectées par la présence d'interférents électroactifs courants dans le sang, tels que l'acide ascorbique et l'acide urique. Ces substances sont facilement oxydées aux potentiels de fonctionnement élevés requis pour la détection de H_2O_2, ce qui entraîne une interférence du signal et une diminution de la sélectivité du capteur. Ces limitations ont conduit au développement de la deuxième génération de capteurs de glucose qui impliquent l'immobilisation de l'enzyme GOx sur un médiateur redox artificiel, remplaçant ainsi le médiateur d'oxygène naturel de la première génération. Dans cette conception, l'enzyme GOx a été immobilisée à proximité d'un médiateur d'électrons synthétique tel que le ferrocène, le ferricyanure, les complexes d'osmium ou les composés de quinone. Ces médiateurs facilitent le transfert rapide d'électrons du centre d'oxydoréduction actif de l'enzyme, le FAD, directement à la surface de l'électrode. Les capteurs enzymatiques à médiation pourraient éliminer les problèmes liés à l'oxygène; par exemple, le capteur a obtenu des lectures plus précises et une meilleure sélectivité en fonctionnant à des potentiels de détection plus bas. Cependant, les capteurs de deuxième génération ont également introduit de nouveaux défis. La toxicité potentielle de certains médiateurs (par exemple, le ferrocène, le ferricyanure ou les composés d'osmium) a suscité des inquiétudes en raison d'une fuite possible dans les tissus environnants. En outre, la complexité de la fabrication des capteurs et l'instabilité des enzymes ont affecté les performances globales et la praticité de ces capteurs de glucose de deuxième génération, limitant ainsi leur application clinique à grande échelle. La troisième génération de capteurs enzymatiques de glucose a été développée pour réaliser un transfert direct d'électrons (DET) entre l'enzyme et l'électrode, éliminant ainsi le besoin d'oxygène et de médiateurs artificiels. Cette avancée a été rendue possible grâce à des innovations dans les matériaux d'électrode et les techniques d'immobilisation des enzymes, permettant à l'enzyme- typiquement GOx- d'être directement immobilisée à la surface de l'électrode dans une configuration qui facilite un transfert d'électrons efficace à partir de son centre d'oxydoréduction actif (FAD). Les capteurs enzymatiques à base de DET ont réussi à surmonter les limitations associées à la dépendance à l'oxygène et à la toxicité liée aux médiateurs. Ils fonctionnent à des potentiels faibles, proches du potentiel d'oxydoréduction de l'enzyme, ce qui réduit considérablement la probabilité d'interférence des substances électroactives. De plus, la réduction des composants de la chaîne de réaction a permis de concevoir des capteurs plus compacts et plus efficaces. Malgré ces progrès, le transfert direct d'électrons du site actif de l'enzyme à l'électrode reste un défi technique important. Dans le cas du GOx, le centre d'oxydoréduction FAD est fermement lié et profondément enfoui dans la matrice du GOx, à environ 13 Å. Cette séparation spatiale empêche un transfert d'électrons efficace, même avec des matériaux d'électrode et des stratégies d'immobilisation améliorés. Un autre inconvénient des capteurs de glucose de troisième génération est qu'ils sont toujours basés sur des enzymes et continuent donc à souffrir de plusieurs limitations inhérentes. Il s'agit notamment de l'instabilité de l'enzyme dans le temps, de la complexité du processus de fabrication et de la nécessité de conditions environnementales spécifiques (pH, température, etc.) pour maintenir l'activité de l'enzyme.

Des efforts considérables ont été déployés pour atténuer les limites des capteurs enzymatiques de glucose et améliorer leur précision, leur sensibilité et leur sélectivité. Par exemple, l'apport d'oxygène à l'électrode par l'incorporation de matériaux riches en oxygène (pâte de carbone riche en oxygène) et l'utilisation de membranes limitant la diffusion ont permis de résoudre le problème du « déficit d'oxygène », assurant ainsi un apport constant d'oxygène pour soutenir la réaction enzymatique, ce qui améliore la précision du capteur. Parallèlement, des efforts ont été faits pour réduire l'interférence des espèces électroactives. L'utilisation de membranes perméables, telles que le Nafion et l'acétate de cellulose, a permis de limiter efficacement l'accès aux espèces interférentes. En outre, des électrocatalyseurs tels que le bleu de Prusse (PB) ou des métaux nobles comme le Rh ont été employés pour abaisser le potentiel de fonctionnement nécessaire à la détection de H_2O_2 dans une plage de +0,0 à –0,20 V. Ces tentatives ont joué un rôle efficace dans l'amélioration de la sélectivité du capteur. Plus important encore, l'incorporation de matériaux nanostructurés tels que les nanoparticules métalliques, les nanostructures d'oxyde métallique, les nanotubes de carbone, le graphène et les polymères conducteurs a considérablement amélioré les stratégies d'immobilisation des enzymes. Ces matériaux offrent une surface élevée, une excellente conductivité électrique et une fonctionnalisation polyvalente de la surface, et ont conduit à des améliorations substantielles des performances globales du capteur en termes de précision, de sélectivité et de sensibilité, ce qui a ouvert la voie au développement de systèmes de surveillance du glucose en continu et en temps réel. Malgré des avancées significatives dans le domaine des capteurs de glucose électrochimiques enzymatiques, ceux-ci sont toujours confrontés à des limitations notables, en particulier en ce qui concerne leur stabilité à long terme. Un problème majeur est la perte progressive de l'activité enzymatique au fil du temps, souvent due à la dénaturation du GOx à la surface de l'électrode. Le GOx est très sensible aux conditions environnementales telles que le pH, la température, les produits chimiques toxiques et l'humidité. En outre, le processus d'immobilisation de l'enzyme est souvent complexe et coûteux, ce qui contribue au coût global des capteurs enzymatiques de glucose. Actuellement, la plupart des capteurs de glucose commerciaux sont basés sur la méthode de la piqûre au bout du doigt, où une lancette (aiguille) est utilisée pour recueillir une goutte de sang, qui est ensuite placée sur une bandelette de test enzymatique jetable insérée dans un dispositif de détection. En quelques secondes, la glycémie est mesurée et affichée. Bien que ces capteurs soient devenus de plus en plus compacts et précis, permettant une autosurveillance efficace de la glycémie (ASG), ils posent encore des problèmes aux personnes atteintes de diabète. Il s'agit notamment de la douleur et de l'inconfort associés aux piqûres répétées et de la nécessité d'effectuer des mesures fréquentes tout au long de la journée pour maintenir un contrôle adéquat de la glycémie.

Les capteurs de surveillance continue du glucose (CGM) ont radicalement changé la gestion du diabète en offrant des informations en temps réel et une surveillance continue des niveaux de glycémie, réduisant ainsi le risque de complications à court et à long terme. Contrairement aux dispositifs traditionnels d'autosurveillance de la glycémie, les systèmes de CGM, disponibles sous forme implantable ou portable, offrent une alternative moins invasive, moins douloureuse et plus pratique pour les personnes vivant avec le diabète. Le concept de base du CGM consiste à implanter un petit capteur, souvent à l'aide d'une aiguille, juste sous la peau. Ce capteur mesure en permanence le taux de glucose interstitiel et transmet sans fil les données à un dispositif de surveillance externe, tel qu'un récepteur ou un portable, un smartphone ou une pompe à insuline. Lorsqu'il est intégré à une pompe à insuline, le système peut fonctionner comme un système en boucle fermée, parfois appelé pancréas artificiel, dans lequel le capteur suit les niveaux de glucose et la pompe ajuste automatiquement l'administration d'insuline en réponse. Cette boucle de rétroaction en temps réel permet un contrôle plus strict de la glycémie, une amélioration de la qualité de vie du patient et une réduction de la charge liée à la surveillance manuelle et à la gestion de l'insuline.

Au cours des deux dernières décennies, des entreprises de premier plan telles que Dexcom, Medtronic et Abbott ont réalisé des avancées significatives dans le domaine des capteurs CGM. Les premières générations de systèmes CGM étaient considérées comme invasives en raison de la nécessité d'effectuer de fréquentes ponctions cutanées pour la détection et l'étalonnage du glucose. Toutefois, des innovations constantes ont permis de mettre au point des capteurs moins douloureux, des capteurs peu invasifs qui nécessitent une fine aiguille placée juste sous la peau, ce qui provoque une douleur minime et élimine la nécessité d'effectuer une prise de sang. Ces capteurs surveillent en permanence les niveaux de glucose dans le liquide interstitiel sous-cutané toutes les quelques minutes, fournissant ainsi une image dynamique des fluctuations du glucose au fil du temps. La plupart des systèmes de CGM actuellement sur le marché sont encore basés sur des capteurs électrochimiques enzymatiques. Une tendance croissante dans ce domaine est le développement de technologies de détection du glucose peu invasives et non invasives, visant à surveiller les niveaux de glucose dans des fluides biologiques alternatifs tels que les larmes, la salive, la sueur, l'urine et le liquide interstitiel sous-cutané. Ces innovations pourraient potentiellement éliminer complètement la nécessité de piquer la peau, ce qui augmenterait encore le confort et l'accessibilité pour les utilisateurs. Au-delà de la commodité, les systèmes CGM modernes offrent des alertes prédictives en temps réel pour les événements hypoglycémiques ou hyperglycémiques potentiels, ce qui permet aux utilisateurs de prendre des mesures proactives et de maintenir un contrôle glycémique plus strict. Malgré ces avantages, des défis subsistent. Les problèmes liés à la précision des capteurs, à la stabilité des signaux et à la fiabilité à long terme, en particulier dans les systèmes portables ou implantables, doivent encore être résolus pour que le potentiel des technologies CGM soit pleinement exploité.

Ces problèmes persistants ont limité l'adoption et la commercialisation des capteurs de glucose enzymatiques de troisième génération, ce qui a incité à se concentrer sur les technologies de détection du glucose non enzymatiques. Afin de surmonter les inconvénients inhérents aux systèmes enzymatiques- en particulier les problèmes liés à l'instabilité et à la dénaturation des enzymes- les chercheurs ont exploré la modification des surfaces des électrodes avec des catalyseurs non biologiques, ce qui a donné naissance à la quatrième génération de capteurs de glucose. Les capteurs de glucose non enzymatiques (NEGS) ne s'appuient pas sur des enzymes comme catalyseurs pour la détection du glucose. Ils utilisent plutôt des matériaux à base de métaux nobles ou de métaux de transition/oxydes métalliques ayant une activité catalytique intrinsèque pour l'oxydation du glucose. Ces catalyseurs permettent l'électrooxydation directe des molécules de glucose à la surface de l'électrode. Dans ce mécanisme, les molécules de glucose subissent une oxydation électrochimique directement sur l'électrode modifiée, générant un signal électrique mesurable en corrélation avec la concentration de glucose dans l'échantillon. Dans les capteurs de glucose non enzymatiques, les atomes actifs présents à la surface de l'électrode modifiée ou du matériau de l'électrode lui-même agissent comme des sites catalytiques pour l'adsorption puis l'oxydation électrocatalytique des molécules de glucose. Ces sites actifs permettent une interaction directe avec le glucose, ce qui entraîne une réponse électrochimique proportionnelle à sa concentration. Pour décrire les mécanismes catalytiques sous-jacents de l'oxydation du glucose sur les NEGS à base de métaux, deux modèles prédominants ont été proposés dans la littérature: (i) le modèle de chimisorption activée et (ii) le médiateur d'adatomes d'oxyde hydrique naissant (IHOAM). Le premier modèle, le modèle de chimisorption activée, proposé par Pletcher, suppose que le processus électrocatalytique d'oxydation du glucose commence par l'adsorption de l'analyte cible, le glucose, sur la surface de l'électrode. Le processus implique l'abstraction d'hydrogène (l'élimination d'un atome d'hydrogène de l'hémiacétalique C1) qui s'accompagne simultanément de la chimisorption d'espèces organiques réactives sur la surface de l'électrode métallique. Ce processus est considéré comme l'étape déterminant le taux dans la plupart des expériences d'électrooxydation du glucose. Le glucose déshydrogéné (espèce organique) s'oxyde en gluconolactone (en libérant $2e^-$ et en éliminant le $2H^+$), qui est ensuite oxydé en acide gluconique par une hydrolyse rapide. Le modèle IHOAM proposé par Burke suggère que les atomes métalliques actifs à la surface de l'électrode sont confrontés à une étape de pré-oxydation par des anions hydroxydes réactifs, formant une couche d'oxyde hydrique naissante (pré-monocouche) qui sert de médiateur à l'oxydation des espèces adsorbées à des potentiels inférieurs. On pense que la couche de OH_{ads} adsorbée joue un rôle crucial dans le processus d'électrocatalyse dans de nombreuses applications, en particulier l'électrooxydation du glucose, et la formation de OH_{ads} augmente dans des conditions fortement alcalines. Il a été rapporté que le modèle IHOAM décrit de manière complémentaire le processus électrocatalytique complexe du glucose avec le modèle de chimisorption activée, alors que ce dernier décrit uniquement le processus d'adsorption du glucose sur la surface métallique sans prendre en compte le rôle oxydatif des radicaux hydroxydes, un rôle qui a été mis en évidence dans de nombreux rapports. Il est essentiel de comprendre ces mécanismes pour optimiser les matériaux des capteurs et améliorer la sensibilité, la sélectivité et la stabilité. Parmi les métaux les plus étudiés pour les NEGS figurent les métaux nobles (par exemple, Au et Pt); cependant, leur application pratique est limitée par plusieurs facteurs: coût élevé, susceptibilité à l'empoisonnement de la surface- en particulier par les ions chlorure- et interférence d'autres espèces électroactives, ce qui peut compromettre la sélectivité et la stabilité à long terme du capteur. Parallèlement, les métaux de transition, tels que le Ni, le Cu et le Co, ont fait l'objet d'une attention particulière en raison de leur faible coût, de leur disponibilité abondante et de leur comportement catalytique prometteur. Contrairement aux métaux nobles, le mécanisme d'oxydation du glucose sur les électrodes à base de métaux de transition ne suit généralement pas les modèles de chimisorption activée ou d'IHOAM. Au lieu de cela, il est principalement régi par des réactions d'oxydoréduction se produisant au niveau des centres métalliques. Pour surmonter les limitations et améliorer les performances des électrodes à base de métaux nobles et non nobles, les chercheurs ont exploré l'incorporation d'alliages métalliques, de composites hybrides et de matériaux nanostructurés. Ces modifications améliorent les propriétés telles que la conductivité électrique, la surface et la densité du site actif, améliorant ainsi la sensibilité, la sélectivité et la stabilité des NEGS pour une surveillance fiable du glucose.

Les oxydes de métaux de transition ont fait l'objet d'une attention particulière dans le développement de capteurs de glucose non enzymatiques (NEGS) en raison de leur stabilité chimique, de leur disponibilité abondante et de leur faible coût. Le mécanisme de détection du glucose dans de nombreux NEGS à base d'oxyde métallique dépend principalement de l'interaction entre la molécule de glucose et les centres d'oxydoréduction actifs de l'oxyde métallique, qui deviennent catalytiquement actifs après l'activation de la surface par les ions hydroxyde (OH^-). Ces capteurs fonctionnent généralement dans des milieux fortement alcalins, généralement autour de pH 13, car la présence d'ions hydroxyde (OH^-) est essentielle pour la formation d'espèces intermédiaires clés à la surface de l'oxyde métallique, qui à leur tour participent au cycle redox requis pour une oxydation efficace du glucose. Les mécanismes de détection du glucose de la plupart des oxydes de métaux de transition tels que Co_3O_4, NiO et CuO sont généralement similaires. Ces matériaux facilitent l'oxydation du glucose par la formation d'intermédiaires redox, qui peuvent ensuite être ramenés à leur état d'oxyde métallique d'origine, comme observé dans le cycle redox de Co_3O_4. L'oxyde de manganèse (MnO_2) fonctionne également en milieu fortement alcalin; cependant, contrairement aux autres oxydes, le MnO_2 interagit directement avec le glucose sans l'intervention de médiateurs redox. Ce mécanisme unique simplifie le processus de détection tout en permettant une détection non enzymatique du glucose. Il a été signalé que les oxydes métalliques susmentionnés présentent une activité catalytique limitée pour l'oxydation du glucose à des niveaux de $pH < 10$, mais leur activité catalytique devient significative avec l'augmentation des valeurs de pH de l'électrolyte, ce qui peut limiter leurs applications cliniques qui nécessitent un pH de l'électrolyte d'environ 7,4 ou neutre. L'oxyde ferrique présente une activité électrocatalytique pour l'oxydation du glucose à sa surface, même dans des conditions de pH neutre. Toutefois, sa sensibilité en pH neutre reste assez faible par rapport aux capteurs fonctionnant à des valeurs de pH plus élevées. Malgré tous les efforts déployés pour comprendre le mécanisme de détection de l'oxydation du glucose par des capteurs non enzymatiques, le processus n'est toujours pas entièrement compris, en particulier lorsqu'il s'agit de capteurs de glucose à base de MnO_2, en raison du manque d'études relatives à ce type de capteurs.

Les NEGS offrent plusieurs avantages, notamment la simplicité, la stabilité et l'indépendance par rapport aux problèmes liés aux enzymes, bien qu'ils puissent présenter une sélectivité inférieure à celle des EGS. Le choix entre les types EGS et NEGS dépend de facteurs tels que les besoins de sélectivité, les exigences de sensibilité, les considérations de coût et les contextes d'application spécifiques. Une attention considérable a été portée à la synthèse de matériaux d'électrode nanostructurés pour les capteurs non enzymatiques, avec des caractéristiques optimisées pour améliorer les performances du capteur. La recherche actuelle se concentre de plus en plus sur le développement de technologies de capteurs électrochimiques de glucose de quatrième génération. Ces capteurs de nouvelle génération visent à surmonter les limites des générations précédentes en améliorant considérablement les performances, la précision et l'expérience de l'utilisateur. Les capteurs de glucose de quatrième génération intègrent souvent des caractéristiques avancées telles qu'une sélectivité accrue, des capacités de surveillance continue, la miniaturisation, la portabilité, la connectivité sans fil, une biocompatibilité améliorée, la longévité et des interfaces conviviales. Bien que les EGS aient été largement utilisés et restent fondamentaux pour la surveillance du glucose, ils sont généralement classés dans les premières générations de technologie des capteurs. Par conséquent, ils ne sont généralement pas considérés comme faisant partie du paradigme émergent des capteurs de quatrième génération. Les technologies émergentes dans ce domaine peuvent englober les NEGS, les capteurs implantables, les capteurs microfluidiques et d'autres approches innovantes qui élargissent les horizons des capacités de détection du glucose. Les matériaux les plus étudiés pour la détection électrochimique du glucose dans les NEGS comprennent les matériaux à base de carbone (tels que les nanotubes de carbone, le graphène et l'oxyde de graphène), les nanoparticules métalliques (notamment Au, Ag et Pt), les polymères conducteurs et les oxydes de métaux de transition. Ces matériaux sont souvent utilisés en combinaison ou en tant que structures composites pour améliorer de manière synergique les performances des capteurs, notamment en termes de sensibilité, de sélectivité et de stabilité à long terme.

Le dioxyde de manganèse (MnO_2) est apparu comme un matériau prometteur pour le développement de capteurs électrochimiques de glucose de quatrième génération, en raison d'une série de propriétés avantageuses. Plusieurs facteurs clés contribuent à sa popularité croissante dans ce domaine: (i) une activité catalytique élevée pour l'oxydation du glucose, permettant une détection rapide et sensible; (ii) sa biocompatibilité, qui lui permet d'interagir avec des échantillons biologiques sans provoquer d'effets indésirables; (iii) une disponibilité abondante et un faible coût, contribuant à la faisabilité de la production de capteurs à grande échelle; et (vi) sa stabilité dans diverses conditions environnementales, garantissant la longévité et la fiabilité des capteurs de glucose. Ces caractéristiques font du MnO_2 un candidat très intéressant pour les plates-formes non enzymatiques de détection du glucose de la prochaine génération. Un autre avantage notable du MnO_2 est sa remarquable polyvalence. Il peut être synthétisé dans une variété de morphologies, ce qui offre une grande flexibilité dans la conception des capteurs et les processus de fabrication. Malgré ces avantages, les capteurs de glucose à base de MnO_2 restent relativement peu explorés dans la littérature. Pour améliorer les performances électrochimiques des matériaux de détection, les chercheurs étudient souvent différentes nanostructures et morphologies. Parmi celles-ci, les structures en nanotiges ont attiré l'attention en raison de leur rapport surface/volume élevé, qui offre une plus grande densité de sites électrochimiquement actifs. Par rapport aux configurations en couches minces, les nanotiges augmentent considérablement la surface électrochimique (*ECSA*), améliorant ainsi la sensibilité et l'efficacité de la détection du glucose. L'architecture tridimensionnelle des nanotiges améliore encore leurs performances électrochimiques en facilitant l'accès des ions de l'électrolyte à la surface de l'électrode, en accélérant la cinétique du transfert de charge et en augmentant la surface effective accessible pour les processus électrochimiques. En outre, la disposition hiérarchique des nanotiges favorise un transport efficace des charges à l'intérieur du matériau de l'électrode, ce qui atténue les limitations de diffusion. Cela améliore non seulement la mobilité des ions, mais aussi l'utilisation de la matière active, contribuant ainsi à une augmentation significative de l'*ECSA*. Enfin, les nanotiges présentent souvent une activité électrochimique accrue, en grande partie grâce à leurs propriétés de surface uniques et à leurs facettes cristallographiques spécifiques, qui permettent une distribution plus dense des sites actifs disponibles pour les réactions électrochimiques. Les propriétés électrocatalytiques favorables de MnO_2 sont étroitement liées à sa cristallographie et à sa morphologie. En ce qui concerne la cristallographie, le MnO_2 possède diverses structures cristallines polymorphes, telles que α, β, R, γ, δ et λ, qui diffèrent en fonction de l'arrangement de l'unité octaédrique de base MnO_6, donnant lieu à la formation de différentes sortes de tunnels, de couches ou de pores 3D au sein de la structure cristalline. Parmi les différents polymorphes de MnO_2, α-MnO_2, connu sous le nom de hollandite, résultant des chaînes octaédriques doubles de MnO_6 partagées au niveau des coins et des arêtes, a suscité plus d'intérêt en tant que matériau catalytique pour les capteurs de glucose en raison de ses cadres de tunnels uniques. Plus précisément, α-MnO_2 présente des tunnels (1x1) de dimensions 1,9 Å x 1,9 Å et des tunnels plus grands (2x2) de dimensions 4,6 Å x 4,6 Å. Ces tunnels structurels facilitent considérablement la diffusion des ions et améliorent la cinétique du transfert d'électrons. Les tunnels (2x2) sont généralement stabilisés par l'incorporation de cations tels que K^+, Ag^+, NH_4^+ et Ba^{2+}, qui sont généralement introduits au cours du processus de synthèse. Ces ions stabilisateurs soutiennent non seulement l'intégrité structurelle du cadre du tunnel, mais influencent également le comportement électrochimique du matériau. En outre, les nanostructures α-MnO_2 peuvent être synthétisées dans une variété de morphologies, y compris des formations de type dendrite, des réseaux de nanotiges, des réseaux de nanotubes, des nanofils et des structures de type nanofleur. Ces diverses morphologies sont souvent obtenues par synthèse hydrothermale, où des paramètres expérimentaux spécifiques tels que la température, le temps de réaction, la concentration du précurseur et le pH jouent un rôle essentiel.

Il est important de noter que les matériaux MnO_x, y compris le MnO_2, souffrent intrinsèquement d'une faible conductivité électrique. Pour surmonter cette limitation et améliorer les performances électrochimiques, il est essentiel d'intégrer le MnO_2 à des substrats hautement conducteurs, en particulier des substrats à base de carbone. Il a été rapporté que la croissance directe de matériaux actifs sur une matrice conductrice, telle que le papier carbone, le tissu de carbone ou les nanotubes de carbone, peut améliorer de manière significative leur performance électrochimique grâce à la formation d'abondants sites actifs. Pour une conductivité et des performances optimales, le catalyseur MnO_2 doit être cultivé directement sur le substrat conducteur sans utiliser de liants ou d'autres additifs, qui peuvent interférer avec les résultats électrochimiques et altérer l'électroactivité du catalyseur. Par conséquent, le développement d'un catalyseur MnO_2 autoportant sur un substrat conducteur en papier carbone est crucial pour améliorer les performances électrocatalytiques du capteur. Étant donné les propriétés distinctives de α-MnO_2, il convient d'accorder une attention particulière à l'optimisation des paramètres de synthèse afin de promouvoir la formation de réseaux de nanotiges α-MnO_2 bien alignés sur la surface du substrat.

À notre connaissance, il y a un manque notable d'études portant spécifiquement sur l'application des nanotiges de MnO_2 pour la détection électrochimique du glucose. Par conséquent, l'objectif principal de ce travail est d'étudier les performances de détection électrochimique des nanotiges de MnO_2 synthétisés par une méthode hydrothermique en une seule étape pour la détection non enzymatique du glucose. Un aspect essentiel de cette étude consiste à évaluer la sensibilité de l'électrode et son efficacité globale dans la détection du glucose, en utilisant diverses techniques électrochimiques tout en examinant l'influence de différents supports catalytiques. L'évaluation de la sensibilité, de la sélectivité et de la stabilité de ce matériau d'électrode rentable et évolutif est essentielle pour déterminer sa viabilité dans les systèmes de surveillance continue du glucose, y compris les dispositifs portables et implantables. En outre, étant donné que les espèces interférentes électroactives peuvent avoir un impact significatif sur les performances du capteur, ce travail vise également à évaluer la sélectivité de l'électrode en examinant sa réponse électrochimique en présence d'agents interférents courants tels que l'acide urique, l'acide ascorbique et le chlorure de potassium. Cette évaluation complète fournira des informations précieuses sur l'utilité des nanotiges de MnO_2 en tant que matériau actif dans les capteurs de glucose de la prochaine génération.

Un capteur électrochimique de glucose efficace doit répondre à plusieurs critères essentiels pour garantir des performances fiables, précises et efficaces, en particulier dans les applications biomédicales. Tout d'abord, il doit faire preuve d'une sensibilité et d'une sélectivité élevées, permettant une détection précise du glucose même à de faibles concentrations, tout en minimisant les interférences dues à d'autres espèces électroactives présentes dans les fluides biologiques. Le capteur doit avoir un temps de réponse rapide, permettant une surveillance en temps quasi réel des fluctuations du glucose, et une large plage linéaire pour détecter avec précision les niveaux de glucose faibles et élevés. La stabilité à long terme et la reproductibilité sont essentielles pour garantir des mesures cohérentes dans le temps, tandis que la biocompatibilité est cruciale si le capteur est en contact direct avec le corps. En outre, la facilité d'étalonnage et l'intégration avec d'autres dispositifs (tels que les pompes à insuline ou les applications mobiles) sont nécessaires pour une utilisation pratique en milieu clinique et dans la vie de tous les jours. Enfin, le capteur doit être rentable, convivial et adaptable à différentes conditions physiologiques, ce qui le rend adapté à la surveillance continue du glucose ou à d'autres applications médicales.

Objectif de la thèse

Cette thèse se compose de sept chapitres principaux et est organisée comme suit:

Chapitre 1: fournit une vue d'ensemble du diabète, en soulignant sa prévalence, son impact et le besoin critique d'une surveillance efficace du glucose dans la gestion de la condition diabétique. Il présente également les capteurs électrochimiques de glucose ainsi qu'une revue détaillée de la littérature sur le développement des capteurs électrochimiques de glucose EGS, CGM, NEGS et NEGS utilisant le MnO_2 comme composant clé. Le chapitre se termine par l'énoncé de la problématique et les objectifs de la thèse.

Chapitre 2: décrit la méthodologie employée dans la thèse, y compris la synthèse des matériaux (NTC et MnO_2), les méthodes et les procédures (configuration de la cellule électrochimique, CVD et HT). Ce chapitre présente également la gamme de méthodes de caractérisation physicochimique et électrochimique utilisées pour analyser les matériaux. Il s'agit notamment des méthodes MEB, EDS, DRX, Raman, CV et CA. En outre, le chapitre aborde les paramètres électrochimiques étudiés, tels que la capacité spécifique et l'*ECSA*, et fournit des procédures détaillées pour effectuer les analyses électrochimiques afin d'évaluer la performance et l'efficacité des capteurs.

Chapitres 3-6: Ils visent à présenter les caractérisations physicochimiques détaillées et les mesures électrochimiques, suivies d'une discussion approfondie des résultats par rapport aux objectifs définis dans la thèse. La structure est la suivante:

Chapitre 3: Caractérisations physicochimiques

Chapitre 4: Études capacitives et mesures électrochimiques de la surface

Chapitre 5: Études de voltampérométrie cyclique pour la détection du glucose sur des électrodes à base d'or, de papier carbone et de dioxyde de manganèse, et l'effet des espèces interférentes

Chapitre 6: Études de chronoampérométrie pour mesurer la sensibilité, la sélectivité et la durabilité du glucose

Chapitres 7: Résume les résultats de mes recherches et présente les défis et les perspectives.

Expérimental

Ce chapitre traite de la méthodologie utilisée dans la thèse, y compris la synthèse des matériaux. Le chapitre décrit en détail le processus de synthèse des nanotubes de carbone (NTC) sur PC via la méthode de dépôt chimique en phase vapeur (CVD), suivi d'une description détaillée de la méthode de synthèse des nanostructures de MnO_2 par méthode hydrothermale.

Le chapitre présente également la gamme des techniques de caractérisation physicochimique et électrochimique utilisées pour analyser les matériaux et décrit les principes de fonctionnement de ces techniques. Ces techniques comprennent la microscopie électronique à balayage (MEB), la spectroscopie dispersive en énergie des rayons X (EDS), la diffraction des rayons X (DRX), la spectroscopie micro-Raman, la voltampérométrie cyclique (CV) et la chronoampérométrie (CA).

Ensuite, le chapitre aborde les paramètres électrochimiques étudiés, tels que la capacité spécifique et l'ECSA, et fournit des procédures détaillées pour effectuer les analyses électrochimiques afin d'évaluer les performances et l'efficacité des capteurs. Ces évaluations comprennent l'évaluation de la sensibilité des électrodes étudiées vis-à-vis du glucose en utilisant CV et CA, l'évaluation de l'effet des espèces interférentes sur la détection du glucose, le test CA anti-encrassement contre le KCl et le test de durabilité électrochimique.

Pour les études électrochimiques, une cellule électrochimique à trois compartiments a été utilisée, et une solution de NaOH 0,1 M a été utilisée comme électrolyte.

Résultats des caractérisations physicochimiques

Le MEB a été utilisé pour étudier la morphologie de la surface du substrat de papier carbone (PC) nu et du PC/NTC tel qu'il a été préparé, ainsi que pour les substrats avec le catalyseur MnO_2 déposé sur le PC et sur les NTC. Les images du PC révèlent un réseau de fibres de carbone dont le diamètre moyen est compris entre 6 et 8 μm. En revanche, les images MEB de PC/NTC présentent une morphologie duveteuse qui recouvre uniformément l'ensemble des fibres de PC. Cela indique que le substrat PC est efficacement et densément recouvert d'une couche continue de NTC, ce qui souligne le succès du dépôt de NTC sur la surface du PC. Les images MEB du PC/MnO_2 montrent clairement que le substrat de PC est recouvert d'un réseau dense de nanotiges de MnO_2 (NRs), d'un diamètre moyen d'environ 200 nm. De même, les images NTC/MnO_2 révèlent une forte densité de nanotiges (NRs) de MnO_2 couvrant uniformément la surface des fibres de carbone et des NTC, ce qui confirme le succès du dépôt du catalyseur MnO_2 sur les substrats.

La technique EDS a été utilisée pour déterminer la composition élémentaire des électrodes synthétisées, à savoir PC/NTC, PC/MnO_2-NRs et NTC/MnO_2-NRs. L'analyse du substrat PC/NTC par EDS révèle un dépôt uniforme de la couche de NTC sur le substrat PC. La cartographie élémentaire et le spectre EDS indiquent la prédominance du carbone (99,07%) à la surface, confirmant la couverture complète des fibres de carbone par les NTC. Pour le substrat PC/MnO_2-NRs, la cartographie EDS montre une distribution uniforme de MnO_2 sur le substrat PC. La cartographie élémentaire et le spectre EDS révèlent la présence constante des éléments C, O, Mn et K à la surface du PC, avec des pourcentages atomiques correspondants de 48,87%, 40,57%, 9,43% et 1,13%, respectivement. L'analyse EDS du substrat NTC/MnO_2-NRs confirme également la distribution uniforme de la couche de MnO_2, avec la présence des éléments C (48,78%), O (41,37%), Mn (8,52%) et K (1,33%) à sa surface. Il est évident que les spectres EDS des substrats PC/MnO_2-NRs et NTC/MnO_2-NRs sont similaires, avec des concentrations atomiques relativement proches. Toutefois, la teneur en carbone des NTC/MnO_2-NRs est inférieure à celle du substrat PC/MnO_2-NRs, ce qui peut être attribué à la couche de catalyseur MnO_2 plus importante sur le substrat NTC/MnO_2-NRs.

Une analyse DRX a été réalisée pour étudier les structures cristallines des substrats sans MnO_2 et des substrats à base de MnO_2. Les diagrammes DRX des substrats PC et PC/NTC présentent un pic bien défini à 26,4° (2θ) ainsi que des pics plus petits qui correspondent aux plans de la structure du carbone graphite. D'autre part, les diagrammes DRX des substrats à base de MnO_2 présentent des pics qui correspondent bien aux plans du cryptomélane, la phase α-MnO_2 tétragonale typique de la famille des oxydes de manganèse, qui se caractérise par la présence d'ions K^+ dans les tunnels (2×2) de la structure cristalline. Cet arrangement structurel stabilise non seulement la structure cristalline de la phase α, mais contribue également à maintenir l'équilibre des charges au sein du matériau. Les pics distincts observés confirment le dépôt réussi de MnO_2 sous la forme cristalline souhaitée sur les substrats PC et NTC.

Le Raman a été utilisé pour étudier les modes vibrationnels et les caractéristiques structurelles des substrats à base de carbone et des substrats MnO_2-baesd. Les spectres Raman des substrats PC et PC/NTC révèlent deux bandes distinctes, identifiées comme la bande D qui correspond à la symétrie A_{1g} associée aux sites de bord ou de défaut du carbone, et la bande G qui est liée à la symétrie E_{2g} pour le carbone sp^2. La bande D plus large dans le spectre des NTC indique la présence d'un plus grand nombre de défauts dans la structure du carbone par rapport au substrat PC, ce qui suggère que les NTC présentent un degré de désordre plus élevé. Ceci est cohérent avec les caractéristiques structurelles des NTC, où les défauts jouent un rôle clé dans les caractéristiques vibrationnelles observées dans le spectre Raman. Quant aux spectres des échantillons contenant du MnO_2, tels que PC/MnO_2-NRs, quatre pics Raman distincts sont observés, qui correspondent aux pics documentés de l'α-MnO_2.

Résultats des études capacitives

Des études électrochimiques ont été réalisées en utilisant CV pour calculer la capacité spécifique et la surface électrochimique pour les électrodes sans MnO_2 et les électrodes à base de MnO_2. Pour les mesures de capacité spécifique (C_p), toutes les électrodes ont été évaluées dans une solution de NaOH 0,1 M à 2 mV/s pour définir les fenêtres électrochimiques de chaque électrode. Les profils CV du PC nu et des NTC nus affichent des courants réguliers, chacun indiquant une capacité de double couche (DL) pure. Cela suggère que les deux substrats présentent un comportement capacitif typique dans l'électrolyte NaOH, le substrat NTC offrant potentiellement une meilleure stabilité électrochimique et une fenêtre électrochimique plus large en raison de l'incorporation des nanotubes de carbone. Les PC/MnO_2-NRs et les NTC/MnO_2-NRs synthétisés présentent des pics symétriques à la fois sur les faces anodiques et cathodiques, à côté de la région DL. Ces observations suggèrent que les deux substrats présentent un comportement redox caractéristique, les NTC/MnO_2-NRs présentant une gamme de pics redox légèrement plus large, qui peut être attribuée à la conductivité et à l'activité électrochimique accrues fournies par les nanotubes de carbone. Les pics d'oxydoréduction observés aux électrodes de MnO_2 indiquent généralement l'implication des ions Mn de surface dans les réactions d'oxydoréduction. Ce comportement souligne la nature pseudocapacitive du mécanisme de stockage de charge, où la charge est stockée par une réaction redox réversible à l'interface électrode/électrolyte. Les pics d'oxydoréduction observés sont attribués aux réactions d'oxydoréduction réversibles des ions Mn dans la structure MnO_2. Plus précisément, ces pics correspondent au couple redox Mn^{3+}/Mn^{4+}. Au cours du processus de réduction, Mn^{4+} est réduit en Mn^{3+}, tandis que Mn^{3+} est oxydé à nouveau en Mn^{4+} au cours du balayage anodique.

Les propriétés capacitives des électrodes ont été évaluées dans une solution de NaOH 0,1 M à différentes vitesses de balayage (2–500 mV/s). Les courbes CV de l'électrode PC présentent des formes rectangulaires presque symétriques, tandis que les courbes CV de l'électrode NTC présentent des formes rectangulaires nettement symétriques, caractéristiques d'un condensateur électrochimique à double couche (EDLC). Ce comportement suggère que les charges sont stockées à la surface du matériau NTC, soulignant les propriétés capacitives améliorées dues à l'inclusion de nanotubes de carbone, qui fournissent une surface accrue et de meilleures capacités de stockage des charges.

La capacité spécifique dérivée des courbes CV est calculée à l'aide de la formule C_p=Q/(2 m x v x DV). Les valeurs C_p résultantes, tracées en fonction de la vitesse de balayage, révèlent que pour les deux électrodes, PC et NTC, la capacité spécifique diminue à mesure que la vitesse de balayage augmente, bien qu'elle montre une légère reprise à des vitesses de balayage plus élevées. Ce comportement est typique des PC nus et des NTC, qui présentent un comportement pur de condensateur électrochimique à double couche (EDLC). À mesure que la vitesse de balayage augmente, la capacité spécifique diminue en raison de la réduction du temps de diffusion des ions et de l'augmentation de la résistance. À des vitesses de balayage plus élevées, la capacité se rétablit quelque peu, car le système passe à un régime contrôlé par la diffusion, où le transport des ions devient le principal facteur limitant. Ce comportement est conforme aux principes généraux des condensateurs électrochimiques, même pour les matériaux présentant des caractéristiques EDLC pures. La capacité spécifique fournie par le PC nu est relativement faible, la valeur la plus élevée atteignant près de 0,0006 F/g à 2 mV/s. Cela souligne l'importance d'incorporer des matériaux, tels que les NTC, qui améliorent les performances électrochimiques et augmentent considérablement les valeurs de capacité par rapport au PC nu. En effet, la capacité fournie par le PC/NTC à 2 mV/s est de 0,5407 F/g, ce qui est 901 fois plus élevé que la capacité fournie par le PC nu.

De même, les capacités spécifiques, déterminées à partir des CVs du PC/MnO_2-NRs et des NTC/MnO_2-NRs, sont tracées en fonction de la vitesse de balayage. Il est évident que la capacité spécifique diminue à mesure que la vitesse de balayage augmente. Ce comportement, caractéristique des oxydes de métaux de transition (TMOs), est dû à la diminution de la diffusion des ions de l'électrolyte dans la matrice du matériau actif à des vitesses de balayage plus élevées, ce qui limite les performances électrochimiques. Une caractéristique notable est le C_p élevé du PC/MnO_2-NRs, qui atteint 42 F/g à 2 mV/s, ce qui est nettement plus élevé que ceux des électrodes de PC et de NTC nus. La capacité spécifique élevée du composite PC/MnO_2-NRs est due aux effets synergiques de la surface nanostructurée de MnO_2 et de ses propriétés de stockage de charges faradiques. La capacité de charge des NTC/MnO_2-NRs atteint la valeur impressionnante de 262,68 F/g à une vitesse de balayage de 2 mV/s. Cette valeur est plus de six fois supérieure aux 42 F/g obtenus par l'électrode PC/MnO_2-NRs, ce qui souligne l'amélioration substantielle de la capacité de stockage de charge due à l'incorporation des NTC. Cette différence significative suggère que la structure à base de NTC améliore la capacité de stockage de charge en raison de facteurs tels que l'amélioration de la conductivité, l'augmentation de la surface et l'accroissement de l'activité électrochimique.

Pour les mesures de la surface électrochimique (*ECSA*), les valeurs I_c ont d'abord été extraites des voltammogrammes cycliques obtenus à différentes vitesses de balayage pour tous les substrats dans la région non faradique. Ensuite, les valeurs de courant ont été tracées en fonction de la vitesse de balayage pour toutes les électrodes. Notamment, toutes les courbes présentent une tendance linéaire sur toute la gamme des vitesses de balayage mesurées. En analysant le tracé des vitesses de balayage en fonction du courant, nous pouvons déduire les valeurs C_{dl} pour tous les échantillons, qui correspondent aux pentes des graphiques. Les valeurs C_{dl} déterminées pour les électrodes sans MnO_2 sont de 0,0006 mF pour le PC nu et de 0,21 mF pour les NTC nus. La valeur C_{dl} beaucoup plus élevée pour les NTC nus est probablement due à la surface plus élevée et à la conductivité accrue des NTC, ce qui indique une plus grande capacité à stocker la charge dans la double couche électrochimique, améliorant ainsi la performance capacitive globale de l'électrode PC/NTC. D'autre part, les valeurs C_{dl} mesurées des électrodes à base de MnO_2 sont de 4,3 mF pour PC/MnO_2-NRs et de 12,2 mF pour NTC/MnO_2-NRs. Le C_{dl} des NTC/MnO_2-NRs est 2,8 plus élevé que celui des PC/MnO_2-NRs, ce qui peut être attribué à la surface et à la conductivité accrues fournies par les NTC, qui facilitent une diffusion plus rapide des ions et un plus grand nombre de sites actifs pour le stockage de la charge. La combinaison des nanotiges de MnO_2 et des NTC contribue probablement de manière synergique à l'amélioration des performances électrochimiques de l'électrode NTC/MnO_2-NRs.

Pour mieux comprendre la relation entre ces propriétés électrochimiques et la performance des électrodes, les valeurs *ECSA* et *RF* ont également été calculées pour toutes les électrodes. Notamment, les valeurs *ECSA* et *RF* de l'électrode NTC/MnO_2-NRs démontrent de manière impressionnante les plus grandes valeurs *ECSA* (305 cm^2) et *RF* (1694.44). L'incorporation de NTC joue un rôle crucial dans cette amélioration, car leur conductivité élevée et leur grande surface facilitent le transfert d'électrons et augmentent le nombre de sites actifs pour les réactions électrochimiques, stimulant ainsi la performance électrochimique globale du matériau hybride. Cette *ECSA* effective plus importante reflète non seulement l'amélioration de la conductivité, mais contribue également à la capacité spécifique plus élevée observée dans les NTC/MnO_2-NRs. Une plus grande surface permet une plus grande adsorption d'ions et un transfert d'électrons pendant les processus électrochimiques, ce qui peut améliorer de manière significative les performances des applications de détection électrochimique.

Résultats des études de voltampérométrie cyclique

Les détections voltampérométriques de Glu, AA et UA sont initialement examinées à l'aide d'une électrode en fil d'or (Au), en tant que catalyseur de référence dont les caractéristiques électrochimiques pour l'oxydation du Glu, de l'AA et de l'UA sont bien documentées. Les résultats de cette étude fourniront un cadre de base pour l'interprétation des résultats obtenus ultérieurement sur les électrodes PC, PC/NTC, PC/MnO_2-NRs et NTC/MnO_2-NRs. Tout d'abord, le CV d'une électrode à fil d'Au dans une solution de NaOH 0,1 M est enregistré. Dans le balayage positif, une région typique de double couche d'Au est observée, suivie par des pics d'oxydation et de réduction distincts. Ces pics sont attribués à la formation anodique et à l'élimination cathodique de l'oxyde d'or de surface, conformément aux résultats de la littérature. En outre, une vague mineure apparaissant avant le processus de formation de l'oxyde de surface suggère une possible oxydation pré-couche de la surface Au.

Lorsqu'une concentration modeste de 1 mM de glucose est introduite dans une solution de NaOH à la même électrode filaire, deux nouvelles caractéristiques apparaissent pendant le balayage vers l'avant. Les deux densités de courant associées à ces caractéristiques augmentent avec la concentration de Glu. Dans des études antérieures, le premier pic était associé à l'oxydation du glucose en gluconolactone, un processus impliquant deux électrons. Le second pic semble être lié à l'oxydation du gluconolactone en acide gluconique. La réponse CV observée pour l'oxydation de 0,2 mM d'AA à une électrode d'or dans une solution de NaOH présente des caractéristiques claires: un pic anodique émerge pendant le balayage du potentiel direct, signifiant l'oxydation de l'AA en acide déhydroascorbique. Inversement, un pic cathodique apparaît pendant le balayage du potentiel inverse, indiquant la réduction de l'acide déhydroascorbique en AA à la surface de l'électrode. Notamment, la densité de courant du pic avant augmente avec l'augmentation des concentrations d'AA. Les résultats CV obtenus lors de l'oxydation de 0,45 mM d'UA à l'électrode à fil Au dans une solution de NaOH 0,1 M révèlent plusieurs caractéristiques: un pic anodique suivi d'une onde large et d'un pic pendant le balayage inverse. Le pic anodique initial s'intensifie avec l'augmentation de la concentration d'UA, ce qui implique son association avec un processus faradique. Par la suite, la densité du pic de courant (extraite des profils CV précédents) a été tracée en fonction de la concentration de Glu (P1), d'AA et d'UA, respectivement, ce qui a permis d'obtenir une bonne relation linéaire dans la gamme de concentration examinée dans cette étude. En ce qui concerne la détection du Glu, l'électrode à fil d'Au présente une sensibilité de 52,487 $\mu A\ mM^{-1}\ cm^{-2}$ et une limite de détection basse (LOD) de 0,095 mM. Notamment, l'AA s'oxyde à des potentiels plus positifs, ce qui garantit une interférence minimale avec la détection de Glu sur l'électrode Au. Cependant, la détection de l'UA s'aligne étroitement sur les potentiels de Glu, ce qui peut affecter la détermination précise de la concentration de Glu.

La détection voltampérométrique du glucose a ensuite été examinée sur les électrodes sans MnO_2 et sur les électrodes à base de MnO_2. Les profils CV des électrodes ont été enregistrés, avec et sans la présence de Glu. Comme pour le fil d'Au, les réponses CV observées s'alignent sur le schéma voltampérométrique typique associé à l'oxydation du Glu; le pic P1 est associé à l'oxydation du glucose en gluconolactone et le second pic P2 semble être lié à l'oxydation du gluconolactone en acide gluconique. Les densités de courant P1 et P2 augmentent avec l'augmentation de la concentration de Glu. Les électrodes à base de MnO_2 présentent des densités de courant significativement plus élevées pour l'oxydation du Glu, ce qui indique une activité électrocatalytique accrue lors du dépôt de MnO_2. La sensibilité du capteur a ensuite été évaluée en examinant la relation entre la densité de crête du courant (P1) et la concentration de Glu. Une analyse de régression linéaire a été effectuée sur le graphique de données obtenu. La valeur de sensibilité est obtenue à partir de la pente de cette ligne de régression, qui indique dans quelle mesure la densité de crête du courant change avec chaque unité d'augmentation de la concentration de glucose. Pour déterminer la limite de détection (LOD), la formule LOD= 3,3 (σ/s) a été utilisée, où σ représente l'écart-type du signal de base et s la pente de la ligne de régression. Cette équation estime la concentration minimale de Glu que le capteur peut identifier de manière fiable, le facteur 3,3 assurant un niveau de confiance approprié dans la détection. Pour les électrodes sans MnO_2, l'électrode PC présente une faible sensibilité de 0,081 $\mu A\ mM^{-1}\ cm^{-2}$ et une limite de détection de 0,425 mM, tandis que l'électrode PC/NTC présente une sensibilité relativement plus élevée de 0,140 $\mu A\ mM^{-1}\ cm^{-2}$ et une limite de détection de 0,269 mM. La grande surface et le C_p élevé des nanotubes de carbone ont amélioré la détection du Glu à l'électrode PC/NTC dans la plage de concentration de 0,01–6 mM et à une limite de détection inférieure. Pour les électrodes à base de MnO_2, l'électrode PC/MnO_2-NRs présente une sensibilité très élevée de 143,82 $\mu A\ mM^{-1}\ cm^{-2}$ et une limite de détection de 0,282 mM, tandis que l'électrode NTC/MnO_2-NRs présente une sensibilité nettement plus élevée de 193,33 $\mu A\ mM^{-1}\ cm^{-2}$ et une limite de détection plus basse de 0,243 mM. En ce qui concerne les performances, l'électrocatalyseur NTC/MnO_2-NRs présente une sensibilité nettement supérieure, environ 3,68 fois plus élevée que celle du fil d'Au, et une densité de crête de courant plus importante, particulièrement évidente avec une concentration de Glu de 6 mM. Cela indique que les électrodes à nanotiges de MnO_2 présentent une activité catalytique exceptionnelle pour l'oxydation du glucose.

Les profils CV des électrodes PC/MnO_2-NRs et NTC/MnO_2-NRs montrent que lors de l'ajout d'AA ou d'UA à 0,1 M NaOH, aucun nouveau pic n'émerge. Au contraire, la densité de courant du pic associé au processus d'oxydoréduction de surface sur MnO_2 diminue avec l'augmentation de la concentration d'AA ou d'UA. Les effets cinétiques des réactions redox plus lentes et le blocage de la surface par des concentrations plus élevées d'AA ou d'UA jouent un rôle dans la réduction observée de la densité de courant du pic. Il est intéressant de noter qu'aucun pic supplémentaire n'apparaît lorsque l'AA et l'UA sont présents simultanément dans l'électrolyte, ce qui indique qu'il n'y a pas de nouveaux processus chimiques. En outre, le pic associé au processus redox de surface à l'électrode MnO_2 diminue lorsque la concentration d'AA est fixée ou augmentée, et inversement, lorsque la concentration d'UA varie. Lors de l'ajout de 7 mM de Glu, la densité du pic de courant de P1 et P2 a augmenté de manière significative, puis s'est stabilisée.

L'augmentation de la densité de courant des pics associés à l'oxydation du Glu avec des concentrations croissantes d'AA ou d'UA indique un effet catalytique potentiel de ces composés sur l'oxydation électrochimique du Glu. Cet effet catalytique peut provenir de la capacité de l'AA et de l'UA à faciliter les processus de transfert d'électrons ou à modifier la surface de l'électrode, améliorant ainsi la réponse électrochimique du Glu. Le plafonnement de la densité de courant au-delà des niveaux physiologiques d'AA (comme dans le cas de P1 à PC/MnO_2-NRs) suggère un effet de saturation, ce qui pourrait impliquer que l'activité catalytique de l'AA atteint un maximum à ces concentrations. Les profils LSV des électrodes PC/MnO_2-NRs et NTC/MnO_2-NRs montrent clairement que la région du potentiel d'amorçage pour le Glu est significativement plus négative que celles de l'AA et de l'UA, ce qui souligne la cinétique plus rapide de l'oxydation du Glu par rapport à celle de l'AA et de l'UA. Les réponses au courant de crête des électrodes PC/MnO_2-NRs et NTC/MnO_2-NRs dans une solution ternaire (composée de 7 mM Glu + 0,11 mM AA + 0,42 mM UA) ont augmenté d'environ 7,1% et 27%, respectivement, par rapport à leurs réponses dans une solution contenant seulement 7 mM de glucose, ce qui indique une sélectivité suffisante pour l'analyse du sang humain.

Résultats des études de chronoampérométrie

Dans ce chapitre, la chronoampérométrie (CA) a été utilisée pour la détection du glucose en raison de ses avantages par rapport au CV. La CA limite les effets du courant capacitif principalement au début de l'étape potentielle, ce qui permet une mesure plus claire du courant faradique car ces effets diminuent avec le temps. La CA est donc particulièrement efficace pour détecter de petites quantités d'espèces électroactives, en fournissant un signal plus net et en améliorant la sensibilité. Ainsi, la CA est souvent le choix préféré pour la surveillance en temps réel et les applications où la sensibilité est critique.

Pour la détection chronoampérométrique du glucose sur les électrodes de nanotiges de MnO_2, les réponses de la CA des électrodes PC/MnO_2-NRs et NTC/MnO_2-NRs ont été enregistrées à une tension de travail de 0,18 V contre Ag/AgCl lors de l'ajout successif de différentes concentrations de Glu de 0,5 à 20 mM dans une solution de NaOH à 0,1 M. La réponse temporelle en matière de détection fait référence à la vitesse à laquelle un capteur détecte et répond aux changements de concentration d'un analyte, tel que le glucose. Il est généralement caractérisé par le temps nécessaire au capteur pour atteindre un signal stable. Les graphiques temps-courant montrent une augmentation progressive du courant correspondant à l'ajout incrémentiel de Glu. L'électrode PC/MnO_2-NRs réagit au Glu en 44 secondes, tandis que l'électrode NTC/MnO_2-NRs a un temps de réponse plus rapide de 22 secondes. Les deux électrodes atteignent un courant stable et montrent une grande sensibilité aux variations des niveaux de Glu. La PC/MnO_2-NRs et les NTC/MnO_2-NRs présentent deux relations linéaires distinctes dans une gamme de concentrations allant de 0,5 mM à 10 mM, bien au-delà des niveaux physiologiques (3–8 mM), avec des corrélations fortes indiquées par des coefficients de détermination (R^2) de 0,9951 pour l'électrode PC/MnO_2-NRs et de 0,9928 pour l'électrode NTC/MnO_2-NRs. La sensibilité de l'électrode PC/MnO_2-NRs vis-à-vis du Glu, déterminée par régression linéaire, est estimée à 176,62 µA mM^{-1} cm^{-2}, tandis que la sensibilité de l'électrode NTC/MnO_2-NRs est beaucoup plus élevée, à 309,73 µA mM^{-1} cm^{-2}. Les deux électrodes présentent notamment une limite de détection similaire de 0,19 mM à un rapport signal/bruit de 3. Toutefois, la sensibilité accrue des NTC/MnO_2-NRs offre un avantage significatif, permettant une détection plus précise et plus rapide des concentrations de Glu. Bien que les deux matériaux puissent détecter efficacement de faibles concentrations de Glu, la sensibilité supérieure des NTC/MnO_2-NRs les positionne comme le choix privilégié pour les applications de détection électrochimique sensible.

Pour évaluer la capacité anti-interférence des capteurs PC/MnO_2-NRs et NTC/MnO_2-NRs, l'étude a consisté à enregistrer les réponses CA des deux électrodes après l'ajout successif de faibles concentrations d'AA (0,02 mM) et d'UA (0,18 mM), ainsi que de concentrations élevées d'AA (0,08 mM) et d'UA (0,42 mM), à une solution contenant 7 mM de glucose. Notamment, il n'y a pas eu de changement significatif dans les densités de courant pour les deux électrodes, en particulier pour les NTC/MnO_2-NRs, où l'augmentation du courant est restée inférieure à 3% pour toutes les concentrations d'interférence testées. Ces observations indiquent que les électrodes PC/MnO_2-NRs et NTC/MnO_2-NRs présentent une forte sélectivité pour le glucose en présence d'interférents potentiels, tels que l'AA et l'UA. La variation minimale des densités de courant pour les NTC/MnO_2-NRs implique un niveau élevé de résistance aux interférences, ce qui en fait un candidat prometteur pour une détection fiable du Glu dans des échantillons biologiques complexes.

Le KCl peut également encrasser (ou empoisonner) les électrodes en adhérant à leur surface, ce qui peut compromettre les performances et la sélectivité du capteur. En tant que sel, le KCl peut également modifier la force ionique de la solution, ce qui peut affecter la réponse électrochimique et la stabilité du capteur. Les réponses en courant du Glu aux NTC/MnO_2-NRs lors de l'ajout successif de concentrations de KCl de 1 mM, 3 mM, et 5 mM. Il est remarquable que la réponse en courant ne soit pas affectée par le KCl, même à la concentration la plus élevée de 5 mM. Cette résistance souligne les propriétés anti-encrassement des électrodes NTC/MnO_2-NRs, mettant en évidence leur efficacité dans le maintien d'une performance stable du capteur en présence de KCl.

Pour le test de durabilité utilisant la chronoampérométrie, la stabilité à moyen terme de l'électrode NTC/MnO_2-NRs a d'abord été évaluée par CV en présence de 7 mM de Glu, en utilisant une vitesse de balayage de 20 mV/s sur 1000 cycles (équivalent à 25 heures). L'électrode NTC/MnO_2-NRs a montré une excellente cyclabilité, sans diminution significative de la densité de courant pendant toute la durée du test. Pour mieux évaluer la durabilité à long terme des performances électrocatalytiques des électrodes telles que préparées, l'oxydation du Glu a été réalisée par chronoampérométrie à une tension constante de 0,18 V par rapport à Ag/AgCl. Les réponses en courant des électrodes PC/MnO_2-NRs et NTC/MnO_2-NRs à 7 mM de glucose dans 0,1 M NaOH pendant 7 jours sont comparées.

Les deux chronoampérogrammes pour l'oxydation du Glu montrent typiquement une forte augmentation initiale du courant, indiquant une oxydation rapide à la surface de l'électrode, suivie d'une forte baisse du courant, qui est souvent attribuée à l'accumulation d'intermédiaires réactionnels, en particulier le peroxyde d'hydrogène, qui bloque progressivement les sites actifs sur l'électrode. Après cette chute initiale, le courant se stabilise à une valeur plus faible, à l'état d'équilibre, reflétant un équilibre dynamique entre l'oxydation du glucose et les effets inhibiteurs des intermédiaires accumulés. Malgré un certain blocage des sites actifs, l'activité électrochimique se poursuit, bien qu'à un taux réduit, comme l'indique le courant d'équilibre. Les données soulignent la remarquable stabilité opérationnelle de l'électrode NTC/MnO_2-NRs pour la détection ampérométrique du glucose. En revanche, l'électrode PC/MnO_2-NRs a montré une désactivation rapide, probablement due à l'accumulation de composés intermédiaires générés pendant l'oxydation du glucose, qui ont eu tendance à recouvrir la surface de l'électrode. La performance supérieure de l'électrode NTC/MnO_2-NRs peut être attribuée à sa surface électroactive significativement plus grande, qui non seulement améliore l'efficacité de l'oxydation du glucose mais aide également à atténuer l'empoisonnement de la surface par les composés intermédiaires adsorbés, maintenant ainsi une performance stable sur des périodes de fonctionnement prolongées.

Conclusions

Dans le chapitre 3, l'analyse MEB a révélé que la surface du PC/NTC est uniformément recouverte d'une couche continue de NTC, ce qui indique que le dépôt de NTC est réussi. Les images PC/MnO_2 et NTC/MnO_2 montrent que les deux substrats sont densément recouverts de nanotiges (NRs) de MnO_2, avec un diamètre moyen d'environ 200 nm. Ces résultats confirment le dépôt efficace de NTC et de catalyseurs MnO_2 sur les surfaces de PC. L'analyse DRX révèle que les PC/MnO_2-NRs et les NTC/MnO_2-NRs présentent des pics distincts correspondant à la phase cryptomélane KMn_8O_{16}, ce qui confirme le succès du dépôt de MnO_2 sous sa forme α-MnO_2 stable. Cela indique que le MnO_2 a été efficacement déposé sur les substrats PC et NTC dans la structure cristalline souhaitée. La spectroscopie Raman des substrats à base de MnO_2 révèle des pics distincts correspondant à l'α-MnO_2, confirmant le dépôt réussi de MnO_2 avec des modes vibrationnels caractéristiques. Notamment, les bandes D et G sont absentes à la fois dans les PC/MnO_2-NRs et les NTC/MnO_2-NRs en raison de l'épaisse couche de MnO_2 qui masque les signaux de carbone sous-jacents.

Dans le chapitre 4, les valeurs C_{dl} pour les électrodes PC/MnO_2-NRs et NTC/MnO_2-NRs ont été déterminées à partir des régions non-faradiques des voltammogrammes, montrant que les NTC/MnO_2-NRs présentaient une valeur C_{dl} 2,8 fois plus élevée que la PC/MnO_2-NRs. Cette augmentation est attribuée à la surface et à la conductivité accrues des NTC, qui améliorent la diffusion des ions et le stockage des charges. En outre, l'électrode NTC/MnO_2-NRs a démontré des valeurs *ECSA* et *RF* significativement plus élevées, reflétant sa performance électrochimique supérieure due à la synergie entre les NTC et le MnO_2. Cette amélioration permet une meilleure adsorption des ions et un meilleur transfert d'électrons, ce qui renforce les capacités de l'électrode dans les applications de détection électrochimique.

Dans le chapitre 5, la détection électrochimique du glucose, de l'acide ascorbique et de l'acide urique à l'aide de différents matériaux d'électrode, notamment l'or, le papier carbone, les nanotubes de carbone et les nanotiges de dioxyde de manganèse, a fait l'objet d'une étude systématique. Les résultats montrent que si l'électrode à fil d'or est efficace pour détecter le glucose, l'acide ascorbique et l'acide urique, elle souffre d'un chevauchement des potentiels d'oxydation, en particulier entre le glucose et l'acide urique, ce qui complique la précision de la détection. L'électrode PC, bien que fonctionnelle, présente une sensibilité plus faible et des limites de détection plus élevées pour le glucose que les électrodes à base de NTC et de MnO_2. L'incorporation de nanotubes de carbone dans l'électrode PC améliore ses performances, en améliorant la sensibilité et en abaissant la limite de détection du glucose. Toutefois, les améliorations les plus significatives ont été observées avec les électrodes à base de MnO_2-NRs. Ces électrodes ont fait preuve d'une grande sensibilité, de limites de détection basses et d'une meilleure performance dans la détection du glucose sur une large gamme de concentrations, dépassant les niveaux physiologiques. L'électrode composite NTC/MnO_2-NRs, en particulier, a présenté la sensibilité la plus élevée et la limite de détection la plus basse, ce qui en fait un candidat prometteur pour les applications de détection du glucose.

Les travaux ont également examiné les effets de l'acide ascorbique et de l'acide urique sur la détection du glucose. Bien que ces substances interférentes aient provoqué une légère augmentation des densités de courant associées à l'oxydation du glucose, les électrodes à base de MnO_2-NRs ont conservé un haut degré de sélectivité pour le glucose. Cela suggère que les électrodes pourraient être utilisées efficacement dans des applications pratiques, où la présence de telles interférences pourrait compromettre la précision des mesures du glucose. Dans l'ensemble, les résultats de cette étude soulignent le potentiel des électrodes PC/MnO_2-NRs et NTC/MnO_2-NRs dans les capteurs électrochimiques pour la surveillance du glucose, avec des avantages considérables en termes de sensibilité, de sélectivité et de limites de détection.

Dans le chapitre 6, la chronoampérométrie a été utilisée pour évaluer les performances de détection du glucose des électrodes de nanotiges de MnO_2, avec et sans modification des nanotubes de carbone. L'étude a démontré que les électrodes PC/MnO_2-NRs et NTC/MnO_2-NRs présentaient toutes deux une excellente sensibilité au glucose, les électrodes NTC/MnO_2-NRs présentant des temps de réponse et une sensibilité supérieurs, en particulier dans la plage des concentrations de glucose de 0,5 à 10 mM. Les électrodes NTC/MnO_2-NRs ont répondu plus rapidement et ont montré une meilleure sensibilité, avec une sensibilité de 309,73 $\mu A\ mM^{-1}\ cm^{-2}$ par rapport à 176,62 $\mu A\ mM^{-1}\ cm^{-2}$ pour PC/MnO_2-NRs. Les deux électrodes ont fait preuve d'une grande linéarité et d'une faible limite de détection de 0,19 mM.

En outre, les deux types d'électrodes ont démontré une sélectivité remarquable et des propriétés anti-interférences en présence d'espèces interférentes communes, telles que l'acide urique et l'acide ascorbique, l'électrode NTC/MnO_2-NRs montrant une variation minimale du courant en présence de concentrations même élevées de ces interférents. Les électrodes NTC/MnO_2-NRs ont également montré de solides propriétés anti-salissures, conservant des performances stables même lorsqu'elles sont exposées au chlorure de potassium (KCl), qui pourrait autrement compromettre la fonction du capteur.

En outre, les tests de durabilité ont confirmé que l'électrode NTC/MnO_2-NRs présentait une excellente stabilité à long terme, conservant des performances électrochimiques stables même après une utilisation prolongée, contrairement à l'électrode PC/MnO_2-NRs, qui présentait une désactivation rapide. La performance supérieure de l'électrode NTC/MnO_2-NRs a été attribuée à sa plus grande surface électroactive, qui a permis une oxydation plus efficace du glucose et une meilleure résistance à l'encrassement et à l'empoisonnement de la surface.

En conclusion, l'électrode NTC/MnO_2-NRs surpasse l'électrode PC/MnO_2-NRs en termes de temps de réponse, de sensibilité, d'anti-interférence, d'anti-salissure et de stabilité à long terme, ce qui en fait un candidat prometteur pour la détection fiable et précise du glucose dans des échantillons biologiques complexes.

TABLE OF CONTENTS

LIST OF FIGURES

LIST OF TABLES

LIST OF ABBREVIATIONS

AA	Ascorbic acid
AE	Augur electrons
Ag/AgCl	Silver/Silver chloride
APTES	3-Aminopropyl triethoxysilane
AuNS	Gold nanostructures
AuNP	Gold nanoparticles
A1C	Glycated hemoglobin
BSE	Backscattered electrons
CA	Chronoamperometry
C_{dl}	Electrochemical double-layer capacitance
CE	Counter electrode
CGM	Continuous glucose monitoring
CGM_S	Continuous glucose monitoring systems
CNF	Carbon nanofiber
CNF@ Ni-Co LDH	Carbon nanofiber coat with nickel-cobalt layered double hydroxide
$CNF@Ni_{0.66}Co_{0.33}(OH)_2$	Carbon nanofiber coat with nickel-cobalt layered double hydroxide (with Ni/Co ratio of 2/1)
CNTs	Carbon nanotubes
$CNTs/MnO_2$	Manganese dioxide on carbon nanotubes
$CNTs/MnO_2$-NRs	Manganese dioxide nanorods on carbon nanotubes
CoO_2	Cobalt(IV) oxide
Co_3O_4	Cobalt(II, III) oxide

CoOOH	Cobalt(III) oxyhydroxide
CP	Carbon paper
C_p	Specific capacitance
CP/CNTs	Carbon nanotubes on carbon paper
CP/MnO_2	Manganese dioxide on carbon paper
CP/MnO_2-NRs	Manganese dioxide nanorods on carbon paper
C_s	Standard specific electrochemical double-layer capacitance
CSF	Carbonized silk fabric
Cu-rGO/CSF	Reduced graphene oxide and carbonized silk fabric decorated with copper nanoflowers
CuO	Copper(II) oxide
$Cu(OH)_2$	Copper(II) hydroxide
CuOOH	Copper(III) oxyhydroxide
CV	Cyclic voltammetry
CVD	Chemical vapor deposition
C_xH_y	Carbon source (carbohydrates)
$C_6H_{12}O_6$	Glucose
$C_6H_{10}O_6$	Gluconolactone
$C_6H_{12}O_7$	Gluconic acid
$C_6H_{11}O_7^-$	Gluconate
DET	Direct electron transfer
dPIn	Doped polyindole
$d\ sin\theta$	Path difference

ECSA	Electrochemical or electroactive surface area
EDS	Energy dispersive x-ray spectroscopy
EGS	Enzymatic glucose sensors
E°	Standard cell potential
E_{pa}	Anodic peak potential
E_{pc}	Cathodic peak potential
FAD	Flavin adenine dinucleotide (oxidized form)
$FADH_2$	Flavin adenine dinucleotide (reduced form)
FeO	Iron(II) oxide
Fe_2O_3	Iron(III) oxide
FPG	Fasting plasma glucose
GDH	Glucose dehydrogenase
Glu	Glucose
GLUT4	Glucose transporter- type 4
GOx	Glucose oxidase
GOx(FAD)	Glucose oxidase in its oxidized form
GOx($FADH_2$)	Glucose oxidase in its reduced form
GR	Graphite rod
G-ZnO/Ni foam	Graphene/zinc oxide nanoparticle nanocomposite modified Ni foam
HT	Hydrothermal
H_2O_2	Hydrogen peroxide
i_c	Charging current
IDF	International Diabetes Federation

IHOAM	Incipient hydrous oxide adatom mediator
I_{pa}	Anodic peak current
I_{pc}	Cathodic peak current
ISF	Interstitial fluid
i_{ss}	Steady-state current
KCL	Potassium chloride
LOD	Limit of detection
LSV	linear sweep voltammetry
M	Metal adsorption sites
M*	Reductive metal adsorption site
Med_{ox}	Mediator in its oxidized form
Med_{red}	Mediator in its ed form
mg/dL	Milligrams per deciliter
mmol/L	Millimoles per liter
MnO_x	Manganese oxide
MnO_2	Manganese(IV) oxide/It is commonly known as Manganese dioxide
MnO_4^{2-}	Manganate
MnO_6	Octahedral unit
MnOOH	Manganese(III) oxyhydroxide
$M[OH]_{ads}$	Oxidative adsorbed hydroxide radical
MWCNTs	Multi-walled carbon nanotubes
MΩ-cm	Megaohms-cm
NEGS	Non-enzymatic glucose sensors

Nf	Nafion
NiO	Nickle(II) oxide
NiOOH	Nickle(III) oxyhydroxide
OCP	Open circuit potential
OECTs	Organic electrochemical transistors
OH^-	Hydroxide ions
OH_{ads}	Adsorbed hydroxide layer
Ox	Oxidized species
PANI	Polyaniline
PB	Prussian blue
PBS	Phosphate-buffered saline
PERfECT	Personalized electronic reader for electrochemical transistors
PNC	Polymer nanocomposites
Ppy	Polypyrrole
RE	Reference electrode
Red	Reduced species
RF	Roughness factor
rGO	Reduced graphene oxide
R-MnO_2	Ramsdellite-manganese dioxide
SE	Secondary electrons
SEM	Scanning electron microscopy
SMBG	Self-monitoring blood glucose
SPCE	Screen-printed carbon electrode

SPR	Surface plasmons resonance
TMOs	Transition metal oxides
UA	Uric acid
USD	United States dollar
WE	Working electrode
XRD	X-ray diffraction
α-MnO_2	Alpha-manganese dioxide
β-MnO_2	Beta-manganese dioxide
β-MnO_2 RA	β-MnO_2 micro/nanorod arrays
β-MnO_2 RP	β-MnO_2 micro/nanorod powder
δ-MnO_2	Delta-manganese dioxide
γ-MnO_2	Gamma-manganese dioxide
λ-MnO_2	Lambda-manganese dioxide
θ	Incident angle
2θ	Deflection angle
ΔV	Potential window of the cyclic voltammogram
v	Scan rate
σ	Standard deviation of the baseline signal

1. INTRODUCTION

1.1 General introduction: overview of diabetes

Glucose is a fundamental source of energy in the human body resulting from the final step of food digestion containing carbohydrates. As a response to its increased amount in the blood, the pancreas secretes a hormone called insulin that allows body cells to absorb it from the blood via glucose transporter-type 4 (GLUT4) and convert it into energy[1]; thereby reducing glucose built-up in the blood and keeping it in proper levels for healthy individuals[2-5]. Blood glucose levels are an important indicator of health, particularly, in diabetes care. They are measured in units of millimoles per liter (mmol/L) or milligrams per deciliter (mg/dL). According to Diabetic Québec, the target blood glucose value for diabetic people is between 4.0 and 7.0 mmol/L fasting or before a meal, and between 5.0 and 10.0 mmol/L two hours after the beginning of a meal[6-7]. When the average level amount of glucose is below 4.0 mmol/L it can lead to a condition called hypoglycemia (low blood glucose)[8], and once exceeds 7.0 mmol/L is referred to as hyperglycemia (high blood glucose)[9], as shown in Figure 1.1. Hypoglycemia often occurs due to the excess of insulin, common in diabetics, especially people with type-I diabetes who primarily depend on insulin for their treatment[10].

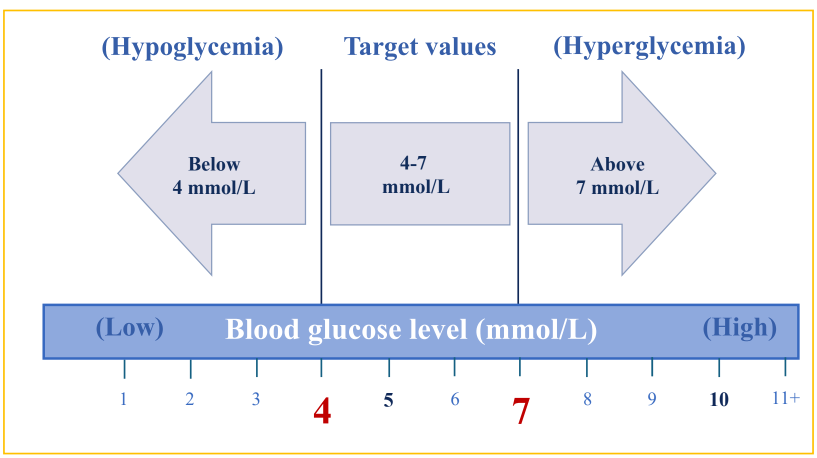

Figure 1.1: Graphic illustration of blood glucose ranges for diabetics while fasting or before a meal

In Canada, glucose concentrations can be established using fasting plasma glucose (FPG) test or/and hemoglobin (A1C) test. FPG test can be self-monitored using blood glucose meters whereas A1C test is performed in a laboratory, measures glycated hemoglobin and determines the average blood glucose levels over a time spam of 2–3 months, in which the target value is less than 7.0%[6]. Table 1.1 demonstrates the diagnostic values for prediabetes and diabetes from Diabetes Canada's 2018 Clinical Practice Guidelines for the Prevention and Treatment of Diabetes in Canada[11-12]. The table below indicates that diabetes is diagnosed with FPG level of ≥ 7.0 mmol/L or A1C level of ≥ 6.5%, while prediabetes is defined with FPG level of ≥ 6.1 to < 7.0 mmol/L or A1C level of ≥ 6.0% to < 6.5%. When the level of blood glucose is ≥ 11.1 mmol/L 2 hours after drinking a liquid containing 75 g of glucose or at any time of day, it also indicates the presence of diabetes[12-13]. The values of (7.0 mmol/L) and (11.1 mmol/L) corresponds to (126 mg/dL) and (200 mg/dL); respectively, (multiply by 18.0182 mg L/mmol dL).

Table 1.1: The suggested reference values for a diagnosis by diabetes Canada 2018 clinical practice guidelines for the prevention and treatment of diabetes in Canada[11-13]

Table removed due to copyrights issues. Information available at :
https://www.diabete.qc.ca/en/diabetes/information-on-diabetes/type-2-diabetes/

Diabetes is a metabolic disorder resulting from the excess blood glucose levels which cannot be regulated solemnly with insulin, which typically plays a crucial part in the control process. There are two main types of diabetes: type I and type II, as illustrated in Figure 1.2. Type I diabetes, known as insulin dependent, is most common in children and teens and represents about 10% of people affected by the disease. In this type of diabetes, the beta cells in the pancreas are destroyed by the autoimmune system[2, 14]; therefore, no insulin being produced, and no glucose is allowed to enter the cells, resulting in the accumulation of glucose in the bloodstream[5]. As for Type II diabetes, known as insulin resistant[14], it regroups the vast majority of people with diabetes (around 90%); mainly adults. In this particular type, the pancreas initially produces sufficient insulin, but the body's cell receptors are inactive to bind to insulin. As a result, the cells refuse to absorb glucose, leading to increase its concentration in the blood[4-5]. To overcome the resistant cells; pancreas releases more and more insulin and eventually the insulin produced by pancreas becomes insufficient[4, 15]. In both glucose types, glucose is unable to enter the body cell, resulting in its accumulation in the bloodstream and damaging blood vessels.

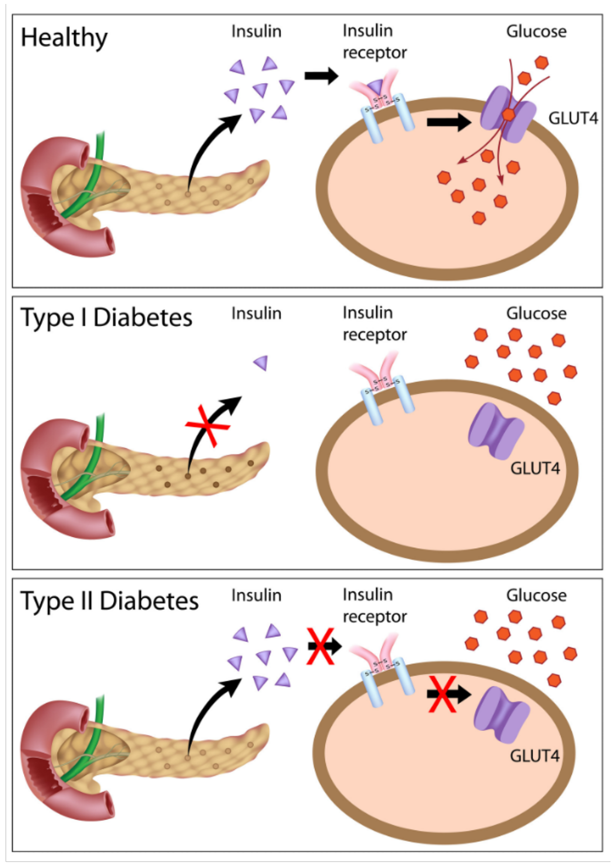

Figure 1.2: Illustration showing the insulin action and diabetes type I and type II[16]

Several factors can cause or contribute to develop diabetes, in particular, type II. Overweight and lack of physical activity are the two main factors; additionally, lifestyle and diet, age, family history, and some medications also have a significant impact on diabetes[2]. Determination of blood glucose concentration is essential in diagnosing and treating the disease; otherwise, serious complications associated with diabetes might appear[14]; for instance, cardiovascular disease, heart attack, arthritis, stroke, loss of sight, renal failure, nerve disease and amputation caused by gangrene.

Statistics collected from the International Diabetes Federation (IDF) reveal that the number of people affected by diabetes is rising remarkably worldwide, as referred in Figure 1.3. The estimated number of adults with diabetes, ages between 20–79 years, increased from 151 million in 2000 to 285 million in 2010. Then, it hit 537 million in 2021. The number is expected to reach 643 million and 783 million by 2030 and

2045, respectively[17]. In 2021, diabetes' cost expenditure was estimated to be 966 billion dollars (USD) and the disease was responsible for around 6.7 million deaths worldwide[17].

a

Figure removed due to copyrights issue

b

c

Figures removed due to copyrights issue

Figure 1.3: a) Number of people with diabetes worldwide and per IDF region in 2021–2045 (20–79 years). b) Estimated of the global prevalence of diabetes in the 20–79 year age group (millions). c) Projections of the global prevalence of diabetes in the 20–79 year age group (millions)[17]

Diabetes Canada reported that about 11 million Canadians have diabetes or prediabetes in 2019. The cost of treating the disease jumped from 14 billion dollars in 2008 to nearly 30 billion dollars in 2019, indicating its massive impact on the health care system[18]. In Québec, 1.2 million people are impacted by diabetes. The estimated direct and indirect costs associated with diabetes are roughly 3 billion dollars annually[19]. Given all of the above, constant monitoring of blood sugar levels is crucial to prevent such consequences. Developing reliable and affordable blood sugar measuring devices is a real challenge.

1.1.1 Common electroactive interferents

It is worth noting that uric acid and ascorbic acid are among other electroactive molecules present in the biological fluid of human (e.g., serum, blood or urine) that can interfere with glucose and cause inaccurate glucose measurements[20]. Uric acid (UA) is the end product of purine metabolism[21], which in turn travels through the blood to be ultimately eliminated by the kidneys. The normal concentration range of uric acid in blood is from 0.18 to 0.42 mmol/L[22]; however, an excessive UA level in blood can lead to what is called hyperuricemia and cause gout and kidney-related risks[21]. Ascorbic acid (AA), also known as vitamin C, although present in the blood in relatively small amounts (0.023–0.085 mmol/L[22-23]) plays many crucial roles in human body; for instance, supporting the immune system and protecting tissues from damaging caused by free radicals. Likewise, high levels of vitamin C can cause health problems like diarrhea, vomiting, headaches, kidney stones, etc., whereas a deficiency in its levels may lead to the risk of developing scurvy. Thus, it is crucial to monitor the concentration levels of such molecules for diagnosis and healthcare[21]. It has been observed that the oxidation potentials of interfering species such as UA and AA are too close to the oxidation potential of glucose, which means that their signals overlap when detecting these electroactive molecules in a sample simultaneously at a bare electrode. As a result, modifying the electrode is essential for detecting electroactive species at different oxidation potentials[21], which in turn determines the sensor's sensitivity and selectivity.

Chloride anions are one of the most important electrolytes in the blood (beside potassium, sodium and bicarbonate) that play an important role in maintaining the physiological balance in the body, such as maintaining acid-base balance (pH balance) in the blood. While the typical reference range of potassium in blood serum is between 3.5–5.0 mmol/L[24], the typical concentration levels of chloride ions range between 96-106 mmol/L[23] (may vary slightly among laboratories); however, deviation from that range (owing to some illnesses like vomiting and diarrhea) can contribute to metabolic issues (such as metabolic alkalosis and metabolic acidosis). To illustrate; low chloride levels (hypochloremia) occur in particular conditions (where there is a loss of chloride ions/a loss of stomach acid) such as in vomiting or the excessive of taking diuretics. As a result, the kidneys tend to compensate the chloride lost by retaining the bicarbonate, leading to a condition called metabolic alkalosis, where the body is too basic. On the other side, high chloride levels (hyperchloremia) arise from the excess of acid /or loss of bicarbonate as in the cases of renal failure or severe diarrhea. Consequently, the kidneys maintain the chloride ions to balance the bicarbonate lost, increasing the acidity of the body, a condition called metabolic acidosis. Chloride ions have been reported to negatively impacts the electrode's sensing capability, causing what is referred to as surface poisoning or fouling. This happens because chloride ions are strongly chemisorbed onto electrode surface (e.g., Pt and Au-based electrodes), inducing significant interference on gold electrode[20, 25] and greatly impairing the sensor activity[26]. These interfering species or fouling substances can affect the overall accuracy. As a result, selectivity is a key factor in determining the accuracy of the sensor[23].

1.1.2 Detection of glucose/ Oxidation reaction of glucose

Glucose ($C_6H_{12}O_6$) is an electroactive molecule that exists in blood and taken up by cells for use, more often in the form (D-β-glucose)[20, 22]. Determination of glucose in electrochemical sensors essentially involves the oxidation reaction of glucose, which results in the release of electrons as a measurable current signal. The reaction requires a selective enzyme to catalyst glucose oxidation into D-glucono-δ-lactone; by releasing two protons and two electrons from glucose molecule. This step is followed by a fast hydrolysis step, in which D-glucono-δ-lactone oxidizes into gluconic acid, as shown in the equation (Figure 1.4)[20].

Figure removed due to copyrights issues

Figure 1.4: Overall process of glucose oxidation

The reaction proceeds from D-glucose into D-glucono-δ-lactone via slow hydrogen abstraction and oxidation, followed by fast hydrolysis into D-gluconic acid[20].

The glucose oxidation reaction is essential for glucose measurements not only in blood glucose monitoring but also in many other fields such as food industries, fuel cells, batteries, etc.

1.2 Electrochemical sensors

Electrochemical sensors are devices that apply electrochemical principles to detect and measure the target analyte of interest; by converting a physicochemical change into quantifiable electrical signal. The main components that make up the electrochemical biosensors are: biological recognition element, electrochemical transducer, signal processing and display system[27-29], as demonstrated in Figure 1.5 (a)[29].

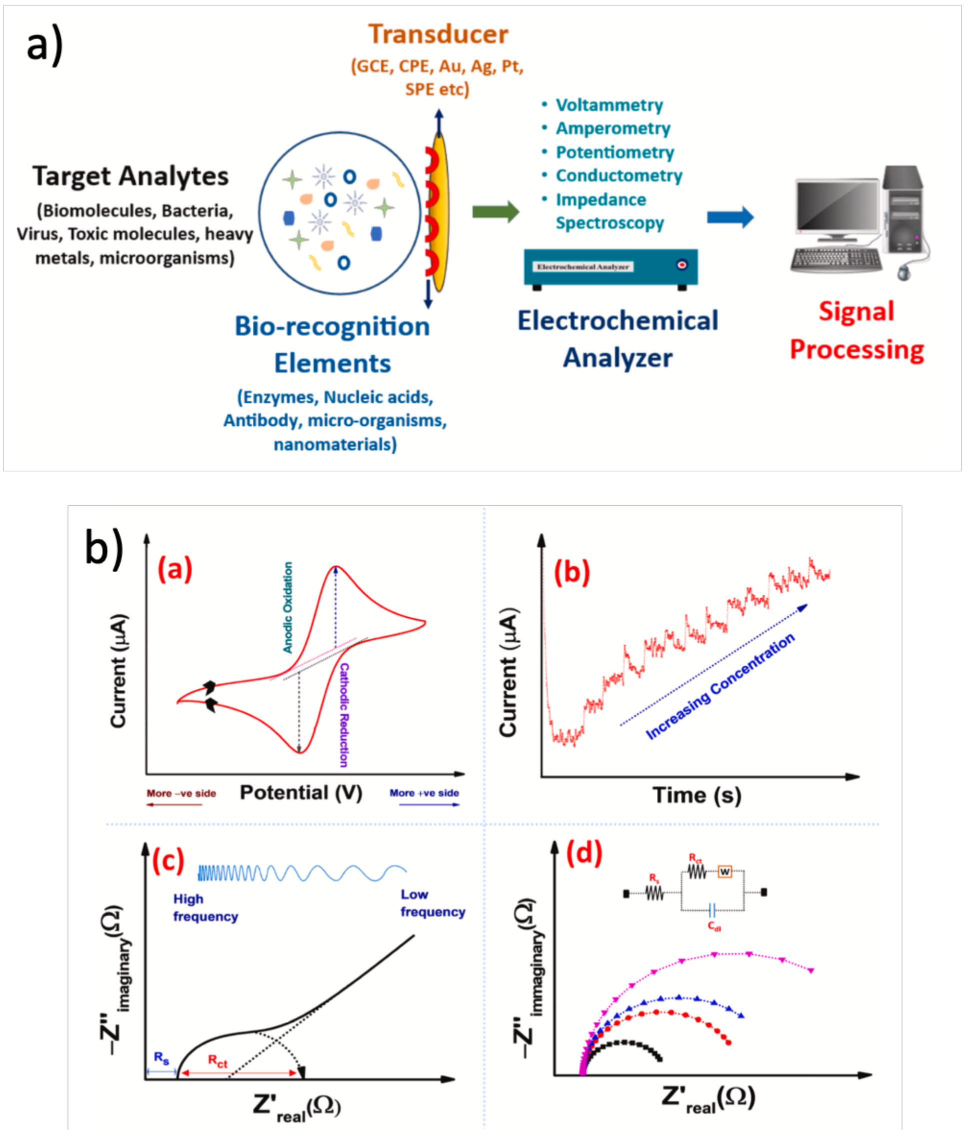

Figure 1.5: a) A schematic representation of electrochemical biosensor and its components. b) A typical: (a) cyclic voltammogram for a reversible system and (b) amperogram. (c) Impedance spectra in the form of Nyquist plot. (d) Variation in impedance resulting from analyte-interface interactions, Inset: The Randle's circuit corresponding to the impedance obtained*[29]*

A biological recognition element (also termed bioreceptor) is a biological recognition molecule (such as an enzyme, antibody, nucleic acid, microbes) that specifically interacts with a target analyte (such as biomolecules, bacteria, virus, heavy metals). If the recognition element (sensing element) is a non-biological molecule (such as a nano molecule) that catalyzes the target analyte of interest, the sensor is free of the term “bio” and called an electrochemical sensor. For glucose electrochemical sensors, in which the measurements are based on electrochemical oxidation of glucose, the recognition element is either an enzyme or nano-catalyst that interacts with glucose in the biological sample. The electrochemical transducer is the working electrode in electrochemical systems, that transforms the recognition information (biological/physiochemical changes after receptor-analyte interaction) into measurable electrical signal which can be analyzed using different methods (in this case, electrochemical techniques). The transformed signal (electrical signal) is then amplified, processed in their respective systems and later displayed as quantifiable signal (curves, graphs, voltammograms, numbers). Figure 1.5 (b) displays quantifiable information in form of voltammograms from different electrochemical techniques[29].

Sensors are categorized into different types depending on the type of receptor and signal transduction system/ detection system. As for glucose detection and according to receptor used, there are two glucose sensors: enzymatic and non-enzymatic glucose sensors, which will be explained in detail in sections (1.3.1 & 1.3.3). Glucose sensors based on the signal transduction system are classified into electrochemical and optical sensors which rely on electrochemical and optical technologies; respectively, to detect recognition changes. Optical sensors utilize optical transduction systems (optical spectroscopic techniques) (e.g., fluorescence, surface plasmons resonance (SPR)) to measure the change of intensity of light, wavelength or polarization, that is proportional to the concentration of glucose, (Figure 1.6a). To illustrate, in both a fluorescence spectroscopy-based glucose sensor and a surface plasmons resonance (SPR)-based glucose sensor, glucose binds reversibly with the molecular recognition element (fluorophores) (Figure 1.6b) and plasmonic nanoparticles (Figure 1.6c); respectively, causing a change in fluorescence intensity of these fluorophores as well as a change in the light reflectance’s angle; these variations are directly proportional to glucose concentrations[27].

Figure removed due to copyrights issues

Figure 1.6: a) A general scheme of an optical (spectroscopic) (b) fluorescence and (c) surface plasmon resonance-based glucose sensor[27]

In counterpart, electrochemical sensors apply electrochemical techniques to detect the electrochemical change (typically, electrical current, potential, conductivity or impedance), which is in good respect to glucose concentration. Accordingly, electrochemical sensors are classified into amperometric, voltammetric, potentiometric, conductometric and impedimetric sensors[28-29]. Amperometric sensors measure the current flow produced by electrochemical redox reactions between the target analyte and the recognition element in an electrochemical cell at a constant applied potential. Voltammetric sensors are like amperometric, rely on measuring the current flow in electrochemical cell between WE and CE; however, the response current in voltammetry is measured as a function of applied potential which varies linearly with time over a pre-determined potential range (e.g., cyclic voltammetry). Potentiometric sensors measure the potential difference between two electrodes in an electrochemical cell owing to the accumulation of ions at WE interface, resulting from analyte and biorecognition element interaction. Conductometric sensors measure the conductivity change of the solution due to the consumption or production of ions resulting from analyte/bioreceptor interaction. Lastly, Impedimetric sensors measure the impedance or resistance changes due recognition process between analyte and recognition element in an electrochemical cell within a wide frequency range with respect to time. The impedance obtained data are often represented by Nyquist plot, translated into an equivalent Randle's circuit model (semi-circular indicates charge transfer resistance while deviation from a perfect arc indicates diffusion-controlled processes), as referred to in Figure 1.5b[28-29]. The measured signal obtained from such sensors is related to the concentration of target analyte in the solution. Electrochemical sensors have advantages compared to others because of their simplicity, stability, fast response, inexpensive, feasibility to miniaturize, their high sensitivity and selectivity[30]. Additionally, they are required in many applications such as food safety, medical diagnostics and health care, industry, and environmental monitoring, biotechnology and bioengineering.

1.3 Advancements in electrochemical glucose sensors: a literature review

Electrochemical glucose sensors have played a pivotal role in diabetes management, by monitoring blood sugar levels. Over the past decades, significant advancements have been made on improving the design, materials and technologies to enhance sensor's performance, user convenience and cost effectiveness, as shown in Figure 1.7.

Figure removed due to copyrights issues

Figure 1.7: Development trend of glucose sensor technology[31]

The figure displays the sensor technology's development from the first enzyme electrode concept by Clark to the launch of the first specialized blood glucose analyzer in the 1970s, followed by the introduction of Dextrometer; the first commercial blood glucose meter with digital display (1979). The 1980s witnessed the use of meters and strips for self-monitoring glucose levels, followed by significant improvements in the development of strips, needles, less use of blood; etc. Later on, in the 1990s, the appearance of minimally invasive devices; like subcutaneous glucose detector with a fine needle and Glucowach for the first real-time CGMS. From the 2000s up to date, improvements on minimally and non-invasive sensors to monitor glucose in tear, sweat, saliva and interstitial fluid are constantly changing and advancing[31]. Below is a review of the evolution of glucose sensors across different generations, including their working principle, chemical reaction mechanisms, advantages and drawbacks.

1.3.1 Enzymatic glucose sensors (first, second and third generation of glucose sensors)

Enzymatic electrochemical sensors are based on the use of enzymes such as glucose oxidase (GOx) or glucose dehydrogenase (GDH) as catalysts for the oxidation of glucose into gluconic acid. Glucose oxidase enzyme (GOx) was preferable for such reaction due to its high specificity towards glucose, in addition to its high stability comparing to other enzymes[20].

The first generation of GOx-based glucose sensors was first introduced by Clark & Lyons in 1962, utilized an enzyme-coated membrane on an oxygen electrode[23, 31], for the catalytic oxidation of glucose by enzyme (GOx) in the presence of natural oxygen as an oxidation mediator (an electron acceptor) to produce gluconic acid and hydrogen peroxide (H_2O_2), Equations (1.1–1.3)[23, 26-27]. The concept of such oxygen-dependant sensors was based on detecting glucose by monitoring the oxygen consumption in the GOx-catalysed reaction.

$$\text{Glucose }(C_6H_{12}O_6) + O_2 \xrightarrow{\text{GOx}} \text{Gluconolactone }(C_6H_{10}O_6) + H_2O_2 \tag{1.1}$$

$$\text{Gluconolactone }(C_6H_{10}O_6) + H_2O \longrightarrow \text{Gluconic acid }(C_6H_{12}O_7) \tag{1.2}$$

Therefore, the overall reaction is:

$$\text{Glucose }(C_6H_{12}O_6) + O_2 + H_2O \xrightarrow{\text{GOx}} \text{Gluconic acid }(C_6H_{12}O_7) + H_2O_2 \tag{1.3}$$

Updike and Hicks later after developed a sensor with two oxygen-working electrodes system to measure the current differential, effectively eliminating noise caused by background oxygen[26]. Subsequently, Guilbault and Lubrano in 1973 introduced their first amperometric glucose sensor and determined glucose concentration by measuring the resulting H_2O_2. The sensor detected the current released from the oxidation of hydrogen peroxide that was proportional to glucose concentrations in the sample, Equation (1.4)[26-27]. However, this reaction to proceed at Pt electrode required elevated operation potentials, about +0.6 V vs Ag/AgCl[32].

$$H_2O_2 \xrightarrow{electrode} O_2 + 2H^+ + 2e^- \tag{1.4}$$

To understand the process of glucose oxidation of first-generation glucose sensors, it is important to consider that the reaction initially takes place on the enzyme layer, specifically, at the active redox center of glucose oxidase (flavin adenine dinucleotide (FAD))[33]. To go into detail, Equation (1.3) will be analyzed in two steps: Equation (1.5) & Equation (1.6). The enzyme in its oxidized form (GOx(FAD)) selectively oxidizes glucose to gluconic acid; then, by accepting 2 electrons and 2 protons from glucose it converts to its reduced form (GOx($FADH_2$)), Equation (1.5). For the enzyme's catalytic activity to continue without interruption at this stage, the redox cycle of the enzyme must be completed by reproducing its oxidized form, which requires the presence of an electron acceptor (natural oxygen mediator), Equation (1.6)[23, 26]. The process progresses at the electrode surface, where hydrogen peroxide oxidizes to release oxygen and generate current signal that is in good respect to blood glucose concentrations, as pointed out in Equation (1.4)[26].

$$\text{Glucose } (C_6H_{12}O_6) + \text{GOx (FAD)} + H_2O \longrightarrow \text{Gluconic acid } (C_6H_{12}O_7) + \text{GOx } (FADH_2) \quad (1.5)$$

$$\text{GOx } (FADH_2) + O_2 \longrightarrow \text{GOx (FAD)} + H_2O_2 \quad (1.6)$$

Despite the high ability of GOx-based sensors to react specifically to glucose and provide quantitative glucose readings, they were limited by inaccuracy issues due to variations and limitations of dissolved oxygen in physiological media, known as “oxygen deficit”[26, 34], directly affecting the sensor’s response. The performance of oxygen dependent sensors was also highly affected by the presence of common interferents in the blood such as ascorbic acid and uric acid, electroactive at the high potentials required for H_2O_2 detection[26, 34]; thus, negatively impacting the sensor selectivity.

These limitations gave rise to the second generation of glucose sensors, which involved the utilization of an artificial redox mediator (either free/diffusing or immobilized on the electrode or the enzyme itself); thereby replacing the first-generation natural oxygen mediator. The use of suitable redox mediator such as ferrocene[35], ferricyanide[36], osmium[37-38] and quinone compounds[39] enables for ease and rapid electron movements from FAD’ active centers to electrode surface[27, 40]. The initial step of the enzymatically catalyzed reaction (Equation (1.7)) is the same as the one mentioned in the first generation (Equation (1.5)), entailed the oxidation of glucose by GOx (FAD) to form gluconic acid and GOx($FADH_2$). Then, the reduced enzyme GOx($FADH_2$) transferred electrons to the artificial electron acceptor (mediator) to produce GOx(FAD) and the reduced mediator Med_{red}, Equation (1.8)[26]. The final step required the oxidation of the latter (Med_{red}) at electrode surface at lower operating potential (+0.2 to +0.4 V vs Ag/AgCl), and the released electrons were used for glucose detection[31], Equation (1.9):

$$\text{Glucose } (C_6H_{12}O_6) + \text{GOx (FAD)} + H_2O \longrightarrow \text{Gluconic acid } (C_6H_{12}O_7) + \text{GOx } (FADH_2) \quad (1.7)$$

$$\text{GOx } (FADH_2) + Med_{ox} \longrightarrow \text{GOx (FAD)} + Med_{red} \quad (1.8)$$

$$Med_{red} \xrightarrow{electrode} Med_{ox} + 2H^+ + 2e^- \quad (1.9)$$

The mediated enzyme sensors could eliminate relevant oxygen issues; for instance, the sensor obtained more accurate readings and improved selectivity being operating at lower detecting potentials. On the other hand, potential toxicity of mediators (e.g, ferrocene and ferricyanide) due to possible leakage into surrounding tissues, complexity in sensor fabrication and enzyme instability affected second-generation glucose sensors' performance and limited their application use[32-33].

The third generation of enzymatic glucose sensors was developed by immobilizing the enzyme on the electrode without using a mediator to enable direct electron transfer between enzyme and electrode, as shown in Figure 1.8. Alike first and second generations, the first step of glucose oxidation into gluconic acid synchronized with the reduction of GOx(FAD) into GOx($FADH_2$), Equation (1.10)[26]. However, for the third generation, the reverse redox reaction towards reproducing GOx(FAD), Equation (1.11), required electron transfer directly to electrode surface through enhancements in electrode materials and enzyme immobilization techniques[31].

$$\text{Glucose } (C_6H_{12}O_6) + \text{GOx (FAD)} + H_2O \longrightarrow \text{Gluconic acid } (C_6H_{12}O_7) + \text{GOx } (FADH_2) \qquad (1.10)$$

$$\text{GOx } (FADH_2) \xrightarrow{electrode} \text{GOx (FAD)} + 2H^+ + 2e^- \qquad (1.11)$$

The direct electron transfer (DET)-based enzymatic sensors managed to avoid the issues associated with oxygen and mediators and provided better advantages. To exemplify, these sensors detected glucose at low potentials (~ –0.32V vs Ag/AgCl), close to the enzyme's redox potential region[34]; namely, lower chance for electroactive interference. Also, the shrinkage of the reaction chain components made it possible for designing more compact and efficient sensors. Yet, achieving the direct electron transfer from the enzyme's active site to the electrode–without using a mediator– is still a technical challenge. This is primarily due to the flavine's redox centre being firmly bound and deeply embedded within the GOx matrix, about 13 Å deep, which hinder efficient electron transfer[34, 41]. The techniques and strategies employed to overcome this challenge include binding electron transfer domains (e.g., cytochrome and ferredoxin) to the enzyme, ensuring proper orientation of the enzyme on the electrode surface (e.g., covalent attachment, non-covalent adsorption, entrapment and cross linking), nanostructuring the electrode (e.g., carbon nanotubes and nanoparticles), and modifying the electrode surface with conductive polymers[42]. Another drawback of third-generation glucose sensors is that they are enzyme-based sensors and therefore still suffer from several limitations related to enzyme instability, manufacturing complexity, and special operating conditions.

Figure removed due to copyrights issues

Figure 1.8: Working principle of different generations of an electrochemical glucose sensor[*27*]

Considerable efforts have been made to minimize the issues related enzymatic sensors and to improve their performance in terms of accuracy, sensitivity and selectivity. For instance, supplying the electrode with oxygen via incorporating oxygen-rich materials (oxygen-rich carbon paste)[43-44] and using diffusion limiting membranes were beneficial to address "oxygen deficit" problem; thus, ensuring constant supply of oxygen to the enzymatic reaction and boosting the sensor's precision. Incorporating nanostructured composites to the sensing electrodes could address the oxygen dependence related issues[45]. Attempts for employing permselective membranes (e.g., Nafion (Nf)[37, 46] and cellulose acetate[47] to limit the access of interferent species[26, 34], and using electrocatalysts (Prussian blue (PB) or noble metal like Rh)[34, 48-49] to lower the operation potential of H_2O_2 at an optimal free-interferents range (+0.0 to –0.20 V)[32, 34], these attempts played an effective role in enhancing the sensor's selectivity. Most importantly, incorporating nanostructured materials (e.g., metal nanoparticles[50] and metal oxide nanostructures[45, 51], carbon nanotubes[38, 52-53], graphene[54-55] and conductive polymer[56-58]) significantly improved enzyme immobilization strategies[36] and contributed to the overall sensor's performance in terms of accuracy, selectivity and sensitivity, and further developing continuous and real-time glucose monitoring systems[26]. For instance, Phasuksom et al.[52] fabricated an enzymatic glucose sensor based on GOx enzyme mixed with chitosan immobilized on a modified electrode surface by a linker of (3-Aminopropyl) triethoxysilane (APTES). The electrode is composed of doped polyindole (dPIn) mixed with multi-walled carbon nanotubes (MWCNTs) modified onto screen-printed carbon electrode (SPCE), as depicted in Figure 1.9a & Figure 1.9b. The sensor exhibited an enhanced sensitivity of 182.9 $\mu A\ mM^{-1}\ cm^{-2}$ with an LOD of 0.01 mM within a concentration range of 0.01−100 mM, compared to its counterpart (SPCE without MWCNTs) that showed a sensitivity of 55.7 $\mu A\ mM^{-1}\ cm^{-2}$ with an LOD of 0.01 mM within a concentration range of 0.01−50 mM. Figure 1.9c shows the development of GOx-based electrode, in which the of graphite rod (GR) electrode was first modified with gold nanostructures (AuNS), followed by the deposition of Prussian blue (PB). Then, the immobilization of GOx was performed, followed by the stabilization with Nafion (Nf)[48]. The synthesized electrode displayed a wide linear range of glucose (0.025–1 mmol/L), low detection of limit of 0.0088 mmol/L and high selectivity over interference molecules thanks to the PB that lowered the operation protentional to -0.05 V vs Ag/AgCl/KCL $_{3molL}{}^{-1}$. Another attempt to develop enzymatic glucose sensors has been made, by applying conductive polymer nanocomposites (PNC) (polyaniline (PANI) and polypyrrole (Ppy)-based nanocomposites) mixed with GOx and gold nanoparticles (AuNPs) on the graphite rod (GR) electrode followed by the immobilization of GOx, Figure 1.9d. The developed electrode exhibited high sensitivity (65.4 and 55.4 µA mM^{-1} cm^{-2}), low limit of detection (0.070 and 0.071 mmol/L), wide linear range (up to 16.5 mmol/L), as well as an excellent anti-interference ability to ascorbic acid and uric acid[56].

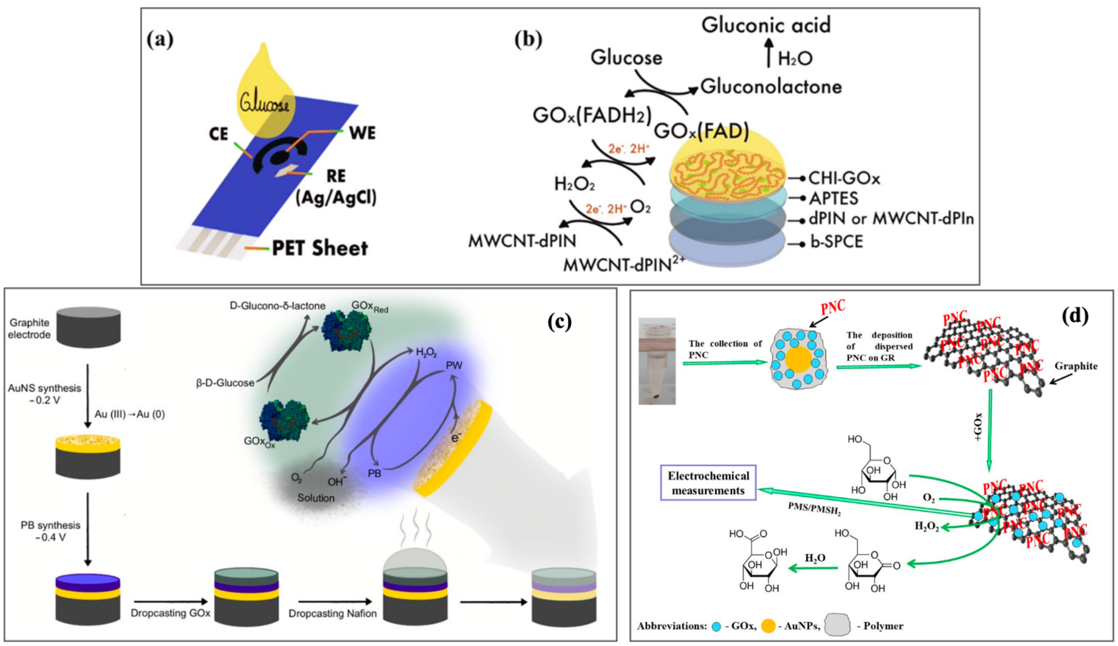

Figure 1.9: Enhancements in enzyme-based glucose sensors

(a) Components of SPCE; and (b) the possible glucose mechanism of the fabricated glucose sensor[52]. (c) Schematic representation of the glucose biosensor preparation and glucose determination. The electrochemical synthesis of AuNS and PB on the GR electrode was performed, followed by GOx immobilization and stabilization by Nf[48]. (d) Schematic representation of the deposition of PANI-AuNPs$_{(6\ nm)}$-GOx or Ppy-AuNPs$_{(6\ nm)}$- GOx nanocomposites (PNC) on the surface of GR electrode with the following additional enrichment by GOx, and glucose determination by the developed enzymatic biosensors[56].

Despite the advancements on enzymatic electrochemical sensors towards glucose sensing, they suffer from a lack of long-term stability (enzyme activity's loss over time) due to GOx denaturation on the electrode surface. GOx can be easily affected by pH, temperature, toxic chemicals and humidity. Furthermore, they are expensive due to the complexity of enzyme immobilization on the electrode surface[33, 40]. Considering all above in mind, the majority of currently available glucose sensors are based on a fingertip prick procedure, in which a lancet (needle) allows a drop of blood to be collected and placed onto a disposable enzyme test strip inserted into the sensing device; thereafter, blood glucose level can be determined and displayed in seconds[59]. Although these sensors have seen significant advancements; becoming more compact and more precise to self-monitoring blood glucose (SMBG), diabetic people still face challenges, such as the pain from needle punctures and the need for frequent measurements throughout the day to monitor their blood sugar levels.

1.3.2 Continuous glucose sensors

Continuous glucose monitoring (CGM) sensors have brought radical changes to diabetes management by offering real-time information and continues monitoring of glycemia levels, reducing the risk of complications. CGM sensors (implantable and wearable types) offer a promising solution for diabetic patients by not only providing continuous glucose monitoring with ease but also reducing the pain and discomfort associated with conventional enzymatic sensors (e.g., SMBG devices). The concept involves implanting the sensor (e.g., needle-based sensor) under the skin and transmitting the information to a monitoring device (e.g., receiver or portable device) that can be linked to an insulin pump[60-61]. This system provides continuous information about interstitial glucose levels; the sensor measures glucose concentration and the pump regulates the insulin dose that has to be injected, so both play in a close circuit that mimics an artificial pancreas[61].

Over the past two decades, considerable enhancements in CGM sensors have been achieved by leading companies such as Dexcom, Medtronic, and Abbott. While early CGM versions improved the glucose monitoring system, they were deemed invasive due to the need for punctures during detection and calibration processes[31]. Advances in studies and research have led to the introduction of less painful sensors, which depend on inserting a fine needle under the skin with minimal pain and without drawing blood, thus measuring sugar levels in the subcutaneous interstitial fluid (ISF) continuously every few minutes. The data then transferred wirelessly to a monitor shows how glucose levels vary over hours to days. Most current CGM sensors available in the market are invasive and minimally invasive devices that are electrochemical enzyme-based sensors[59, 62]. Figure 1.10(A) displays a schematic of minimally invasive subcutaneous glucose sensors for continuous glucose monitoring currently available on the market. The system is based on either (i) electrochemical enzymatic sensors with a combination of natural or synthetic mediators, or (ii) optical means that employ a fluorescent probe coupled to a fluorescent detection system. Figure 1.10(B) describes an example of modern non-invasive wearable sensors that measure glucose in biofluids other than blood (e.g., wearable sweat glucose sensor using a sampling patch). Figure 1.10(C) shows a typical self-monitoring blood glucose (SMBG) sensor that apply blood vessel puncture procedure, an invasive sensor[59].

Figure removed due to copyrights issues

Figure 1.10: Schemes for the sensors and systems for A; CGM, B; wearable sensor, and C; self-monitoring of blood glucose (SMBG), including location of sampling, and system components

A: General layout of a subcutaneously implanted, minimally invasive glucose sensors for continuous glucose monitoring, which are currently on the market. B: Example of a wearable sensor targeting glucose monitoring in the sweat using sampling patch. C: Representative sensor and monitor for SMBG[59].

The trend towards developing minimally invasive[62] or non-invasive technologies[63-65] has become a key focus of research, driving innovation of various sensors capable of measuring glucose in biological fluids other than blood, such as tears, saliva, sweat, urine, and interstitial fluid (ISF)[59, 62-63, 66]. Bai et al.[62] proposed a coin-sized, fully integrated and minimally invasive (wearable) glucose monitoring system based on organic electrochemical transistors (OECTs), particularly capable of combining electrochemistry and transistor amplification; thus, enhancing overall sensing performance. As depicted in Figure 1.11 , the

OECT-CGM technology comprises of the following elements: (i) a hollow microneedle patch, serving as the minimally invasive bridge between ISF and the OECT-CGM sensor (ii) a firm, adhesive and enzyme-loaded hydrogel buffer membrane, sandwiched between the microneedle and the OECT sensor, to enhance the skin-device interface and boost sensing reliability (iii) an OECT-based glucose sensor, acts as a glucose biosensor for signal amplification (iv) a miniaturized OECT readout system; personalized electronic reader for electrochemical transistors (PERfECT) and (v) a three-dimensional (3D)–printed resin encapsulation layer[62]. Besides the benefits of CGM sensors in helping users in managing their diabetes, by providing real-time glucose measurements continuously on their personal smart devices, they also offer the capability to deliver real-time predictive alerts for potential hypo/ hyperglycemic incidents[61].

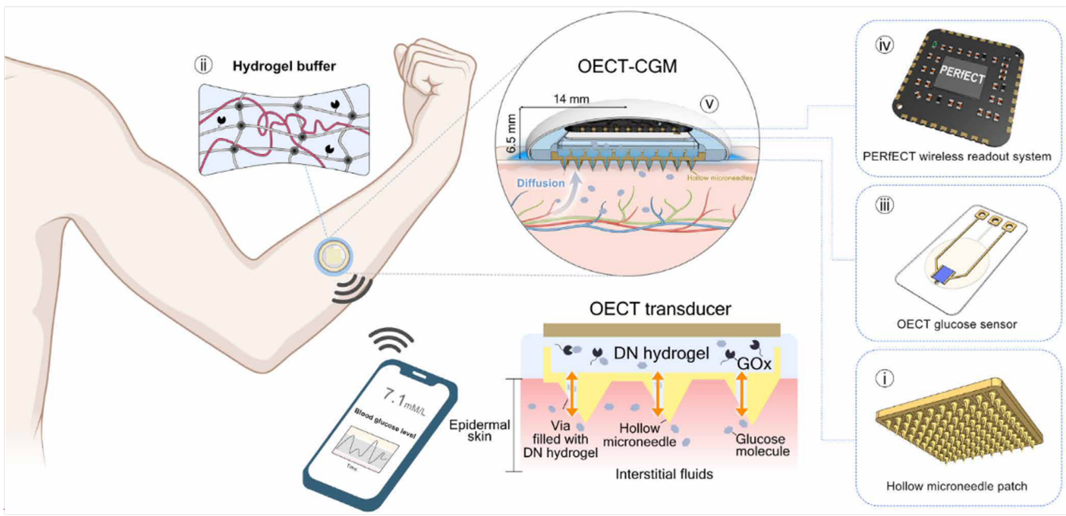

Figure 1.11: The concept and design principle of the OECT-CGM system

The OECT-CGM consists of: (i) a microneedle patch, (ii) a soft and adhesive hydrogel buffer membrane, (iii) an OECT glucose sensor, (iv) a miniaturized OECT readout system (PERFECT), and (v) a 3D-printed resin encapsulation case. The integration was strategically optimized to minimize the overall size of the system for a comfort wearability[62].

Although major efforts have been made to develop implantable and wearable continuous glucose sensors, a lack of accuracy and stability have been reported[27]. It should be noted that these sensors require advanced electrode materials that possess specific characterizations. First, the material reactivity must be superior towards glucose and must yield a greater current density response than others. Sensitivity towards glucose must be maximum, where the measured signal (current) must be proportional to glucose concentration; thus, quantitative information can be determined from the calibration curve. Stability of the sensor, so that the measured current must be stable over time and corresponding to the same blood sugar. Selectivity, in which the sensor's material must not be sensitive to interference species such as ascorbic and uric acids and must not be poisoned by chloride ions. Compatibility and durability, so material inserted in the body must not deteriorate over time and does not get rejected by the body. Furthermore, it must stand the physiological environment conditions. Finally, the reproducibility of the material, so the material must have the same characteristics under the same synthesis conditions[29].

1.3.3 Non-enzymatic glucose sensors (fourth generation glucose sensors)

To overcome the drawbacks linked to the enzyme-based sensors (e.g., intrinsic enzyme instability problems), modifying the electrode surface with a non-biological catalyst was a promising approach towards the direct glucose electrooxidation on electrode surface[27, 67], emerging of the fourth-generation glucose sensors[40, 68], as demonstrated in Figure 1.8. Non-enzymatic glucose sensors (NEGS) do not rely on enzymes as catalysts for glucose detection. Instead, they employ materials based on noble metal or transition metals/ metal oxides with intrinsic catalytic activity towards glucose oxidation[69]. These catalysts enable the direct electrooxidation of glucose molecules on electrode surface, generating an electrochemical signal correlating with the glucose concentration. In non-enzymatic glucose sensors, the active atoms on the surface of modified electrode or electrode itself serve as available active sites for the adsorption of glucose molecule for electrocatalytic oxidation[40]. Two major models have been proposed in literature to explain the catalytic mechanism of electrochemical oxidation of glucose on metal-based NEGS: (i) Activated chemisorption model and (ii) Incipient hydrous oxide adatom mediator (IHOAM)[20, 22, 26, 40]. The first model, activated chemisorption model, proposed by Pletcher assumes that the electrocatalytic process of glucose oxidation begins with the adsorption of target analyte glucose on electrode surface. The process involves the hydrogen abstraction (the removal of a hydrogen atom from the hemiacetalic C1) which is simultaneously accompanied by the chemisorption of reactive organic species onto metal electrode surface, Figure 1.12a. This process is seen as the rate-determining step in most glucose electrooxidation experiments[40]. The dehydrogenated glucose (organic species) oxidizes into gluconolactone (by releasing $2e^-$ and removing $2H^+$), which is further oxidized to gluconic acid via a fast hydrolysis, Figure 1.4[20].

(a)

Figure removed due to copyrights issue

(b)

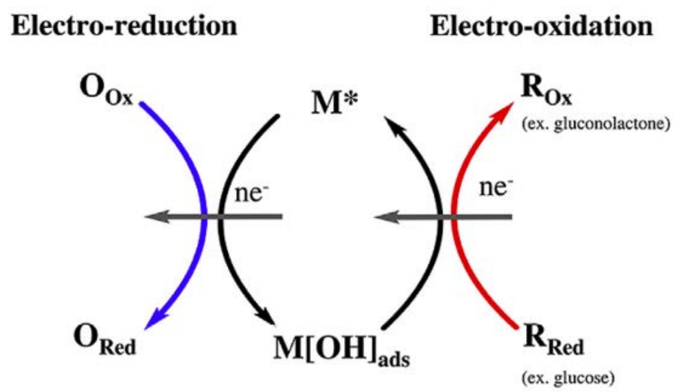

Figure 1.12: a) The chemisorption mechanism of glucose oxidation. b) Incipient hydrous oxide/adatom mediator model a) The reactant (glucose) is chemically adsorbed first, through concerted process of hydrogen abstraction and chemisorption of reactive intermediate onto the metal electrode surface, before it is further oxidized. b) The presence of reactive hydrous oxide (OH_{ads}) layer on the electrode is believed to promote fast electro-oxidation of glucose into glucono-δ-lactone [20, 22].

The IHOAM model proposed by Burke suggests that the active metal atoms on electrode surface faced a pre-oxidation step by reactive hydroxide anions, formed an incipient hydrous oxide layer (pre-monolayer) that mediates the oxidation of adsorbed species at lower potentials[22]. Atoms across metal surface, grain boundaries and edges are more prone to direct exposure to solution relative to the bulk crystal structure; thus, suffering from a lack stabilization energy and becoming more reactive and further facing pre-monolayer oxidation at low potentials[22]. The process can be illustrated as in the following equations[26]: First, the production of active OH^- anions, produced from the water dissociation:

$$H_2O \rightarrow H^+ + OH^- \qquad (1.12)$$

Followed by the chemisorption of active OH^- onto the reactive metal adsorption sites (M) to form the oxidative adsorbed hydroxide radical $M[OH]_{ads}$ layer:

$$M + OH^- \rightarrow MOH_{ads} \qquad (1.13)$$

The adsorbed OH_{ads} layer is believed to have a crucial role for electrocatalysis process in many applications, particularly, glucose electrooxidation[40]. It was also observed that the formation of OH_{ads} increases in strong alkaline conditions (abundant of OH^- anions)[26]. Figure 1.12b illustrates IHOAM mode, in which the oxidative and reductive processes are catalysed at the metal surface through the reductive metal adsorption site M* and the oxidative adsorbed hydroxide radical $M[OH]_{ads}$[22]. It has been reported that the IHOAM model complementarily describes the complex electrocatalytic process of glucose along with the activated chemisorption model[20, 26], whereas the latter describes only the adsorption process of glucose on metal-based surface without taking into account the oxidative role of hydroxide radicals[70], a role that was evident in many reports[22, 40]. Understanding these models and the conditions under which each mechanism prevails, are crucial for designing more efficient glucose sensors. Figure 1.13a & Figure 1.13b demonstrate glucose oxidation mechanism on gold and platinum surfaces by activated chemisorption and IHOAM models; respectively[30], though some previous studies suggested the dependence of glucose oxidation mechanism on the presence of Au(OH) on gold surface[20].

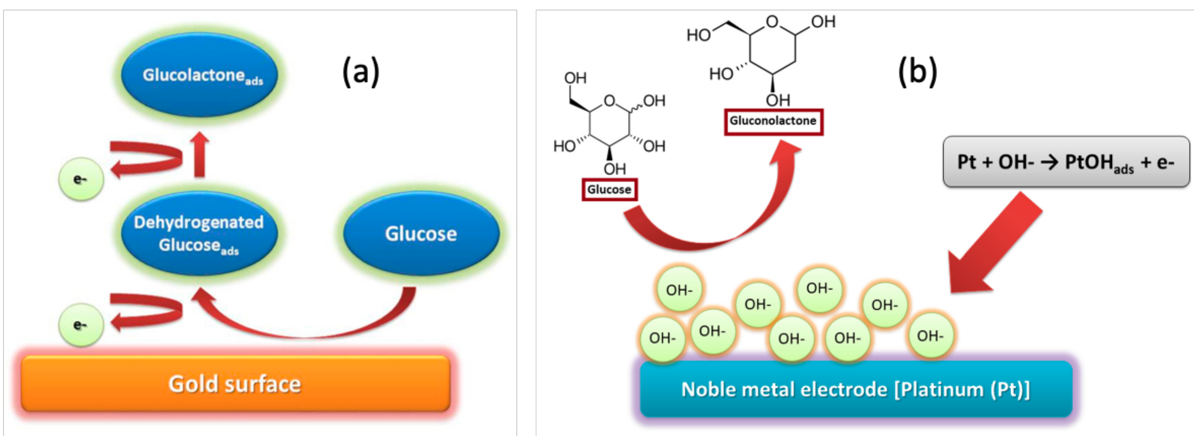

Figure 1.13: (a) Mechanism of glucose oxidation in Chemisorption Model. (b) Mechanism of glucose oxidation in IHOAM Model[30]

Among the most studied metals for NEGS are noble metals (e.g., Au and Pt); however, their application use is restricted by their high cost, risk of poisoning by chloride ions, and susceptibility of interference with other electroactive species[26, 40]. Transition metals (such as Ni, Cu and Co, etc.)[71] have also been investigated for NEGS. Despite their low cost compared to noble metals, their sensing mechanism towards glucose oxidation does not follow the above models, and rather it can be explained by the redox reaction occurring at the transition metal centers[20], as described later on. It has been noted that the sensing mechanism depends directly on the metal catalyst type constituting the electrode surface[26], and each catalyst has its own characteristics. As such, improvements have been made to noble and non-noble metal-based electrodes, by incorporating metal alloys, hybrid composites and nanostructured materials to improve their catalytic properties[26, 72].

Transition metal oxides have attracted more attention due to their stability and availability[73]. The sensing mechanism of many metals oxide-based NEGS relies on the interaction between glucose molecule and the metal oxide redox centres, which are provided following the surface activation of metal oxide by hydroxide ions[73-74]. The direct oxidation reaction of glucose often operates under strong alkaline medium (e.g., pH 13)[73]. Thus, the presence of strong hydroxide ions (OH^-) is a prerequisite for the formation of intermediates that are necessary for facilitating the electrocatalytic oxidation of glucose and boosting the sensor's performance[30]. The electrode surface is often modified with nanoporous metals (e.g., nanoporous gold) or carbon materials with high surface area to enhance the availability of active sites and promote efficient electron transfer[74]. The glucose sensing mechanisms of most metal oxides (like Co_3O_4, NiO and CuO) are similar and result in the formation of intermediates, which could be reduced back to the original metal oxide form as in the case of Co_3O_4[73], as illustrated in Figure 1.14. Manganese oxide (MnO_2) also operates in strong basic pH medium; however, MnO_2 directly interacts with glucose without forming any mediators for the accomplishment of non-enzymatic glucose sensing[30, 73].

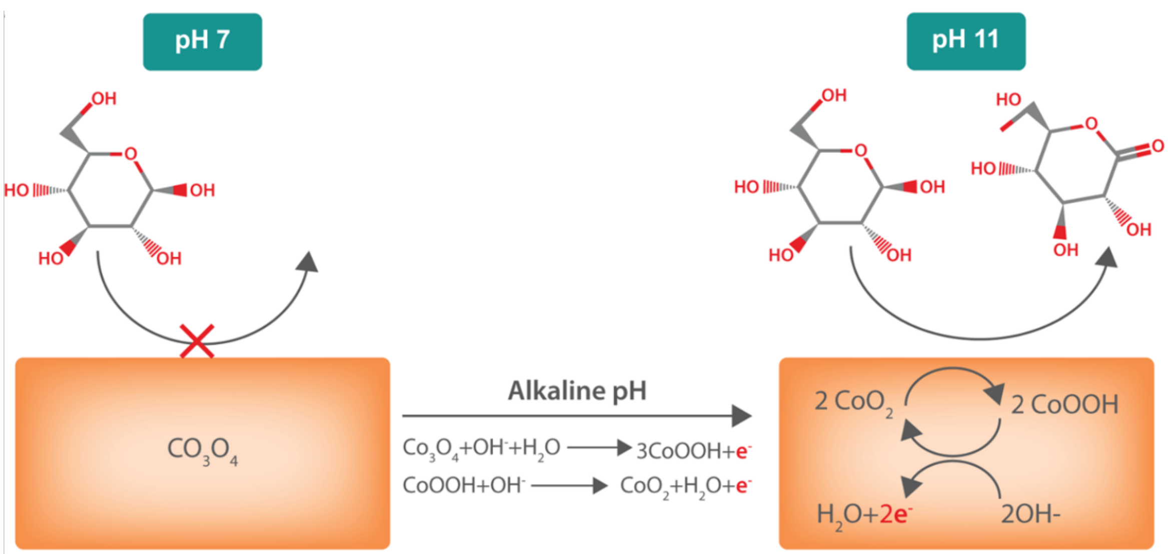

Figure 1.14: Sensing mechanism of Co_3O_4 contacts

At pH 7, the contact is primarily Co_3O_4, which does not oxidize glucose. In alkaline conditions (pH ≥ 11), the contact is now mainly CoO_2. CoO_2 species react with glucose and are converted to CoOOH. This CoOOH is then oxidized back to CoO_2. For every oxidized glucose molecule, the contact collects two electrons measured as I_g[74].

The sensing mechanisms of aforementioned metal oxides are demonstrated in the following equations[73]:

$$Co_3O_4 + OH^- + H_2O \longleftrightarrow 3CoOOH + e^- \quad (1.14)$$

$$CoOOH + OH^- \longleftrightarrow CoO_2 + H_2O + e^- \quad (1.15)$$

$$2CoO_2 + C_6H_{12}O_6 \text{ (glucose)} \rightarrow 2CoOOH + C_6H_{10}O_6 \text{ (gluconolactone)} \tag{1.16}$$

As shown in Figure 1.14, at high pH, two CoO_2 species oxidize one molecule of glucose to gluconolactone and are simultaneously reduced to two CoOOH intermediates species. These intermediates are subsequently oxidized back to two CoO_2, releasing two electrons that are detected as a current signal.

The mechanism of NiO involves the electrooxidation of Ni(II) oxide to Ni(III) oxyhydroxide intermediates, which oxidize glucose into gluconolactone, as represented by the following reaction[73]:

$$NiO + OH^- \rightarrow NiOOH + e^- \tag{1.17}$$

$$2NiOOH + C_6H_{12}O_6 \text{ (glucose)} \rightarrow 2NiO + C_6H_{10}O_6 \text{ (gluconolactone)} + 2H_2O \tag{1.18}$$

Similarly, the mechanism of CuO is based on the electrooxidation of Cu(II) oxide to Cu(III) oxyhydroxide species that play crucial role for the catalytic oxidation of glucose into gluconolactone [30, 73, 75]:

$$CuO + OH^- \rightarrow CuOOH + e^- \tag{1.19}$$

$$Cu(OH)_2 + OH^- \rightarrow CuOOH + H_2O + e^- \tag{1.20}$$

$$2CuOOH + C_6H_{12}O_6 \text{ (glucose)} \rightarrow 2Cu(OH)_2 + C_6H_{10}O_6 \text{ (gluconolactone)} \tag{1.21}$$

As for MnO_2 mechanism, glucose is directly oxidized by Mn(IV) oxide at high pH, eliminating the need for mediating species:

$$2MnO_2 + C_6H_{12}O_6 \text{ (glucose)} \rightarrow 2MnOOH + C_6H_{10}O_6 \text{ (gluconolactone)} \tag{1.22}$$

It has been reported that the above-mentioned metal oxides show limited catalytic activity towards glucose oxidation at pH levels < 10, but their catalytic activity becomes significant with the increase of electrolyte pH values, which may restrict their clinical applications that necessitate an electrolyte pH to be approximately 7.4 or neutral[30, 73]. Ferric oxide has been reported to exhibit catalytic activity for glucose oxidation on its surface at neutral pH, but its sensitivity in neutral pH is rather low compared to those operating at higher pH values[30, 73].

$$2Fe(III) + C_6H_{12}O_6 \text{ (glucose)} \rightarrow 2Fe(II) + C_6H_{10}O_6 \text{ (gluconolactone)} + 2H^+ \tag{1.23}$$

$$C_6H_{10}O_6 \text{ (gluconolactone)} + H_2O \rightarrow C_6H_{11}O_7^- \text{ (gluconate)} + H^+ \tag{1.24}$$

$$2Fe(II) \rightarrow 2Fe(III) + 2e^- \tag{1.25}$$

Another approach to describe the mechanism of non-enzymatic glucose detection has been stated in Dong's review[73], which depicts the formation of Schottky barriers; when metal oxides (e.g., nickel oxide, titanium oxide, and zinc oxide) are brought into contact with noble metals (e.g., platinum or gold) on their interfaces, and the process mainly relies on the wide band gap of the metal oxide. However, it has been stated that this approach still needs to be studied carefully before being viable[73].

Despite all the efforts made to understand the mechanism behind glucose oxidation sensing by non-enzymatic sensors, the process is still not fully understood; especially when it comes to glucose sensors based on MnO_2 due to the lack of studies related to this type of sensors. For example, the above studies[30, 73] indicated that manganese oxide oxidizes glucose directly to gluconolactone and then to gluconic acid without the need to form intermediates as other metal oxides-based catalysts do. On the other hand, another study revealed the reaction of glucose oxidation by the formation of (Mn^{6+}) intermediate, resulting from the oxidation of (Mn^{4+}) by hydroxyl ions in an alkaline condition, as the following[76]:

$$MnO_2 + 2OH^- \rightarrow MnO_4^{2-} + 2H^+ + 2e^- \tag{1.26}$$

$$MnO_4^{2-} + \text{Glucose } (C_6H_{12}O_6) \rightarrow \text{Gluconolactone } (C_6H_{10}O_6) + MnO_2 + 2OH^- \tag{1.27}$$

$$\text{Gluconolactone } (C_6H_{10}O_6) + H_2O \rightarrow \text{Gluconic acid } (C_6H_{12}O_7) \tag{1.28}$$

NEGS offer advantages including simplicity, stability, and independence from issues associated with enzyme, although they may demonstrate lower selectivity compared to EGS. The choice between EGS and NEGS types depends on factors such as selectivity needs, sensitivity requirements, cost considerations, and specific application contexts. Considerable attention has been drawn toward the synthesis of nanostructured electrode materials for non-enzymatic sensors with optimized characteristics to enhance the sensor performance, as shown in Figure 1.15. Electrodes tailored with nanomaterials have added significant enhancements; for instance, Fu et al. developed an electrode sensor based on carbon nanofiber coat with nickel-cobalt layered double hydroxide (CNF@ Ni-Co LDH) (Figure 1.15(A)), which displayed a high sensitivity of 1.47 mA mM^{-1} cm^{-2} with a wide linear range of 1–2000 µM and low detection limit of 0.03 µM[77]. Wei et al. synthesized non-enzymatic glucose sensors based on hybrid reduced graphene oxide (rGO) and carbonized silk fabric (CSF) decorated with Cu nanoflowers, (Cu-rGO/CSF) (Figure 1.15(B)). The morphology of the fabricated electrodes depended significantly on the time of Cu deposition on rGO/CSF, for 2, 4, 6 and 8 min, as shown in Figure 1.15(B): d, e, f and g; respectively. The optimum sensor exhibited high glucose sensitivities of 6613.3 µA mM^{-1} cm^{-2} and 1541.7 µA mM^{-1} cm^{-2} within two separated linear regions of 0.05–4.0 mM and 4.0–7.0 mM; respectively, and the LOD was of 2.27 µM[75]. An attempt made by Miao et al. to fabricate an electrode based on graphene/zinc oxide nanoparticle nanocomposite modified Ni foam (G-ZnO/Ni foam) (Figure 1.15(C)) showed a high sensitivity towards glucose of 1635.52 µA mM^{-1} cm^{-2} within a linear range of 50–1000 µmol with a correlation coefficient of 0.986[78].

(A)

Figures removed due to copyrights issue

(B)

Figures removed due to copyrights issue

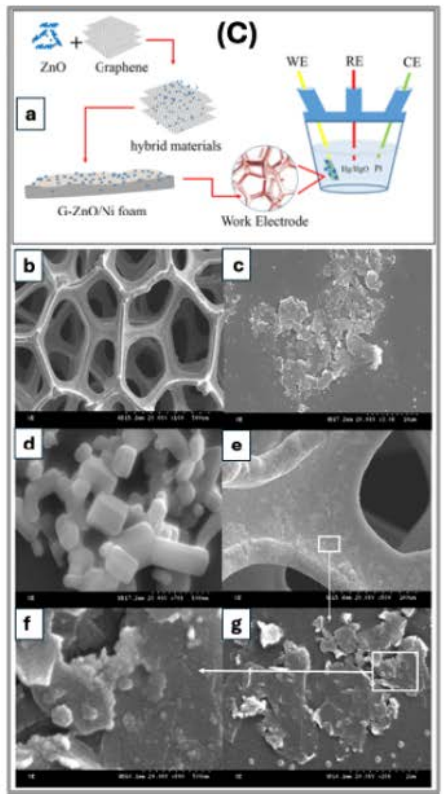

Figure 1.15: An illustration shows different methods for synthesizing different nanostructures materials for non-enzymatic glucose electrodes

(A): (a) The preparation process of the CNF@Ni-Co LDH. SEM micrographs of (b) CNF, (c) CNF@$Ni_{0.66}Co_{0.33}(OH)_2$ and (d) enlarged view of CNF@$Ni_{0.66}Co_{0.33}(OH)_2$[23, 77]. (B) (a) Schematic illustration of the preparation of the proposed reduced graphene oxide and carbonized silk fabric decorated with Cu nanoflowers (Cu-rGO/CSF) electrode. SEM micrographs of (b) CSF, (c) rGO/CSF, (d) Cu-rGO/CSF- 2 min, (e) Cu-rGO/CSF- 4 min, (f) Cu-rGO/CSF-6 min and (g) Cu-rGO/CSF-8 min[23, 75]. (C): (a) The schematic depiction of preparation of G-ZnO/Ni foam electrode. (b) SEM image of Ni foam. (c) SEM image of graphene. (d) SEM image of ZnO nanoparticles. (e)–(g) SEM image of G-ZnO/Ni foam electrode[78].

Currently, research is proceeding towards the advancement of fourth-generation electrochemical sensor technologies. These innovations are designed to address the constraints of earlier generations while enhancing performance, accuracy, and user satisfaction. These sensors typically combine innovative features and advanced materials to enhance glucose monitoring capabilities. Fourth-generation glucose sensors often incorporate advanced features such as enhanced selectivity, continuous monitoring capabilities, miniaturization, wearability, wireless connectivity, improved biocompatibility, longevity, and user-friendly interfaces[62, 79]. While EGS have been widely used and remain foundational for glucose monitoring, they are classified within earlier generations of glucose sensing technology. Consequently, they are typically not considered part of the fourth generation of glucose sensors. Emerging technologies in this domain may encompass NEGS, implantable sensors, microfluidic sensors, and other innovative approaches that enlarge the horizons of glucose sensing capabilities. The most studied materials for electrochemical detection of glucose in NEGS include carbon-based materials (carbon nanotubes, graphene, and graphene oxide)[23, 53], metal nanoparticles (Au, Ag, and Pt)[30, 72], conducting polymers[57, 80], and metal oxides[40]. These materials are often used in various combinations or composite forms to enhance the performance of NEGSs in terms of sensitivity, selectivity, and stability[81-85].

1.3.4 Non-enzymatic glucose sensors based on manganese dioxide

Manganese dioxide (MnO_2), in which the transition element manganese is in the (+4) oxidation state, is one of the most common and extensively studied forms of manganese oxides, including MnO, Mn_2O_3, and Mn_3O_4, among others. The diversity of manganese oxides arises from manganese's ability to adopt multiple oxidation states, ranging from +2 to +7—a characteristic that enables reversible redox transitions. These properties make manganese oxides, particularly MnO_2, highly valuable in a broad range of electrochemical applications, such as supercapacitors, batteries, and sensors. MnO_2 is among the interesting materials that hold promise for the development of fourth-generation glucose electrochemical sensors due to several advantageous properties. Some key reasons for its popularity in this field include (i) high catalytic activity towards glucose oxidation, which is crucial for achieving rapid and sensitive detection; (ii) biocompatibility[86-88], making it suitable for interfacing with biological samples without causing adverse effects; (iii) abundant availability and cost-effective[89], contributing to the feasibility of large-scale sensor fabrication and (vi) stability under various environmental conditions, ensuring the longevity and reliability of glucose sensors. Another benefit of MnO_2 lies in its versatility[90]. It can be synthesized in diverse forms providing flexibility in sensor design and manufacturing[91]. Despite these benefits, there are comparatively few reports in the literature on MnO_2-based glucose sensors[92-95]. Researchers frequently investigate various morphologies and nanostructures of materials, such as nanowires, nanosheets, and nanoparticles, aiming to bolster their electrochemical capabilities for glucose detection. In contrast to film structures, nanorods boast a high surface-to-volume ratio[96], which offers a greater abundance of active sites for electrochemical reactions, consequently leading to enhanced electrochemical surface area (*ECSA*). Their three-dimensional architecture enables improved accessibility of electrolyte ions to the electrode surface, facilitating swifter charge transfer kinetics and expanding the effective surface area accessible for electrochemical processes[97]. Moreover, the hierarchical arrangement of nanorods promotes efficient charge transport within the electrode material, mitigating diffusion limitations and augmenting the utilization of active material, thereby elevating *ECSA*. Lastly, nanorods often manifest heightened electrochemical activity attributable to their unique surface properties and crystallographic facets, yielding a denser distribution of active sites available for electrochemical reactions[98-100]. It has been observed that favourable electrocatalytic properties of MnO_2 are closely related to its crystallography and morphology[101]. As for the crystallographic, MnO_2 has varied polymorphic crystal structures, such as α, β, R, γ, δ and λ, that differ depending on the different arrangement of the basic octahedral MnO_6 unit, giving rise to the formation of different sorts of tunnels, layers or 3D pores within the crystal structure[102-103]. α-MnO_2 known as hollandite, resulting from the corner and edge-shared double octahedral MnO_6 chains, has gained more interest as a catalyst material for glucose sensors due to its unique tunnels; a (1x1) tunnel with dimensions of 1.9 Å x 1.9 Å and a (2x2) tunnel measuring 4.6 Å x 4.6 Å, which enhance electron transfer kinetics[104-105]. The tunnels (2x2) are commonly stabilized by cations such as (K^+, Ag^+, NH_4^+, Ba^{2+}, etc.) that are introduced during the synthesis process[105-106]. Other crystal structures containing tunnels encompass; β-MnO_2 or pyrolusite with (1x1) tunnels, R-MnO_2 or ramsdellite with (2x1) tunnels and γ-MnO_2 or nsutite with mixed (1x1) and (2x1) tunnels (an intergrowth of β and R types with different fractions of β/R). δ-MnO_2 or birnessite is characterized by the layer stacking arrangement, while λ-MnO_2 or spinel is depicted by its 3-dimensional pores[102-103], as shown in Figure 1.16.

Figure removed due to copyrights issues

Figure 1.16: Crystal structures of MnO_2 polymorphs (Mn: magenta and O: red)

The structure of γ-MnO_2 consists of an intergrowth between 1×1 and 2×1 tunnels. The ratio of 1×1 tunnel over 1×1 and 2×1 tunnels is called Pr (0% < Pr < 100%). The shown γ-MnO_2 compound has Pr= 50%. Water molecules and guest cations are omitted for clarity[103].

Besides, α-MnO_2 nanostructures have various morphologies[91], including; dendrite-like[107], curled sheet-like[108], nanorod arrays[96], nanotube arrays[109], nanowires and nanoflowers array[88], which can be obtained via hydrothermal synthesis under different experimental procedures and conditions[110]. The morphology of MnO_x nanostructures can be tuned and optimized through controlled synthesis (e.g., by varying one of the synthesis parameters)[108]. Zhang, Y. group achieved different morphologies of MnO_2 nanostructures such as sheet-like, curled sheet-like, rod-like and particle-like by only increasing the temperature to 100 °C, 120 °C, 140 °C and 160 °C; respectively, while fixing all other synthesis parameters.

1.4 Research topic presentation

1.4.1 Problem statement: key issues and challenges

As far as we know, there is a lack of studies specifically investigating the use of MnO_2 nanorods for glucose electrochemical sensing. Therefore, the primary aim of this work is to assess the electrochemical sensing capabilities of MnO_2 nanorods synthesized through a one-step hydrothermal technique for glucose detection. It is of great importance to also evaluate how effectively the electrode detects glucose, by employing different electrochemical sensing techniques and varying the catalyst support. Evaluating the sensitivity of the reliable and cost-effective synthesized electrode is an essential step in determining its potential use in non-enzymatic continuous glucose monitoring systems (wearable and implantable types). It must be considered that the interfering factor of electroactive species significantly impacts the sensor performance towards glucose detecting. Therefore, we aim to concurrently evaluate the electrochemical activity against interfering molecules such as uric acid (UA), ascorbic acid (AA) and potassium chloride (KCl).

It should be taken into account that MnO_x has poor electrical conductivity; therefore, to boost its conductivity, it is essential to choose an excellent conductive substrate (e.g., carbon-based substrate)[111]. Weina et al. reported that the direct growth of active materials on a conductive matrix (such as carbon materials) can enhance their electrochemical performance through the formation of abundant active sites. They fabricated two electrodes for non-enzymatic glucose sensors; β-MnO_2 micro/nanorod arrays (β-MnO_2 RA) directly grown on carbon fiber fabric and β-MnO_2 micro/nanorod powder (β-MnO_2 RP) immobilized on graphite electrode by Nafion binder. The results obtained from the self-mounting catalyst-based electrode (β-MnO_2 RA) provided high sensitivity towards glucose oxidation of 1650.6 $\mu A\ mM^{-1}\ cm^{-2}$ within wide linear range up to 4.5 mM compared to its counterpart (β-MnO_2 RP) that gave a sensitivity of 1.7 fold less[104]. Therefore, to ensure the best conductivity and most effective performance, the catalyst (MnO_2) must be directly grown onto the substrate (carbon paper) on many active sites as possible without the inclusion of a binder or other additives, which might cause any potential interference with the electrochemical results and impair the electroactivity of the catalyst. Thus, the development of self-supporting MnO_2 catalyst on a conductive carbon paper substrate is crucial for enhancing the electrocatalytic performance of the sensor. Based on the distinctive properties of α-MnO_2, it is important to consider finding a way to optimize and tune the experimental conditions to ensure α-MnO_2 nanorod arrays morphology on the substrate surface.

1.4.2 Key criteria for effective glucose electrochemical sensors

A glucose electrochemical sensor must meet several essential criteria to ensure reliable, accurate, and efficient performance, Figure 1.17. It should demonstrate high sensitivity and selectivity, enabling precise detection of glucose even at low concentrations, without interference from other substances in biological fluids. The sensor should have a rapid response time, allowing for near real-time monitoring of glucose fluctuations, and a wide linear range to accurately detect both low and high glucose levels. Long-term stability and reproducibility are key to ensuring consistent measurements over time, while biocompatibility is critical if the sensor is in direct contact with the body. Additionally, ease of calibration, and integration with other devices (such as insulin pumps or mobile apps) are necessary for practical use in both clinical and everyday settings. Finally, the sensor should be cost-effective, user-friendly, and adaptable to different physiological conditions, making it suitable for continuous glucose monitoring or other medical applications.

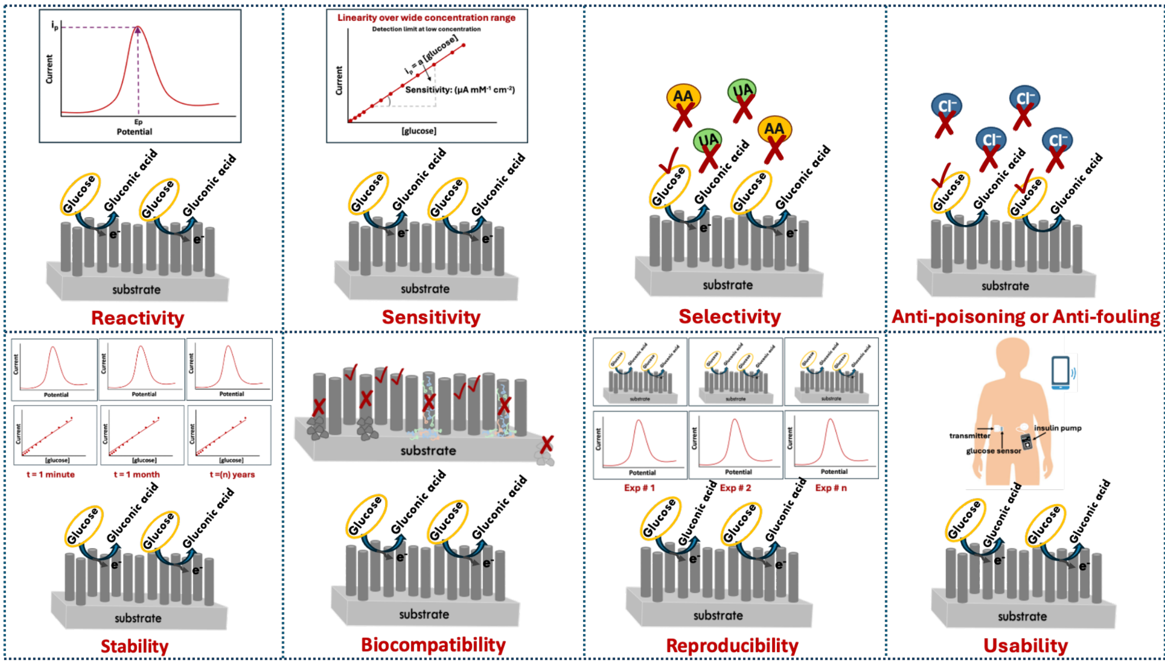

Figure 1.17: Schematic representation of the key criteria of electrode materials required for effective glucose sensors

1.4.3 Thesis objectives

The primary objective of this project is to design and develop electrochemical non-enzymatic glucose sensor based on MnO_2 nanostructures. More specifically, the project seeks:

- **To Synthesize and Characterize MnO_2 Nanorods on Carbon Paper Substrates**
    - Synthesize MnO_2 nanorods and deposit them onto carbon paper substrates, optimizing the structure to maximize surface area and catalytic activity for glucose oxidation.
- **To Integrate Carbon Nanotubes (CNTs) for Enhanced Conductivity and Stability**
    - Integrate carbon nanotubes (CNTs) onto the MnO_2 nanorod-carbon paper substrate to enhance the electrical conductivity, stability, and electrochemical performance of the glucose sensor.
- **To Optimize the Nanostructure and Electrochemical Parameters for High Sensitivity and Selectivity**

- Optimize the MnO_2 nanorod structure and CNT integration to enhance the sensor's sensitivity, selectivity, and detection limit for glucose, with a focus on electrochemical parameters potential, potential window, and applied currents.

- **To Investigate Voltammetry and Chronoamperometry for Improved Selectivity**
    - Explore voltammetry and chronoamperometry as electrochemical techniques to enhance the sensor's selectivity for glucose, minimizing interference from other common electroactive species such as ascorbic acid, uric acid and KCl in biological samples.
- **To Evaluate the Stability and Reproducibility of the MnO_2/CNT-Based Sensor**
    - Assess the long-term stability, reproducibility, and performance consistency of the MnO_2 nanorod and CNT-based electrochemical sensor in varying conditions, ensuring reliable glucose detection for potential clinical or personal use.

1.5 Organization of the thesis

This thesis consists of seven main chapters and is organized as follows:

Chapter 1: Provides an overview of diabetes, highlighting its prevalence, impact and the critical need for efficient glucose monitoring in managing the diabetes condition. It also introduces electrochemical glucose sensors as well as a detailed literature review on the electrochemical glucose sensor's development of EGS, CGM, NEGS and NEGS utilizing MnO_2 as a key component. The chapter concludes with the problematic statement and thesis objectives.

Chapter 2: Outlines the methodology employed in the thesis, including the material synthesis (CNTs and MnO_2), methods and procedures (electrochemical cell setup, CVD and HT). The chapter also introduces the range of physicochemical and electrochemical characterization methods utilized to analyze the materials. These includes SEM, EDS, XRD, Raman, CV and CA. Additionally, the chapter discusses the electrochemical parameters investigated, such as specific capacitance and ECSA and provides detailed procedures for conducting the electrochemical analyses to evaluate the performance and efficiency of the sensors.

Chapters 3-6: Aim to present the detailed physicochemical characterizations and electrochemical measurements, followed by an in-depth discussion of the results in relation to the objectives outlined in the thesis. The structure is as follows:

- **Chapter 3:** Physicochemical characterizations
- **Chapter 4:** Capacitive studies and electrochemical surface area measurements

- **Chapter 5:** Cyclic voltammetry studies for glucose detection on electrodes based on gold, carbon paper and manganese dioxide, and the effect of interfering species
- **Chapter 6:** Chronoamperometry studies to measure glucose sensitivity, selectivity and durability

Chapters 7: Summarizes the findings of my research and provides challenges and perspectives.

2. EXPERIMENTAL

2.1 Material synthesis

2.1.1 Synthesis of CNTs by chemical vapour deposition (CVD) method

Carbon nanotubes (CNTs) were directly synthesized on CP substrates using a chemical vapor deposition (CVD) method, following refined protocols developed in our lab[112-114]. Particularly, CNTs were directly grown on a conductive CP substrate at an elevated temperature of 700 °C, employing nickel as catalyst. The synthesis of CNTs on CP substrate involved two processes:

2.1.1.1 Synthesis of Ni film on CP via sputtering deposition:

This process implicated the deposition thin film of Ni (from a Nickle target (Kurt J. Lesker Company, 99.99% pure. 57 mm Diameter x 0.1 mm Thick) as a source) on one side of CP substrate (Toray carbon paper, TGP-H-60) through sputtering method. To initiate the process, it was crucial to thoroughly clean the chamber with isopropanol in order to eliminate any impurities or contaminants. This step ensures a pristine environment before carefully positioning the target nickel and CP substrate. Once properly aligned, both components were securely placed inside the sputtering chamber. The sputtering process was carried out under vacuum with a controlled flow of argon gas (Ar), following specific sputtering parameters. These included a current of 20 mA, a nickel target density of 8.92 g/cm^3 and a target film thickness of 5 nm, ensuring optimal deposition conditions for the desired outcome. Subsequently, a plasma was generated as the argon gas was ionized, while the ions being attracted to the negatively charged nickel target. This interaction resulted in the removal, or sputtering, of a small amount of the nickel target, which was then deposited onto the CP substrate, forming a thin film layer[115]. Once the desired film thickness was achieved, the sputtering process was automatically terminated. The nickel-coated CP substrate was then ready for use as a catalyst for the growth of CNTs.

2.1.1.2 Synthesis of CNTs on CP via chemical vapour deposition:

The growth of CNTs on CP was carried out by introducing acetylene (C_2H_2) as the precursor carbon-containing gas. The setup of the CVD synthesis is illustrated in Figure 2.1(a). The process started by positioning the Ni-coated CP substrate at the center of a tubular furnace. Argon gas was then introduced at a flow rate of 100 cm^3 min^{-1} (standard cubic centimeters per minute, sccm) for a duration of 5 minutes. The flow of Ar gas, acting as a carrier, was necessary for flushing out any oxygen in the tube, ensuring an oxygen-free environment. Following this, a mixture of Ar and H_2 gases were introduced into the tube, with flow rates of 70 sccm and 30 sccm, respectively, for 5 minutes. The furnace was then programmed to heat to 700 °C and maintained at this temperature for 30 minutes, with H_2 gas flowing at 70 sccm. This step was essential for the reduction of the nickel film into nanoparticles, which are crucial for catalyzing the growth of CNTs.

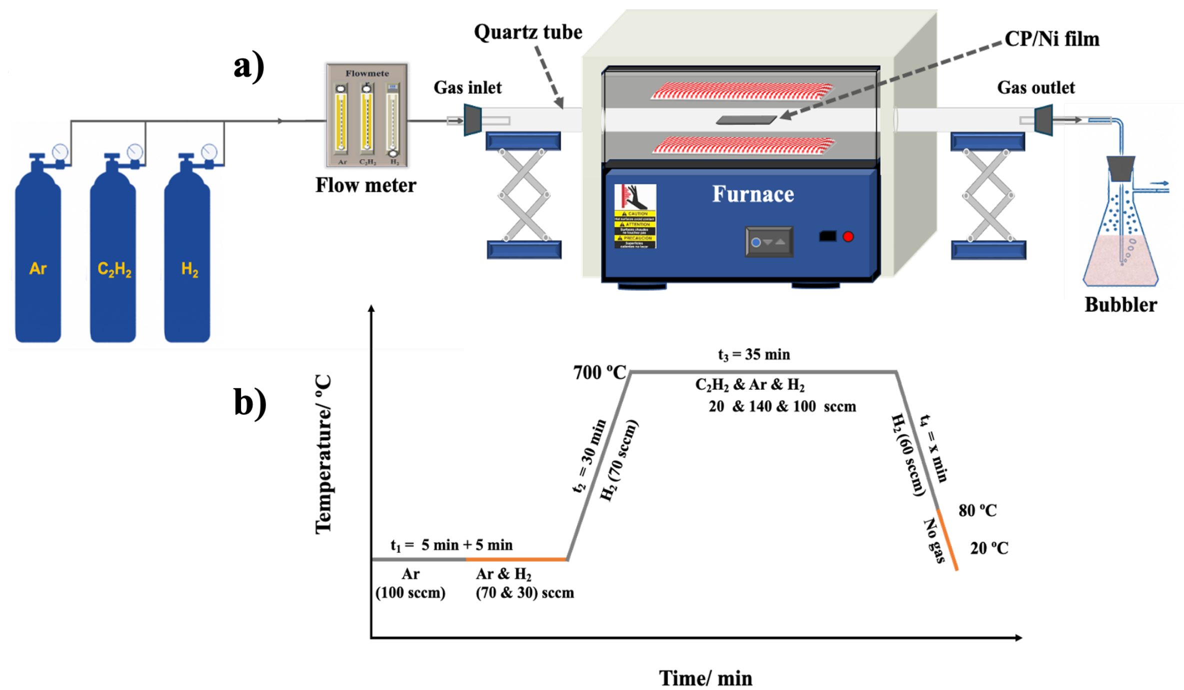

Figure 2.1: a) A scheme illustration of CVD for the CNTs synthesis. b) Temperature vs. time graph during CVD process

Once the furnace temperature reached 700 °C, C_2H_2, Ar and H_2 gases were introduced simultaneously, with flow rates set at 20, 140 and 100 sccm, respectively. This gas mixture was maintained for a growth period of 35 minutes, which was sufficient for the formation and growth of CNTs on the CP substrate. After the growth period concluded, the flow of both C_2H_2 and Ar gases was stopped, and only H_2 gas continued to flow at a rate of 60 sccm. This was maintained until the furnace temperature decreased to 80 °C. Once this temperature was reached, the H_2 gas flow was also halted, and the furnace was allowed to cool naturally to ambient temperature, as shown in Figure 2.1(b). The synthesis mechanism of CNTs via the CVD method involves the decomposition of the precursor carbon source C_xH_y (e.g., C_2H_2), at high temperature (700 °C) in the presence of the metal catalyst, such as Ni nanoparticles on the CP substrate. This decomposition produces carbon species[116], which then assemble and migrate towards the heated substrate. simultaneously, the hydrogen gas, which play a crucial role in facilitating the reaction, is carried away with the gas flow, promoting the growth of CNTs on the substrate. The decomposed carbon species were then diffused through the surface of the catalyst, where they contributed to the growth of the CNTs. The CNTs continued to grow as long as the carbon atoms were able to diffuse into the catalyst. Depending on the interaction between the catalyst and the substrate, two distinct growth models could occur: (i) the tip-growth model, and (ii) the root-growth model, as illustrated in Figures 2.2(a) and 2.2(b), respectively.

Figure removed due to copyrights issues

Figure 2.2: (a) Tip-growth and (b) root-growth models for fabricating CNTs[117-119]

In the tip-growth model, carbon species diffuse into the catalyst surface and are precipitated between the catalyst and the substrate, driven by the weak interaction between the catalyst and substrate. This results in the catalyst being pushed upward as the CNT grow. Growth continues as long as carbon atoms can diffuse into the catalyst, and once the catalyst reaches a saturation point, the growth stops. In contrast, in the root-growth model, where the catalyst exhibits a strong interaction with the substrate, the diffused carbon atoms accumulate on top of the catalyst. The CNTs continue to grow vertically from the catalyst until it is completely covered, at which point growth saturation[117-119].

2.1.2 Synthesis of MnO_2 nanostructures by hydrothermal method

To facilitate the direct synthesis of MnO_2 catalysts on substrates such as carbon paper (CP) or carbon nanotubes (CNTs), we employed the hydrothermal method, utilizing potassium permanganate ($KMnO_4$) as the precursor. The hydrothermal method is a straightforward treatment process in which an aqueous mixture of precursors is exposed to elevated temperatures and high pressure within a sealed stainless steel autoclave reactor[70]. This process facilitates the formation of highly crystalline nanostructures over a controlled time period, ensuring precise synthesis of the desired materials. The hydrothermal method offers several advantages over other techniques, including its simplicity, low cost, and capability to produce nanomaterials with tailored properties[120]. However, to achieve the desired shape and structure of the crystals, it is crucial to carefully control the reaction condition, as they play significant role in determining the final characteristics of the nanomaterials. This implies that careful tuning and management of various factors involved in the process, such as temperature, pressure, or precursor concentration, are essential. These factors significantly influence the morphology and crystal structure of the synthesized product, making precise control critical for achieving the desired outcomes. To initiate the process, 1.67 mmol (equivalent to 0.266 g) of $KMnO_4$ (Fisher Scientific, 99%) was dissolved in 18.75 mL of ultrapure deionized water (Millipore Milli-Q, resistivity 18.2 MΩ·cm) and stirred for 15 minutes until fully dissolved. Subsequently, 0.42 mL of concentrated HCl (Sigma-Aldrich, 37% w/w) was added, and the mixture was stirred continuously for an additional 2 minutes. Next, a piece of carbon paper (CP) or carbon nanotubes on carbon paper (CP/CNTs) was carefully placed into a 25 mL Teflon-lined stainless-steel autoclave, into which the $KMnO_4$-HCl solution was also carefully added, ensuring the solution completely covered the used substrate. The volume of the solution added is less than the total volume of the autoclave, which is 25 mL. The autoclave was sealed and heated in an oven at 140°C for 12 hours, as shown in Figure 2.3.

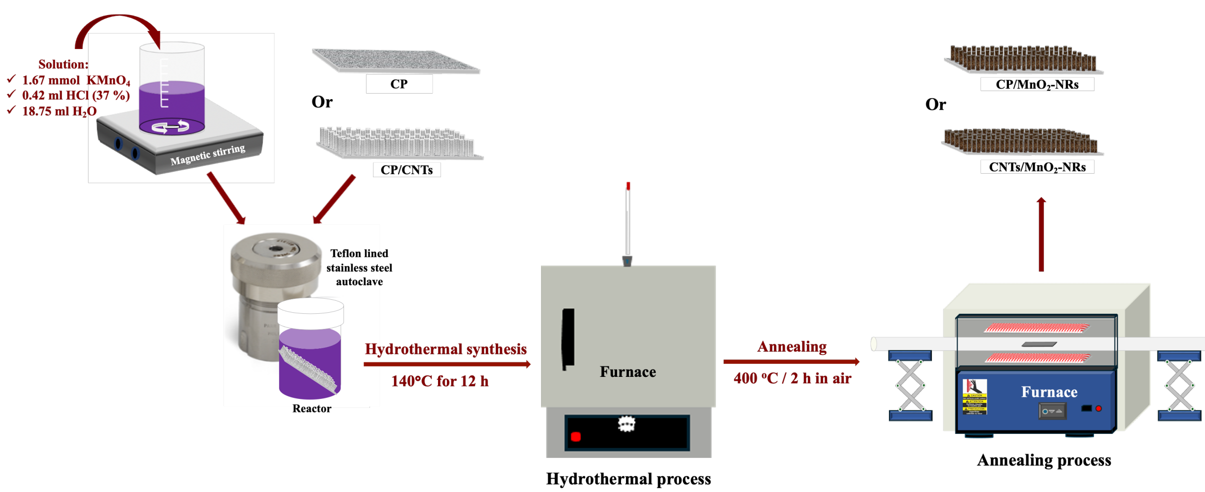

Figure 2.3: Hydrothermal synthesis of MnO_2 nanorods on a carbon-based substrate

Once the synthesis was complete, the reactor was allowed to cool to room temperature. The resulting manganese dioxide samples, either CP/MnO_2 or CP/CNTs/MnO_2, were then thoroughly washed with deionized water to remove any residual impurities. Following this, the samples were annealed in air at 400 °C for 2 hours. Annealing the sample is a heat treatment that involves heating the sample at a specific temperature (e.g., 400 °C), holding at that temperature for a particular time (e.g., 2 hours), then slowly cooling the furnace to room temperature. The purpose of annealing is to enhance the crystallinity of the material and modify its morphology. Specifically, it helps breaking any thin film be present on the sample into nanoparticles and alter the structure to achieve the desired properties.

The growth mechanism of MnO_2 nanostructures through hydrothermal synthesis, as described in the literature, involves a redox reaction between the manganese precursor (e.g., $KMnO_4$) and the reducing agent (e.g., HCl) under elevated temperature and pressure conditions. This reaction promotes the formation of MnO_2 nuclei, which then grow into nanorods or other morphologies. The reaction can be represented by the following equation[121]:

$$2MnO_4^- + 8H^+ + 6Cl^- \Leftrightarrow 2MnO_2 + 3Cl_2 + 4H_2O \tag{2.1}$$

When HCl is the limiting reagent, there is no longer an available supply of Cl^- to reduce the excess of $KMnO_4$ (the excess reagent). In this scenario, the carbon substrate itself serves as "in-situ" reducing agent. This allows the direct growth of MnO_2 on CP-based substrate through the in-situ reduction process, where the carbon substrate acts both as a support and as a reducing agent, as represented in the following equation[108, 122]:

$$4MnO_4^- + 3C + H_2O \rightarrow 4MnO_2 + CO_3^{2-} + 2HCO_3^- \tag{2.2}$$

The generated manganese species nucleated and grew at the surface of the carbon substrate as the reaction progressed, leading to the formation MnO_2 nanostructures, governed by the Ostwald ripening principle[122]. Initially, the reduced MnO_2 species produced from the redox reaction formed small nuclei. Over time, these smaller nuclei dissolved into the solution and redeposited as larger, more stable particles. This process ultimately resulted in the growth of uniform and well-defined nanostructures, such as nanorods as the reaction continued.

Four electrodes were investigated in this project: CP, CP/MnO_2, CP/CNTs, and CNTs/MnO_2. Figure 2.4 summarizes and the steps of fabricating these electrodes, starting from CP substrate, as a reference substrate: (a) The as prepared CP electrode. (b) Synthesis of CP/MnO_2 nanorods electrode. (c) Synthesis of CP/CNTs electrode. (b) synthesis of CNTs/MnO_2 nanorods electrode.

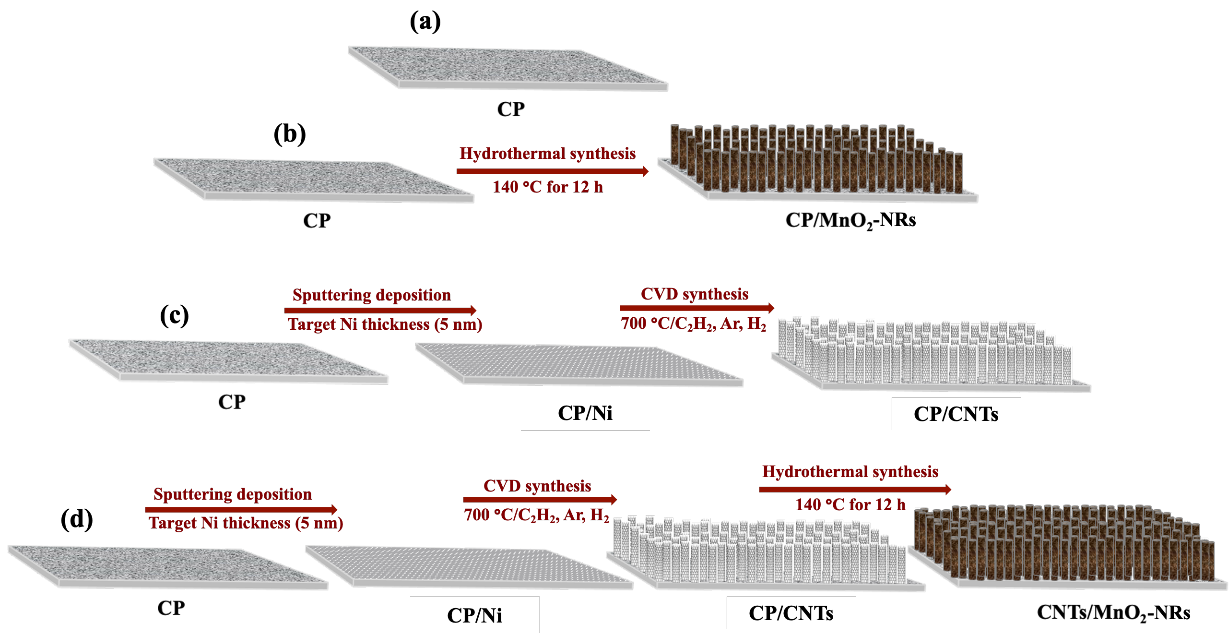

Figure 2.4: Synthesis of carbon-based electrodes for non-enzymatic glucose sensors

2.2 Physicochemical characterizations

To gain a deeper understanding of the physicochemical properties of the electrode materials, such as the synthesized CNTs and MnO_x nanostructures, various characterization techniques were employed. These included scanning electron microscopy (SEM) for detailed imaging of the material's surface morphology, energy dispersive X-ray spectroscopy (EDS) for elemental analysis, X-ray diffraction (XRD) for crystallographic structure analysis, and micro-Raman spectroscopy for the investigation of vibrational modes and structural characteristics of the materials.

2.2.1 Scanning electron microscopy (SEM)

Scanning electron microscopy (SEM) is a powerful technique that provides high resolution images of the surface topography and structural morphology of materials. It involves scanning the surface of a sample with a focused primary electron (PE) beam and detecting the signals emitted by the material, as illustrated in Figure 2.5. These signals include secondary electrons (SE), backscattered electrons (BSE), characteristic X-rays and other emissions like Augur electrons. The images obtained are an interpretation of these signals. SEM images primarily rely on secondary electrons, which result from the inelastic interaction between the incident electron beam and the sample. These secondary electrons are low in energy and have a penetration limited depth of only few nanometers from the sample surface, making them ideal for imaging surface topography[123-125]. The surface characteristics of the synthesized samples were examined using SEM (TESCAN VEGA3, Brno, Czech Republic), operating at 20.0 kV.

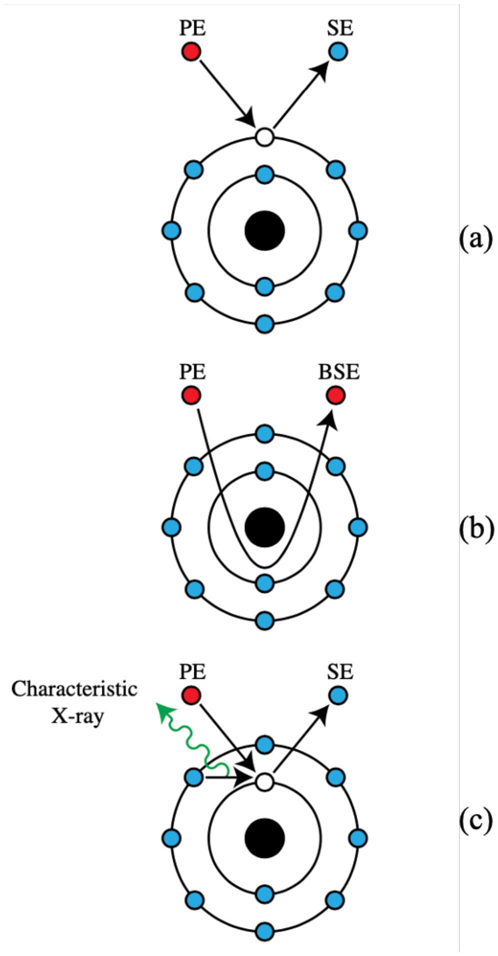

Figure 2.5: Mechanisms of emission of secondary electrons, backscattered electrons, and characteristic X-rays from atoms of the sample[126]

2.2.2 Energy dispersive X-ray spectroscopy (EDS)

Energy dispersive X-ray spectroscopy (EDS) is a valuable analytical technique used to determine the elemental composition of samples. It is commonly employed in conjunction with electron microscopy techniques such as SEM, where the X-rays emitted from the sample are detected and analyzed to provide detailed qualitative and quantitative information about the material. The principle behind EDS, as shown in Figure 2.5(c), is that when the primary electron beam strikes the sample, it causes the ejection of secondary electrons from the inner shells of the atoms. This creates vacancies, which are filled by electrons from higher energy levels. As electrons transition from higher to lower energy states, they emit characteristic X-rays, which are specific to the elements present in the sample. These X-rays are detected and displayed as an EDS spectrum or element mapping, offering valuable insights into the elemental composition of the material[123-125].

2.2.3 X-ray diffraction (XRD)

X-ray diffraction (XRD) is a powerful characterization technique used to gather information about the crystalline structure of a sample. When a monochromatic beam of parallel X-rays passes through the crystal lattice of a sample with a specific incident angle (θ), it is diffracted and scattered by the lattice components, as shown in Figure 2.6a. Scattered X-rays that are in phase and constructively interfere are allowed to pass into the detector, while scattered X-rays that are out of phase and interfere destructively are filtered out. Thus, diffraction occurs according to Bragg's law, as described by Equation (2.3). When the angle of incidence (θ) is equal to the angle of the scattered rays, and the waves constructively interfere, the path difference ($d \sin\theta$) must be an integer multiple of the wavelength (λ), as illustrated in Figure 2.6b[127-128]. This condition is expressed as :

$$2d \sin\theta = n\lambda \qquad (2.3)$$

where n= 0, 1, 2 ,3, ... is the order of diffraction, d represents the interplanar distance between the Bragg planes (crystal planes).

The intensity of detected X-rays is plotted as a function of the beam deflection angle, 2θ, resulting in an XRD pattern, also known as a diffractogram. This pattern is the characteristic for the crystal structure of the sample under investigation. By analyzing the observed peaks in the spectrum and comparing them with a spectra database, it is possible to identify the crystalline structure of the sample and determine properties such as the crystallite size[127-128].

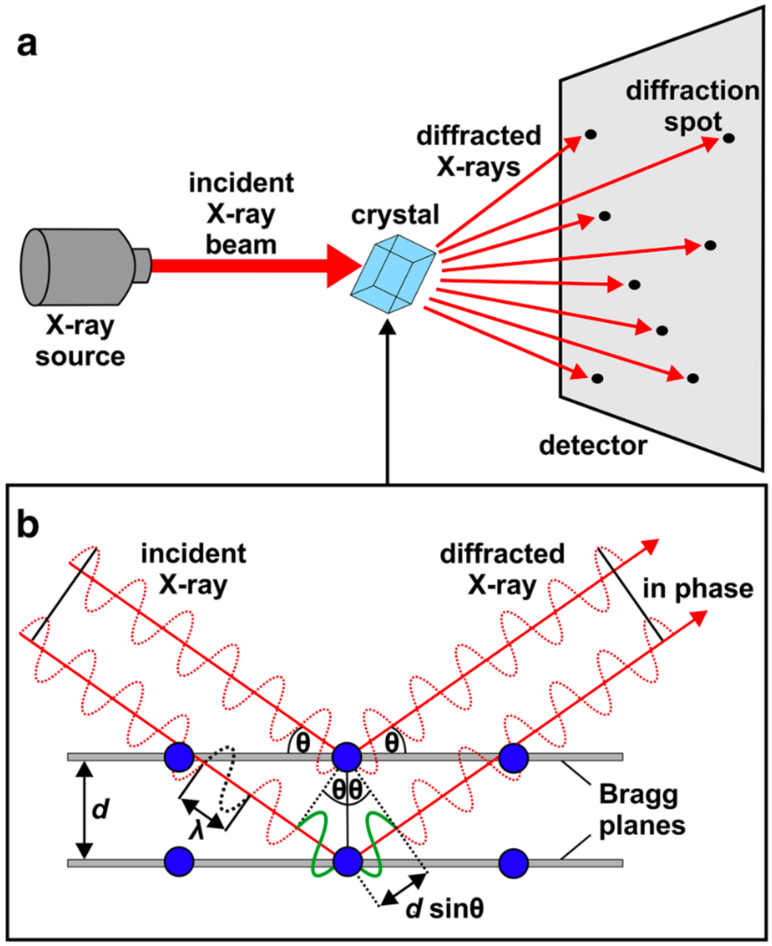

Figure 2.6: X-ray diffraction experiment. (a) Basic scheme of an X-ray diffraction experiment. (b) Diffraction according to Bragg's Law[127]

In this study, crystallinity was assessed using X-ray diffraction (XRD) with a Bruker D8 Advance diffractometer, equipped with a Cu Kα source, and operated at 40 kV and 40 mA. Diffraction patterns were collected with a step size of 0.04° and an acquisition time of 2 second per step.

2.2.4 Micro-Raman spectroscopy

Micro-Raman spectroscopy is a vibrational technique that provides qualitative information about the vibrational modes of bonds in a material, such as its composition, molecular bonding, defects, or molecular structure, through the analysis of the Raman spectrum. Essentially, it offers a molecular fingerprint that helps identify specific molecules. Additionally, it provides quantitative information regarding the concentrations of vibrating molecules in a sample, which can be determined by the intensity values of the spectral lines.

Figure removed due to copyrights issues

Figure 2.7: Schematic diagram of Raman spectroscopy principles: (A) light scattering modes of molecules and (B) energy-level states involved in Raman spectra[129]

The principle of micro-Raman spectroscopy involves exciting a sample with a monochromatic light (e.g., laser) and selectively measuring the spectrum of the inelastically scattered light. Most of the light is scattered elastically, meaning it does not interact with the molecules in the sample and does not provide any molecular information, as there is no change in the frequencies of the incident and scattered light. This is known as Rayleigh scattering[129]. However, a minute portion of the scattered light (about 1 in a 10 million) interacts with the molecules in the sample and undergoes a shift in frequency compared to the incident light. This phenomenon is known as inelastic scattering or Raman scattering, as illustrated in Figure 2.7. Consequently, two types of Raman scattering are observed: Stokes scattering and Anti-Stokes scattering.

Stokes scattering occurs when the scattered photon has a lower frequency than incident photon[130]. In this case, the energy difference between the initial state of the electron and the final vibration state is positive, meaning the electron absorbs energy from the incident photon.

Anti-Stokes scattering occurs when the scattered photon has a higher frequency than the incident photon. Here, the energy difference between the initial state and the final vibration state is negative, meaning the electron releases energy to the scattered photon.[129-132]

In this study, Micro-Raman spectroscopy was employed to assess the structural quality of the samples. Raman spectra in the range of 100 to 2000 cm^{-1} using a Renishaw (inVia Reflex, Mississauga, ON, Canada) instrument, with a 532 nm laser operating at a low power of 0.1 mW (1% of 10 mW). The spot size analyzed was 2 µm, and three spectra were collected for each sample, each with a 50-second acquisition time, to ensure the acquisition of an average spectrum.

2.3 Electrochemical measurements

To investigate the electrochemical performance, an electrochemical analyzer (Eco Chemie PGSTAT302 potentiostat/galvanostat, Metrohm Autolab, Utrecht, The Netherlands) was used in conjunction with a three-electrode electrochemical cell at room temperature. Two electrochemical techniques, cyclic voltammetry (CV) and chronoamperometry (CA) were employed. These techniques were performed utilizing a potentiostat/galvanostat to control the applied potential-either by scanning it in CV or holding it to a constant value in CA- while recording the resulting current response.

2.3.1 Electrochemical cell setup

Electrochemical measurements of cyclic voltammetry were conducted at room temperature using a three-compartment electrochemical cell (Figures 2.8(A) and 2.8(B)), which consisted of a platinum coil as the counter electrode, an Ag/AgCl reference electrode with a 4 M KCl solution, and a rectangular CP-based substrate (0.4 cm x 0.8 cm) as the working electrode. To minimize the effect of ohmic drop, the reference electrode was positioned close to the working electrode and isolated from the electrolyte by a Luggin capillary. A 0.1 M aqueous NaOH solution was used as the electrolyte, which was deoxygenated by bubbling argon gas for 20 to 30 minutes before each electrochemical measurement. Removing oxygen is a crucial step for accurate glucose measurement, as it eliminates interference from oxygen. This provides a clear initial baseline, after which glucose detection can be performed in real physiological fluids, such as blood plasma, where oxygen is present at much lower concentrations. In this study, NaOH was chosen for its ability to enhance the electrochemical performance of non-enzymatic glucose sensors by optimizing the oxidation reaction of glucose at the electrode surface, thus improving sensitivity and reliability. This approach is commonly used in the sensor community, as NaOH provides an alkaline environment that facilitates the electrochemical processes involved. While we acknowledge that NaOH does not replicate physiological conditions (pH ~7.4), future studies will focus on testing the sensor in more physiologically relevant solutions (e.g., phosphate-buffered saline) to better mimic the conditions of the human body, ensuring long-term stability and biocompatibility for potential implantable applications. All potentials in this project were referenced to the Ag/AgCl.

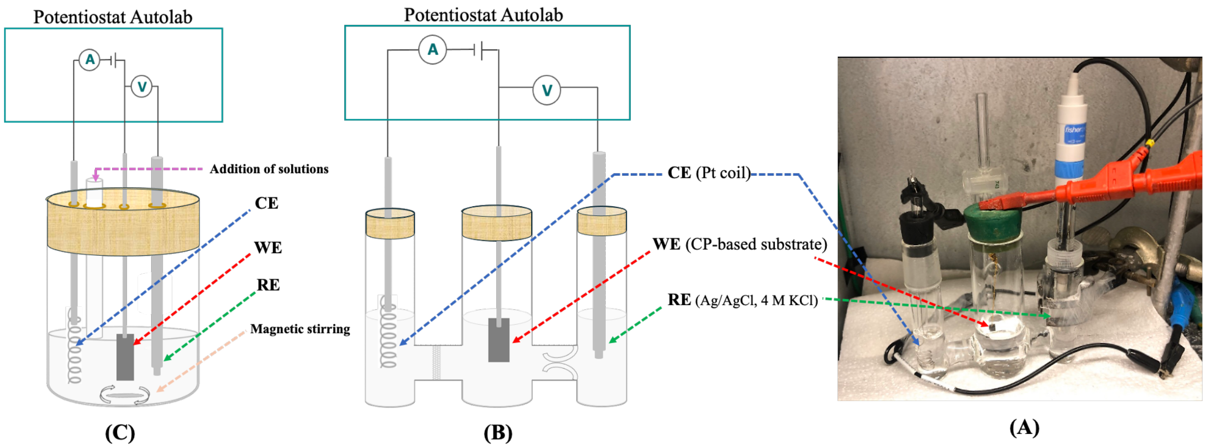

Figure 2.8: Three-electrode electrochemical cell set up. Experimental set up (A). Schematic diagram of the electrochemical cell set up for: Cyclic voltammetry (B) and chronoamperometry (C) experiments

For the chronoamperometry measurements, a one-compartment three-electrode electrochemical cell (e.g., sealed beaker with three electrodes, Figure 2.8(C)) was used under magnetic stirring to ensure homogenous mixing during successive additions of glucose or interferent solutions to the electrolyte.

2.3.2 Cyclic voltammetry (CV)

The most widely used technique to begin electrochemical characterizations of redox species of interest is CV. It involves scanning the potential of a working electrode linearly with time at a constant scan rate (Equation 2.4, excitation signal), as shown in Figure 2.9a, while measuring the corresponding current as a function of potential (Equation 2.5, corresponding voltammogram). During the process, the potential is scanned through a pre-defined range, allowing the analysis of redox behavior of the species in the electrochemical system.

$$E(t)= E_i \pm v\, t \quad (2.4)$$

$$I= f(E) \quad (2.5)$$

where:

E is the potential (V vs Ag/AgCl)
$E(t)$ is the potential at a given time t (V)
E_i is the initial potential (V)
t is the time (s)
v is the scan rate (V/s)
I is the resulting current (A)

Scanning towards more positive potentials generates an anodic current due to the oxidation of electroactive species (Red), which gradually increase until reaching maximum. The scan then reverses direction towards negative potentials. During backward or cathodic scan, the oxidized species (Ox) are reduced, resulting in a cathodic current that gradually increases until reaching a maximum value, then ramps down until reaches the first start potential, completing one full cycle, as illustrated in Figure 2.9b. Multiple cycles can be applied if desired. The resulting profile is called voltammogram, from which several key features can be extracted, including the standard redox potential (E°), anodic peak current (I_{pa}), anodic peak potential (E_{pa}), cathodic peak current (I_{pc}), cathodic peak potential (E_{pc}). These features allow for further quantitative analysis of the system.

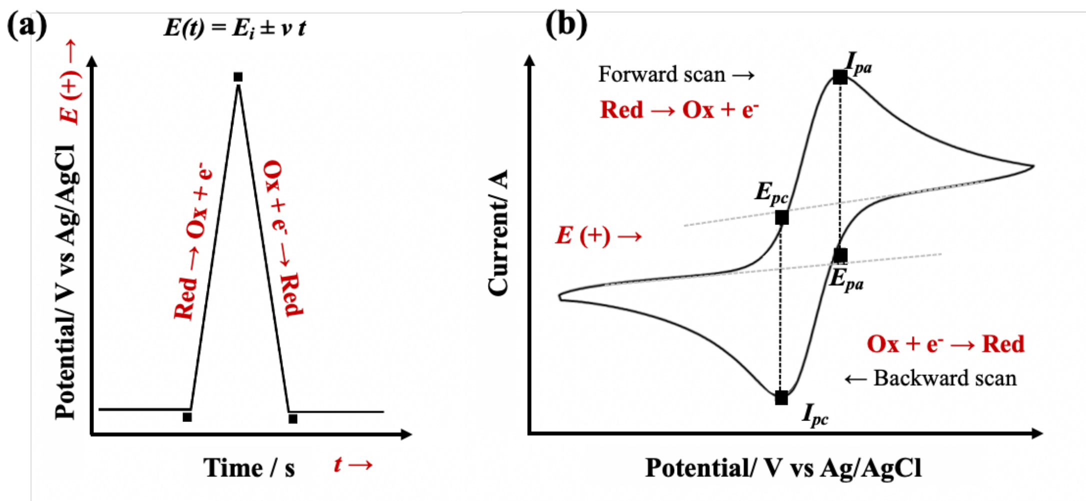

Figure 2.9: (a) Excitation signal (b) Corresponding cyclic voltammogram (CV)

A cyclic voltammogram is deemed as the fingerprint that provides information on the electrochemical processes of the redox reaction such as the mechanisms (e.g., kinetic-controlled, mixed-controlled or diffusion-controlled), the transport mode of the species and the kinetics (e.g., reversible, quasi-reversible or irreversible), anodic limit (e.g., O_2 evolution) and cathodic limit (e.g., H_2 evolution), and more. These insights are crucial for understanding the electrochemical behavior of the system and for evaluating the efficiency and performance of the materials involved.

2.3.3 Chronoamperometry (CA)

Chronoamperometry is an electrochemical technique in which a potential jump is applied to the working electrode, and the resulting faradaic current from the redox reaction at the electrode surface is plotted as a function of time. In this technique, the applied potential is instantaneously stepped from one value (E_1) to another (E_2), known as the excitation signal, Figure 2.10(a). The measured current initially increases with the amplitude of the potential jump until it reaches a maximum value, after which it begins to decrease over time (the corresponding response), Figure 2.10(b). This behavior provides insights into how long the current will persist, which reflects the stability of the catalyst over time.

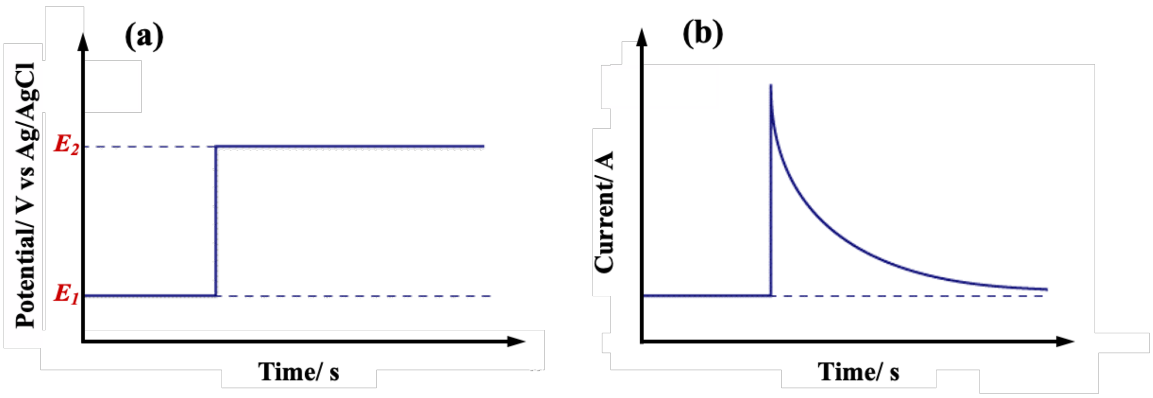

Figure 2.10: (a) Excitation signal (b) Corresponding CA response

In time-current measurements, distortion of the curves occurs at the very beginning (t < 1 ms), which corresponds to the charging of the electrical double layer when the potential is first applied. This initial distortion is due to the capacitive current, which is associated with the accumulation of charge at the electrode surface. Once the potential becomes constant, the capacitive current disappears, and the observed current becomes purely faradaic, reflecting the redox processes occurring at the electrode surface. Chronoamperometry is a valuable tool for assessing the long-term performance and stability of electrochemical systems.

2.3.4 Capacitive studies

Specific capacitance (C_p) is a key parameter in electrochemical systems, particularly in sensors, as it quantifies the ability of an electrode material to store charge per unit mass. It is typically expressed in farads per gram (F/g) and is key factor in determining the accuracy and performance of electrochemical sensors. An electrode with a higher specific capacitance enhances the sensor's sensitivity, signal strength, and response time, ultimately improving its accuracy in detecting the target species. The specific capacitance, based on CV measurements recorded at different scan rates ranging from 2 to 500 mV/s, can be calculated using the following equation:

$$C_p = Q/(2\,m \times v \times \Delta V) \quad (2.6)$$

where:

C_p is the specific capacitance (F/g)
Q is the voltametric charge, which is determined by integrating either the oxidation and the reduction areas of the CV curve (A V)
m is the mass loading of the active material on the working electrode (g)
v is the scan rate (V/s)
ΔV is the potential window of the cyclic voltammogram (V)

The factor of 2 in the denominator accounts for the fact that the capacitance measured from a CV curve reflects both the forward and reverse scans. This effectively doubles the charge contribution. Since the integration of the CV curve includes both charging and discharging phases, and it is assumed that these contribute equally to the total charge, we only consider the discharging part when calculating the specific capacitance. Therefore, the area must be divided by 2 to accurately reflect the specific capacitance.

2.3.5 Electrochemical surface area

The electrochemical or electroactive surface area (*ECSA*) plays a critical role in optimizing and enhancing the performance of electrochemical systems, as it significantly influences the rate of electrochemical reactions. A larger *ECSA* indicates more active sites are available for reactions, thereby improving the overall kinetics and efficiency of catalysts, and facilitating faster charge transfer processes. Among various techniques, CV stands out due to its simplicity, rapid data acquisition, and ability to establish direct relationships between peak currents and the *ECSA*. This technique enables the estimation of the electrochemical double-layer capacitance (C_{dl}) from CV plots of non-redox regions[133], offering valuable insights into the surface characteristics of the electrode material. The C_{dl} can then be calculated using the following relationship:

$$I_c = v \times C_{dl} \tag{2.7}$$

where I_c represents the double-layer charging current, which is the non-redox current extracted from cyclic voltammograms at various scan rates, and v is the scan rate. By plotting I_c as a function of v, a linear correlation is established, where the slope corresponds to C_{dl}, as illustrated in Figure 2.11.

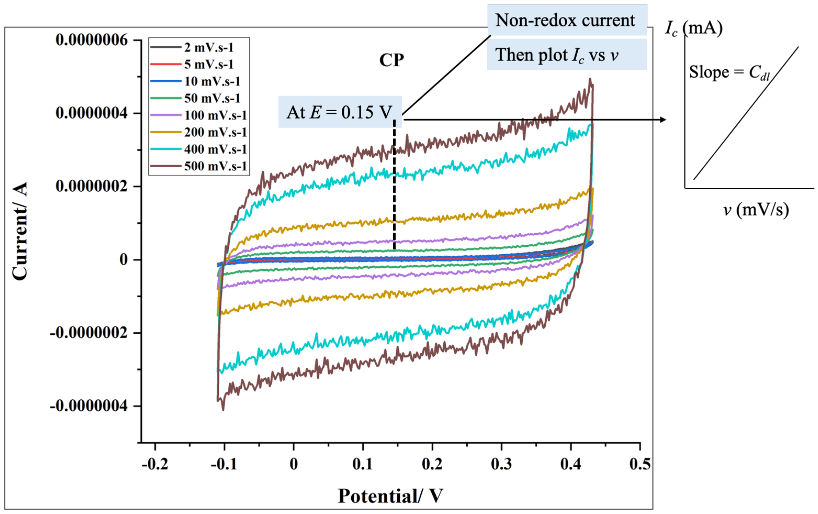

Figure 2.11: (On left) The non-redox currents (I_c) at E= 0.15 V are extracted from cyclic voltammogram of CP electrode, recorded in 0.1 M NaOH at various scan rates (2–500 mV/s) within a potential window (–0.108 V to +0.43 V vs Ag/AgCl). (On right) Plot of I_c vs v for C_{dl} estimation

Once C_{dl} is determined[133], the *ECSA* of a carbon-based electrode can be estimated using following equation:

$$ECSA = C_{dl} / C_s \tag{2.8}$$

where C_s represents the standard specific electrochemical double-layer capacitance of the material, which reflects the capacitance of a smooth, planar surface per unit area under identical electrolyte conditions. While the creation of ideal smooth surfaces for each catalyst would improve the accuracy of C_s measurements and *ECSA* estimations, this approach is often impractical due to the complexities of synthesizing certain catalysts, as well as the inherent material limitations that necessitate the use of rough or porous structures. For reference, a C_s of 40 µF/cm^2 has been reported for metal electrodes in 1 M NaOH solution[134], while for carbon-based materials, C_s is approximately 13 µF/cm^2, with average values ranging from 5 to 20 µF/cm^2 reported[135-136]. The roughness factor (*RF*) is determined by dividing the calculated *ECSA* by the electrode's geometric area (A_g)[133], which in this case is 0.180 cm^2 , corresponding to the geometric area of the part immersed in the electrolyte solution.

$$RF = ECSA / A_g \tag{2.9}$$

2.3.6 Electrochemical detection of glucose, ascorbic acid and uric acid

2.3.6.1 Cyclic voltammetry measurements

The electrochemical properties of the CP-based electrodes towards glucose, ascorbic acid, and uric acid electrooxidation were investigated using the CV technique. Glu, AA and UA (all from Sigma-Aldrich, 99%)

and NaOH (Fisher Scientific, +97%) were used without further purification. Prior to each electrochemical experiment, a 0.1 M NaOH solution was purged with Argon gas for approximately 20 minutes to remove any dissolved oxygen.

Preliminary assessments were conducted to optimize the experimental conditions for the electrochemical measurements. These included:

(i) Determination of the potential window for CV scanning: This step involved scanning the deaerated 0.1 M NaOH solution across broad potential ranges to establish the cathodic limit (–0.3 V vs Ag/AgCl) and the anodic limit (+0.6 V vs Ag/AgCl) of the electrolyte.

(ii) Determination of glucose oxidation peaks: The procedure began by scanning the electrode sample in 0.1 M NaOH solution without glucose to establish the baseline response. Then, the solution was spiked with 1 M glucose concentration to observe glucose-specific oxidation peaks. Once well-defined peaks appeared, a series of glucose concentrations (0.01, 0.2, 0.5, 1, 4, 6, 10, 15, 20, 50 and 100 mM) were tested. The focus of this study was on the oxidation peaks (P1 & P2) in the anodic sweep, corresponding to the oxidation of glucose into gluconolactone and gluconic acid, respectively, as referred to in Figure 2.12.

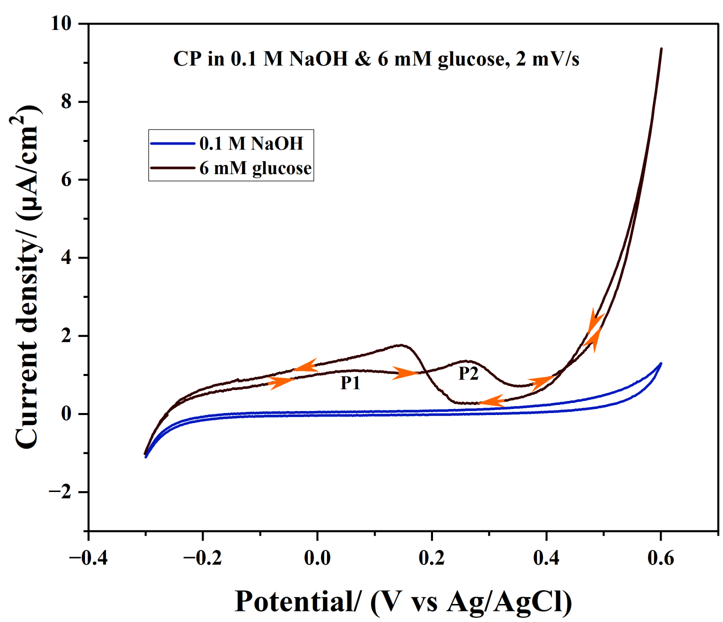

Figure 2.12: CV responses of CP electrode in 0.1 M NaOH at 2 mV/s. Without glucose (blue color). With 6 mM glucose (black color), showing two anodic oxidation peaks of glucose P_1 & P_2. Arrows show the direction of the potential sweep

After performing these preliminary tests, CV measurements were conducted to evaluate the sensitivity of the investigated electrodes towards glucose. Additionally, the potential interference form AA and UA on glucose detection was also assessed. The electrodes studied in these investigations included Au as the benchmark catalyst, CP, CNTs, CP/MnO_2-NRs, CNTs/MnO_2-NRs.

Sensitivity assessments of such electrodes towards glucose: these studies were carried out by immersing the investigated electrodes into a deaerated 0.1 M NaOH solution. Initially, the background response was recorded without glucose present, followed by measurements in the presence of glucose at different concentrations (0.01, 0.2, 0.5, 1, 4, 6, 10, 15, 20, 50 and 100 mM). For each concentration, 3 cycles were recorded at 2 mV/s, starting from the open circuit potential (OCP). The potential was swept within the pre-determined window, anodically up to the first vertex of +0.6 V, followed by a reverse cathodic scan down to the second vertex of –0.3 V. Afterward, the anodic peak current I_{pa} (μA) values were extracted from the resulting voltammograms (potential-current graphs) and expressed as current peak densities (μA cm^{-2}), by dividing the peak current values by the surface area of the electrode exposed to the reaction. The average current peak density from at least three repeated experiments was then plotted against glucose concentration to obtain a linear regression with the standard deviations included. The sensitivity of the sensor (expressed in μA mM^{-1} cm^{-2}) was derived from the slope of this linear regression line, representing the change in current peak density per unit change in glucose concentration. The limit of detection (LOD) (mM) was calculated using the formula:

$$\mathrm{LOD} = 3.3\,(\sigma / s) \tag{2.9}$$

where σ represents the standard deviation of the baseline signal, and s is the slope of the linear regression line. This formula provides an estimate of the lowest concentration of glucose that can be reliably detected by the sensor, where the factor 3.3 accounting for the desired confidence level of detection.

Sensitivity tests for the detection of AA and UA: These tests were performed on electrodes following the same procedure as for glucose detection, where each species was investigated at different concentrations. For CP-based electrodes, only MnO_2-based electrodes were tested for AA and UA detection, as these electrodes demonstrated better glucose sensitivity compared to their MnO_2-free counterparts. The goal was to assess whether any response, such as the appearance of peaks associated with AA and UA, occurred. The interference of AA and UA was further studied in binary solutions of (Glu, AA) and (Glu, UA), as well as in a ternary solution of (Glu, AA, UA) was further investigated using CV, considering the typical concentrations of these species in physiological media, and examining how increasing the concentration of one component affected the detection of the others.

2.3.6.2 Chronoamperometry measurements

In CA, the methodology for constructing a calibration curve involved applying a potential step to the working electrode while measuring the resulting current response over time. The excitation signal to the working electrode consisted of a potential jump from an initial potential value, E_1 (e.g., OCP, where no reaction and no faradic current flow occur), to pre-determined potential, E_2 (e.g., 0.18 V vs Ag/AgCl; at which the analyte undergoes oxidation), for a duration of 3600 s. After applying the potential, the current was monitored as it evolved until reaching a steady-state value. This steady-state current (I_{ss}) (μA), which reflects the maximum electron transfer rate at the electrode, was then expressed as the steady-state current density (μA cm^{-2}) and plotted against the corresponding analyte concentrations. The linear response of the calibration curve, along with the standard deviation markers obtained from the average steady-state current density (of three repeated experiments) versus glucose concentration plot, allowed for the determination of the sensor's sensitivity (μA mM^{-1} cm^{-2}), linear concentration range (mM), response time (s), and limit of detection (mM). The electrodes investigated via CA were CP/MnO_2-NRs and CNTs/MnO_2-NRs, due to their higher sensitivity observed in CV compared to other samples. CA measurements were performed on these two electrodes because of their high precision, which is attributed to the absence of capacitive current effects during measurements.

To evaluate the sensitivity of the synthesized MnO_2 electrodes towards glucose using CA, a concentrated glucose stock solution was first prepared. Successive and calculated additions of the stock solution were added using a micropipette to a 0.1 M NaOH solution under continuous stirring, allowing for increasing glucose concentrations (0.5, 1, 4, 6, 8, 10, 15, and 20 mM) to be achieved. The oxidation currents resulting from each addition were measured, and each addition was allowed to reach a steady-state current before the next one was added. The I_{ss} was then extracted from the time-current graph and plotted against glucose concentration to construct the calibration curve.

For the CA detection of interfering species in the presence of glucose, we investigated both low and high concentrations of AA (0.02 mM & 0.08 mM) and UA (0.18 mM and 0.42 mM) that can occur in physiological conditions. Successive addition of low concentrations of AA (0.02 mM) and UA (0.18 mM), as well as higher concentrations of AA (0.08 mM) and UA (0.42 mM), were made to a solution containing 7 mM glucose. The procedure began with preparing a 7 mM glucose in 0.1M NaOH solution and stock solutions of AA and UA. The glucose solution was purged with Ar for about 20 minutes, then CV measurements of the synthesized electrode in the 7 mM glucose solution were recorded, to confirm that glucose oxidation occurred at 0.18 V. Following this, CA measurements were performed by applying a fixed potential of 0.18 V to the working electrode. Once the oxidation current of glucose reached a steady state, a specific amount of AA stock solution was added to reach a 0.02 mM of AA. When I_{ss} for AA was reached, UA stock solution was added to reach a 0.18 mM of UA. The process was completed once the oxidation current of UA stabilized. This procedure was repeated with the solution containing higher concentrations of the interferents (7 mM Glu, 0.08 AA and 0.42 mM UA).

2.3.7 Anti-fouling CA test against KCl

CA was carried out to assess the anti-fouling capability of the CNTs/MnO_2-NRs, which demonstrated the highest CV and CA sensitivity among the electrodes investigated. The process began by measuring I_{ss} of the CNTs/MnO_2-NRs electrode in deaerated 0.1 M NaOH solution containing 4 mM glucose. Then, successive additions of KCl stock solution were made to reach KCl concentrations of 1, 3 and 5 mM. For each addition, the current was allowed to stabilize before proceeding the next concentration, and continuous magnetic stirring was employed to ensure homogeneous mixing throughout the solution. Finally, a 7 mM glucose solution was introduced to the cell to assess the sensor's response to glucose in the presence of the fouling species of KCl.

2.3.8 Electrochemical durability test

The electrochemical durability tests were performed on the MnO_2-based electrodes exhibiting the best electrochemical performance, namely CNTs/MnO_2-NRs and CP/MnO_2-NRs, using both CV and CA techniques. A medium-term stability test was first conducted by performing CV in the presence of 7 mM glucose, using a scan rate of 20 mV/s over 1000 cycles (equivalent to 25 hours). The procedure began by scanning the investigated electrode in deaerated 0.1 M NaOH solution over the entire potential widow (from –0.3 V to +0.6 V) at 2 mV/s for 2 cycles to establish the baseline response of the electrode. Next, a calculated amount of glucose stock solution was added to the solution to achieve a final glucose concentration of 7 mM, and the solution was stirred for 2–3 minutes to ensure homogenous mixing. After stopping the stirring, CV corresponding to 7 mM glucose concentration was recorded after 2 cycles at 20 mV/s. Then, CV parameters were adjusted to perform multi-cycle testing, spanning 1000 cycles with data saved every 100 cycle, at scan rate of 20 mV/s. The potential sweep began from the OCP, was anodically scanned to the first vertex (+0.6 V), and then reversed to the second vertex of (–0.3 V). The process took approximately 25 hours to complete, resulting in ten plots, each plot representing 100 cycles. Subsequently, a long-term stability test was carried out using CA for 7 days continuous stirring in the presence of 7 mM Glu. The procedure commenced with recording the CV background response of the investigated electrode in deaerated 0.1 M NaOH for 2 cycles at 2 mV/s and within the potential window of –0.3 to +0.6 V. A specific volume of glucose stock solution was then added to achieve a final glucose concentration of 7 mM, and the solution was stirred for 2–3 minutes. Following the cessation of stirring, CV measurements were performed again at 2 mV/s for 2 cycles, to confirm the glucose oxidation region (between –0.3 V and +0.6 V) and verify that the applied potential for the CA (e.g., 0.18 V) was within this range. For the long-term CA test, the parameters were set for a duration of one week (t= 604800 s) with interval time of 70 s, and applied potential of 0.18 V. The current-time profiles obtained from both the CNTs/MnO_2-NRs and CP/MnO_2-NRs electrodes were compared to assess which electrode exhibited better durability and stability over the test period.

3. PHYSICOCHEMICAL CHARACTERIZATIONS

3.1 Scanning electron microscopy (SEM)

The surface morphology of the bare carbon paper (CP) substrate and the as prepared CP/CNTs is illustrated in Figure 3.1(a1–a3) and (b1–b3), respectively, using the SEM technique. The CP images (a1–a3) reveal a network of carbon fibers with an average diameter ranging from 6 to 8 µm. In contrast, the SEM images of CP/CNTs, (b1–b3), captured at progressively increasing magnifications, showcase a fluff-like morphology that uniformly covers the entire CP fibers. This indicates that the CP substrate is effectively and densely coated with a continuous layer of CNTs, highlighting the successful deposition of CNTs on the CP surface.

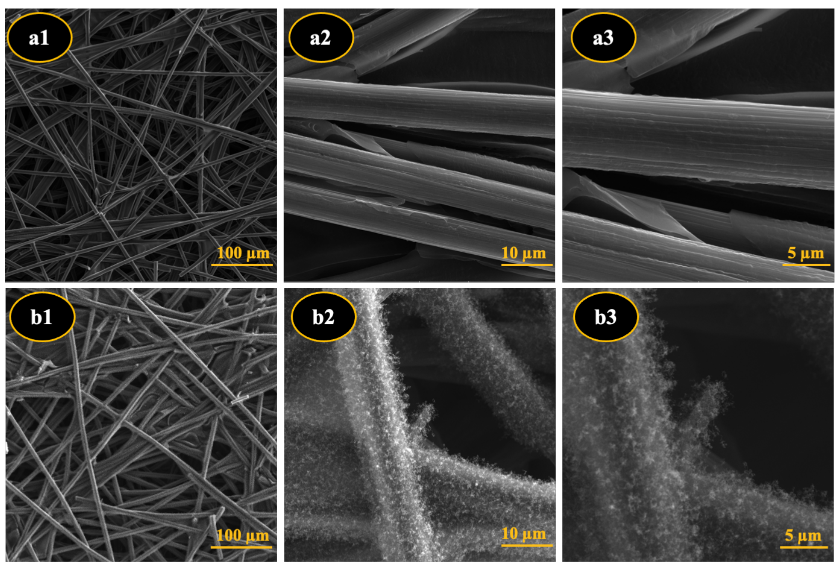

Figure 3.1: SEM images of (a1–a3) bare CP substrate and (b1–b3) CP/CNTs at increasing magnifications (100, 10 and 5 µm)

Additionally, SEM images were obtained at progressively higher magnifications for substrates with MnO_2 catalyst deposited on CP and on CNTs, as shown in Fig. 3.2(a1–a4) and (b1–b4), respectively. The CP/MnO_2 images, (a1–a4), clearly demonstrate that the CP substrate is coated with a dense array of MnO_2 nanorods (NRs), with an average diameter of approximately 200 nm. Similarly, the CNTs/MnO_2 Images, (b1–b4), reveal a high density of MnO_2 nanorods (NRs) uniformly covering the surface of the carbon fibers and CNTs, further confirming the successful deposition of the MnO_2 catalyst onto the substrates.

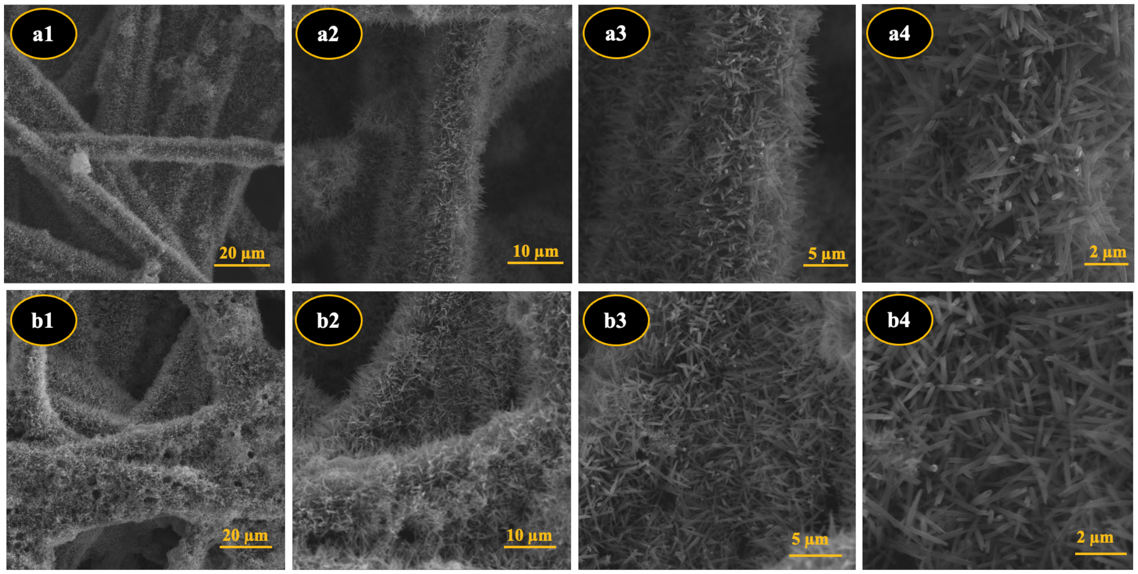

Figure 3.2: SEM images of (a1–a4) CP/MnO_2-NRs substrate and (b1–b4) CNTs/MnO_2-NRs substrate at increasing magnifications (20, 10, 5 and 2 µm)

3.2 Energy dispersive X-ray spectroscopy (EDS)

The EDS technique was employed to determine the elemental composition for the synthesized electrodes namely CP/CNTs, CP/MnO_2-NRs and CNTs/MnO_2-NRs as shown in Figure 3.3(a), (b) and (c), respectively. The analysis of the CP/CNTs substrate via EDS, Figure 3.3(a), reveals the dominance of carbon (99.07%) on the surface.

For the CP/MnO_2-NRs substrate, EDS mapping demonstrates a uniform distribution of MnO_2 across the CP substrate. Both the elemental mapping and the EDS spectrum, shown in Figure 3.3(b), reveal consistent presence of C, O, Mn, and K elements on the CP surface, with corresponding atomic percentage of 48.87%, 40.57%, 9.43% and 1.13%, respectively, as summarized in Table 3.1.

The EDS analysis of the CNTs/MnO_2-NRs substrate also confirms the uniform distribution of the MnO_2 layer, with the presence of C (48.78%), O (41.37%), Mn (8.52%), and K (1.33%) elements on its surface, as shown in Figure 3.3(c). It is evident that the EDS spectra for both CP/MnO_2-NRs and CNTs/MnO_2-NRs substrates are similar, with relatively close atomic concentrations. However, the carbon content in the CNTs/MnO_2-NRs (c) is lower than that in the CP/MnO_2-NRs substrate (b), which can be attributed to the higher MnO_2 catalyst coating on the CNTs/MnO_2-NRs substrate.

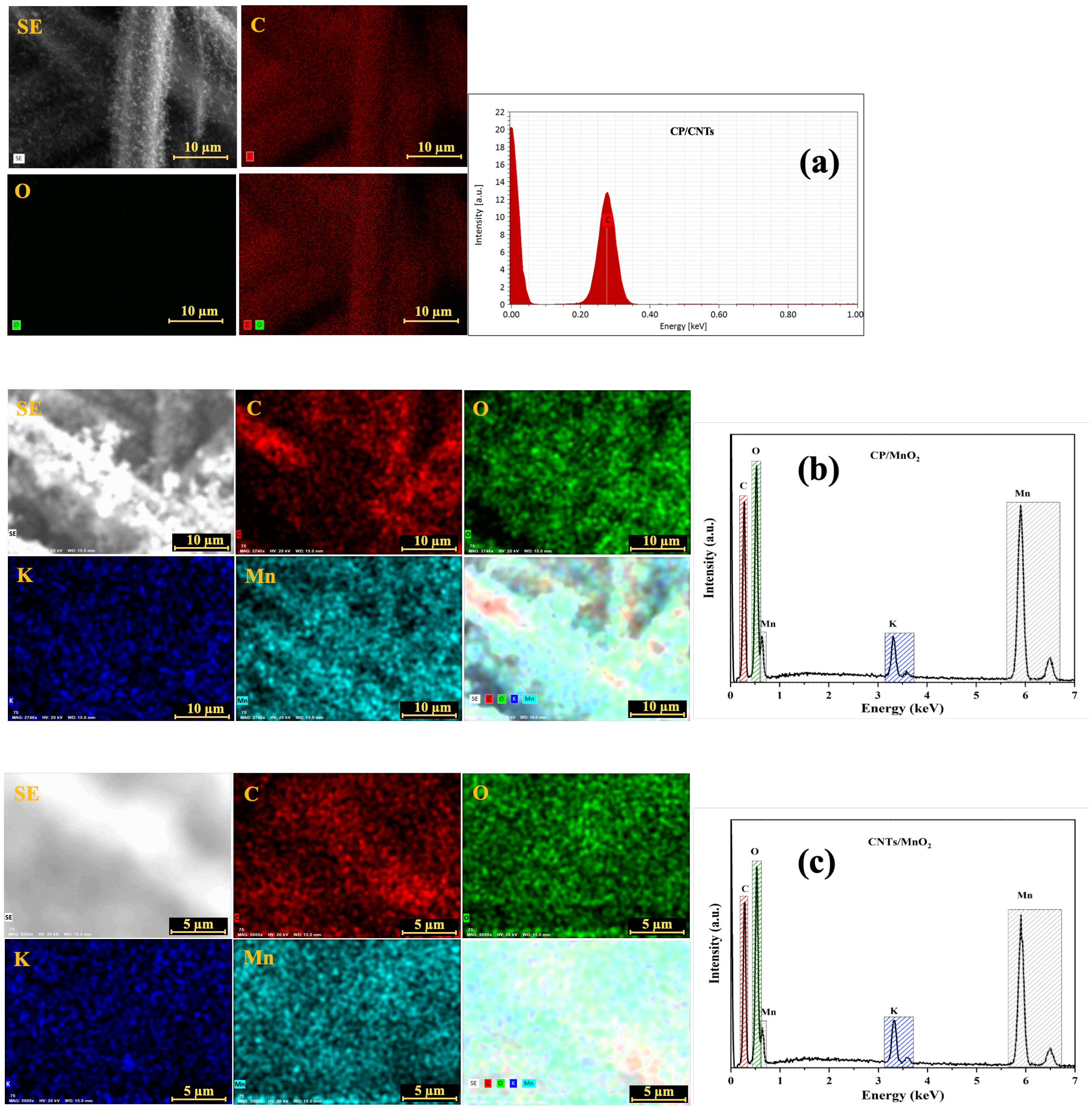

Figure 3.3: EDS analysis of the synthesized electrodes: (a) CP/CNTs. (b) CP/MnO_2-NRs. (c) CNTs/MnO_2-NRs. The EDS analysis of each substrate comprises of the elemental mapping (images of the elements in different colors) and the EDS spectrum (energy vs intensity graph)

Table 3.1: Atomic concentrations of EDS analysis

Substrate	K%	Mn%	C%	O%
CP/CNTs			99.07	0.93
CP/MnO_2-NRs	1.13	9.43	48.87	40.57
CNTs/MnO_2-NRs	1.33	8.52	48.78	41.37

3.3 X-ray diffraction (XRD)

XRD analysis was performed to investigate the crystal structures of both the MnO_2-free substrates and the MnO_2-based substrates. Figure 3.4(a) presents the XRD patterns of the CP and CP/CNTs substrates. The CP substrate displays a well-defined peak at 26.4^o (*2θ*) along with four smaller peaks at 42.7^o, 44.4^o, 54.5^o and 77.6^o, which correspond to the (002), (100), (101), (004), and (110) planes of the graphite carbon structure, respectively (JCPDS #41-1487). Similarly, the CNTs substrate exhibits the same prominent peak at 26.4^o (*2θ*), accompanied by three smaller peaks at 42.7^o, 54.5^o and 77.6^o, which correspond to the (002), (100), (004), and (110) planes of the graphite carbon structure, respectively (JCPDS #41-1487).

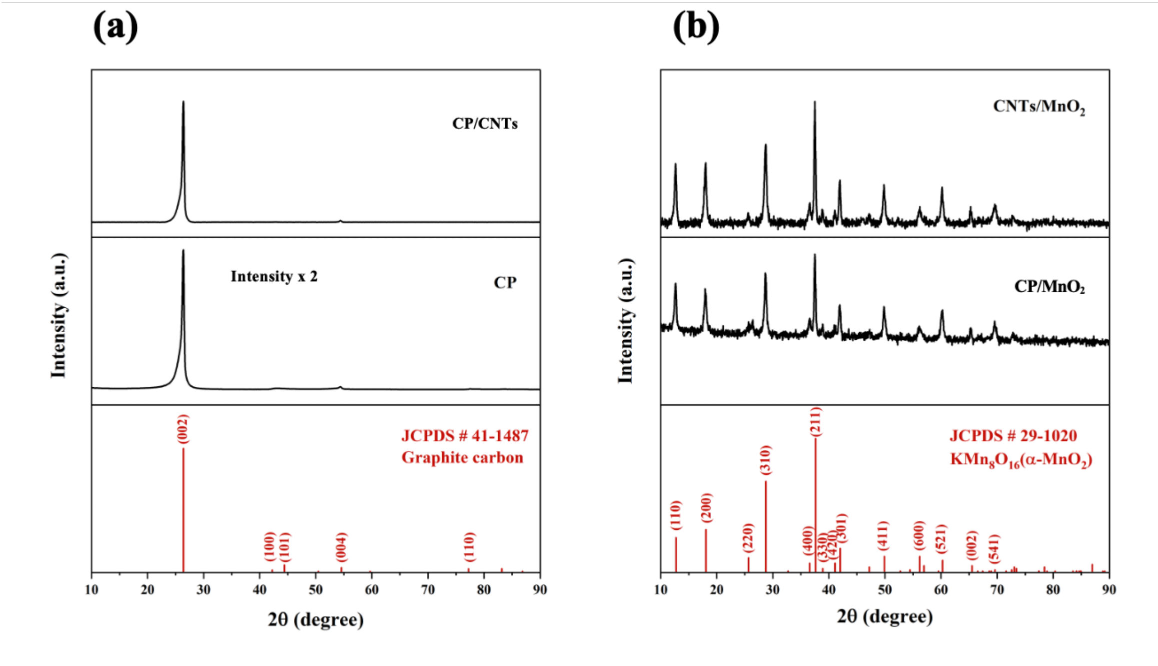

Figure 3.4: XRD patterns of (a) CP and CP/CNTs substrates (b) CP/MnO_2-NRs and CNTs/MnO_2-NRs substrates

On the other hand, Figure 3.4(b) shows the XRD profiles of CP/MnO_2-NRs and CNTs/MnO_2-NRs substrates. The XRD patterns of the MnO_2-based substrates display peaks that are well-matched with the planes of cryptomelane KMn_8O_{16} (JCPDS #29-1020). This compound corresponds to the typical tetragonal α-MnO_2 phase within the manganese oxide family, which is characterized by the presence of K^+ ions in the the 2×2 tunnels of the crystal structure[137]. This structural arrangement not only stabilizes the crystalline structure of the α phase but also helps maintains charge balance within the material[138]. The distinct peaks observed confirm the successful deposition of MnO_2 in the desired crystalline form on both CP and CNTs substrates.

3.4 Micro-Raman spectroscopy

Raman was used to investigate the vibrational modes and structural characteristics of carbon-based substrates and MnO_2-baesd substrates, with the Raman spectra presented in Figure 3.5(a & b) and (c & d) respectively. The Raman spectrum of the CP substrate (Figure 3.5(a)) reveals two distinct bands at approximately 1350 and 1580 cm^{-1}. These bands are identified as the D band, which corresponds to A_{1g} symmetry associated with edge or defect sites of carbon[139], and the G band, which is linked with E_{2g} symmetry for sp^2 carbon[140-141]. The I_G/I_D ratio of pristine CP is determined to be 10.96 based on the deconvolution area. This high ratio indicates a low level of disorder or defects in the CP and suggests a larger average size of sp^2 carbon domains.

Similarly, the Raman spectrum of the CP/CNTs substrate (Figure 3.5(b)) also exhibits two prominent bands: the D band at approximately 1343.7 cm^{-1} and G band at 1590.6 cm^{-1}. The broader D band in the CNTs spectrum and the small ratio I_G/I_D of CP/CNTs (0.90) indicate the presence of more defects in the carbon structure compared to the CP substrate, suggesting that the CNTs have a higher degree of disorder. This is consistent with the structural characteristics of CNTs, where defects play a key role in the vibrational features observed in the Raman spectrum.

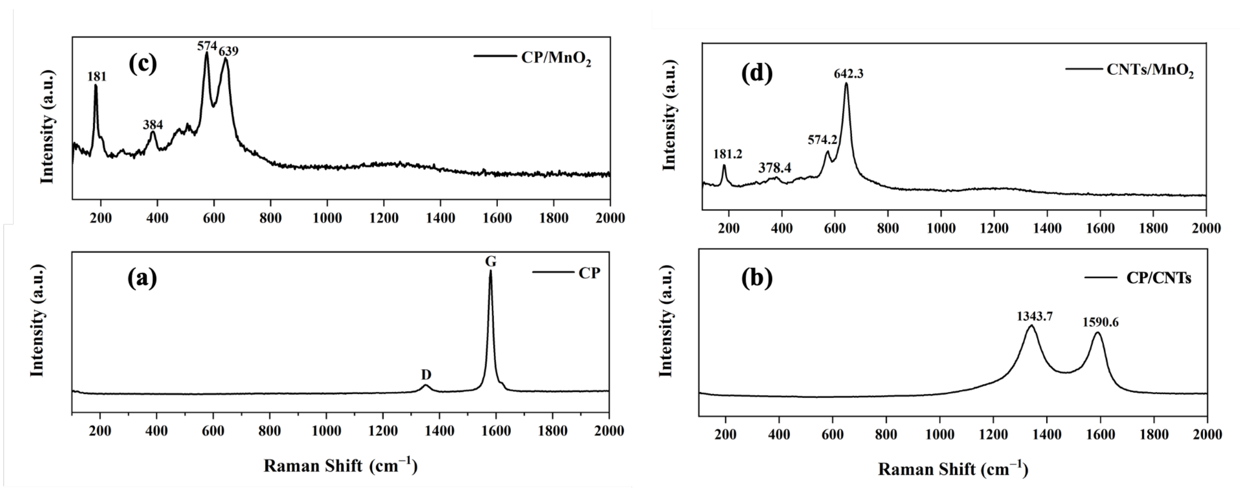

Figure 3.5: Raman spectra of (a) CP (b) CP/CNTs (c) CP/MnO_2-NRs (d) CNTs/MnO_2-NRs substrates

As for the spectra of samples containing MnO_2, such as CP/MnO_2-NRs, as shown in Figure 3.5(c), four distinct Raman peaks are observed at approximately 181, 384, 574, and 639.5 cm^{-1}, which correspond to documented peaks of α-MnO_2[142]. The Raman band centered at 639.5 cm^{-1} is assigned to the symmetric stretching vibration of the Mn−O bond perpendicular to the direction of the [MnO_6] octahedral double chains, belonging to the A_g symmetry spectroscopic, as determined through factor group analysis. Similarly, the band at approximately 574 cm^{-1}, which is also an A_g symmetric mode, corresponds to the stretching vibration of the Mn−O bond along the direction of [MnO_6] octahedra double chains. The peak at around 384 cm^{-1}, an E_g symmetry vibration mode, is associated with the bending vibration of the Mn−O bond. Additionally, the sharp peak at roughly 181 cm^{-1}, also an E_g symmetry vibration mode, indicates the translational motion of [MnO_6] octahedra induced by tunnel ions of K^+[142-143]. These observations confirm that all the bands are characteristic of tetragonal α-MnO_2[142-144].

The CNTs/MnO_2-NRs spectrum shown in Figure 5.3(d) displays four distinct Raman peaks at 181.2, 378.4, 574.2, and 642.3 cm^{-1}, all of which are consistent with the features of tetragonal α-MnO_2. Interestingly, the Raman spectra of CP/MnO_2-NRs and CNTs/MnO_2-NRs do not exhibit the D or G band features that are characteristic of the CP and CNTs substrates. This absence of these bands is attributed to the dense, thick layer of α-MnO_2 that uniformly coats the CP and CNTs substrates, effectively masking the underlying carbon-based signals.

3.5 Conclusion

The SEM analysis revealed that the CP/CNTs surface is uniformly coated with a continuous layer of CNTs, indicating successful CNT deposition. The CP/MnO_2 and CNTs/MnO_2 images demonstrate that both substrates are densely coated with MnO_2 nanorods (NRs), with an average diameter of approximately 200 nm. These results confirm the effective deposition of CNTs and MnO_2 catalysts onto the CP surfaces. XRD analysis reveals that CP/MnO_2-NRs and CNTs/MnO_2-NRs, exhibit distinct peaks matching the cryptomelane KMn_8O_{16} phase, confirming the successful deposition of MnO_2 in its stable α-MnO_2 form. This indicates that MnO_2 was effectively deposited on both CP and CNTs substrates in the desired crystalline structure. Raman spectroscopy of the MnO_2-based substrates reveals distinct peaks corresponding to α-MnO_2, confirming successful deposition of MnO_2 with characteristic vibrational modes. Notably, the D and G bands are absent in both CP/MnO_2-NRs and CNTs/MnO_2-NRs due to the thick MnO_2 layer masking the underlying carbon signals.

4. CAPACITIVE STUDIES

4.1 Specific capacitance measurements

4.1.1 Measurements for MnO_2-free electrodes

A comparison of the electrochemical windows between bare CP and bare CNTs in a 0.1 M NaOH solution at 2 mV/s is illustrated in Figures 4.1a1 and 4.1a2. Within the oxidation and reduction boundaries of NaOH, the CV profiles of both bare CP and bare CNTs display steady currents, each indicating a pure double layer (DL) capacitance. This suggests that both substrates exhibit typical capacitive behavior in the NaOH electrolyte, with the CNTs substrate potentially offering enhanced electrochemical stability and a broader electrochemical window due to the incorporation of carbon nanotubes. As observed in the two figures, the potential window of the CP substrate ranges from –0.108 V to 0.43 V, while for the CP/CNTs substrate, it extends slightly wider—from –0.23 V to 0.43 V.

The capacitive properties of both CP and CNTs were further evaluated via cyclic voltammetry in a 0.1 M NaOH solution at different scan rates (2, 5, 10, 50, 100, 200, 400 and 500 mV/s). The results are depicted in Figure 4.1b1 for CP and Figure 4.1b2 for CNTs. The CV curves of the CP electrode exhibit nearly symmetrical rectangular shapes. In contrast, the CV curves for the CNTs electrode show distinctly symmetrical rectangular shapes, characteristic of an electrochemical double layer capacitor (EDLC). This behavior suggests that the charges are stored on the surface of the CNTs material, highlighting the enhanced capacitive properties due to the inclusion of carbon nanotubes, which provide increased surface area and improved charge storage capabilities. Capacitive behavior for the CP electrode is observed within a potential window of 0.54 V, whereas for the CNTs electrode, it is observed within a slightly higher potential window of 0.66 V. The specific capacitance derived from the CV curves, shown in Figures 4.1b1 and 4.1b2, is calculated using the formula $C_p = Q/(2\ m \times v \times \Delta V)$. In this equation, Q (A V) is the voltametric charge obtained by integrating the areas of both oxidation and reduction on the CV curve, m (g) is the mass of the active material on the working electrode, v is the scan rate (V/s), and ΔV (V) indicates the potential window of the CV. This formula allows for the calculation of the specific capacitance, which quantifies the material's ability to store charge per unit mass at a given scan rate. The resulting C_p values, plotted against the scan rate in Figures 4.1c1 and 4.1c2, reveal that for both electrodes, CP and CNTs, the specific capacitance decreases as the scan rate increases, although it shows a slight recovery at higher scan rates. This behavior is typical for both bare CP and CNTs, which exhibit pure electrochemical double-layer capacitor (EDLC) behavior. As the scan rate increases, the specific capacitance decreases due to reduced ion diffusion time and increased transfer resistance of the ions in the electrode matrix (intrinsic resistance). At higher scan rates, the capacitance shows some recovery as the system transitions to a diffusion-controlled regime, where ion transport becomes the primary limiting factor. Increasing the scan rate to some point (50 mV/s in case of CP or 10 mV/s in case of CP/CNTs), ion electrolyte transport to the interior surface becomes the limiting factor, and the process of storing charge primarily depends on how fast the electrolyte ions reach the deeper pores. The relatively high conductivity and large surface area of CP/CNTs electrode facilitate efficient ion accessibility to the inner pores of the electrode at higher scan rate, thus increasing the measured capacitance. This behavior aligns with the general principles of electrochemical capacitors, even for materials exhibiting pure EDLC characteristics. This kind of scan-rate dependence is quite common in materials like CNTs. The hydrophobic nature of as-made CNTs can significantly impact their electrochemical performance, particularly in terms of ion accessibility and wettability. Hydrophobic CNTs tend to have poor electrolyte interaction, limiting the ion diffusion into the CNTs structure, especially at lower scan rates. This could result in lower capacitance values due to ineffective electrolyte penetration. Activation, such as through CV, can help improve the wettability and surface chemistry of the CNTs, making them more hydrophilic and enhancing the ion diffusion during the charge-discharge process. As a result, activation can increase the electrochemical performance by allowing better electrolyte interaction, leading to higher capacitance. It is also noteworthy that the specific capacitance provided by the bare CP is relatively small, with the highest value reaching close to 0.0006 F/g at 2 mV/s. This emphasized the importance of incorporating materials, such as CNTs, which enhance the electrochemical performance and significantly improve capacitance values compared to the bare CP. Indeed, the C_p provided by the CP/CNTs at 2 mV/s is 0.5407 F/g, which is 901 times higher than the capacitance delivered by the bare CP.

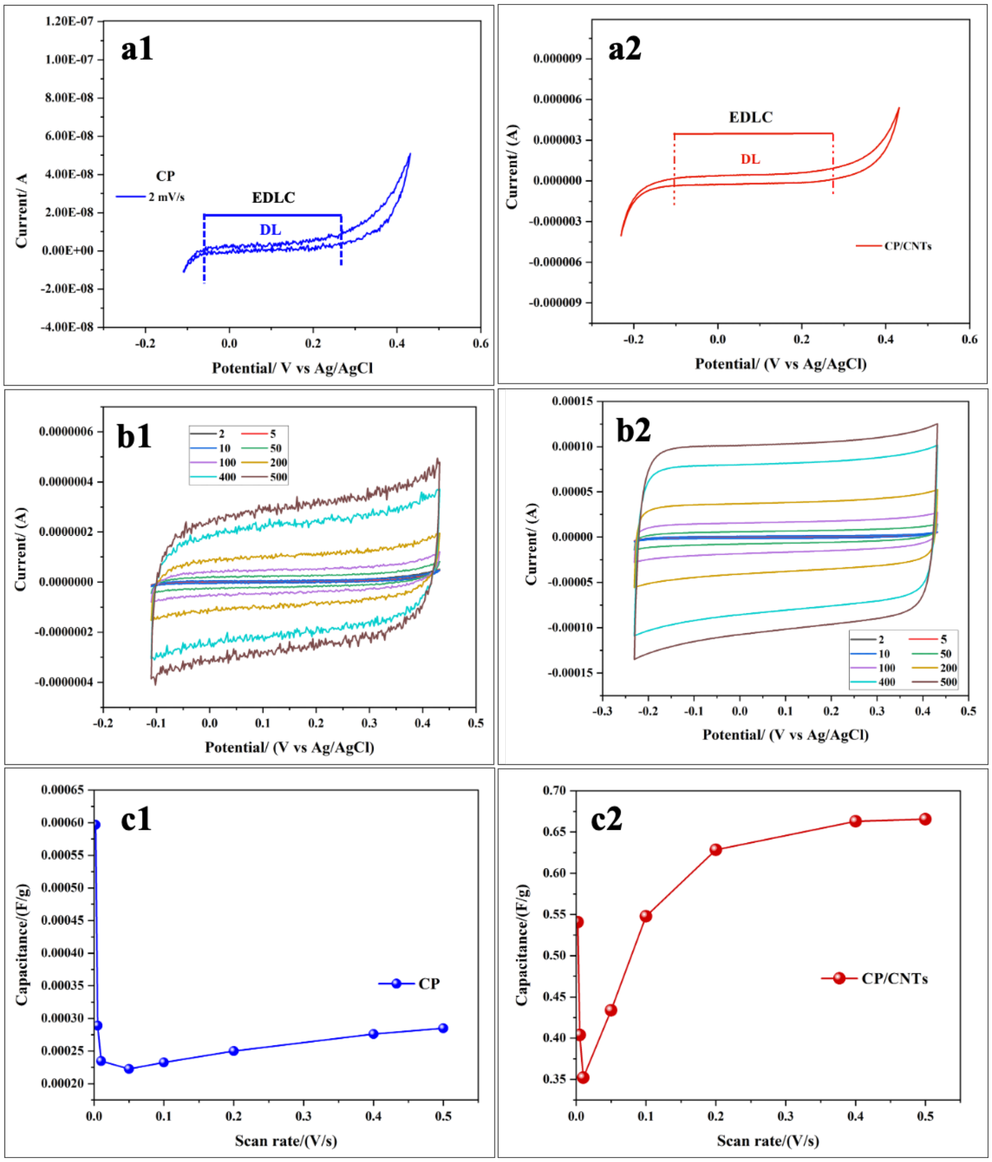

Figure 4.1: (a1 and a2) Electrochemical windows of bare CP and CP/CNTs in 0.1 M NaOH solution at 2 mV/s. (b1 and b2) capacitive behavior of bare CP and CP/CNTs, respectively. Numbers indicate the scan rate in mV/s. (c1 and c2) Specific capacitance versus scan rate for bare CP and CP/CNTs, respectively

4.1.2 Measurements for MnO_2-based electrodes

The synthesized CP/MnO_2-NRs and CNTs/MnO_2-NRs exhibit symmetric peaks on both the anodic and cathodic sides, alongside the DL region, as illustrated in Figures 4.2a1 and 4.2a2. The redox peaks of CP/MnO_2-NRs are within the 0.15 V and 0.2 V region (as shown in Figure 4.2a1), while the redox peaks for the CNTs/MnO_2-NRs are observed within the region of 0.1 V and 0.24 V (Figure 4.2a2). These observations suggest that both substrates exhibit characteristic redox behavior, with the CNTs/MnO_2-NRs showing a slightly broader redox peak range, which may be attributed to the enhanced conductivity and electrochemical activity provided by the carbon nanotubes. The redox peaks observed at the MnO_2 electrodes typically indicate the involvement of surface Mn ions in redox reactions. This behaviour underscores the pseudocapacitive nature of the charge storage mechanism, where charge is stored through reversible redox reaction at the electrode/electrolyte interface[145]. The observed redox peaks are attributed to the reversible redox reactions of Mn ions within the MnO_2 structure. Specifically, these peaks correspond to the Mn^{3+}/Mn^{4+} redox couple. During the reduction process, Mn^{4+} is reduced to Mn^{3+}, while Mn^{3+} is oxidized back to Mn^{4+} during the anodic sweep. The Mn ions that participate in this redox reaction are typically the surface Mn^{3+} and Mn^{4+} ions, which are involved in the charge storage mechanism through reversible electron transfer at the electrode/electrolyte interface[146-147]. This pseudocapacitive behavior is a key feature of the MnO_2 material, enhancing its electrochemical performance. The capacitive properties of both CP/MnO_2-NRs and CNTs/MnO_2-NRs were evaluated via cyclic voltammetry in a 0.1 M NaOH solution at different scan rates (2, 5, 10, 50, 100, 200, 400 and 500 mV/s). It is observed that the capacitive potential window for CP/MnO_2-NRs (Figure 4.2b1) expands to 0.65 V, compared to 0.54 V for bare CP. Similarly, the capacitive potential window for CNTs/MnO_2-NRs (Figure 4.2b2) is also 0.65 V.

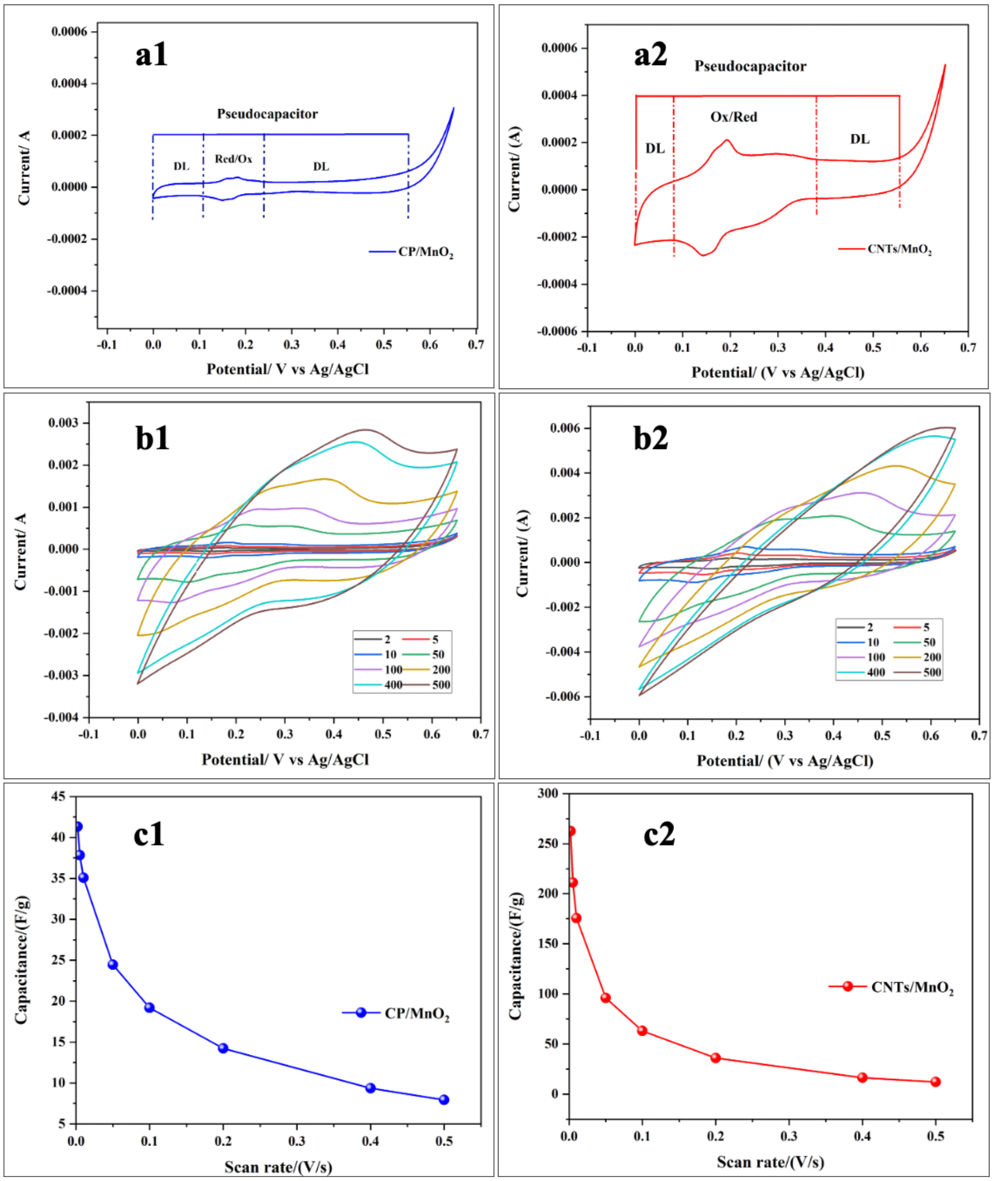

Figure 4.2: (a1 and a2) Electrochemical windows of CP/MnO$_2$-NRs and CNTs/MnO$_2$-NRs electrodes in 0.1 M NaOH solution at 2 mV/s. (b1 and b2) capacitive behavior of CP/MnO$_2$-NRs and CNTs/MnO$_2$-NRs, respectively. Numbers indicate the scan rate in mV/s. (c1 and c2) Specific capacitance versus scan rate for CP/MnO$_2$-NRs and CNTs/MnO$_2$-NRs, respectively

Specific capacitances, determined from the CVs shown in Figures 4.2b1 and 4.2b2, are plotted against the scan rate, in Figures 4.2c1 and 4.2c2. The rate performance of the CP/MnO$_2$-NRs electrode, illustrated in Figure 4.2c1, shows how the specific capacitance varies with scan rate. It is evident that the specific capacitance diminishes as the scan rate increases. A notable feature of Figure 4.2c1 is the high specific capacitance of CP/MnO$_2$-NRs, reaching 42 F/g at 2 mV/s, significantly higher than those of the bare CP and bare CNTs electrodes. The large specific capacitance of the CP/MnO$_2$-NRs composite can be attributed to both structural and electrochemical factors. The unique structure of the MnO$_2$ nanorod arrays, with their highly exposed active surfaces, facilitates rapid electrolyte diffusion and fast Na^+ transfer, contributing significantly to the capacitance. Additionally, the high specific capacitance is also a result of the faradaic charge storage capability of MnO_2. This faradaic behavior involves redox reactions that provide an enhanced charge storage mechanism beyond the contributions from surface area alone. Consequently, the high specific capacitance of the CP/MnO_2-NRs composite is due to the synergistic effects of the nanostructured surface of MnO_2 and its faradaic charge storage properties. However, the specific capacitance markedly declines at scan rates above 10 mV/s. This behavior, characteristic of transition metal oxides (TMOs), is due to the decreased diffusion of electrolyte ions into the active material matrix at higher scan rates, limiting the electrochemical performance. The observed decline emphasizes the inherent challenge of fast ion diffusion in transition metal oxides, which is particularly pronounced at high scan rates.

A similar performance trend is observed for the CNTs/MnO_2-NRs electrode, as illustrated in Figure 4.2c2, where the C_p diminishes with the increase of scan rate. The C_p of CNTs/MnO_2-NRs reaches an impressive value of 262.68 F/g at a scan rate of 2 mV/s. This value is over six times greater than the 42 F/g achieved by the CP/MnO_2-NRs electrode, highlighting the substantial enhancement in charge storage capacity due to the incorporation of carbon nanotubes. This significant difference suggests that the CNTs-based structure enhances charge storage capacity due to factors such as improved conductivity, increased surface area, and greater electrochemical activity.

Among all the investigated electrodes, CNTs/MnO_2-NRs exhibits the highest specific capacitance, as illustrated in Figure 4.3 (left). The figure on (right) shows the calculated *Cp* values of CP, active CNTs on the CP/CNTs composite, active MnO_2 on the CP/MnO_2-NRs composite, and active MnO_2 on the CNTs/MnO_2-NRs composite. For instance, the *Cp* of active MnO_2 on CP/MnO_2-NRs composite can be estimated using the following formula:

$$Cp\ \mathrm{MnO_2} = \frac{Cp\ (\mathrm{nanocomposite}) - Cp\ (\mathrm{CP})}{wt\%\ \mathrm{MnO2}} \tag{4.1}$$

This significant difference suggests that the CNTs-based structure plays a crucial role in boosting the electrochemical performance[53, 148]. The improved charge storage capacity can be attributed to several factors, including enhanced conductivity, which facilitates faster electron transfer; increased surface area, which provides more active sites for charge storage; and greater electrochemical activity, which likely enhances the overall performance of the electrode.

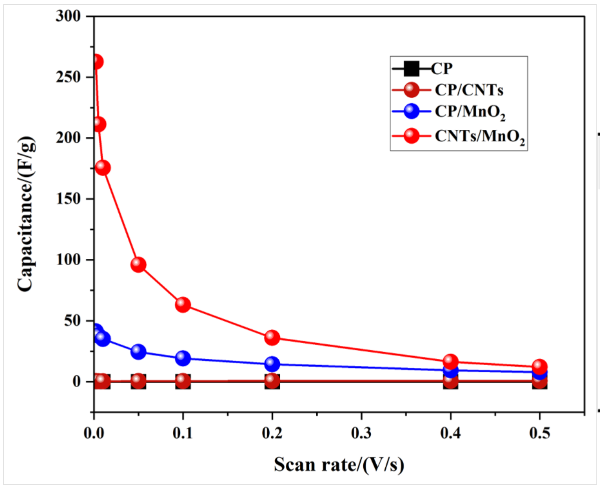

	CP	CNT/CP	CP/MnO_2	CNT/MnO_2
v (V/s)	*Cp* (F/g)	*Cp* (F/g)	*Cp* (F/g)	*Cp* (F/g)
0.002	0.0006	0.5407	41.3215	262.6886
0.005	0.0003	0.4040	37.8308	211.3261
0.01	0.0002	0.3521	35.0811	175.6649
0.05	0.0002	0.4338	24.4599	95.9789
0.1	0.0002	0.5479	19.1776	63.0627
0.2	0.0002	0.6284	14.2303	36.0651
0.4	0.0003	0.6630	9.3601	16.3817
0.5	0.0003	0.6655	7.9284	12.1332

Figure 4.3: (Left) Specific capacitance versus scan rate of all investigated electrodes. (Right) Specific capacitance values of CP, active CNTs on CP/CNTs, active MnO_2 on CP/MnO_2-NRs and active MnO_2 on CNTs/MnO_2-NRs substrates at scan rate range of (2–500 mV/s)

The synergistic effect of MnO_2 nanorods on the CNTs further improves the material's electrochemical behavior, making CNTs/MnO_2-NRs a highly promising electrode material for supercapacitor applications.

4.2 Electrochemical surface area measurements

4.2.1 Measurements for MnO_2-free electrodes

First, the I_c values were extracted for CP and CNTs substrates within the non-faradic region, at E= 0.15 V from the cyclic voltammograms shown in Figures 4.1b1 and 4.1b2. Following this, the C_{dl} was evaluated for both CP and CNTs/CP electrodes within the same non-faradic region. Figures 4.4a1 and 4.4a2 illustrate the current values plotted against the scan rate for both electrodes. Notably, both curves exhibit a linear trend across the entire range of measured scan rates. By analyzing the plot of scan rates versus current, we can derive the C_{dl} values for both samples, which correspond to the slopes of the graphs. The determined C_{dl} values are 0.0006 mF for bare CP and 0.21 mF for bare CNTs. The much higher C_{dl} value for bare CNTs compared to bare CP suggests a significantly larger electrochemical surface area for the CNTs electrode, which is likely due to the higher surface area and enhanced conductivity of the CNTs. This higher C_{dl} value indicates a greater ability to store charge in the electrochemical double layer, thereby improving the overall capacitive performance of the CP/CNTs electrode.

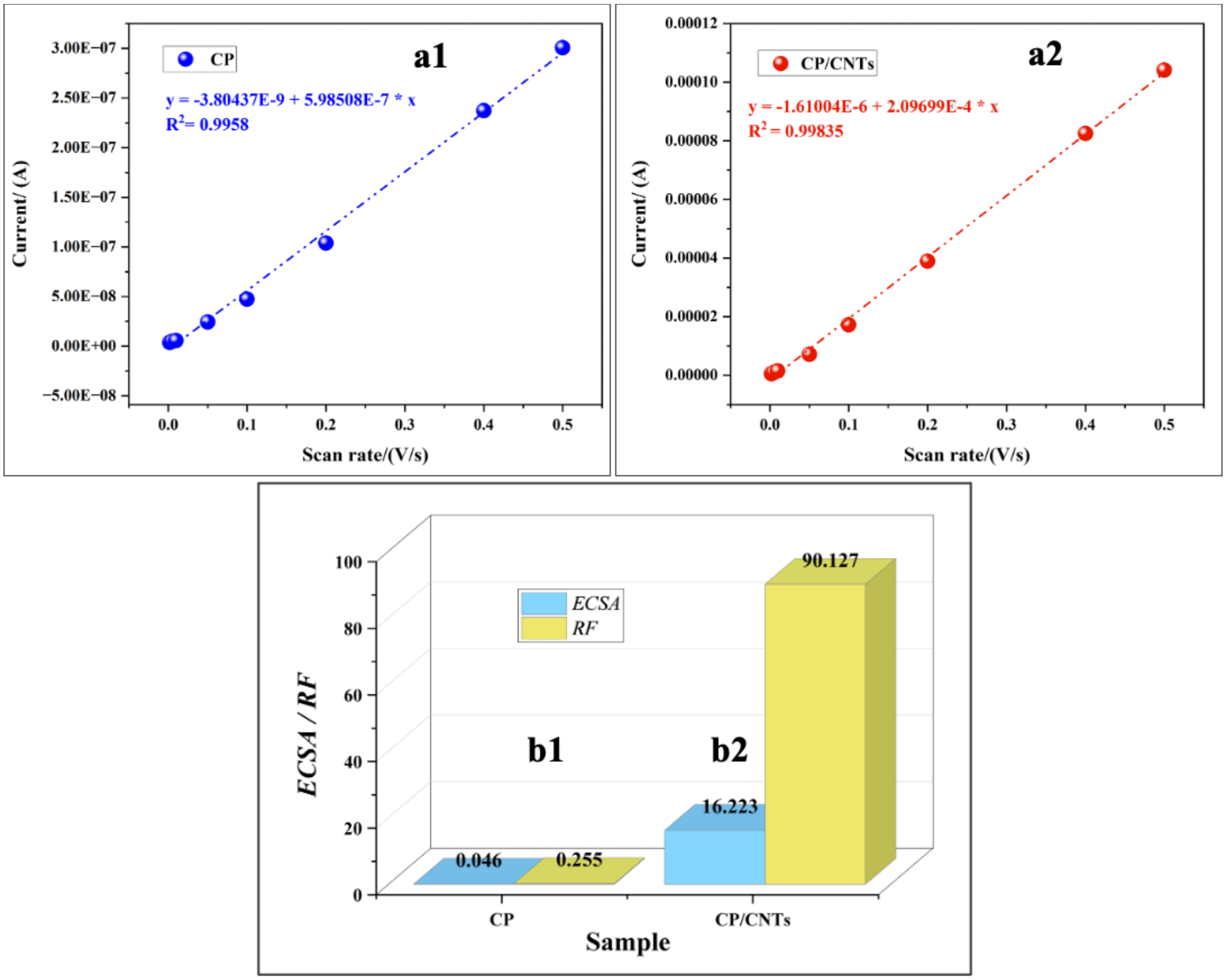

Figure 4.4: (a1 and a2) Non-faradic anodic currents (extracted from CV curves at *E*= 0.15 V) vs. scan rate. (b1 and b2) Estimated *ECSA* (cm^2) and *RF* parameters for the catalyst-free substrates

Subsequently, Figure 4.4(b1 and b2) displays the calculated *ECSA* and *RF* values for each sample. The *ECSA* and *RF* values of CP are observed to be 0.046 cm^2 and 0.225, respectively. In contrast, the estimated *ECSA* and *RF* values for the CNTs are much higher, at 16.223 cm^2 and 90.127, respectively. The relatively small *ECSA* and *RF* values for CP can be attributed to the smooth and planar surface of the CP substrate, which limits the available active sites for electrochemical reactions, resulting in a reduced *ECSA*. This limited surface area is a characteristic feature of bare CP, as its structure does not provide many pores or defects to facilitate ion absorption or the adsorption of electrolytes. Additionally, the CP substrate may exhibit a lower density of active sites per unit area, further contributing to the smaller *ECSA*. On the other hand, the much higher *ECSA* and *RF* values for CNTs suggest that the incorporation of CNTs significantly enhances the surface area and roughness of the electrode, providing more available active sites for electrochemical reactions. This improvement in surface area and roughness leads to a larger number of electrochemically active sites and thus a higher capacitance, which is consistent with the enhanced electrochemical performance observed for CP/CNTs in earlier measurements.

4.2.2 Measurements for MnO_2-based electrodes

Similarly to the MnO_2-free electrodes, the C_{dl} values were evaluated for CP/MnO_2-NRs and CNTs/MnO_2-NRs electrodes within the non-faradic regions of voltammograms shown in Figures 4.2b1 and 4.2b2. The I_c values of CP/MnO_2-NRs were extracted at E= 0.6 V. It can be noted from the voltammograms that beside the redox region there are two DL capacitance regions, and the wider DL region is presented at higher positive potentials. Since the voltammograms are slightly shifted towards more positive potentials when rising the scan rates, the only non-faradic region involved in all investigated scan rates is at a potential value of 0.6 V, which is within the electrochemical stability window of the CP/MnO_2-NRs electrode (0.0 V to 0.65 V) and the potential range of the electrolyte (–0.3 V to 0.6V). Therefore, ensuring that the system is stable and both the electrode and the electrolyte are not oxidizing or decomposing. For CNTs/MnO_2-NRs, the non-faradaic currents were obtained from two regions: the first region at E= 0.5 V (for low *scan rates* of 2–10 mV/s) and the second one at E= 0.626 V (for high *scan rates* from 50 to 500 mV/s). The reason for this approach is that there is no single potential region from which non-redox (non-Faradaic) current values can consistently be extracted to calculate double-layer capacitance. The current measured at 0.5 V represents the last observable non-Faradaic contribution at low scan rates. It is also adjacent to the second region, at 0.626 V, where non-Faradaic current values can still be extracted at higher potentials. Figures 4.5a1 and 4.5a2 illustrate the extracted I_c values as a function of scan rates. Both curves exhibit a linear trend across the entire range of measured scan rates. By analyzing the scan rate versus current plots, C_{dl} values were derived from the slops of the linear regression lines. The measured C_{dl} values are 4.3 mF for CP/MnO_2-NRs and 12.2 mF for CNTs/MnO_2-NRs. The C_{dl} of CNTs/MnO_2-NRs is 2.8 higher than that of the CP/MnO_2-NRs. This significant increase in C_{dl} for the CNTs/MnO_2-NRs electrode can be attributed to the enhanced surface area and improved conductivity provided by the CNTs, which facilitate faster ion diffusion and a greater number of active sites for charge storage. The combination of MnO_2 nanorods with CNTs likely synergistically contributes to the enhanced electrochemical performance of the CNTs/MnO_2-NRs electrode.

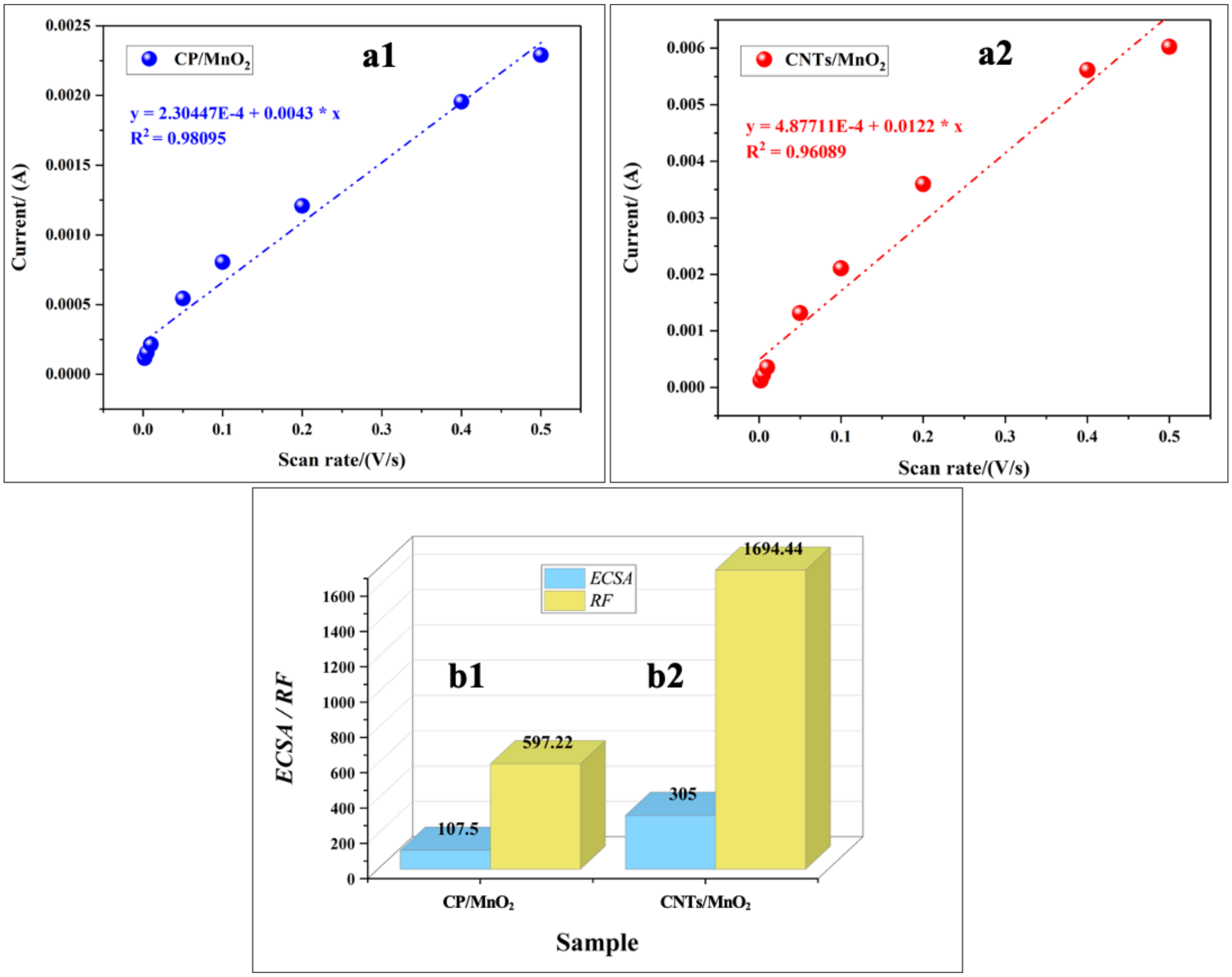

Figure 4.5: (a1 and a2) Non-faradic anodic currents (extracted from CV curves, at *E*= 0.6 V for CP/MnO_2-NRs electrode and at *E*= 0.5 V (for the low scan rates of 2–10 mV/s) and at *E*= 0.626 V (for the high scan rates of 50–500 mV/s) for CNTs/MnO_2-NRs electrode) vs. scan rate. (b1 and b2) Estimated *ECSA* (cm^2) and *RF* parameters for the synthesized MnO_2 substrates

To further understand the relationship between these electrochemical properties and the performance of the electrodes, the *ECSA* and *RF* values were also calculated for both electrodes. Figure 4.5(b1 and b2) presents the calculated *ECSA* and *RF* values for CP/MnO_2-NRs and CNTs/MnO_2-NRs. Notably, the *ECSA* and *RF* values of the CP/MnO_2-NRs are estimated at 107.5 cm^2 and 597.2, while the CNTs/MnO_2-NRs demonstrate impressively large values of *ECSA* (305 cm^2) and *RF* (1694.4). The incorporation of CNTs plays a crucial role in this enhancement, as their high conductivity and large surface area facilitate improved electron transfer and increased active sites for electrochemical reactions, thereby boosting the overall electrochemical performance of the hybrid material. This larger effective *ECSA* not only reflects the improved conductivity but also contributes to the higher specific capacitance observed in the CNTs/MnO_2-NRs. A greater surface area allows for more ion adsorption and electron transfer during electrochemical processes, which can significantly enhance the performance of electrochemical sensing applications.

4.3 Conclusion

The C_{dl} values for CP/MnO_2-NRs and CNTs/MnO_2-NRs electrodes were determined from the non-faradaic regions of voltammograms, showing that CNTs/MnO_2-NRs exhibited a C_{dl} value 2.8 times higher than CP/MnO_2-NRs. This increase is attributed to the enhanced surface area and conductivity of CNTs, which improve ion diffusion and charge storage. Additionally, the CNTs/MnO_2-NRs electrode demonstrated significantly larger *ECSA* and *RF* values, reflecting its superior electrochemical performance due to the synergy between CNTs and MnO_2. This enhancement leads to better ion adsorption and electron transfer, boosting the electrode's capabilities in electrochemical sensing applications.

5. CYCLIC VOLTAMMETRY STUDIES

5.1 Voltammetric detection of Glu, AA, and UA at Au wire electrode

In this section, we will initially examine gold as a benchmark catalyst whose electrochemical characteristics towards the oxidation of Glu, AA, and UA is well documented. The outcomes of this study will provide a foundational framework for interpreting the results obtained later on CP, CP/CNTs, CP/MnO_2-NRs and CNTs/MnO_2-NRs electrodes. Figure 5.1 illustrates a CV of an Au wire electrode in a 0.1 M NaOH solution. In the positive-going scan, a typical double layer region of Au is observed between –0.1 and 0.2 V vs Ag/AgCl, followed by a distinct peak at 0.440 V vs Ag/AgCl and a reduction peak at 0.175 V vs Ag/AgCl. These peaks are attributed to the anodic formation and cathodic removal of surface gold oxide, consistent with findings in the literature[149-150]. Additionally, a minor wave appearing around 0.288 V vs Ag/AgCl prior to the surface oxide formation process suggests a possible premonolayer oxidation of the Au surface.

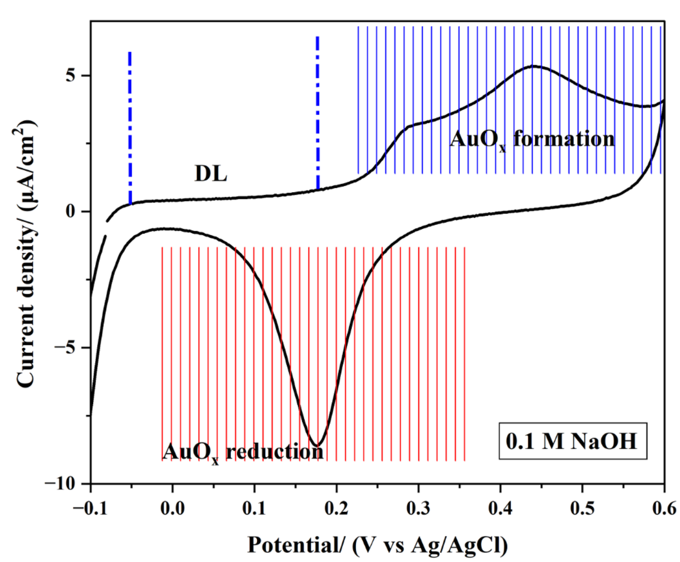

Figure 5.1: Electrochemical window of Au wire electrode in 0.1 M NaOH solution recorded with a scan rate of 2 mV/s

When a modest concentration of 1 mM of glucose is introduced into a NaOH solution at the same wire electrode, two new features emerge during the forward scan, as shown in Figure 5.2a. Firstly, a wave appears at –0.036 V vs Ag/AgCl, followed by a peak at 0.255 V vs Ag/AgCl. Both the current densities associated with these features increase with the increasing concentration of Glu, as illustrated in Figure

5.2b. It is noteworthy that the wave at –0.036 V transforms into a distinct peak with the rise in Glu concentration. The observed CV response aligns with the typical voltammetric pattern associated with glucose oxidation at Au electrode[151-152]. In earlier studies, the first peak was associated with the oxidation of glucose to gluconolactone, a process involving two electrons. The second peak, on the other hand, appears to be related to the oxidation of gluconolactone to gluconic acid[151-152]. Despite numerous attempts to understand the mechanism of glucose oxidation on gold electrodes, this process is complex and not yet fully understood, and a precise and specific mechanism has yet to be identified. As previously mentioned in the sections 1.1.2 and 1.3.3, there are two proposed mechanisms for glucose oxidation on gold electrodes. Some studies indicate that glucose oxidation on the gold surface occurs via the chemisorption model, while other studies emphasize the role of gold oxide or gold hydroxide[153] in glucose oxidation[154] (incipient hydrous oxide adatom mediator (IHOAM model)). Based on the findings in the literatures, Maxime et. al provided a clear explanation for the formation of peaks P1 and P2[155], in which the first peak P1 is likely due to the glucose electrosorption, a process that involves the hydrogen abstraction from the hemiacetal C1 of glucose molecule simultaneously with adsorption of intermediate species of glucose. As glucose adsorbs, the intermediates accumulate and block the active sites on the gold surface, causing a decrease in the current. As the potential increases, the AuOH species begin to form and catalyze the oxidation of these intermediates, freeing up active sites for direct glucose oxidation and resulting in the appearance of the second peak P2. Then, the subsequent current decline after the second peak P2 is attributed to the formation of gold oxide that further inhibits glucose oxidation. The observed peak during the reversed scan is attributed to the reoxidation of glucose on the gold surface, which was restored during the preceding reduction of gold oxides[25, 155]. Olejnik et.al reported that there are two proposed mechanisms for glucose oxidation on gold surface in the literature[156]: (i) the chemisorption model, in which glucose molecules in aqueous solution and at low potentials are chemisorbed onto gold surface, Equation 5.1. The process involves the hemiacetal hydrogen to be abstracted and simultaneously electron transfer (oxidation) occurs. Ultimately, the adsorbed molecule is further oxidized to gluconolacton[157] or similar compound[158], across a wide range of potentials, Equation 5.2. At higher potentials, the gold surface is oxidized to form Au oxide species, at which glucose can be oxidized under diffusion control.

$$\text{Glucose}_{(eq)} \rightarrow \text{Dehydrogenated Glucose}_{(ads)} + e^{-} \quad (5.1)$$

$$\text{Dehydrogenated Glucose}_{(ads)} \rightarrow \text{Gluconolactone}_{(ads)} + e^{-} \quad (5.2)$$

(ii) the (IHOAM) model, in which the $Au(OH)_{ads}$ layer, formed on gold surface at moderated anodic potentials, acts as electron mediator and oxidizes glucose to gluconolactone[25], Equations 5.3 and 5.4. The regeneration of the layer results in an oxidation current, as shown in the following equations:

$$\text{Glucose}_{(eq)} \leftrightarrow \text{Glucose}_{(ads)} \quad (5.3)$$

$$\text{Glucose}_{(ads)} + 2\ \text{Au OH}_{(ads)} \rightarrow \text{Gluconolactone} + 2\ \text{Au} \quad (5.4)$$

$$\text{Au} + \text{OH}^- \rightarrow \text{AuOH}_{(ads)} + e^- \quad (5.5)$$

The CV response observed for the oxidation of 0.2 mM AA at a gold electrode in a NaOH solution displays clear characteristics: an anodic peak emerges during the forward potential scan, positioned at 0.250 V vs Ag/AgCl, signifying the oxidation of AA to dehydroascorbic acid (Figure 5.2c). Conversely, a cathodic peak appears during the reverse potential scan at 0.187 V vs Ag/AgCl, denoting the reduction of dehydroascorbic acid back to AA at the electrode surface—a reversible process under alkaline conditions[159]— along with the reduction of gold oxide to gold (refer to Figure 5.1). This suggests that reoxidation peak might be due to the oxidation of new or remaining AA on a refreshed Au surface. Notably, the current density of the forward peak increases with increasing concentrations of AA (Figure 5.2d). Figure 5.2e illustrates the CV results obtained from oxidizing 0.45 mM UA at the Au wire electrode within a 0.1 M NaOH solution, spanning the potential range from –0.15 V vs Ag/AgCl to 0.6 V vs Ag/AgCl. The CV reveals several features: an anodic peak emerging at 0.027 V vs Ag/AgCl, succeeded by a broad wave spanning from 0.4 V vs Ag/AgCl to 0.6 V, vs Ag/AgCl and a peak positioned at 0.170 V vs Ag/AgCl during the reversal scan. However, interpreting the latter two processes proves challenging due to their overlap with the regions associated with Au oxide formation and reduction. Initially, the anodic peak at 0.027 V was attributed to the saturated adsorption of UA at the Au electrode in the 0.1 M NaOH solution, as suggested by Md. Rezwan Miah[160]. Nevertheless, our findings diverge, revealing that this peak intensifies with increasing UA concentration, implying its association with a faradic process, as shown in Figure 5.2f. The electrochemical oxidation of UA at an Au electrode in a NaOH solution is a complex process with multiple steps. There may not be a single universally accepted mechanism, as researchers are continuously investigating and refining our understanding of these processes through theoretical modeling, spectroscopic studies, and electrochemical techniques. However, there are general trends commonly proposed in the literature. These steps typically involve the adsorption of UA molecules onto the surface of the Au electrode followed by their electrochemical oxidation, leading to the formation of UA radicals. These radicals may then undergo further oxidation, resulting in the formation of intermediate products such as allantoin or UA derivatives[161]. However, it's worth noting that discussing the detailed mechanism is not the primary focus of the present work. Instead, our interest lies in the detection of uric acid using technical voltammetry.

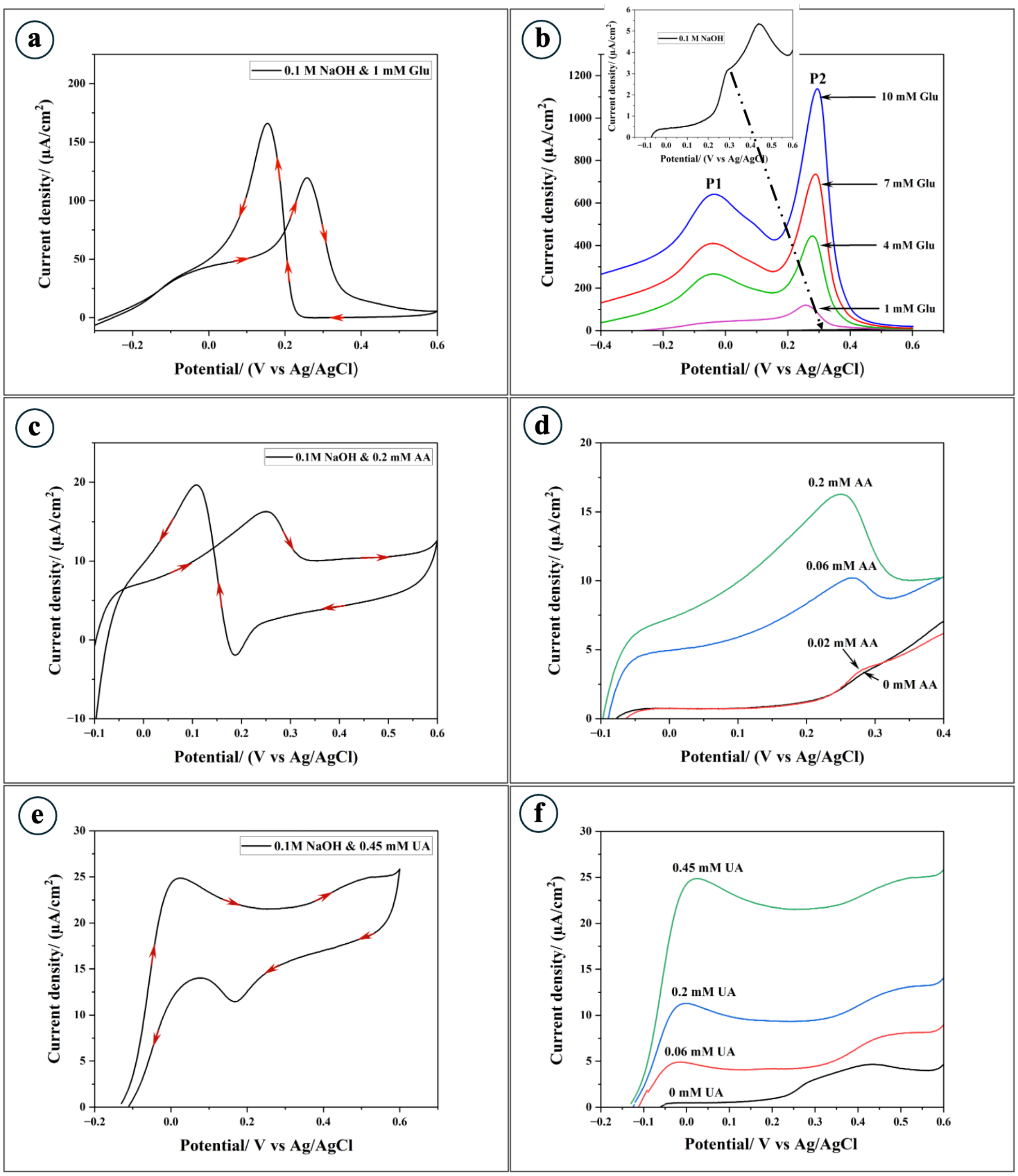

Figure 5.2: Electrochemical oxidation of Glu (a, b), AA (c, d) and UA (e, f) on Au-wire electrode in 0.1 M NaOH solution recorded with a scan rate of 2 mV/s

In summary, Figure 5.3 illustrate the correlation between current peak density extracted from Figures 5.2b, 5.2d, and 5.2f and the concentration of Glu (P1), AA, and UA respectively, indicating a good linear relationship within the concentration range examined in this study. Concerning Glu detection, the Au wire electrode demonstrates a sensitivity of 52.487 μA mM^{-1} cm^{-2} and a low detection limit (LOD) of 0.095 mM. Figure 5.3(bottom right) further provides a summary of the potentials at which Glu, AA, and UA are detected. Notably, AA exhibits oxidation at more positive potentials, ensuring minimal interference with

Glu detection on the Au electrode. However, UA detection closely aligns with Glu potentials, potentially affecting the accurate determination of Glu concentration.

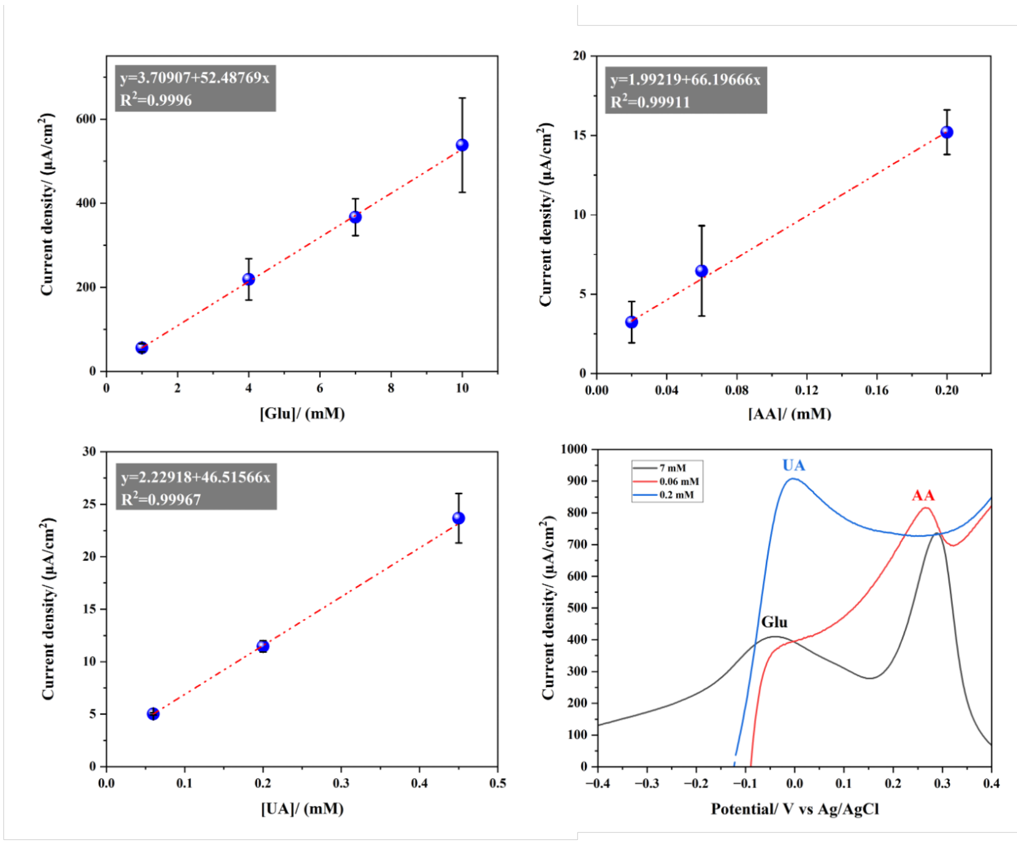

Figure 5.3: Comparison of current peak densities with respect to the concentration of Glu, AA, and UA. Overview of the potential ranges for the oxidation of Glu, AA, and UA, Figure 5.3 (bottom right). Concentrations used: [Glu]= 7 mM, [AA]= 0.06 mM, [UA]= 0.2 mM. Scale: peak current density is normalized, with Glu as the reference (x1), AA and UA scaled by a factor of 80

5.2 Voltammetric detection of glucose at MnO_2-free electrodes

In Figure 5.4a, the CV profile of the CP electrode is presented, both with and without the presence of Glu. Upon the addition of glucose, a noticeable activity towards Glu oxidation is observed at the CP electrode. Two anodic peaks, labeled as P1 and P2, are evident at potentials around 0.069 V and 0.260 V (vs Ag/AgCl), respectively. Subsequently, to establish a quasi-steady state, slow linear sweep voltammetry (LSV) measurements were carried out with a scan rate of 2 mV/s in a 0.1 M NaOH solution containing various concentrations of glucose (Glu), as depicted in Figure 5.4b. It is observed that the current peak densities of both P1 and P2 increase with rising Glu concentration. Focusing on the maximum current peak, P1, for each Glu concentration, its dependency on Glu concentration is illustrated in Figure 5.4c. Notably, a strong linear correlation (R^2= 0.9969) is observed in the range of 1 to 15 mM, extending far beyond the physiological levels (3–8 mM)[162]. However, the CP electrode demonstrates low sensitivity of 0.081 μA mM^{-1} cm^{-2} and a LOD of 0.425 mM.

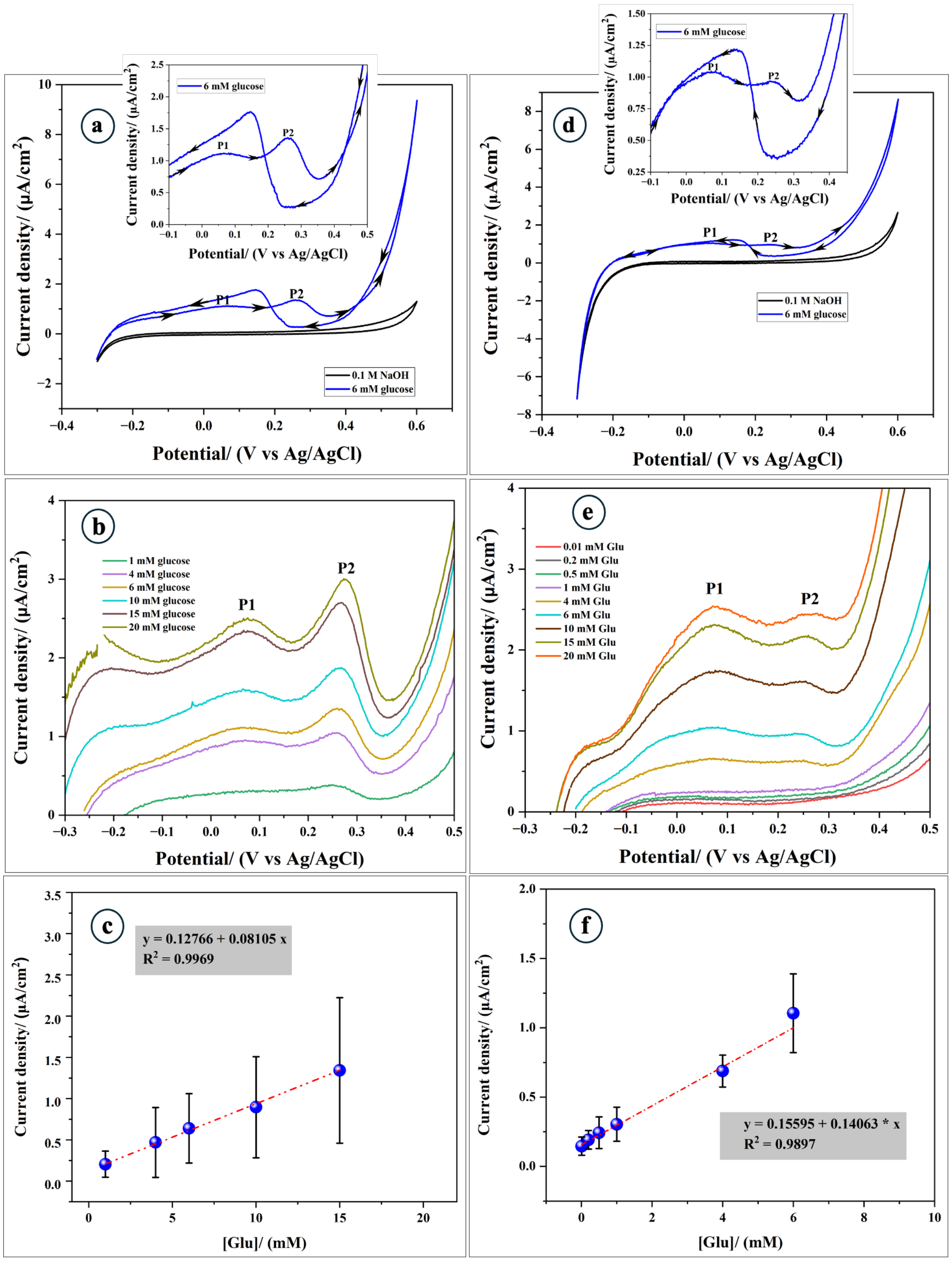

Figure 5.4: Electrochemical oxidation of Glu (a, b, c) on CP electrode, and (d, e, f) CP/CNTs nanorods electrode in 0.1 M NaOH solution recorded with a scan rate of 2 mV/s. The current densities in Figure c and f correspond to P1

In contrast, Figure 5.4d shows the CV profile of the CP/CNTs electrode with and without glucose (Glu). Similar to the Au wire and CP electrode, the CV of Glu oxidation at CP/CNTs exhibits two peaks, marked as P1 and P2, in the forward scan, appearing at potentials of 0.082 V and 0.234 V vs Ag/AgCl, respectively. Both current densities of P1 and P2 increased with the rise in Glu concentration, as depicted in Figure 5.4e. A linear relationship (R^2= 0.9897) is evident in the range of 0.01 to 6 mM for peak P1, as shown in Figure 5.4f. This electrode exhibits a relatively higher sensitivity of 0.140 µA mM^{-1} cm^{-2} and a LOD of 0.269 mM. The high surface area and the high C_p of the carbon nanotubes enhanced the detection of Glu at CP/CNTs electrode within 0.01–6 mM concentration range and at lower detection limit.

5.3 Voltammetric detection of glucose at MnO_2 nanorods electrodes

The enhanced *ECSA* and specific capacitance of MnO_2-NRs electrodes might significantly improve electrochemical sensing by increasing sensitivity through a greater number of active sites for analyte interaction, enabling the detection of lower concentrations. Their superior conductivity and ion transport may lead to faster response times, making the sensors more effective for real-time monitoring. Therefore, we undertook studies on glucose detection using these composites. Figure 5.5a illustrates the CV profile of the CP/MnO_2-NRs electrode, with and without the presence of Glu. The addition of glucose reveals a noticeable activity for Glu oxidation, indicated by two anodic peaks, P1 and P2, at approximately 0.210 V and 0.297 V (Ag/AgCl), respectively. It is noteworthy that the first peak (P1), associated with the oxidation of glucose to gluconolactone, becomes more pronounced in modified electrodes—particularly CP/MnO_2-NRs—compared to bare CP and bare CNTs substrates. This enhancement can be attributed to the increased number of active surface sites available for glucose oxidation. To achieve a quasi-steady state, slow LSV measurements were conducted at a scan rate of 2 mV/s in a 0.1 M NaOH solution with various Glu concentrations, as illustrated in Figure 5.5b. It was found that the current peak densities for both P1 and P2 increased with higher Glu concentrations. Figure 5.5c illustrates the relationship between the maximum current peak, P1, and Glu concentration for the CP/MnO_2-NRs electrode. A strong linear correlation (R^2= 0.9865) is observed between 0.01 and 15 mM, which exceeds typical physiological glucose levels (3–8 mM). Furthermore, the electrode exhibits a very high sensitivity of 143.82 µA mM^{-1} cm^{-2} and a LOD of 0.282 mM.

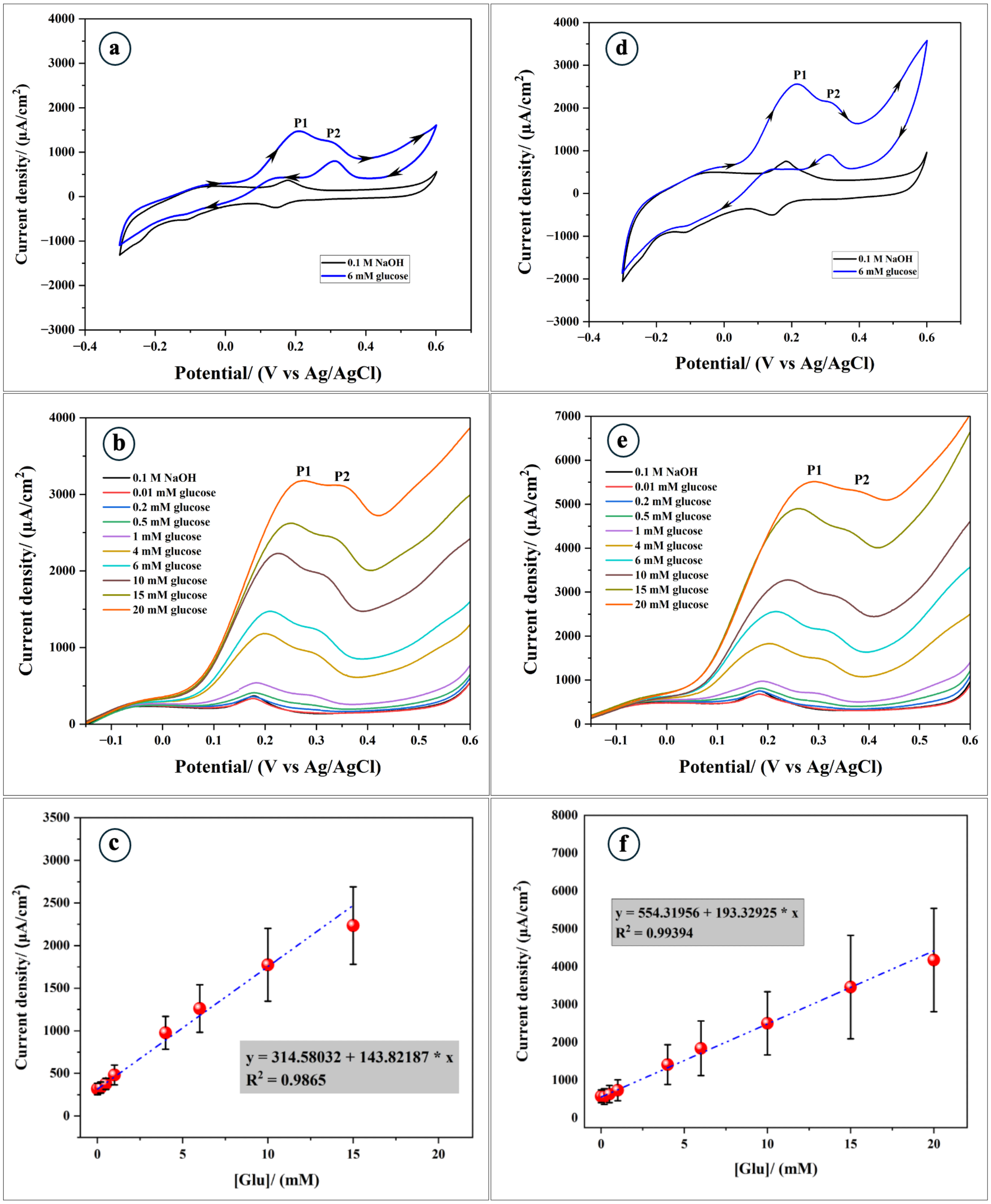

Figure 5.5: Electrochemical oxidation of Glu (a, b, c) on CP/MnO_2-NRs electrode, and (d, e, f) on CNTs/MnO_2-NRs electrode in 0.1 M NaOH solution recorded with a scan rate of 2 mV/s. The current densities in Figure c and f correspond to P1

The CNTs/MnO_2-NRs electrode exhibited similar characteristics but displayed significantly higher current densities compared to the CP/MnO_2-NRs electrode, as depicted in Figures 5.5d and 5.5e. The observed CV response aligns with the typical voltammetric pattern associated with Glu oxidation[151-152]. In these studies, the peak P1 was associated with the oxidation of glucose to gluconolactone, a process involving two electrons. The second peak P2, on the other hand, appears to be related to the oxidation of gluconolactone to gluconic acid. The comparison between the CP/MnO_2-NRs and CNTs/MnO_2-NRs electrodes reveals that the latter exhibits significantly higher current densities for Glu oxidation, indicating enhanced electrocatalytic activity upon the CNTs incorporation. Subsequently, the sensor's sensitivity was assessed by examining the relationship between current peak density (P1) and Glu concentration. A linear regression analysis was conducted on the resulting data plot. The CNTs/MnO_2-NRs electrode shows a stronger linear relationship (R^2= 0.9939) for peak P1 over a range of 0.01 to 20 mM, with significantly higher sensitivity of 193.33 μA mM^{-1} cm^{-2} and a lower LOD of 0.243 mM, as shown in Figure 5.5f.

While certain aspects of CV behavior may exhibit similarities among Au, CP, CP/CNTs, CP/MnO_2-NRs and CNTs/MnO_2-NRs electrodes, it is crucial to consider the distinctive characteristics of each electrode material when comparing their electrochemical responses. For instance, a significant disparity among the Au wire, MnO_2-free electrodes and MnO_2 nanorods-based electrodes is the narrower separation Δ (P2 – P1) between the P1 and P2 peaks observed in the MnO_2-NRs electrodes (CP/MnO_2-NRs and CNTs/MnO_2-NRs), as shown to Figure 5.6a.

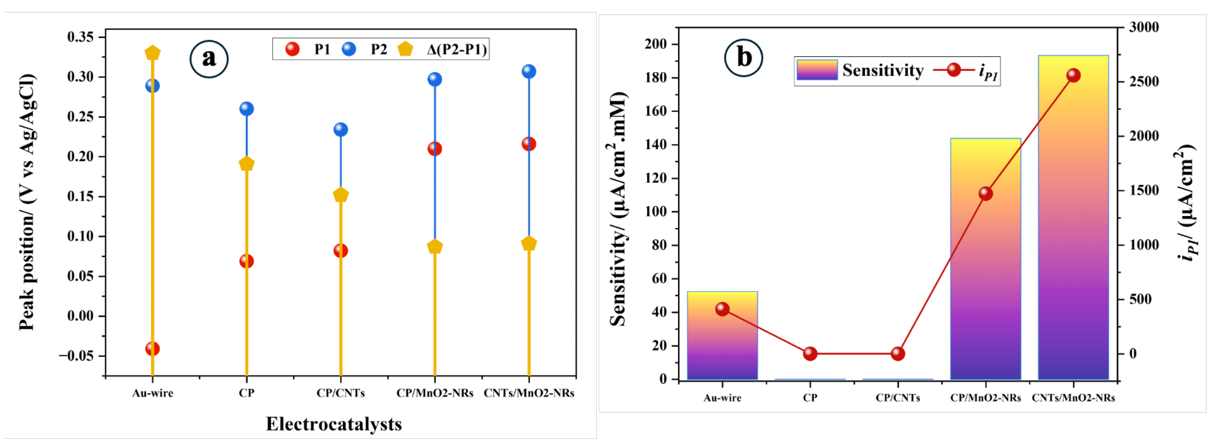

Figure 5.6: (a) Peak potentials: P1 and P2, and Δ (P2 – P1) separation. (b) Current density of peak P1 and sensitivity of investigated substrates. Glucose peaks correspond to [Glu]= 7 mM at the Au and [Glu]= 6 mM at the other substrates

Regarding performance, the CNTs/MnO_2-NRs electrocatalyst demonstrates markedly superior sensitivity, 3.68 times higher than that of the Au wire, and greater current peak density, particularly evident with a Glu concentration of 6 mM, as illustrated in Figure 5.6b. This indicates that the MnO_2 nanorod electrodes exhibit exceptional catalytic activity for glucose oxidation, potentially due to both their intrinsic properties—such as crystal structure and redox characteristics—and extrinsic advantages, such as increased surface area and improved accessibility of active sites. The electrochemical oxidation of glucose at a MnO_2 electrode in

NaOH electrolyte typically involves a multi-step process. Initially, glucose is oxidized to gluconolactone or gluconic acid, producing electrons that are transferred to the electrode surface, as referred to the introduction (Equations 1.22, 1.26–1.28).

5.3.1 Voltammetric detection of ascorbic acid and uric acid on MnO_2 nanorods electrodes: interference studies

For CP/MnO_2-NRs, Figures 5.7a and 5.7b illustrate that upon the addition of AA or UA to 0.1 M NaOH, no new peak emerges. Instead, the current density of the peak associated with the surface redox process at MnO_2 diminishes with increasing AA or UA concentration. This observed behavior could be attributed to several potential factors. The adsorption of AA or UA or their reaction byproducts onto the MnO_2 electrode surface could prompt the formation of a passivating layer, thereby impeding electron transfer processes and reducing current density. Additionally, the observed decrease in peak current density with increasing concentrations of AA or UA can be attributed to a combination of factors. While the initial explanation focused on the potential kinetic limitations of the redox reactions, where slower reaction rates of AA or UA compared to MnO_2 could reduce the overall current density, surface blocking effects are also significant. As the concentration of AA or UA increases, their surface coverage on the MnO_2 electrode also rises, which can hinder the access of other reactants to the active sites and contribute to a decrease in current density. Therefore, both the kinetic effects of slower redox reactions and the surface blocking by higher concentrations of AA or UA play a role in the observed decrease in peak current density. A comprehensive understanding of the precise mechanism necessitates further experimentation and analysis, including the examination of reaction kinetics and the characterization of MnO_2 electrode surface chemistry under varied conditions. In Figures 5.7c and 5.7d, one can observe the LSVs recorded in a NaOH solution comprising both AA and UA. In these plots, one concentration remains constant while the other varies. Interestingly, no additional peaks emerge when both AA and UA are concurrently present in the electrolyte, indicating no new chemical processes. Additionally, the peak associated with the surface redox process at the MnO_2 electrode diminishes as the concentration of AA is either fixed or increased, and conversely, as UA concentration varies.

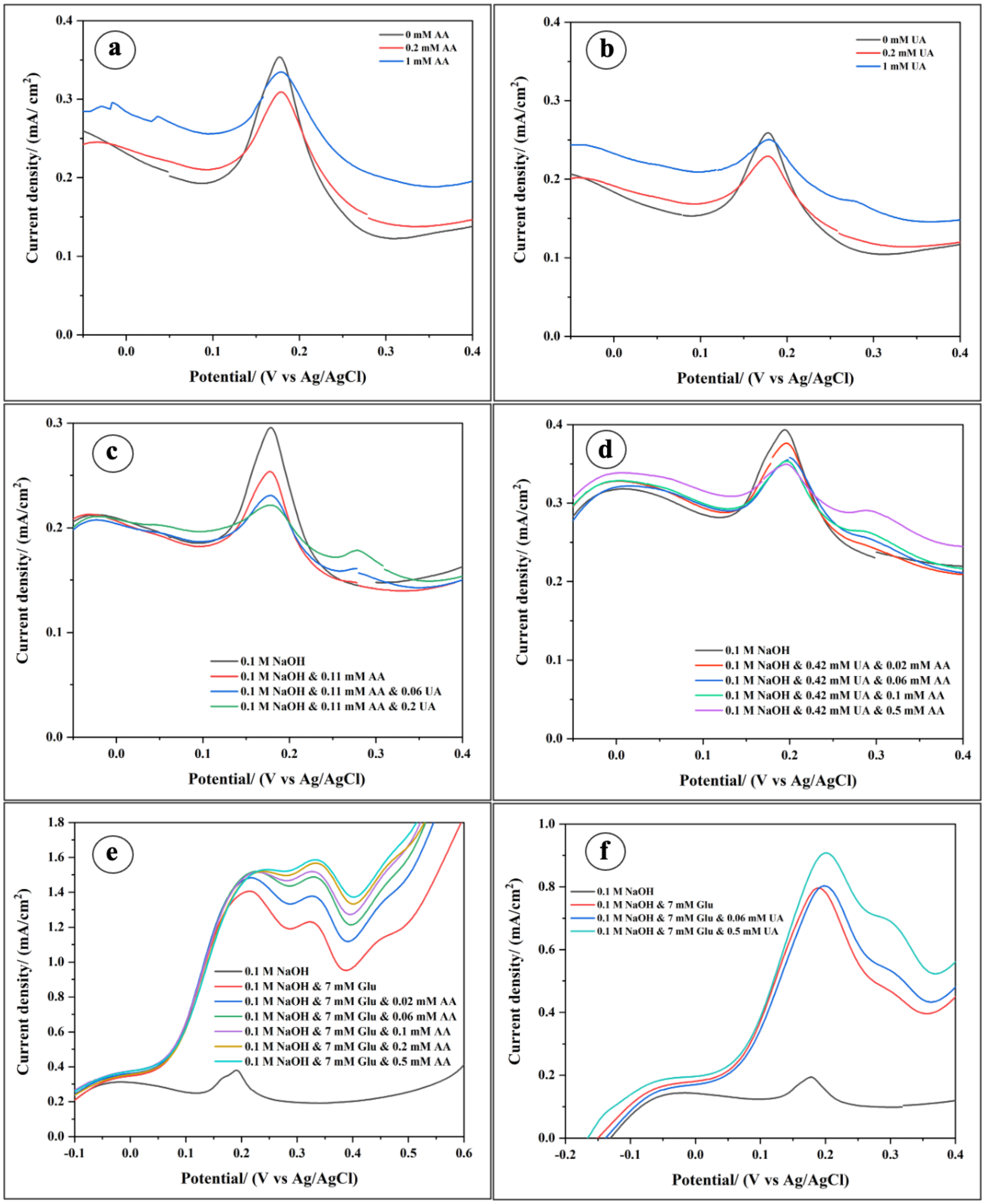

Figure 5.7: Electrochemical oxidation of a) AA; b) UA; c, d) AA+UA; e) Glu+AA and f) Glu+UA on CP/MnO_2 nanorods electrode in 0.1 M NaOH solution recorded with a scan rate of 2 mV/s

In contrast, a completely different trend is observed when Glu is in the presence of either AA or UA, as depicted in Figures 5.7e and 5.7f. At a fixed Glu concentration of 7 mM, representative of normal physiological levels, the current density of the initial peak associated with Glu oxidation to gluconolactone increases with rising AA or UA content. Specifically, with AA concentration rising from 0.02 to 0.06 mM, the current density of this peak rises, plateauing for higher AA concentrations (beyond physiological levels), as shown in Figure 5.7e. Conversely, the second peak (P2), linked to the further oxidation of gluconolactone to gluconic acid, becomes more pronounced with increasing AA concentration. With 7 mM of Glu in the presence of UA, a notable surge in the current density of P1 is observed only when UA concentration reaches 0.5 mM, while the resolution of the P2 peak remains unaffected by the presence of UA, as depicted in Figure 5.7f.

These observations suggest complex interactions between Glu, AA, and UA in the electrochemical milieu. The increase in current density of the peaks associated with Glu oxidation with increasing concentrations of AA or UA indicates a potential catalytic effect of these compounds on the electrochemical oxidation of Glu. This catalytic effect may stem from the ability of AA and UA to facilitate electron transfer processes or modify the electrode surface, enhancing the electrochemical response of Glu. The plateauing of the current density beyond physiological levels of AA suggests a saturation effect, where further increases in AA concentration do not significantly influence the electrochemical behavior of Glu. This could imply that the catalytic activity of AA reaches a maximum at those concentrations. Overall, these observations provide valuable insights into the complex electrochemical behavior of Glu in the presence of AA and UA, which could have implications for the development of electrochemical sensors or bioanalytical techniques for glucose monitoring in physiological or clinical settings. Note that in Figures 5.7e and 5.7f, the effect of adding UA and AA on the background current was evaluated, and it was found to remain unaffected across various conditions. This consistent background current ensures that the observed changes in peak currents are attributable to the electrochemical processes of the analytes rather than background interference.

Figure 5.8a outlines the distinct oxidation regions for Glu, AA, and UA, and shows that the onset potential regions of AA and UA occur at the same potential as the surface Mn redox peak, for their effects are more pronounced in the voltammogram. The LSV profiles clearly show that the onset potential region for Glu is significantly more negative compared to those for AA and UA. This highlights the faster kinetics of Glu oxidation compared to that of AA and UA. Subsequently, a mixed solution of Glu+ AA+ UA was tested to investigate the selectivity of CP/MnO_2 nanorods electrode. The normal physiological glucose concentration ranges from 4 to 7 mM, which is significantly higher than the maximum concentrations of interfering species such as AA (0.11 mM) and UA (0.42 mM). As depicted in Figure 5.8b, the introduction of 0.11 mM AA and 0.42 mM UA only results in a 7.1% increase in current compared to 7 mM glucose, indicating sufficient selectivity for the analysis of human blood[162].

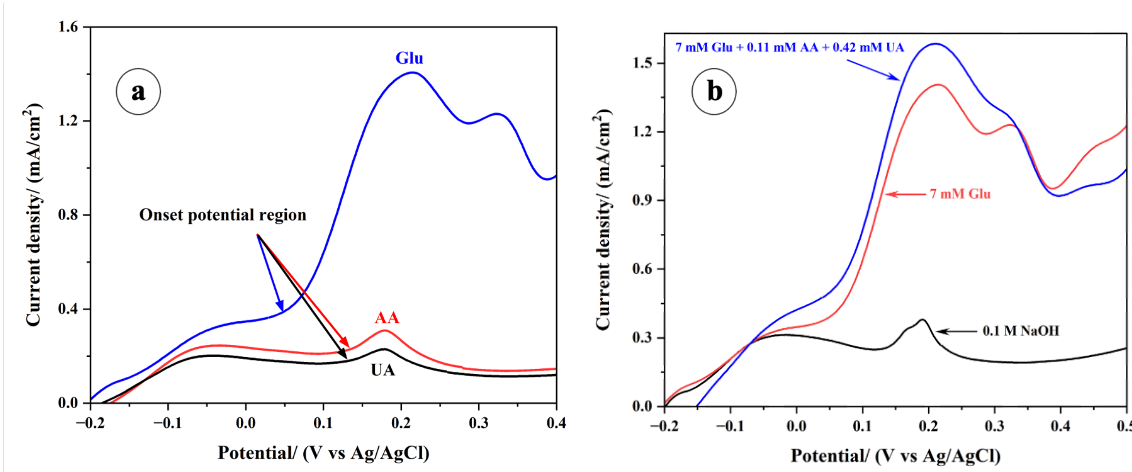

Figure 5.8: a) Individual electrochemical oxidation of Glu, AA and UA on CP/MnO_2 nanorods electrode, b) Electrochemical oxidation of ternary Glu+AA+UA on CP/MnO_2 nanorods electrode in 0.1 M NaOH solution recorded with a scan rate of 2 mV/s

Similar trend was observed at CNTs/MnO_2-NRs for interferents such as AA and UA, where no new peak emerges following individual addition of AA and UA to the electrolyte. In addition, a decrease in peak current density related to the surface redox process at MnO_2 was observed upon the addition of AA and UA, whether in electrolyte with one analyte, as shown in Figures 5.9a, 5.9b, or in electrolyte with binary solutions, as in Figure 5.9c and 5.9d. This decrease was also attributed to the slower redox reaction rates of AA and UA, and due to the increase of surface concentrations of AA and UA that further block the reactant accessibility to active sites. Upon the addition of 7 mM Glu, Figure 5.9e and 5.9f, the current peak density of P1 and P2 significantly increased. When AA or UA were then introduced, their effects on P1 were not as significant as those observed with the CP/MnO_2-NRs. Instead, the responses fluctuated with slight increases or decreases, suggesting that the carbon nanotubes help resist the influence of interfering species on glucose oxidation. However, an increase in the current density of P2 was noted with the rising of AA concentrations from 0.02 to 0.06 mM due to a possible catalytic interference of AA. Then, the peak current levels off when AA reaching the saturation. It can also be noted that the steady background current guarantees that any changes in peak current are due to the electrochemical processes of the analytes, rather than background interference.

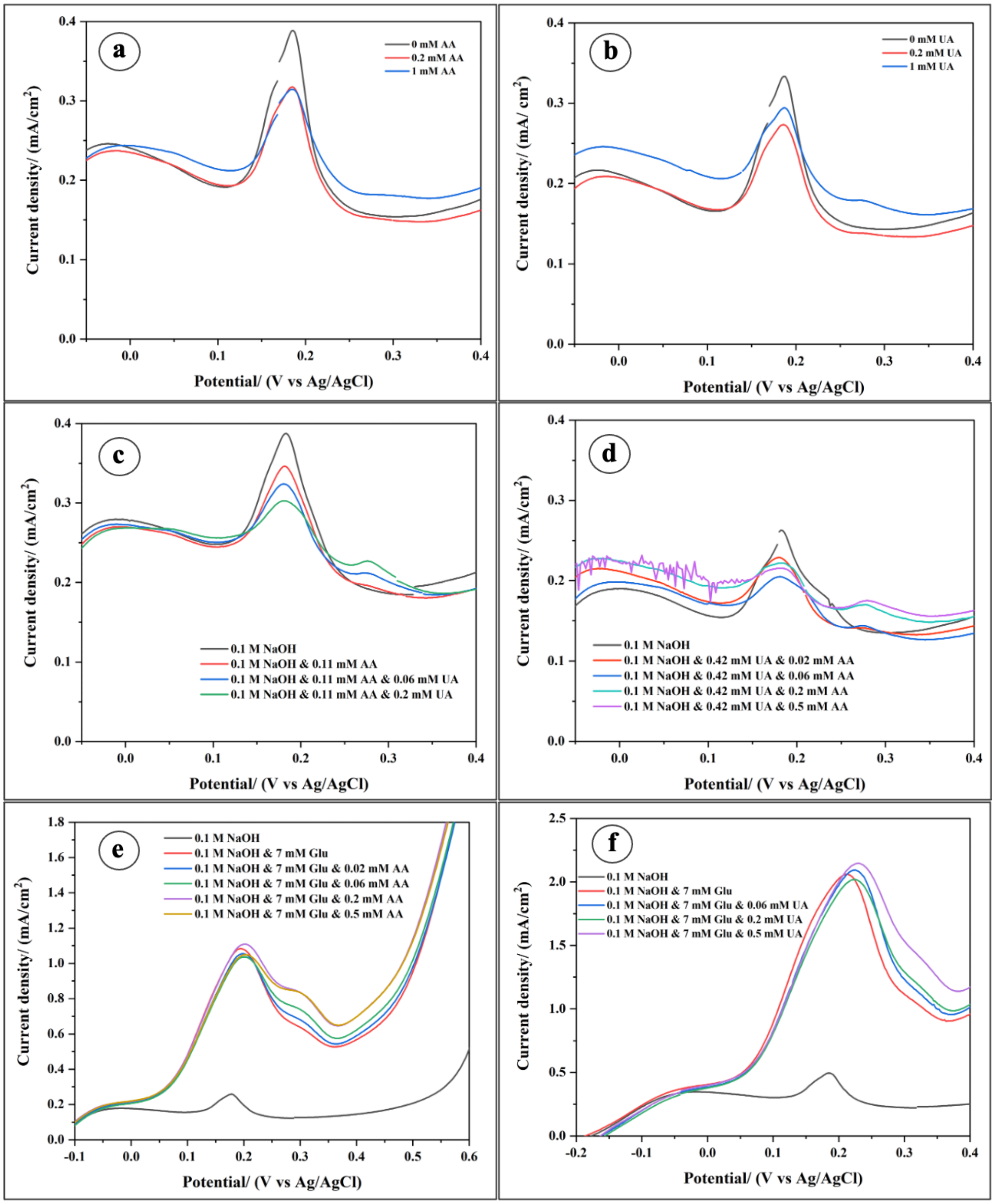

Figure 5.9: (a) Electrochemical oxidation of a) AA; b) UA; c, d) AA+UA; e) Glu+AA and f) Glu+UA on CNTs/MnO_2 nanorods electrode in 0.1 M NaOH solution recorded with a scan rate of 2 mV/s

Like CP/MnO_2-NRs electrode, the onset oxidation region for Glu at CNTs/MnO_2-NRs electrode occurs at more negative potentials than AA and UA, emphasizing the faster kinetics of Glu oxidation on MnO_2-NRs compared to the oxidation kinetics of AA and UA, as shown in Figure 5.10a.

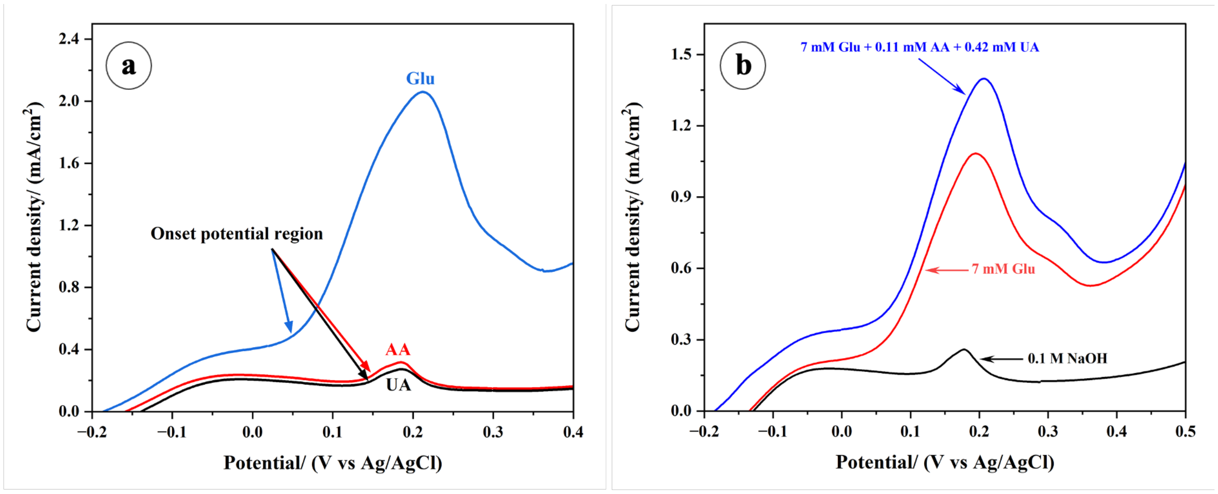

Figure 5.10: a) Individual electrochemical oxidation of Glu, AA and UA on CNTs/MnO_2 nanorods electrode, b) Electrochemical oxidation of ternary Glu+AA+UA on CNTs/MnO_2 nanorods electrode in 0.1 M NaOH solution recorded with a scan rate of 2 mV/s

Figure 5.10b reveals that the peak current response of CNTs/MnO_2-NRs in ternary solution composing of 7mM Glu+ 0.11 mM AA+ 0.42 mM UA (blue curve) has increased by about 27% compared to its response in a solution with only 7mM glucose, indicates sufficient selectivity for the analysis of human blood[162].

From the observations shown in Figures 5.8a and 5.10a, it is evident that MnO_2-NRs electrodes are excellent electrode materials for constructing non-enzymatic glucose sensors, showing greater electroactivity towards glucose (with high oxidation currents) and faster oxidation kinetics (with low onset potentials).

5.4 Conclusion

In this chapter, the electrochemical detection of glucose, ascorbic acid, and uric acid using various electrode materials, including gold, carbon paper, carbon nanotubes, and manganese dioxide nanorods has been systematically investigated. The results demonstrate that while the Au wire electrode is effective for detecting glucose, ascorbic acid, and uric acid, it suffers from overlapping oxidation potentials, particularly between glucose and uric acid, which complicates accurate detection. The CP electrode, although functional, exhibits lower sensitivity and higher detection limits for glucose compared to the CNTs and MnO_2-based electrodes. The incorporation of carbon nanotubes into the CP electrode enhances its performance, improving sensitivity and lowering the limit of detection for glucose. However, the most significant improvements were observed with the MnO_2-NRs-based electrodes. These electrodes demonstrated high sensitivity, low detection limits, and better performance in detecting glucose over a wide concentration range, exceeding physiological levels. The CNTs/MnO_2-NRs composite electrode, in particular, exhibited the highest sensitivity and lowest detection limit, making it a promising candidate for glucose sensing applications.

The work further examined the effects of ascorbic acid and uric acid on glucose detection. While these interfering substances caused a slight increase in the current densities associated with glucose oxidation, the MnO_2-NRs-based electrodes maintained a high degree of selectivity for glucose. This suggests that the electrodes could be effectively used in practical applications, where the presence of such interference might otherwise compromise the accuracy of glucose measurements. Overall, the findings of this study highlight the potential of CP/MnO_2-NRs and CNTs/MnO_2-NRs electrodes in electrochemical sensors for glucose monitoring, with considerable advantages in terms of sensitivity, selectivity, and detection limits.

6. CHRONOAMPEROMETRY STUDIES

6.1 Chronoamperometry detection of glucose at MnO_2 nanorods electrodes

When studying sensing capabilities, the choice between CV and chronoamperometry (CA) hinges on the specific application requirements, the nature of the analytes, and the sample matrix. Researchers often use both techniques complementarily for optimal results. CV is advantageous for identifying multiple analytes with different redox potentials, but it has the drawback of continuous capacitive current, which can obscure signals from low-concentration analytes. This background noise complicates the detection of target species, especially at low concentrations. Even with background subtraction, completely eliminating the capacitive current from CV is not feasible. Any remaining trace of the capacitive current, even if low, may be comparable to the current associated with the target species, as the concentrations of analytes in sensors are often very small. In contrast, CA limits capacitive current effects primarily to the beginning of the potential step, allowing for a clearer measurement of the faradaic current as these effects diminish over time[163]. This makes CA particularly effective for detecting small amounts of electroactive species, providing a cleaner signal and enhancing sensitivity. Thus, CA is often the preferred choice for real-time monitoring and applications where sensitivity is critical.

Figure 6.1a presents the CA response curves of CP/MnO_2-NRs and CNTs/MnO_2-NRs at a working voltage of 0.18 V vs Ag/AgCl, showing the effects of successive additions of different Glu concentrations from 0.5 to 20 mM in a 0.1 M NaOH solution. The potential of 0.18 V was chosen for both CP/MnO_2-NRs and CNTs/MnO_2-NRs based on practical considerations. This potential is selected just before the peak oxidation potential for glucose oxidation. It is important to note that chronoamperometry cannot be conducted at the peak position because, at this point, glucose oxidation is already occurring at maximum efficiency, and no further glucose is available for oxidation. By choosing 0.18 V, we ensure that the measurement occurs in a region where glucose is still present and being oxidized. Additionally, this potential allows for a fair comparison between the two catalysts, as it is close to the onset of glucose oxidation for both materials. This approach is widely used in electrocatalysis to compare the performance of different catalysts, ensuring that both systems are tested under similar conditions and facilitating a meaningful performance comparison.

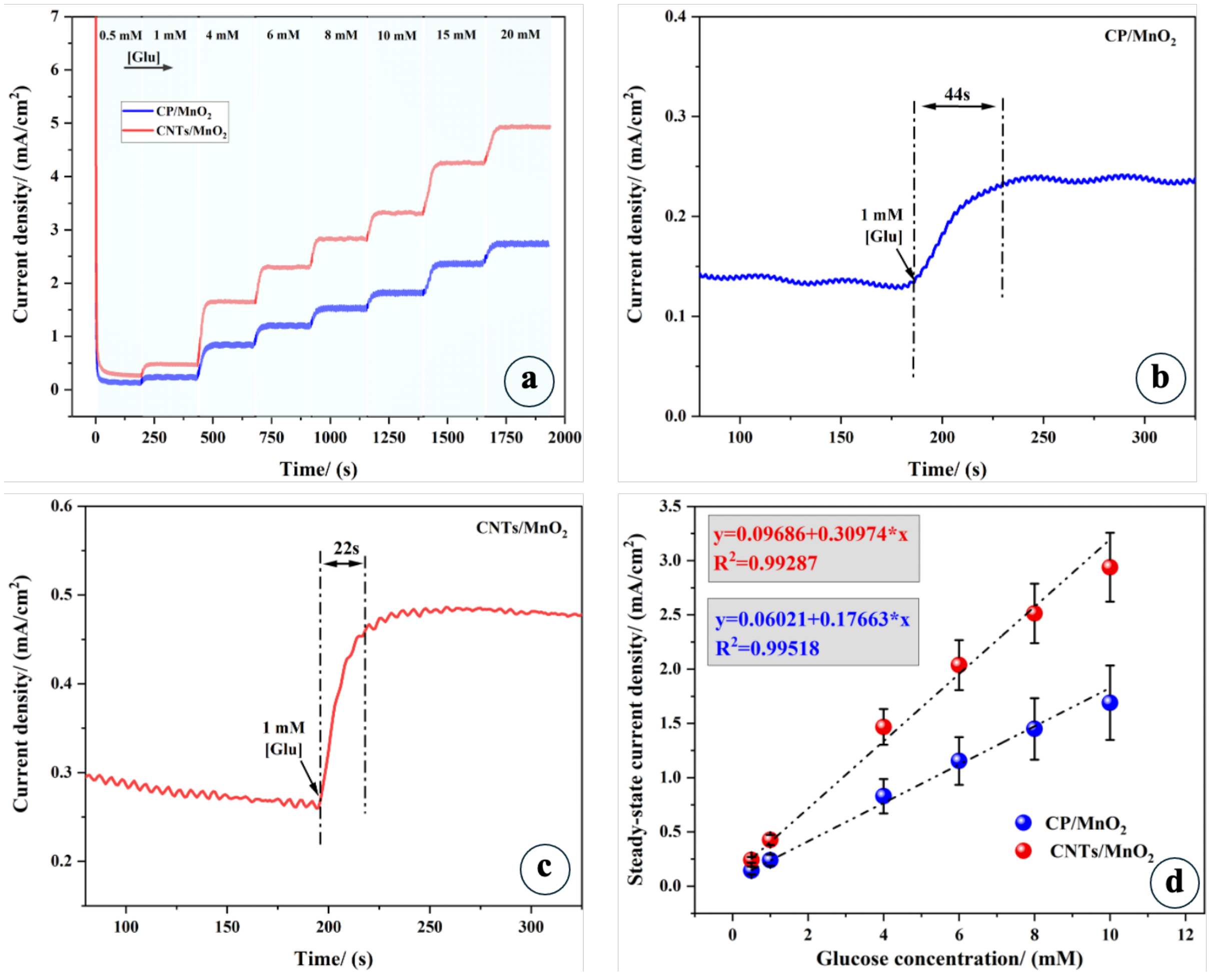

Figure 6.1: (a) Chronoamperometric (i–t) curve recorded for CP/MnO_2-NRs and CNTs/MnO_2-NRs electrodes for various concentrations of Glu (0.5 mM–20 mM) in 0.1 M NaOH solution. Response time for glucose detection: (b) CP/MnO_2-NRs electrode, and (c) CNTs/MnO_2-NRs electrode. (d) Steady-state current density vs [Glu] calibration plot

Time response in sensing refers to the speed at which a sensor detects and responds to changes in the concentration of an analyte, such as glucose. It is typically characterized by the time it takes for the sensor to reach a steady signal. A fast time response is critical in applications requiring real-time monitoring, such as in clinical diagnostics for diabetes, where timely feedback on glucose levels is necessary for effective insulin management. A slow time response can lead to delayed detection, inaccurate readings, or insufficient data for decision-making, compromising the efficiency of systems that depend on real-time information. Therefore, a sensor's fast time response is essential for providing reliable, timely data, particularly in fields like medical diagnostics, where quick, accurate decisions are necessary.

The time-current graphs (Figure 6.1a) demonstrate a stepwise increase in current corresponding to the incremental addition of Glu. The CP/MnO_2-NRs electrode responds to Glu in 44s (Figure 6.1b), while the CNTs/MnO_2-NRs electrode has a quicker response time of 22 seconds (Figure 6.1c). Both electrodes reach steady-state current and show high sensitivity to changes in Glu levels. The CNTs/MnO_2-NRs electrode's efficiency stems from to the excellent conductivity and larger surface area of CNTs[139], enhancing charge transfer and interaction with glucose. Additionally, the unique structural properties of CNTs likely improve electron transport and catalytic activity, contributing to its faster response time. This is supported by the calibration curve showing the sensor's response current versus Glu concentrations, as shown in Figure 6.1d. Both CP/MnO_2-NRs and CNTs/MnO_2-NRs demonstrate distinct linear relationships across a concentration range from 0.5 mM to 10 mM, outside the physiological levels (3–8 mM), with strong correlations indicated by coefficients of determination (R^2) of 0.9951 for CP/MnO_2-NRs electrode and 0.9928 for CNTs/MnO_2-NRs electrode. The sensitivity of CP/MnO_2-NRs towards Glu, as determined through linear regression (Figure 6.1d) is estimated to be 176.62 $\mu A\ mM^{-1}\ cm^{-2}$, while the sensitivity of CNTs/MnO_2-NRs is much higher, at 309.73 $\mu A\ mM^{-1}\ cm^{-2}$. Notably, both electrodes exhibit a similar LOD of 0.19 mM at a signal-to-noise ratio of 3. However, the enhanced sensitivity of the CNTs/MnO_2-NRs offers a significant advantage, enabling more precise and faster detection of Glu concentrations. While both materials can effectively detect low Glu concentrations, the superior sensitivity of CNTs/MnO_2-NRs positions them as the preferred choice for sensitive electrochemical sensing applications.

6.2 Chronoamperometry detection of interfering species at MnO_2 nanorods electrodes and their effects on glucose sensing

Oxidizable compounds, UA and AA, commonly co-exist with glucose on physiological fluids and can interfere with glucose detection in various sensors, including non-enzymatic glucose sensors, leading to inaccurate measurements. The normal physiological level of Glu approximately 3–8 mM is significantly higher than the concentrations of interfering species like UA (0.18–0.42 mM) and AA (0.02–0.08 mM). To evaluate the anti-interference capability of the CP/MnO_2-NRs and CNTs/MnO_2-NRs sensors, we focused on both low and elevated concentrations of AA (0.02 mM & 0.08 mM) and UA (0.18 mM & 0.42 mM) that can occur in physiological conditions. Figures 6.2a and 6.2b present comparative interference studies of CP/MnO_2-NRs and CNTs/MnO_2-NRs. These studies involved the successive addition of low concentrations of AA (0.02 mM) and UA (0.18 mM), as well as elevated concentrations of AA (0.08 mM) and UA (0.42 mM), to a solution containing 7 mM glucose. Notably, there was no significant change in current densities for either electrode, particularly for the CNTs/MnO_2-NRs, where the current increase remained below 3% across all interference concentrations tested, as demonstrated in Figure 6.2c.

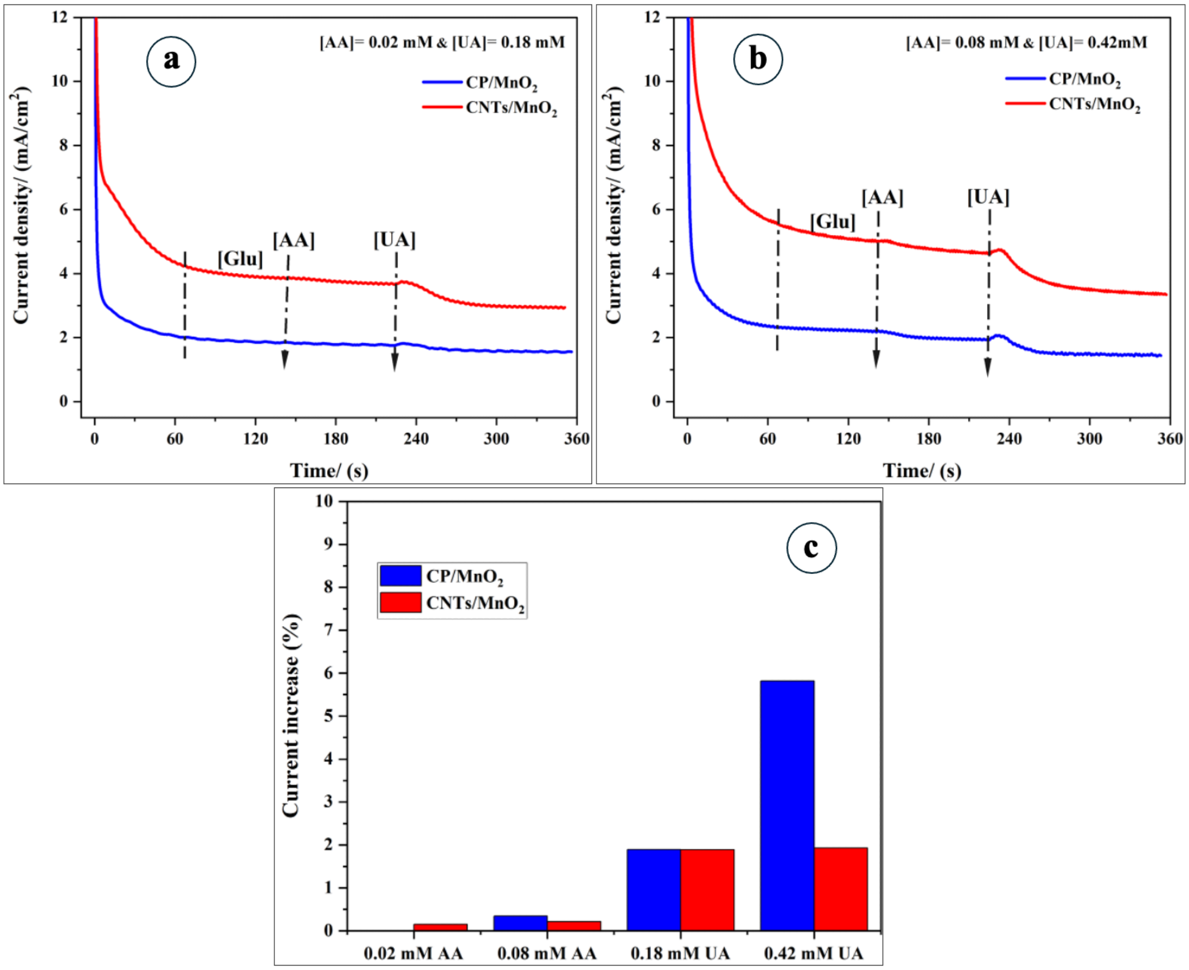

Figure 6.2: Chronoamperometric (i–t) curve recorded for CP/MnO_2-NRs and CNTs/MnO_2-NRs electrodes for 7 mM Glu after addition of: (a) low concentrations of AA (0.02 mM) & UA (0.18 mM); (b) high concentrations of AA (0.08 mM) & UA (0.42 mM). (c) Percentage increase in steady-state current following the addition of UA and AA

These observations indicate that both the CP/MnO_2-NRs and CNTs/MnO_2-NRs electrodes exhibit strong selectivity toward glucose in the presence of potential interferents, such AA and UA. The minimal change in current densities for the CNTs/MnO_2-NRs implies a high level of resistance to interference, making it a promising candidate for reliable Glu detection in complex biological samples.

6.3 Anti-fouling chronoamperometry test against KCl

KCl can also potentially foul (or poison) electrodes by adhering to their surfaces, which can compromise sensor performance and selectivity. As a salt, KCl can also alter the ionic strength of the solution, potentially affecting the electrochemical response and stability of the sensor. In physiological blood, KCl concentrations typically range from approximately 3.5 to 5.0 mM[164-165], although individual variations in health and hydration can lead to fluctuations in these levels. Figure 6.3 shows the current responses of Glu at the CNTs/MnO_2-NRs upon the successive addition of KCl concentrations of 1 mM, 3 mM, and 5 mM. Remarkably, the current response remains largely unaffected by KCl, even the highest concentration of 5 mM. This resilience underscores the anti-fouling properties of the CNTs/MnO_2-NRs electrodes, highlighting their effectiveness in maintaining stable sensor performance in the presence of KCl.

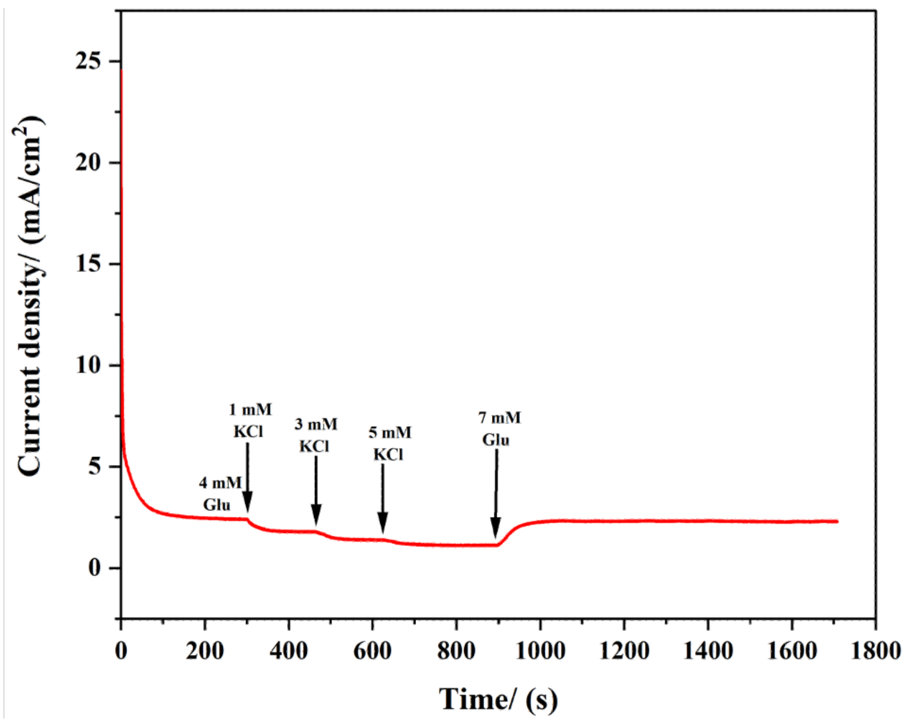

Figure 6.3: Chronoamperometric curve after addition of various concentrations of KCl

6.4 Durability/ stability test using chronoamperometry

The medium-term stability of CNTs/MnO_2-NRs electrode was first evaluated by CV in the presence of 7 mM Glu, using a scan rate of 20 mV/s over 1000 cycles (equivalent to 25 hours). As shown in Figure 6.4a, the CNTs/MnO_2-NRs electrode exhibited excellent cyclability, with no significant decrease in current density throughout the duration of the test. To further assess the long-term durability of the electro-catalytic performance of the as-prepared electrodes, oxidation of Glu was conducted with chronoamperometry at a constant voltage of 0.18 V vs Ag/AgCl. Figure 6.4b presents a comparison of the current responses of the CP/MnO_2-NRs electrode and the CNTs/MnO_2-NRs electrode when exposed to 7 mM glucose in 0.1 M NaOH over a period of 7 days. A chronoamperogram for Glu oxidation typically shows a sharp initial increase in current, indicating rapid oxidation at the electrode surface. This is followed by a sharp decline in current, which is often attributed to the buildup of reaction intermediates, particularly hydrogen peroxide, that progressively block the active sites on the electrode[166-168]. After this initial drop, the current stabilizes at a lower, steady-state value, reflecting a dynamic equilibrium between glucose oxidation and the inhibitory effects of the accumulated intermediates. Despite some blockage of active sites, electrochemical activity continues, albeit at a reduced rate, as indicated by the steady-state current.

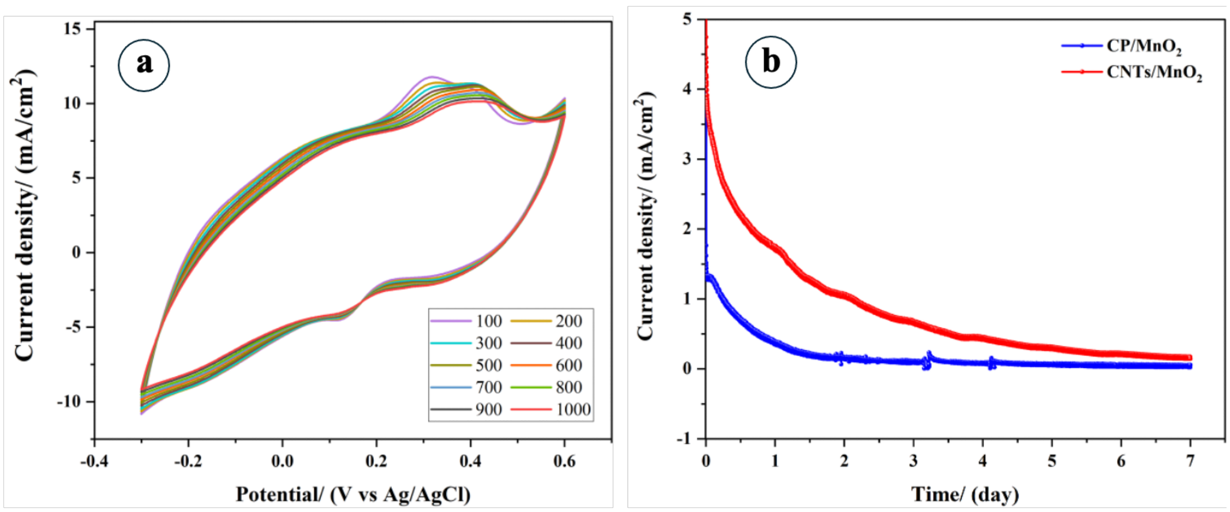

Figure 6.4: (a) CVs from stability studies upon 1000 cycles at 20 mV/s recorded in 7 mM Glu. The numbers indicate the cycle intervals (every 100 cycles). (b) Chronoamperometric long-term durability studies over 7 days in 7 mM Glu at a constant potential of 0.18 V vs Ag/AgCl

The data shown in Figure 6.4b highlight the remarkable operational stability of the CNTs/MnO_2-NRs electrode for amperometric glucose detection. In contrast, the CP/MnO_2-NRs electrode demonstrated rapid deactivation, likely due to the accumulation of intermediate compounds generated during glucose oxidation, which tended to coat the electrode surface. The superior performance of the CNTs/MnO_2-NRs electrode can be attributed to its significantly larger electroactive surface area, which not only enhances glucose oxidation efficiency but also helps mitigate surface poisoning by adsorbed intermediates, thus maintaining stable performance over extended periods of operation.

6.5 Conclusion

In this chapter, chronoamperometry was employed to evaluate the glucose detection performance of MnO_2 nanorods electrodes, both with and without carbon nanotube modification. The study demonstrated that both CP/MnO_2-NRs and CNTs/MnO_2-NRs electrodes exhibited excellent sensitivity to glucose, with the CNTs/MnO_2-NRs electrodes showing superior response times and sensitivity, particularly in the range of 0.5 to 10 mM glucose concentrations. The CNTs/MnO_2-NRs electrodes responded more quickly and exhibited enhanced sensitivity, with a sensitivity of 309.73 $\mu A\ mM^{-1}\ cm^{-2}$ compared to 176.62 $\mu A\ mM^{-1}$

cm^{-2} for CP/MnO_2-NRs. Both electrode systems displayed strong linearity and a low limit of detection of 0.19 mM.

Additionally, both electrode types demonstrated remarkable selectivity and anti-interference properties in the presence of common interfering species, such as uric acid and ascorbic acid, with the CNTs/MnO_2-NRs electrode showing minimal change in current in the presence of even high concentrations of these interferents. The CNTs/MnO_2-NRs electrodes also exhibited robust anti-fouling properties, maintaining stable performance even when exposed to potassium chloride (KCl), which could otherwise compromise sensor function.

Furthermore, durability tests confirmed that the CNTs/MnO_2-NRs electrode demonstrated excellent long-term stability, maintaining stable electrochemical performance even after extended use, unlike CP/MnO_2-NRs, which exhibited rapid deactivation. The superior performance of the CNTs/MnO_2-NRs electrode was attributed to its larger electroactive surface area, which allowed for more efficient glucose oxidation and better resistance to surface fouling and poisoning.

In conclusion, the CNTs/MnO_2-NRs electrode outperforms the CP/MnO_2-NRs electrode in terms of response time, sensitivity, anti-interference, anti-fouling, and long-term stability, making it a promising candidate for reliable and precise glucose detection in complex biological samples.

7 CONCLUSIONS AND PERSPECTIVES

7.1 Conclusions

This thesis has addressed the development of non-enzymatic glucose sensors, with a particular focus on designing catalysts that exhibit high sensitivity, selectivity, and antifouling capabilities. In this concluding chapter, the main findings are summarized, their implications discussed, and avenues for future research are outlined.

In chapter 3, the SEM analysis confirmed the successful deposition of CNTs onto the CP substrate, revealing a uniform and continuous coating across the CP surface. The SEM images of CP/MnO_2 and CNTs/MnO_2 samples further demonstrated dense and homogeneous coverage with MnO_2 nanorods (NRs), with an average diameter of approximately 200 nm. These observations validate the effective incorporation of both CNTs and MnO_2 catalysts onto the CP substrates. XRD analysis of CP/MnO_2-NRs and CNTs/MnO_2-NRs revealed distinct diffraction peaks matching the cryptomelane-type KMn_8O_{16} phase, confirming the successful deposition of MnO_2 in its stable α-MnO_2 crystalline structure. Complementary Raman spectroscopy analysis further supported this, with characteristic vibrational peaks attributed to α-MnO_2, observed in both MnO_2-samples. Notably, the D and G bands typically associated with carbon materials were absent in the Raman spectra of CP/MnO_2-NRs and CNTs/MnO_2-NRs, likely due to the thick MnO_2 layer masking the underlying carbon signals.

In chapter 4, the double layer capacitance, C_{dl} values for CP/MnO_2-NRs and CNTs/MnO_2-NRs electrodes were determined from the non-faradaic regions of the cyclic voltammograms. The CNTs/MnO_2-NRs electrode exhibited a C_{dl} value of approximately 2.8 times higher than that of the CP/MnO_2-NRs, indicating a significantly enhanced electrochemically active surface. This improvement is attributed to the increased surface area and superior electrical conductivity provided by the CNTs, which facilitate more efficient ion diffusion and charge accumulation. Additionally, the CNTs/MnO_2-NRs electrode showed markedly higher values for both the *ECSA* and roughness factor (*RF*), reflecting its superior electrochemical performance. These enhancements are the result of a synergistic interaction between the CNTs and MnO_2 nanorods, which promotes improved ion adsorption and faster electron transfer kinetics. Collectively, these properties significantly boost the electrode's potential in high-performance electrochemical sensing applications.

In chapter 5, the electrochemical detection of glucose, ascorbic acid, and uric acid was systematically investigated using a range of electrode materials, including gold, carbon paper, carbon nanotubes, and manganese dioxide nanorods. The results showed that while the Au wire electrode is capable of detecting all three analytes, it suffers from overlapping oxidation potentials, particularly between glucose and uric acid, which hampers selective detection. The CP electrode, though functional, demonstrated low sensitivity and high detection limits for glucose compared to the CNTs and MnO_2-based electrodes. The incorporation of CNTs into the CP electrode significantly enhanced electrode performance by increasing sensitivity and lowering the detection limit for glucose. However, the most pronounced improvements were observed with MnO_2-NRs-based electrodes. These demonstrated high sensitivity, low detection limits, and consistent performance across a wide glucose concentration range, including levels exceeding physiological norms. Notably, the CNTs/MnO_2-NRs composite electrode demonstrated the highest sensitivity and the lowest detection limit among all materials tested, highlighting its potential as a highly effective platform for non-enzymatic glucose sensing applications.

The study also investigated the influence of common interfering species, specifically ascorbic acid and uric acid, on the electrochemical detection of glucose. Although, the presence of these substances resulted in a slight increase in current density during glucose oxidation, the MnO_2-NRs-based electrodes demonstrated a high degree of selectivity toward glucose. This indicates their robustness in distinguishing glucose signals even in the presence of electroactive interferents, a critical factor for practical sensing applications. These results underscore the potential of both CP/MnO_2-NRs and CNTs/MnO_2-NRs electrodes as promising candidates for non-enzymatic electrochemical glucose sensors. Their strong performance marked by high sensitivity, excellent selectivity, and low detection limits positions them as valuable materials for reliable glucose monitoring in complex biological environments.

In chapter 6, chronoamperometry was employed to assess the glucose sensing performance of MnO_2 nanorods electrodes, both with and without carbon nanotube modification. The results demonstrated that both CP/MnO_2-NRs and CNTs/MnO_2-NRs electrodes exhibited excellent sensitivity and reliable response toward to glucose. Notably, the CNTs/MnO_2-NRs electrodes outperformed their unmodified counterparts, particularly within the glucose concentration range of 0.5 to 10 mM, which encompasses and exceeds typical physiological levels. The CNTs/MnO_2-NRs electrodes showed significant response times and higher sensitivity, achieving a sensitivity of 309.73 $\mu A\ mM^{-1}\ cm^{-2}$, compared to 176.62 $\mu A\ mM^{-1}\ cm^{-2}$ for the CP/MnO_2-NRs electrodes. Both electrode systems exhibited strong linearity across the tested concentration range and demonstrated a low limit of detection (LOD) of 0.19 mM.

Additionally, both electrode types demonstrated remarkable selectivity and anti-interference capabilities in the presence of common electroactive species, such as uric acid and ascorbic acid. The CNTs/MnO_2-NRs electrode, in particular, demonstrated minimal variation in current response, even when exposed to high concentrations of these potential interferents. Moreover, the CNTs/MnO_2-NRs electrodes showed robust anti-fouling properties, maintaining consistent performance despite exposure to potassium chloride (KCl), a compound known to potentially degrade sensor performance.

Furthermore, durability tests confirmed that the CNTs/MnO_2-NRs electrode demonstrated excellent long-term stability, maintaining stable electrochemical performance even after extended use. In contrast, the CP/MnO_2-NRs exhibited noticeable performance degradation and rapid deactivation under similar testing conditions. The enhanced durability and stability of the CNTs/MnO_2-NRs electrode are attributed to its larger electroactive surface area, which facilitates more efficient glucose oxidation and provides greater resistance to surface fouling and poisoning.

In summary, this thesis successfully developed and evaluated non-enzymatic glucose sensors based on MnO_2 nanorods and carbon nanotube-modified electrodes, demonstrating significant improvements in sensitivity, selectivity, antifouling, and long-term stability. The CNTs/MnO_2-NRs composite electrode consistently outperformed its counterparts, showing excellent performance across a wide glucose concentration range, even in the presence of interfering species and under extended use. These findings underscore the strong potential of CNTs/MnO_2-NRs as a robust and reliable platform for practical, high-performance glucose sensing applications.

7.2 Perspectives

Future work will focus on the design and fabrication of a nanostructured electrode based on CNTs/MnO_2 nanorods integrated onto a screen-printed electrode (SPE) platform, intended to serve as the working electrode for a practical electrochemical glucose sensing device. This electrode will undergo testing in human serum samples, followed by direct comparisons with existing commercial glucose sensors to evaluate its real-world applicability and performance.

We acknowledge that the current use of NaOH as the electrolyte does not fully replicate the physiological conditions, particularly in terms of pH and ionic complexity. While NaOH provides a simplified and controlled environment that enhances glucose oxidation and improves signal response suitable for fundamental electrochemical characterization, it does not reflect the physiological environment of the human body, where the pH is approximately 7.4 and the ionic milieu includes biologically relevant species such as Na^+, K^+, Cl^-, and Ca^{2+}. Recognizing this limitation, future work will involve transitioning to more physiologically relevant testing media, such as phosphate-buffered saline (PBS) and artificial interstitial fluid. These media more accurately mimic the ionic composition and pH of the human body, and will allow for a more comprehensive evaluation of the sensor’s long-term stability, accuracy, and biocompatibility. These studies will be essential in advancing the practical deployment of CNTs/MnO_2-based sensors in real-world and potentially implantable glucose monitoring applications.

We also acknowledge the potential issue of performance drift during long-term electrochemical measurements, a critical challenge for continuous glucose monitoring applications. To address this, future work will focus on optimizing sensor stability and systematically investigating the long-term performance behavior of the electrodes under continuous operation. This effort will aim to identify the underlying causes of drift and develop strategies, to mitigate its impact. Approaches under consideration include surface engineering of the electrode to minimize degradation, as well as the development of more robust materials such as advanced CNTs/MnO_2 nanocomposites with enhanced structural and chemical stability. Additionally, the integration of adaptive data correction algorithms, including periodic calibration protocols and real-time baseline adjustment mechanisms, will be explored to compensate for any signal fluctuations observed during extended usage. These combined strategies are expected to significantly improve the reliability and longevity of the sensor for practical, real-time glucose monitoring.

Moreover, two additional directions may be considered in the future to further advance the practical applicability of the developed sensor. The first involves the integration of the sensor into wearable or portable electronic platforms. Embedding the CNTs/MnO_2-based electrode into flexible, low-power systems capable of wireless data transmission could enable real-time, non-invasive glucose monitoring. Developing compact electronics and incorporating the sensor into smart wearable devices such as patches or smartphone-connected modules may significantly improve accessibility and usability in daily life.

The second potential direction is the evaluation of biocompatibility and cytotoxicity of the sensor materials. For in vivo or implantable applications, it will be essential to assess the biological safety of the electrode, particularly the MnO_2 nanorods and their composites. Future studies may include in vitro testing with cell cultures, as well as surface modifications using biocompatible coatings to minimize immune response and enhance tissue compatibility. These investigations would be critical for translating the sensor into clinical and biomedical contexts.

We are entering a new era where the convergence of materials science, biosensing, and artificial intelligence (AI) is transforming the landscape of healthcare technologies. As such, a third direction that may be considered for future development is the integration of AI and machine learning (ML) algorithms into the glucose sensing system. AI has the potential to revolutionize the way electrochemical data is processed—enabling real-time signal analysis, dynamic calibration, and predictive modeling for more accurate and adaptive glucose monitoring.

By training machine learning models on complex datasets, it becomes possible to enhance sensor accuracy, correct for drift, reduce noise, and personalize glucose readings based on individual user profiles. Moreover, AI can support early detection of abnormal glucose patterns, automate baseline adjustments, and improve decision-making in clinical and at-home settings. The synergy between intelligent data processing and advanced sensing materials such as CNTs/MnO_2 nanocomposites could pave the way for the next generation of smart, connected, and self-optimizing glucose monitoring devices.

8 BIBLIOGRAPHY

1. Nurkolis, F.; Kurniawan, R.; Wiyarta, E.; Syahputra, R. A.; Surya, R.; Taslim, N. A.; Tallei, T. E.; Tjandrawinata, R. R.; Adashi, E. Y.; Kim, B., Unraveling Light-Activated Insulin Action in Regulating Blood Glucose: New Photoactivatable Insight as a Novel Modality in Diabetes Management. *Molecules* 2024, *29* (6).

2. Tan, S. Y.; Mei Wong, J. L.; Sim, Y. J.; Wong, S. S.; Mohamed Elhassan, S. A.; Tan, S. H.; Ling Lim, G. P.; Rong Tay, N. W.; Annan, N. C.; Bhattamisra, S. K.; Candasamy, M., Type 1 and 2 diabetes mellitus: A review on current treatment approach and gene therapy as potential intervention. *Diabetes & metabolic syndrome* 2019, *13* (1), 364-372.

3. Chadt, A.; Al-Hasani, H., Glucose transporters in adipose tissue, liver, and skeletal muscle in metabolic health and disease. *Pflugers Archiv: European journal of physiology* 2020, *472* (9), 1273-1298.

4. Hendriks, A. M.; Schrijnders, D.; Kleefstra, N.; de Vries, E. G. E.; Bilo, H. J. G.; Jalving, M.; Landman, G. W. D., Sulfonylurea derivatives and cancer, friend or foe? *European journal of pharmacology* 2019, *861*, 172598.

5. Alila Medical Media, Diabetes Type 1 and Type 2, Animation. In *Diabetes*, Alila Medical Media,: 2014.

6. Diabetes Québec's team of health professionals Target blood glucose levels. https://www.diabete.qc.ca/en/diabetes/diabetes-management/target-blood-glucose-levels-2/ (accessed 2025).

7. Imran, S. A.; Agarwal, G.; Bajaj, H. S.; Ross, S., Targets for Glycemic Control. *Canadian journal of diabetes* 2018, *42 Suppl 1*, S42-S46.

8. Diabetes Québec Team of Health Care Professionals Hypoglycemia in an individual with diabetes. https://www.diabete.qc.ca/en/hypoglycemia-low-blood-sugar-in-an-individual-with-diabetes/ (accessed 2025).

9. Diabetes Québec Team of Health Care Professionals Understanding and treating hyperglycemia. https://www.diabete.qc.ca/en/diabetes/diabetes-management/hyperglycemia/understanding-and-treating-hyperglycemia/ (accessed 2025).

10. Cleveland Clinic Hypoglycemia (Low Blood Sugar). https://my.clevelandclinic.org/health/diseases/11647-hypoglycemia-low-blood-sugar#diagnosis-and-tests (accessed 2025).

11. Team of Diabetes Québec health professionals Diagnosis of type 2 diabetes. https://www.diabete.qc.ca/en/diabetes/information-on-diabetes/type-2-diabetes/ (accessed 2025).

12. Punthakee, Z.; Goldenberg, R.; Katz, P., Definition, Classification and Diagnosis of Diabetes, Prediabetes and Metabolic Syndrome. *Canadian journal of diabetes* 2018, *42 Suppl 1*, S10-S15.

13. Ekoe, J. M.; Goldenberg, R.; Katz, P., Screening for Diabetes in Adults. *Canadian journal of diabetes* 2018, *42 Suppl 1*, S16-S19.

14. Mulyani, D. E.; Maksum, I. P., Detection of Biomarker Using Aptasensors to Determine the Type of Diabetes. *Diagnostics (Basel)* 2023, *13* (12).

15. National Center for Chronic Disease Prevention and Health Promotion; Diabetes About Insulin Resistance and Type 2 Diabetes. https://www.cdc.gov/diabetes/about/insulin-resistance-type-2-diabetes.html (accessed 2025).

16. Alila Medical Media, Insulin action and diabetes type 1 and 2. Alila Medical Media: 2023; Vol. 2000x2500 pixels.

17. International Diabetes Federation. IDF Diabetes Atlas, 10th edn. Brussels, Belgium: International Diabetes Federation, 2021. http://www.diabetesatlas.org (accessed 2024).

18. Calder, S. New diabetes rates released with urgent plea for governments to implement national diabetes strategy. https://www.diabetes.ca/media-room/press-releases/new-diabetes-rates-released-with-urgent-plea-for-governments-to-implement-national-diabetes-strategy (accessed 2025).

19. Diabetes Québec Statistics on diabetes. https://www.diabete.qc.ca/en/diabetes/information-on-diabetes/myths-and-statistics/ (accessed 2025).

20. Hwang, D. W.; Lee, S.; Seo, M.; Chung, T. D., Recent advances in electrochemical non-enzymatic glucose sensors - A review. *Analytica chimica acta* 2018, *1033*, 1-34.

21. Hang, C.; Qin, Y.; Tian, G.; Hu, J.; Li, W.; Wu, J., New Insight into the Mechanism of Simultaneous Determination of Ascorbic Acid, Dopamine, and Uric Acid with Graphene Encapsulated CoFe Alloys Electrochemical Sensor. *Advanced Materials Interfaces* 2022, *9* (21).

22. Toghill, K. E.; Compton, R. G., Electrochemical Non-enzymatic Glucose Sensors: A Perspective and an Evaluation. *International Journal of Electrochemical Science* 2010, *5* (9), 1246-1301.

23. Gupta, S.; Tai, N.-H., Carbon nanomaterials and their composites for electrochemical glucose biosensors: A review on fabrication and sensing properties. *Journal of the Taiwan Institute of Chemical Engineers* 2024, *154*.

24. Cooper, L. B.; Savarese, G.; Carrero, J. J.; Szabo, B.; Jernberg, T.; Jonsson, A.; Dahlbom, C.; Dahlstrom, U.; Larson, A.; Lund, L. H., Clinical and research implications of serum versus plasma potassium measurements. *European journal of heart failure* 2019, *21* (4), 536-537.

25. Kangkamano, T.; Numnuam, A.; Limbut, W.; Kanatharana, P.; Thavarungkul, P., Chitosan cryogel with embedded gold nanoparticles decorated multiwalled carbon nanotubes modified electrode for highly

sensitive flow based non-enzymatic glucose sensor. *Sensors and Actuators B: Chemical* 2017, *246*, 854-863.

26. Hassan, M. H.; Vyas, C.; Grieve, B.; Bartolo, P. Recent Advances in Enzymatic and Non-Enzymatic Electrochemical Glucose Sensing *Sensors* [Online], 2021.

27. Adeel, M.; Rahman, M. M.; Caligiuri, I.; Canzonieri, V.; Rizzolio, F.; Daniele, S., Recent advances of electrochemical and optical enzyme-free glucose sensors operating at physiological conditions. *Biosensors and Bioelectronics* 2020, *165*, 112331.

28. Han, Q.; Wang, H.; Wang, J., Multi-Mode/Signal Biosensors: Electrochemical Integrated Sensing Techniques. *Advanced Functional Materials* 2024, *34* (39).

29. Shanbhag, M. M.; Manasa, G.; Mascarenhas, R. J.; Mondal, K.; Shetti, N. P., Fundamentals of bio-electrochemical sensing. *Chemical Engineering Journal Advances* 2023, *16*.

30. Naikoo, G. A.; Salim, H.; Hassan, I. U.; Awan, T.; Arshad, F.; Pedram, M. Z.; Ahmed, W.; Qurashi, A., Recent Advances in Non-Enzymatic Glucose Sensors Based on Metal and Metal Oxide Nanostructures for Diabetes Management- A Review. *Frontiers in chemistry* 2021, *9*, 748957.

31. Huang, Q.; Chen, J.; Zhao, Y.; Huang, J.; Liu, H., Advancements in electrochemical glucose sensors. *Talanta* 2025, *281*, 126897.

32. Wang, J., Electrochemical Glucose Biosensors. *Chem. Rev* 2008, *108*, 814-825.

33. Tee, S. Y.; Teng, C. P.; Ye, E., Metal nanostructures for non-enzymatic glucose sensing. *Materials science & engineering. C, Materials for biological applications* 2017, *70* (Pt 2), 1018-1030.

34. Teymourian, H.; Barfidokht, A.; Wang, J., Electrochemical glucose sensors in diabetes management: an updated review (2010–2020). *Chemical Society Reviews* 2020, *49* (21), 7671-7709.

35. Jiang, Z.; Shangguan, Y.; Zheng, Q., Ferrocene-Modified Polyelectrolyte Film-Coated Electrode and Its Application in Glucose Detection. *Polymers* 2019, *11* (3).

36. Lin, M. J.; Wu, C. C.; Chang, K. S., Effect of Poly-l-Lysine Polycation on the Glucose Oxidase/Ferricyanide Composite-Based Second-Generation Blood Glucose Sensors. *Sensors (Basel)* 2019, *19* (6).

37. Bennett, R.; Leech, D., Improved operational stability of mediated glucose enzyme electrodes for operation in human physiological solutions. *Bioelectrochemistry* 2020, *133*, 107460.

38. Jayakumar, K.; Bennett, R.; Leech, D., Electrochemical glucose biosensor based on an osmium redox polymer and glucose oxidase grafted to carbon nanotubes: A design-of-experiments optimisation of current density and stability. *Electrochimica Acta* 2021, *371*.

39. Morshed, J.; Nakagawa, R.; Hossain, M. M.; Nishina, Y.; Tsujimura, S., Disposable electrochemical glucose sensor based on water-soluble quinone-based mediators with flavin adenine dinucleotide-dependent glucose dehydrogenase. *Biosensors & bioelectronics* 2021, *189*, 113357.

40. Zhu, H.; Li, L.; Zhou, W.; Shao, Z.; Chen, X., Advances in non-enzymatic glucose sensors based on metal oxides. *Journal of materials chemistry. B* 2016, *4* (46), 7333-7349.

41. Moumene, M.; Tabet-Aoul, A.; Gougis, M.; Rochefort, D.; Mohamedi, M., Laser Pulse Deposited Nanosized Ceria for Direct Electron Transfer of Glucose Oxidase. *International Journal of Electrochemical Science* 2014, *9* (1), 176-184.

42. Lee, H.; Reginald, S. S.; Sravan, J. S.; Lee, M.; Chang, I. S., Advanced strategies for enzyme-electrode interfacing in bioelectrocatalytic systems. *Trends in biotechnology* 2025, *43* (6), 1328-1355.

43. Yang, J.; Zheng, S.; Ma, D.; Zhang, T.; Huang, X.; Huang, S.; Chen, H.-j.; Wang, J.; Jiang, L.; Xie, X., Masticatory system–inspired microneedle theranostic platform for intelligent and precise diabetic management. *Science Advances* 2022, *8* (50), eabo6900.

44. Khan, A. Y.; Noronha, S. B.; Bandyopadhyaya, R., Superior performance of a carbon-paste electrode based glucose biosensor containing glucose oxidase enzyme in mesoporous silica powder. *Advanced Powder Technology* 2016, *27* (1), 85-92.

45. Xu, J.; Yang, K.; Zhang, X.; Lei, Y.; Meng, X.; Wang, Z., TiO_2/CeO_2-$CePO_4$-decorated enzymatic glucose biosensors operating in oxygen-restrictive environments. *Journal of Solid State Electrochemistry* 2021, *25* (7), 1937-1947.

46. Yang, P.-H.; Huang, J.-M.; Chang, Y.-S.; Chan, C.-T.; Hu, H.-J., Fabrication and Characterization of MgO-Based Enzymatic Glucose Biosensors. *IEEE Sensors Journal* 2023, *23* (23), 28587-28596.

47. Ahmadi, A.; Khoshfetrat, S. M.; Kabiri, S.; Fotouhi, L.; Dorraji, P. S.; Omidfar, K., Impedimetric paper-based enzymatic biosensor using electrospun cellulose acetate nanofiber and reduced graphene oxide for detection of glucose from whole blood. *IEEE sensors journal* 2021, *21* (7), 9210-9217.

48. Sakalauskiene, L.; Brasiunas, B.; Popov, A.; Kausaite-Minkstimiene, A.; Ramanaviciene, A., The Development of Reagentless Amperometric Glucose Biosensor Based on Gold Nanostructures, Prussian Blue and Glucose Oxidase. *Biosensors* 2023, *13* (10).

49. Guo, X.; Liang, B.; Jian, J.; Zhang, Y.; Ye, X., Glucose biosensor based on a platinum electrode modified with rhodium nanoparticles and with glucose oxidase immobilized on gold nanoparticles. *Microchimica Acta* 2014, *181*, 519-525.

50. Zhou, F.; Jing, W.; Liu, S.; Mao, Q.; Xu, Y.; Han, F.; Wei, Z.; Jiang, Z., Electrodeposition of gold nanoparticles on ZnO nanorods for improved performance of enzymatic glucose sensors. *Materials Science in Semiconductor Processing* 2020, *105*.

51. Thi Phong Thu, D.; Thi Xuan, C.; Oanh, V. T.; Viet, N. X.; Tu, L. M.; Loan, T. T.; Van Tuan, C.; Ha, N. H.; Thi Thanh Le, D.; Hoa, N. D., One-Step Method for the Direct Growth of NiO Nanoflowers on Pencil Graphite Electrode for Highly Sensitive Non-Enzymatic Glucose Sensing. *Journal of The Electrochemical Society* 2024, *171* (1).

52. Phasuksom, K.; Sirivat, A., Chronoampermetric detection of enzymatic glucose sensor based on doped polyindole/MWCNT composites modified onto screen-printed carbon electrode as portable sensing device for diabetes. *RSC advances* 2022, *12* (44), 28505-28518.

53. Yuwen, T.; Shu, D.; Zou, H.; Yang, X.; Wang, S.; Zhang, S.; Liu, Q.; Wang, X.; Wang, G.; Zhang, Y.; Zang, G., Carbon nanotubes: a powerful bridge for conductivity and flexibility in electrochemical glucose sensors. *Journal of nanobiotechnology* 2023, *21* (1), 320.

54. Zhou, F.; Jing, W.; Xu, Y.; Chen, Z.; Jiang, Z.; Wei, Z., Performance enhancement of ZnO nanorod-based enzymatic glucose sensor via reduced graphene oxide deposition and UV irradiation. *Sensors and Actuators B: Chemical* 2019, *284*, 377-385.

55. Settu, K.; Chiu, P. T.; Huang, Y. M., Laser-Induced Graphene-Based Enzymatic Biosensor for Glucose Detection. *Polymers* 2021, *13* (16).

56. German, N.; Ramanaviciene, A.; Ramanavicius, A., Dispersed Conducting Polymer Nanocomposites with Glucose Oxidase and Gold Nanoparticles for the Design of Enzymatic Glucose Biosensors. *Polymers* 2021, *13* (13).

57. Zeng, H.; Xie, Y.; Liu, T.; Chu, Z.; Dempsey, E.; Jin, W., Conductive polymer nanocomposites: recent advances in the construction of electrochemical biosensors. *Sensors & Diagnostics* 2024, *3* (2), 165-180.

58. Shrestha, B. K.; Ahmad, R.; Shrestha, S.; Park, C. H.; Kim, C. S., Globular Shaped Polypyrrole Doped Well-Dispersed Functionalized Multiwall Carbon Nanotubes/Nafion Composite for Enzymatic Glucose Biosensor Application. *Scientific reports* 2017, *7* (1), 16191.

59. Lee, I.; Probst, D.; Klonoff, D.; Sode, K., Continuous glucose monitoring systems - Current status and future perspectives of the flagship technologies in biosensor research. *Biosensors & bioelectronics* 2021, *181*, 113054.

60. Klonoff, D. C.; Ahn, D.; Drincic, A., Continuous glucose monitoring: A review of the technology and clinical use. *Diabetes research and clinical practice* 2017, *133*, 178-192.

61. Facchinetti, A., Continuous Glucose Monitoring Sensors: Past, Present and Future Algorithmic Challenges. *Sensors (Basel)* 2016, *16* (12).

62. Bai, J.; Liu, D.; Tian, X.; Wang, Y.; Cui, B.; Yang, Y.; Dai, S.; Lin, W.; Zhu, J.; Wang, J., Coin-sized, fully integrated, and minimally invasive continuous glucose monitoring system based on organic electrochemical transistors. *Science Advances* 2024, *10* (16), eadl1856.

63. Radwan, A. B.; Paramparambath, S.; Cabibihan, J. J.; Al-Ali, A. K.; Kasak, P.; Shakoor, R. A.; Malik, R. A.; Mansour, S. A.; Sadasivuni, K. K., Superior Non-Invasive Glucose Sensor Using Bimetallic CuNi Nanospecies Coated Mesoporous Carbon. *Biosensors* 2021, *11* (11).

64. Zhang, S.; Zhao, W.; Zeng, J.; He, Z.; Wang, X.; Zhu, Z.; Hu, R.; Liu, C.; Wang, Q., Wearable non-invasive glucose sensors based on metallic nanomaterials. *Materials today. Bio* 2023, *20*, 100638.

65. Qian, X.; Ko, A.; Li, H.; Liao, C., Flexible non-enzymatic glucose strip for direct non-invasive diabetic management. *Microchemical Journal* 2024, *197*, 109818.

66. Chen, Y.; Sun, Y.; Li, Y.; Wen, Z.; Peng, X.; He, Y.; Hou, Y.; Fan, J.; Zang, G.; Zhang, Y., A wearable non-enzymatic sensor for continuous monitoring of glucose in human sweat. *Talanta* 2024, *278*, 126499.

67. Su, Y.; Luo, B.; Zhang, J. Z., Controllable Cobalt Oxide/Au Hierarchically Nanostructured Electrode for Nonenzymatic Glucose Sensing. *Analytical chemistry* 2016, *88* (3), 1617-24.

68. Mohammadpour-Haratbar, A.; Mohammadpour-Haratbar, S.; Zare, Y.; Rhee, K. Y.; Park, S. J., A Review on Non-Enzymatic Electrochemical Biosensors of Glucose Using Carbon Nanofiber Nanocomposites. *Biosensors* 2022, *12* (11).

69. Tian, K.; Baskaran, K.; Tiwari, A., Nonenzymatic glucose sensing using metal oxides – Comparison of CuO, Co_3O_4, and NiO. *Vacuum* 2018, *155*, 696-701.

70. Lakshmy, S.; Santhosh, S.; Kalarikkal, N.; Rout, C. S.; Chakraborthy, B., A review of electrochemical glucose sensing based on transition metal phosphides. *Journal of Applied Physics* 2023, *133* (7).

71. Farid, A.; Khan, A. S.; Javid, M.; Usman, M.; Khan, I. A.; Ahmad, A. U.; Fan, Z.; Khan, A. A.; Pan, L., Construction of a binder-free non-enzymatic glucose sensor based on Cu@Ni core-shell nanoparticles anchored on 3D chiral carbon nanocoils-nickel foam hierarchical scaffold. *Journal of colloid and interface science* 2022, *624*, 320-337.

72. Iyer, K. A.; Tenchov, R.; Ralhan, K.; Bird, R. E.; Lotti Diaz, L. M.; Hughes, K. J.; Ganesan, M.; Ivanov, J. M.; Zhou, Q. A., Nanoscale Materials in Biomedical Applications of Sensors: Insights from a Comprehensive Landscape Analysis. *ACS Applied Nano Materials* 2025, *8* (3), 1305-1331.

73. Dong, Q.; Ryu, H.; Lei, Y., Metal oxide based non-enzymatic electrochemical sensors for glucose detection. *Electrochimica Acta* 2021, *370*.

74. Strakosas, X.; Selberg, J.; Pansodtee, P.; Yonas, N.; Manapongpun, P.; Teodorescu, M.; Rolandi, M., A non-enzymatic glucose sensor enabled by bioelectronic pH control. *Scientific reports* 2019, *9* (1), 10844.

75. Wei, L.; Li, J.-H.; Chen, C.; Lv, Q.; Lv, R.; Ma, L.; Shen, W.; Kang, F.; Huang, Z.-H., Ultrasensitive Non-Enzymatic Glucose Sensors Based on Hybrid Reduced Graphene Oxide and Carbonized Silk Fabric Electrodes Decorated with Cu Nanoflowers. *Journal of The Electrochemical Society* 2020, *167* (12).

76. Kim, S. E.; Yoon, J. C.; Tae, H. J.; Muthurasu, A., Electrospun Manganese-Based Metal-Organic Frameworks for MnO_x Nanostructures Embedded in Carbon Nanofibers as a High-Performance Nonenzymatic Glucose Sensor. *ACS omega* 2023, *8* (45), 42689-42698.

77. Fu, R.; Lu, Y.; Ding, Y.; Li, L.; Ren, Z.; Si, X.; Wu, Q., A novel non-enzymatic glucose electrochemical sensor based on CNF@Ni-Co layered double hydroxide modified glassy carbon electrode. *Microchemical Journal* 2019, *150*.

78. Miao, F.; Wu, W.; Miao, R.; Cong, W.; Zang, Y.; Tao, B., Graphene/nano-ZnO hybrid materials modify Ni-foam for high-performance electrochemical glucose sensors. *Ionics* 2018, *24* (12), 4005-4014.

79. Naikoo, G. A.; Awan, T.; Salim, H.; Arshad, F.; Hassan, I. U.; Pedram, M. Z.; Ahmed, W.; Faruck, H. L.; Aljabali, A. A. A.; Mishra, V.; Serrano-Aroca, A.; Goyal, R.; Negi, P.; Birkett, M.; Nasef, M. M.; Charbe, N. B.; Bakshi, H. A.; Tambuwala, M. M., Fourth-generation glucose sensors composed of copper nanostructures for diabetes management: A critical review. *Bioengineering & translational medicine* 2022, *7* (1), e10248.

80. Wu, B.; Xue, Q.; Fan, Y.; Cui, D.; Sun, Y.; Xu, B. B.; Wei, H.; Wasnik, P.; Sridhar, D.; Algadi, H., Multifunctional polymer nanocomposites for non-enzymatic glucose detection: a brief review. *ES Food & Agroforestry* 2023, *12* (4), 859.

81. Waqas, M.; Yang, L.; Wei, Y.; Sun, Y.; Yang, F.; Fan, Y.; Chen, W., Controlled fabrication of nickel and cerium mixed nano-oxides supported on carbon nanotubes for glucose monitoring. *Electrochimica Acta* 2023, *440*, 141735.

82. Ramesh, M.; Sankar, C.; Umamatheswari, S.; Balamurugan, J.; Jayavel, R.; Gowran, M., Hydrothermal synthesis of $ZnZrO_2$/chitosan ($ZnZrO_2$/CS) nanocomposite for highly sensitive detection of glucose and hydrogen peroxide. *International journal of biological macromolecules* 2023, *226*, 618-627.

83. Rashed, M. A.; Nayem, N.; Rahman, M. H.; Faisal, M.; Algethami, J. S.; Alsareii, S.; Islam, M. K.; Harraz, F. A., A sensitive, selective non-enzymatic electrochemical detection and kinetic study of glucose over Pt nanoparticles/SWCNTs/NiO ternary nanocomposite. *Journal of the Taiwan Institute of Chemical Engineers* 2023, *151*, 105113.

84. Deshmukh, M. A.; Kang, B.-C.; Ha, T.-J., Non-enzymatic electrochemical glucose sensors based on polyaniline/reduced-graphene-oxide nanocomposites functionalized with silver nanoparticles. *Journal of Materials Chemistry C* 2020, *8* (15), 5112-5123.

85. Lotfi, Z.; Gholivand, M.; Shamsipur, M., Non-enzymatic glucose sensor based on a g-C_3N_4/NiO/CuO nanocomposite. *Analytical biochemistry* 2021, *616*, 114062.

86. Chen, L.; Tiwari, S. R.; Zhang, Y.; Zhang, J.; Sun, Y., Facile Synthesis of Hollow MnO_2 Nanoparticles for Reactive Oxygen Species Scavenging in Osteoarthritis. *ACS biomaterials science & engineering* 2021, *7* (4), 1686-1692.

87. Lin, J.; Song, T.; Liu, Z.; Yang, D.; Xiang, R.; Hua, W.; Wan, H., Effects of biodegradable biomedical porous MnO_2 nanoparticles on blood components and functions. *Colloids and surfaces. B, Biointerfaces* 2022, *217*, 112667.

88. Li, Q.; Xia, Y.; Wan, X.; Yang, S.; Cai, Z.; Ye, Y.; Li, G., Morphology-dependent MnO_2/nitrogen-doped graphene nanocomposites for simultaneous detection of trace dopamine and uric acid. *Materials science & engineering. C, Materials for biological applications* 2020, *109*, 110615.

89. Song, X.; Wang, H.; Li, Z.; Du, C. F.; Guo, R., A Review of MnO_2 Composites Incorporated with Conductive Materials for Energy Storage. *Chem Rec* 2022, *22* (10), e202200118.

90. Hong, S.; Jin, S.; Deng, Y.; Garcia-Mendez, R.; Kim, K.-i.; Utomo, N.; Archer, L. A., Efficient Scalable Hydrothermal Synthesis of MnO_2 with Controlled Polymorphs and Morphologies for Enhanced Battery Cathodes. *ACS Energy Letters* 2023, *8* (4), 1744-1751.

91. Sohal, N.; Maity, B.; Shetti, N. P.; Basu, S., Biosensors Based on MnO_2 Nanostructures: A Review. *ACS Applied Nano Materials* 2021, *4* (3), 2285-2302.

92. Xiao, F.; Li, Y.; Gao, H.; Ge, S.; Duan, H., Growth of coral-like PtAu-MnO_2 binary nanocomposites on free-standing graphene paper for flexible nonenzymatic glucose sensors. *Biosensors & bioelectronics* 2013, *41*, 417-23.

93. Ponnusamy, R.; Gangan, A.; Chakraborty, B.; Late, D. J.; Rout, C. S., Improved Nonenzymatic Glucose Sensing Properties of Pd/MnO_2 Nanosheets: Synthesis by Facile Microwave-Assisted Route and Theoretical Insight from Quantum Simulations. *The journal of physical chemistry. B* 2018, *122* (31), 7636-7646.

94. Hao, L.; Li, S.-S.; Wang, J.; Tan, Y.; Bai, L.; Liu, A., MnO_2/multi-walled carbon nanotubes based nanocomposite with enhanced electrocatalytic activity for sensitive amperometric glucose biosensing. *Journal of Electroanalytical Chemistry* 2020, *878*.

95. Chang, H. W.; Dong, C. L.; Chen, Y. H.; Xu, Y. Z.; Huang, T. C.; Chen, S. C.; Liu, F. J.; Lai, Y. H.; Tsai, Y. C., Extended Graphite Supported Flower-like MnO_2 as Bifunctional Materials for Supercapacitors and Glucose Sensing. *Nanomaterials (Basel)* 2021, *11* (11).

96. Li, J.; Shen, H.; Yu, S.; Zhang, G.; Ren, C.; Hu, X.; Yang, Z., Synthesis of a manganese dioxide nanorod-anchored graphene oxide composite for highly sensitive electrochemical sensing of dopamine. *The Analyst* 2020, *145* (9), 3283-3288.

97. Guo, X.; Zhang, W.; Qian, C.; Yang, H.; Fan, T., MnO_2/C composite with 3D hierarchical architecture for high-performance supercapacitor electrodes. *Ceramics International* 2018, *44* (8), 9696-9702.

98. Xing, Y.; Dittrich, P. S., One-Dimensional Nanostructures: Microfluidic-Based Synthesis, Alignment and Integration towards Functional Sensing Devices. *Sensors (Basel)* 2018, *18* (1).

99. Wei, Q.; Xiong, F.; Tan, S.; Huang, L.; Lan, E. H.; Dunn, B.; Mai, L., Porous One-Dimensional Nanomaterials: Design, Fabrication and Applications in Electrochemical Energy Storage. *Adv Mater* 2017, *29* (20).

100. Chakraborty, P.; Dhar, S.; Deka, N.; Debnath, K.; Mondal, S. P., Non-enzymatic salivary glucose detection using porous CuO nanostructures. *Sensors and Actuators B: Chemical* 2020, *302*.

101. Sumboja, A.; Ge, X.; Goh, F. W. T.; Li, B.; Geng, D.; Hor, T. S. A.; Zong, Y.; Liu, Z., Manganese Oxide Catalyst Grown on Carbon Paper as an Air Cathode for High-Performance Rechargeable Zinc-Air Batteries. *ChemPlusChem* 2015, *80* (8), 1341-1346.

102. Kitchaev, D. A.; Dacek, S. T.; Sun, W.; Ceder, G., Thermodynamics of Phase Selection in MnO_2 Framework Structures through Alkali Intercalation and Hydration. *Journal of the American Chemical Society* 2017, *139* (7), 2672-2681.

103. Shin, J.; Seo, J. K.; Yaylian, R.; Huang, A.; Meng, Y. S., A review on mechanistic understanding of MnO_2 in aqueous electrolyte for electrical energy storage systems. *International Materials Reviews* 2019, *65* (6), 356-387.

104. Weina, X.; Guanlin, L.; Chuanshen, W.; Hu, C.; Wang, X., A novel β-MnO_2 micro/nanorod arrays directly grown on flexible carbon fiber fabric for high-performance enzymeless glucose sensing. *Electrochimica Acta* 2017, *225*, 121-128.

105. Yuan, Y.; Nie, A.; Odegard, G. M.; Xu, R.; Zhou, D.; Santhanagopalan, S.; He, K.; Asayesh-Ardakani, H.; Meng, D. D.; Klie, R. F.; Johnson, C.; Lu, J.; Shahbazian-Yassar, R., Asynchronous Crystal Cell Expansion during Lithiation of K^+-Stabilized alpha-MnO_2. *Nano letters* 2015, *15* (5), 2998-3007.

106. Zhu, G.; Zhu, J.; Li, W.; Yao, W.; Zong, R.; Zhu, Y.; Zhang, Q., Tuning the K^+ Concentration in the Tunnels of α-MnO_2 To Increase the Content of Oxygen Vacancy for Ozone Elimination. *Environmental science & technology* 2018, *52* (15), 8684-8692.

107. Zhao, Y.; Dai, M.; Zhao, D.; Xiao, L.; Wu, X.; Liu, F., Asymmetric pseudo-capacitors based on dendrite-like MnO_2 nanostructures. *CrystEngComm* 2019, *21* (21), 3349-3355.

108. Zhang, Y.; Mao, T.; Cheng, L.; Wu, H.; Wu, R.; Zheng, L., Tunable morphology and property of a MnO_2/carbonized cotton textile hybrid electrode for electrochemical capacitors. *Journal of Alloys and Compounds* 2017, *729*, 655-662.

109. Li, X.; Wang, L.; You, W.; Xing, L.; Yang, L.; Yu, X.; Zhang, J.; Li, Y.; Che, R., Enhanced polarization from flexible hierarchical MnO_2 arrays on cotton cloth with excellent microwave absorption. *Nanoscale* 2019, *11* (28), 13269-13281.

110. Deng, J.; Ge, Y.; Tan, C.; Wang, H.; Li, Q.; Zhou, S.; Zhang, K., Degradation of ciprofloxacin using α-MnO_2 activated peroxymonosulfate process: Effect of water constituents, degradation intermediates and toxicity evaluation. *Chemical Engineering Journal* 2017, *330*, 1390-1400.

111. Govindaraj, M.; Srivastava, A.; Muthukumaran, M. K.; Tsai, P. C.; Lin, Y. C.; Raja, B. K.; Rajendran, J.; Ponnusamy, V. K.; Arockia Selvi, J., Current advancements and prospects of enzymatic and non-enzymatic electrochemical glucose sensors. *International journal of biological macromolecules* 2023, *253* (Pt 2), 126680.

112. Hamoudi, Z.; Khakani, M. A. E.; Mohamedi, M., Binderless Nanothin Catalyst Layers for Next Generation of Micro-Fuel Cells: Concept, Fabrication, Results and Prospective. *Journal of The Electrochemical Society* 2012, *159* (3), B331-B339.

113. Tabet-Aoul, A.; Mohamedi, M., 3D hierarchical cauliflower-like carbon nanotubes/platinum–tin nanostructure and its electrocatalytic activity for ethanoloxidation. *J. Mater. Chem.* 2012, *22* (6), 2491-2497.

114. Gougis, M.; Tabet-Aoul, A.; Ma, D.; Mohamedi, M., Laser synthesis and tailor-design of nanosized gold onto carbon nanotubes for non-enzymatic electrochemical glucose sensor. *Sensors and Actuators B: Chemical* 2014, *193*, 363-369.

115. Impedans Plasma Measurement Sputtering. https://www.impedans.com/sputtering/ (accessed 2025).

116. Li, Q.; Yan, H.; Zhang, J.; Liu, Z., Effect of hydrocarbons precursors on the formation of carbon nanotubes in chemical vapor deposition. *Carbon* 2004, *42* (4), 829-835.

117. Afsarimanesh, N.; Nag, A.; Eshrat e Alahi, M.; Sarkar, S.; Mukhopadhyay, S.; Sabet, G. S.; Altinsoy, M. E., A critical review of the recent progress on carbon nanotubes-based nanogenerators. *Sensors and Actuators A: Physical* 2022, *344*.

118. Wang, X.-D.; Vinodgopal, K.; Dai, G.-P., Synthesis of Carbon Nanotubes by Catalytic Chemical Vapor. *Perspective of carbon nanotubes* 2019, 13.

119. Kumar, M.; Ando, Y., Chemical vapor deposition of carbon nanotubes: a review on growth mechanism and mass production. *Journal of nanoscience and nanotechnology* 2010, *10* (6), 3739-58.

120. Gupta, T.; Samriti; Cho, J.; Prakash, J., Hydrothermal synthesis of TiO_2 nanorods: formation chemistry, growth mechanism, and tailoring of surface properties for photocatalytic activities. *Materials Today Chemistry* 2021, *20*.

121. Li, Y.; Wang, J.; Zhang, Y.; Banis, M. N.; Liu, J.; Geng, D.; Li, R.; Sun, X., Facile controlled synthesis and growth mechanisms of flower-like and tubular MnO_2 nanostructures by microwave-assisted hydrothermal method. *Journal of colloid and interface science* 2012, *369* (1), 123-8.

122. Xu, Z.; Sun, S.; Cui, W.; Lv, J.; Geng, Y.; Li, H.; Deng, J., Interconnected network of ultrafine MnO_2 nanowires on carbon cloth with weed-like morphology for high-performance supercapacitor electrodes. *Electrochimica Acta* 2018, *268*, 340-346.

123. Williams, D. B.; Carter, C. B., Transmission electron microscopy. *Systematic Materials Analysis* 1978, *4*, 407.

124. NanoScience Instruments Scanning Electron Microscopy. https://www.nanoscience.com/techniques/scanning-electron-microscopy/ (accessed 2025).

125. Mohammed, A.; Abdullah, A. In *Scanning electron microscopy (SEM): A review*, Proceedings of the 2018 international conference on hydraulics and pneumatics—HERVEX, Băile Govora, Romania, 2018; pp 7-9.

126. Hurt, R. Scanning electron microscope. https://en.wikipedia.org/wiki/Scanning_electron_microscope#/media/File:Electron_emission_mechanisms.svg (accessed 2025).

127. Bijelic, A.; Rompel, A., Polyoxometalates: more than a phasing tool in protein crystallography. *Chemtexts* 2018, *4* (3), 10.

128. Pandey, A.; Dalal, S.; Dutta, S.; Dixit, A., Structural characterization of polycrystalline thin films by X-ray diffraction techniques. *Journal of Materials Science: Materials in Electronics* 2021, *32*, 1341-1368.

129. Wu, L.; Tang, X.; Wu, T.; Zeng, W.; Zhu, X.; Hu, B.; Zhang, S., A review on current progress of Raman-based techniques in food safety: From normal Raman spectroscopy to SESORS. *Food Res Int* 2023, *169*, 112944.

130. Bumbrah, G. S.; Sharma, R. M., Raman spectroscopy–Basic principle, instrumentation and selected applications for the characterization of drugs of abuse. *Egyptian Journal of Forensic Sciences* 2016, *6* (3), 209-215.

131. Edinburgh Instruments What is Raman Spectroscopy? https://www.edinst.com/resource/what-is-raman-spectroscopy/ (accessed 2025).

132. Renishaw apply innovation What is Raman scattering. https://www.renishaw.com/de/what-is-raman-scattering--25805.

133. Roy, A.; Ray, A.; Saha, S.; Ghosh, M.; Das, T.; Nandi, M.; Lal, G.; Das, S., Influence of electrochemical active surface area on the oxygen evolution reaction and energy storage performance of MnO_2-multiwalled carbon nanotube composite. *International Journal of Energy Research* 2021, *45* (11), 16908-16921.

134. Connor, P.; Schuch, J.; Kaiser, B.; Jaegermann, W., The Determination of Electrochemical Active Surface Area and Specific Capacity Revisited for the System MnO_x as an Oxygen Evolution Catalyst. *Zeitschrift für Physikalische Chemie* 2020, *234* (5), 979-994.

135. Zhang, F.; Liu, T.; Zhang, J.; Cui, E.; Yue, L.; Jiang, R.; Hou, G., The potassium hydroxide-urea synergy in improving the capacitive energy-storage performance of agar-derived carbon aerogels. *Carbon* 2019, *147*, 451-459.

136. Ji, H.; Zhao, X.; Qiao, Z.; Jung, J.; Zhu, Y.; Lu, Y.; Zhang, L. L.; MacDonald, A. H.; Ruoff, R. S., Capacitance of carbon-based electrical double-layer capacitors. *Nature communications* 2014, *5*, 3317.

137. Gao, T.; Glerup, M.; Krumeich, F.; Nesper, R.; Fjellvåg, H.; Norby, P., Microstructures and spectroscopic properties of cryptomelane-type manganese dioxide nanofibers. *The Journal of Physical Chemistry C* 2008, *112* (34), 13134-13140.

138. Chen, Q.; Li, J.; Liao, C.; Liang, W.; Lou, X.; Liu, Z.; Zhang, J.; Tang, Y.; Mai, L.; Zhou, L.; Amine, K., High mass loading potassium ion stabilized manganese dioxide nanowire forests for rechargeable Zn batteries. *Nano Energy* 2024, *126*.

139. Li, D.; Zhao, L.; Xia, Q.; Wang, J.; Liu, X.; Xu, H.; Chou, S., Activating MoS_2 Nanoflakes via Sulfur Defect Engineering Wrapped on CNTs for Stable and Efficient Li-O_2 Batteries. *Advanced Functional Materials* 2021, *32* (8).

140. Sun, Z.; Fang, S.; Hu, Y. H., 3D Graphene Materials: From Understanding to Design and Synthesis Control. *Chemical reviews* 2020, *120* (18), 10336-10453.

141. Lara-Romero, J.; Ocampo-Macias, T.; Martínez-Suarez, R.; Rangel-Segura, R.; López-Tinoco, J.; Paraguay-Delgado, F.; Alonso-Nuñez, G.; Jiménez-Sandoval, S.; Chiñas-Castillo, F., Parametric Study of the Synthesis of Carbon Nanotubes by Spray Pyrolysis of a Biorenewable Feedstock: α-Pinene. *ACS Sustainable Chemistry & Engineering* 2017, *5* (5), 3890-3896.

142. Wang, F.; Deng, J.; Impeng, S.; Shen, Y.; Yan, T.; Chen, G.; Shi, L.; Zhang, D., Unraveling the effects of the coordination number of Mn over α-MnO_2 catalysts for toluene oxidation. *Chemical Engineering Journal* 2020, *396*.

143. Yuan, Y.; Zhan, C.; He, K.; Chen, H.; Yao, W.; Sharifi-Asl, S.; Song, B.; Yang, Z.; Nie, A.; Luo, X.; Wang, H.; Wood, S. M.; Amine, K.; Islam, M. S.; Lu, J.; Shahbazian-Yassar, R., The influence of large cations on the electrochemical properties of tunnel-structured metal oxides. *Nature communications* 2016, *7*, 13374.

144. King'ondu, C. K.; Opembe, N.; Chen, C.-h.; Ngala, K.; Huang, H.; Iyer, A.; Garcés, H. F.; Suib, S. L., Manganese Oxide Octahedral Molecular Sieves (OMS-2) Multiple Framework Substitutions: A New Route to OMS-2 Particle Size and Morphology Control. *Advanced Functional Materials* 2011, *21* (2), 312-323.

145. Ingole, S. M.; Navale, S. T.; Navale, Y. H.; Dhole, I. A.; Mane, R. S.; Stadler, F. J.; Patil, V. B., Galvanostatically electroplated MnO_2 nanoplate-type electrode for potential electrochemical pseudocapacitor application. *Journal of Solid State Electrochemistry* 2017, *21* (6), 1817-1826.

146. Wei, W.; Cui, X.; Chen, W.; Ivey, D. G., Manganese oxide-based materials as electrochemical supercapacitor electrodes. *Chem Soc Rev* 2011, *40* (3), 1697-721.

147. Zhou, Y.; Cheng, X.; Tynan, B.; Sha, Z.; Huang, F.; Islam, M. S.; Zhang, J.; Rider, A. N.; Dai, L.; Chu, D.; Wang, D.-W.; Han, Z.; Wang, C.-H., High-performance hierarchical MnO_2/CNT electrode for multifunctional supercapacitors. *Carbon* 2021, *184*, 504-513.

148. Saleh Ahammad, A. J.; Lee, J. J.; Rahman, M. A., Electrochemical sensors based on carbon nanotubes. *Sensors (Basel)* 2009, *9* (4), 2289-319.

149. Hamelin, A.; Sottomayor, M.; Silva, F.; Chang, S.-C.; Weaver, M. J., Cyclic voltammetric characterization of oriented monocrystalline gold surfaces in aqueous alkaline solution. *Journal of electroanalytical chemistry and interfacial electrochemistry* 1990, *295* (1-2), 291-300.

150. Burke, L. D.; Nugent, P. F., The electrochemistry of gold: I the redox behaviour of the metal in aqueous media. *Gold Bull* 1997, *30*, 43.

151. Larew, L. A.; Johnson, D. C., Concentration dependence of the mechanism of glucose oxidation at gold electrodes in alkaline media. *Journal of electroanalytical chemistry and interfacial electrochemistry* 1989, *262* (1-2), 167-182.

152. Adzic, R.; Hsiao, M.; Yeager, E., Electrochemical oxidation of glucose on single crystal gold surfaces. *Journal of electroanalytical chemistry and interfacial electrochemistry* 1989, *260* (2), 475-485.

153. Brouzgou, A.; Tsiakaras, P., Electrocatalysts for Glucose Electrooxidation Reaction: A Review. *Topics in Catalysis* 2015, *58* (18-20), 1311-1327.

154. Nikolaeva, N.; Khazova, O.; Vasil'ev, Y. B., Main characteristics of glucose electrooxidation on a gold anode. *Elektrokhimiya* 1983, *19*, 1042-1048.

155. Gougis, M.; Pereira, A.; Ma, D.; Mohamedi, M., Oxygen Gas Assisted Laser Deposition of Gold Thin Films: Electrooxidation of Glucose. *International Journal of Electrochemical Science* 2014, *9* (7), 3588-3601.

156. Olejnik, A.; Karczewski, J.; Dołęga, A.; Siuzdak, K.; Grochowska, K., Insightful Analysis of Phenomena Arising at the Metal|Polymer Interphase of Au-Ti Based Non-Enzymatic Glucose Sensitive Electrodes Covered by Nafion. *Coatings* 2020, *10* (9).

157. Cheng, P.; Wang, H.; Shi, X., The effect of phenylalanine ligands on the chiral-selective oxidation of glucose on Au(111). *Nanoscale* 2020, *12* (5), 3050-3057.

158. Pasta, M.; La Mantia, F.; Cui, Y., Mechanism of glucose electrochemical oxidation on gold surface. *Electrochimica Acta* 2010, *55* (20), 5561-5568.

159. Yin, X.; Chen, K.; Cheng, H.; Chen, X.; Feng, S.; Song, Y.; Liang, L., Chemical Stability of Ascorbic Acid Integrated into Commercial Products: A Review on Bioactivity and Delivery Technology. *Antioxidants (Basel)* 2022, *11* (1).

160. Miah, M. R.; Masud, J.; Ohsaka, T., In situ fabricated iodine-adlayer assisted selective electrooxidation of uric acid in alkaline media. *Electrochimica Acta* 2008, *54* (2), 316-321.

161. Arvand, M.; Pourhabib, A.; Giahi, M., Square wave voltammetric quantification of folic acid, uric acid and ascorbic acid in biological matrix. *Journal of pharmaceutical analysis* 2017, *7* (2), 110-117.

162. Guo, C.; Li, H.; Zhang, X.; Huo, H.; Xu, C., 3D porous CNT/MnO_2 composite electrode for high-performance enzymeless glucose detection and supercapacitor application. *Sensors and Actuators B: Chemical* 2015, *206*, 407-414.

163. Bard, A. J.; Faulkner, L. R.; White, H. S., *Electrochemical methods: fundamentals and applications*. John Wiley & Sons: 2022.

164. Conen, K.; Scanni, R.; Gombert, M. T.; Hulter, H. N.; Krapf, R., Effects of potassium citrate or potassium chloride in patients with combined glucose intolerance: A placebo-controlled pilot study. *Journal of diabetes and its complications* 2016, *30* (6), 1158-61.

165. Kettritz, R.; Loffing, J., Potassium homeostasis - Physiology and pharmacology in a clinical context. *Pharmacology & therapeutics* 2023, *249*, 108489.

166. Thatikayala, D.; Ponnamma, D.; Sadasivuni, K. K.; Cabibihan, J. J.; Al-Ali, A. K.; Malik, R. A.; Min, B., Progress of Advanced Nanomaterials in the Non-Enzymatic Electrochemical Sensing of Glucose and H_2O_2. *Biosensors* 2020, *10* (11).

167. Yang, Y. J.; Hu, S., Electrodeposited MnO_2/Au composite film with improved electrocatalytic activity for oxidation of glucose and hydrogen peroxide. *Electrochimica Acta* 2010, *55* (10), 3471-3476.

168. Hosseini, H.; Rezaei, S. J. T.; Rahmani, P.; Sharifi, R.; Nabid, M. R.; Bagheri, A., Nonenzymatic glucose and hydrogen peroxide sensors based on catalytic properties of palladium nanoparticles/poly(3,4-ethylenedioxythiophene) nanofibers. *Sensors and Actuators B: Chemical* 2014, *195*, 85-91.

9 APPENDIX

List of scientific paper publications during the thesis

1. Ahmed, K. H.; Mohamedi, M., Microfibrous Carbon Paper Decorated with High-Density Manganese Dioxide Nanorods: An Electrochemical Nonenzymatic Platform of Glucose Sensing. Sensors 2024, 24 (18), 5864.
2. Ahmed, K. H.; Zuria, A. M.; Mohamedi, M., Integration of Carbon Nanotubes into Manganese Dioxide Nanorods for Enhanced Enzymeless Electrochemical Glucose Sensing with High Sensitivity and Selectivity. Biosensors 2025, 15 (4), 215.

Conference presentations

1. Khawtar Hasan Ahmed, Xiaoying Zheng, Mohamed Mohamedi, Development of Carbon-Based Manganese Dioxide for the Electrochemical Sensing of Glucose, Poster; ECS Canada Section 2021 Fall Symposium; November 27, 2021.
2. Khawtar Hasan Ahmed, Xiaoying Zheng, Mohamed Mohamedi, Fourth Generation Non-Enzymatic Electrochemical Sensors for Diabetes Monitoring, Poster; INRS Scientific Day; February 18, 2022.
3. Khawtar Hasan Ahmed, Alonso Moreno Zuria, Mohamed Mohamedi, Enhanced Electrochemical Nonenzymatic Glucose Sensing Using Microfibrous Carbon Paper Decorated with High-Density Manganese Dioxide Nanorods and Integrated Carbon Nanotubes for High Sensitivity and Selectivity, Poster; 247th ECS Meeting; May 18-22, 2025.